On the Role of Conformational Dynamics in Allostery and Cooperativity in Protein Kinase A

A Dissertation
SUBMITTED TO THE FACULTY OF
UNIVERSITY OF MINNESOTA
BY

Geoffrey Chan Li

IN PARTIAL FULFILLMENT OF THE REQUIREMENTS
FOR THE DEGREE OF
DOCTOR OF PHILOSOPHY

Dr. Gianluigi Veglia

February 2017

Acknowledgements

This work would not have been possible without the support and contribution of many people. First and foremost, I would like to express my deepest gratitude to my advisor and mentor, Dr. Gianluigi Veglia, for his guidance and patience with me throughout my graduate school. His persistent motivation has pushed me to become a better scientist and has challenged me to overcome the seemingly insurmountable obstacles. I am grateful for the training that I had in his lab.

I would like to acknowledge the previous and current members of the Veglia lab who have helped me along the journey. I am thankful to Dr. Larry Masterson and Dr. Frank Chao for training me when I first joined the group. I would like to thank Dr. Jonggul Kim for his excellent insights and continued assistance in accomplishing this work. I am especially grateful to Dr. Atul Srivastava and Dr. Manu Veliparambil Subrahmanian for our fruitful discussions, for their constant motivation, and for being such great friends. I also would like to thank Dr. Cristina Olivieri for our great collaboration, for the camaraderie, and for being helpful in times of need. I am also indebted to Dr. Youlin Xia for his exceptional assistance in helping me run my NMR experiments. I also would like to acknowledge my awesome undergraduates, Callahan Clark and Mitchell Hesse, for their aid in the lab and for allowing me to mentor them.

I am honored to be given the opportunity to work with different collaborators. I thank Dr. Matthew Neibergall from Bethel University for his great help and encouragement. I also would like to thank Dr. Joseph Muretta from the Thomas lab for training me with fluorescence spectroscopy. I am also thankful to Dr. Michael Walters from the Center for Drug Design for providing me the balanol.

I am thankful to my friends outside of my work who made my Minnesota life a remarkable experience, particularly, Johnny, Tony, Chendong, Tien, Fadel, Alex, and Pastor Malone. Their constant support has alleviated my stress in graduate school. Last but not the least, I would like to thank my brother, Lance, and my mother, Caridad, for their unrelenting encouragement.

Ad majorem Dei gloriam

Dedication

This work is especially dedicated to my loving mother, Caridad Li, who is currently fighting cancer while I am finishing this work. Though we're thousands of miles apart, her unparalleled sacrifices and unconditional love have inspired me to persevere to achieve my goals. I love you and this work is for you…

ABSTRACT

Protein kinases are a large class of enzymes that regulate a wide array of vital cellular processes. Their dysregulation has been associated with fatal diseases including cancer, cardiovascular, and metabolic diseases. Hence, they have been important drug targets for years. While an enormous wealth of information about the structure and functions of kinases is available to date, a comprehensive mechanism of allosteric regulation of activity remains elusive. This thesis aims to investigate the role of conformational dynamics in the allosteric regulation and binding cooperativity of kinases using the cAMP-dependent protein kinase (PKA) as a model system. In this work, we demonstrated how allostery in PKA is propagated by changes in the hydrogen bond network between residues. We showed that different nucleotides and inhibitors modulate the allosteric cooperativity of PKA to different extent. Using NMR spectroscopy, we established how ligands influence substrate binding affinity by altering the kinase's conformational dynamics through suppression and formation of sparsely-populated high-energy states. The findings of this work provide a new paradigm for designing more effective therapeutic agents that can steer the conformational landscape of kinases to better fine-tune their activity and functions.

Table of Contents

List of Tables

List of Figures

CHAPTER 1 INTRODUCTION

1.1 Cyclic AMP-dependent Protein Kinase A

1.1.1 Architecture and Function

Protein kinases are an important class of enzymes responsible for catalyzing phosphoryl transfer. Protein phosphorylation, which is the transfer of the γ-phosphate group from adenosine triphosphate (ATP) to the hydroxyl group of serine, threonine, or tyrosine residues, represents a vital regulatory mechanism in modulating the activities of a multitude of proteins central to cell survival and growth in eukaryotic cells [1]. In fact, protein kinases constitute 2% of the human genome and approximately 30% of human proteins are phosphorylated [2]. Since these proteins are involved in crucial cellular processes such as cell cycle, cell proliferation, metabolism, and muscle contractility [3], improper regulation of protein kinases is associated with fatal diseases including cancer, cardiovascular diseases, and diabetes [4-7].

Among the 518 known protein kinases in the mammalian genome [2], the catalytic subunit of the cyclic-AMP dependent protein kinase A (PKA) was the first protein kinase to be crystallized [8, 9]. In the inactive state, PKA exists as a heterotetrameric holoenzyme consisting of two catalytic (PKA-C) and two regulatory (PKA-R) subunits, which, upon cyclic AMP binding, dissociate to release the active catalytic subunits [10, 11]. PKA is a serine/threonine phosphoryl transferase that recognizes the amino acid sequence R-R-X-S/T-Ψ where X is any amino acid and Ψ is a hydrophobic residue [12, 13]. The core of the catalytic subunit of PKA consists of a small lobe (N-lobe), and a large lobe (C-lobe). These lobes are connected by a linker, and flanked by two motifs, a helical motif in the N-terminus (αA) and a loosely structured tail in the C-terminus, which wraps around the kinase (Figure 1.1)[8, 9, 14]. Its bilobal architecture is highly conserved in the eukaryotic protein kinase (EPK) superfamily. Hence, it serves as a model kinase where basic biophysical questions widely applicable for the EPK superfamily can be addressed. The small lobe, consisting of five antiparallel β strands and a conserved helix (αC helix), binds and orients the phosphates of ATP for efficient phosphoryl transfer, while the large lobe, which is mainly α-helical, provides the

scaffold for substrate binding [14]. Between the two lobes lies the active site cleft, composed of several loops and short β-strands, where most of the conserved residues converge to orchestrate the phosphoryl transfer.

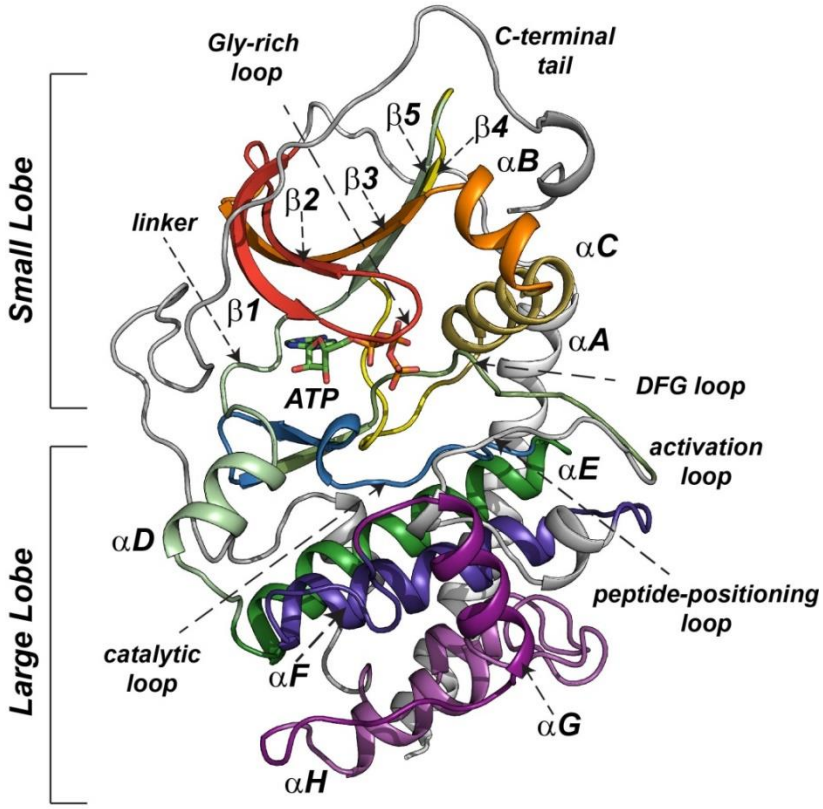

Figure 1.1. Architecture of the catalytic subunit of cAMP-dependent protein kinase.
The subdomains of PKA-C, color-coded according to the regions defined by Hanks and Hunter [15]. The catalytic subunit is composed of a small lobe or N-lobe that binds and orients ATP for phosphoryl transfer, and a large lobe or C-lobe that serves as a docking site for substrate. Between the two lobes is the active site cleft where most conserved residues important for catalysis converge. PDB ID: 1ATP.

Within the small lobe is the highly dynamic glycine-rich loop (GxGxxG), whose orientation correlates with the opening and closing of the active site cleft during catalysis [14]. The backbone amide group of Ser53 in this loop orients the γ-phosphate of ATP for transfer (**Figure 1.2A**). Another key element in the small lobe is the highly conserved C-helix, which brings the different segments of the kinase together and whose orientation determines kinase activity. The C-helix in an active kinase must be positioned properly such that its conserved Glu91 will form an ion pair with the conserved Lys72 of β-strand 3, which interacts with the α and β phosphates of ATP (**Figure 1.2B**). In the inactive

conformation, the C-helix is either disordered or rotated out with Glu91 residue facing the solvent [16, 17]. This configuration is typical of inactive kinases, such as Src-family tyrosine kinases and the cyclin-dependent kinases. For cyclin-dependent kinases, the C-helix is normally displaced from the active site and the conserved salt-bridge is not formed [18]. Only upon binding of cyclin does the C-helix undergo a conformational change to position the Glu51 in the active state [19] (**Figure 1.2C**). In addition, the C-helix also interacts with the different domains of the kinase. For PKA, His87 interacts with the phosphorylated Thr197 in the activation loop in the closed conformation; Lys92 forms an ion pair with the carboxylate ion of the C-terminal residue Phe350; and the side chain of Arg93 forms a cation-π interaction with the aromatic ring of Trp30 of the A-helix (**Figure 1.2B**). All these interactions are important to stabilize the C-helix in the orientation that is optimal for catalysis [14].

The linker region (residues 120-127) interacts with the adenine ring of ATP by hydrogen bonding between backbone carbonyl of Glu121 and N6 of the adenine ring, and backbone amide of Val123 and N1 of the adenine ring, while the side chain of Glu127 interacts with the 2' and 3' OH groups of the ribose ring (**Figure 1.2A**). Most ATP-competitive inhibitors bind in the hydrophobic pocket occupied by the adenine ring and form hydrogen bonds with one or more residues in the linker region.

The large lobe, on the other hand, contains conserved loops situated at the active site cleft that play a pivotal role in catalysis (**Figure 1.2A**). The catalytic loop (residues 166-171) contains Asp166 that functions as a catalytic base, Lys168 that interacts with the γ-phosphate of ATP, and Asn171 that interacts with the secondary Mg^{2+} ion (termed Mg2) that is coordinated with the α and γ phosphates of ATP. The conserved DFG loop (residues 184-187) includes the Asp184 that binds to the primary Mg^{2+} ion (termed Mg1) that bridges the β and γ phosphates of ATP. The activation loop contains the phosphorylation site Thr197 that, upon phosphorylation, becomes more ordered and shifts the enzyme in an active conformation. The peptide positioning loop (or P + 1 loop) provides the site for the tethering of the substrate. Specifically, the side chains of Leu198, Pro202, and Leu205 form a hydrophobic pocket for the P + 1 residue of substrate (**Figure 1.2D**). Glu203 binds with the P-6 Arg, and Tyr204 makes a hydrogen bond with Glu230, which binds with the P-2 Arg of the substrate. The entire segment from DFG loop to the conserved APE motif, better known as the activation

segment, is one of the two elements that distinguish eukaryotic from eukaryotic-like kinases in prokaryotes [20, 21]. The activation segment is fixed to the F helix via the conserved ion pair interaction between Glu208 of the APE motif and Arg280 (F**igure 1.2D**).

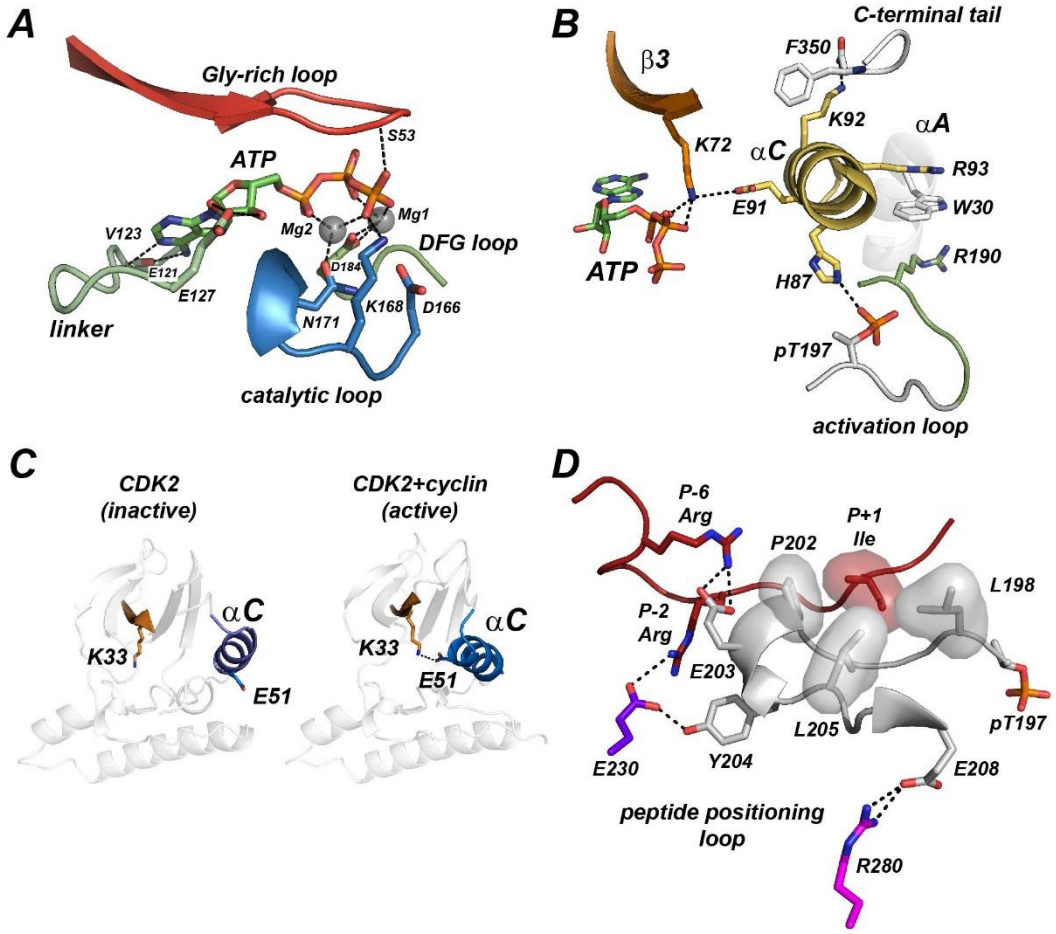

Figure 1.2. Important motifs in eukaryotic protein kinases.
(A) Interactions between ATP and residues in the active site cleft. (B) Interactions of the side chains of the αC residues with different motifs of the protein. (C) The orientation of the C-helix, that is important for the activity of kinases such as CDK2, is determined by the formation of the conserved salt bridge between Lys in β3 and Glu in αC. (D) Interactions between the peptide positioning loop and pseudosubstrate, as well as other motifs of the large lobe of PKA-C. PDB ID: 1HCL (inactive CDK2), 1FIN (active CDK2), 1ATP (PKA)

At the core of the large lobe are the highly stable helices (αE, αF, and αH) that are found to be resistant to H/D exchange (except for αG) [22]. The highly hydrophobic

F-helix, located at the interior of the large lobe, serves as a hub where the stacks of hydrophobic side chains traversing both lobes called spines (discussed later) are firmly anchored and helps secure the key residues for substrate binding, catalysis, and regulation[23]. The G, H, and I helices (termed as GHI subdomain), unique to eukaryotic protein kinases, serve as a docking site for substrate or regulatory proteins [20, 24].

Flanking either end of PKA-C are two segments that optimize the catalytic efficiency and increase the stability of the enzyme. The N-terminal segment, contains a myristoylation motif (GNAAAAK) followed by an amphipathic A-helix (residues 10-30). The A-helix tethers to the C-helix through cation-π interactions between Trp30 and the side chains of Arg93 (C-helix) and Arg190 (β-strand 9) [25] (**Figure 1.2B**). The N-terminal portion is also the site of different post-translational modifications including myristoylation of N-terminal Gly, deamidation of Asn2, and phosphorylation at Ser10 [14]. On the other hand, the C-terminal tail consists of a flexible segment that wraps around both lobes with each end firmly anchored to each lobe. The C-terminal tail has been described into three main segments: N-lobe tether (residues 340-350), active site tether (residues 320-339), and the C-lobe tether (residues 300-319) [26]. The N-lobe tether contains the FxxF motif at the C-terminus, which is found to be the recognition site of PDK1, docks into the hydrophobic or PDK1 interacting fragment (PIF) pocket in the small lobe and contributes to the stability of the C-helix [27]. The portion of the active site tether composed of residues 320-327 acts as a gate that controls entry and exit of ATP [28], while that containing residues 328-334 contains an acidic cluster that helps attract basic substrates to the active site with Tyr330 participating in the P-3 recognition site upon adopting a closed conformation [29]. Within the C-terminal tail is another phosphorylation site, Ser338, which is performed in a cis-fashion, i.e. its active site catalyzes its own phosphorylation, during the kinase maturation process and is critical for a fully functional kinase [30].

Although the analysis of structure-function relationships illuminated many of the conserved features of kinases, the role of many highly conserved residues has been difficult to rationalize on the basis of the primary sequence alone. Using a bioinformatics method, known as local spatial pattern alignment, Kornev and Taylor aligned several structures of Ser/Thr and Tyr kinases in their active and inactive states, and identified a series of residues that were highly conserved spatially. These motifs, which were

hydrophobic in nature, were named as spines [16, 23, 31, 32](**Figure 1.3**). Eventually, a unifying hypothesis by which eukaryotic protein kinases are activated or inactivated through the assembly and disassembly of these hydrophobic spines has been proposed [16, 23, 32]. In PKA, the regulatory or R-spine is composed of two residues from the N-lobe: Leu95 from C-helix and Leu106 from β strand 4, and two residues from the C-lobe: Tyr164 from the HRD (or YRD for PKA) motif of the catalytic loop and Phe185 from DFG loop (**Figure 1.3A**). Protein kinases constantly switch between active (assembled R spine) and inactive (broken R spine) states. Disassembly of R spine (**Figure 1.3B**) most commonly stem from flipping of the phenylalanine residue of the DFG loop ("DFG-out" conformation) or displacement of C-helix. Either phosphorylation of activation loop, which would bring the phenylalanine side chain in the DFG loop in its proper conformation ("DFG-in"), or binding of regulatory molecules such as cyclins for CDK2, which would fix the alignment of C-helix, would assemble the R-spine (**Figure 1.2C**). On the other hand, the catalytic or C-spine, composed of Val57, Ala70, Met128, Leu172, Leu173, Ile174, Leu227, and Met231, is completed by the adenine ring upon ATP binding, where it fuses the side chains of the C-spine, coupling the two lobes of the kinase together and committing it to catalysis (**Figure 1.3A**). Both of the spines are docked into the highly hydrophobic F-helix, fixing the positions of the nucleotide, substrate, and the residues in the catalytic machinery [23]. The hydrophobic side chains surrounding the spine, termed as *shell*, contribute to the catalytic activity of the enzyme by stabilizing the R-spine residues in the small lobe. In PKA, the shell residues include Val104, Met120 (also known as gatekeeper residue), and Met118 [16].

Using the hydrophobic spine model, kinases can be viewed as having two functions: the canonical (or catalytic) function, which is the transfer of phosphate, and the noncanonical (or scaffolding) function, which involves the allosteric activation of other kinases [32]. The latter function is aptly exemplified by pseudokinases, which are kinases that do not possess the ability to transfer phosphate due to lack of conserved residues required for catalysis or occupation of adenine binding site by other hydrophobic side chain, but can still either function as scaffolds, allosteric activators, or catalysts by nonconventional mechanism [33, 34]. Recent work has shown that ATP-competitive inhibitors such as PLX4720 can paradoxically activate BRAF probably via the noncanonical function as allosteric activator [35]. Furthermore, by mutating the C-

spine residue (A481F) in BRAF, it has been shown that a pseudokinase can be formed in which the adenine binding site is blocked by the phenylalanine side chain but can still activate wild-type BRAF or CRAF through dimerization [36]. Based on these findings, we examined how the chemical groups occupying the active site can possibly uncouple the two functions of a kinase.

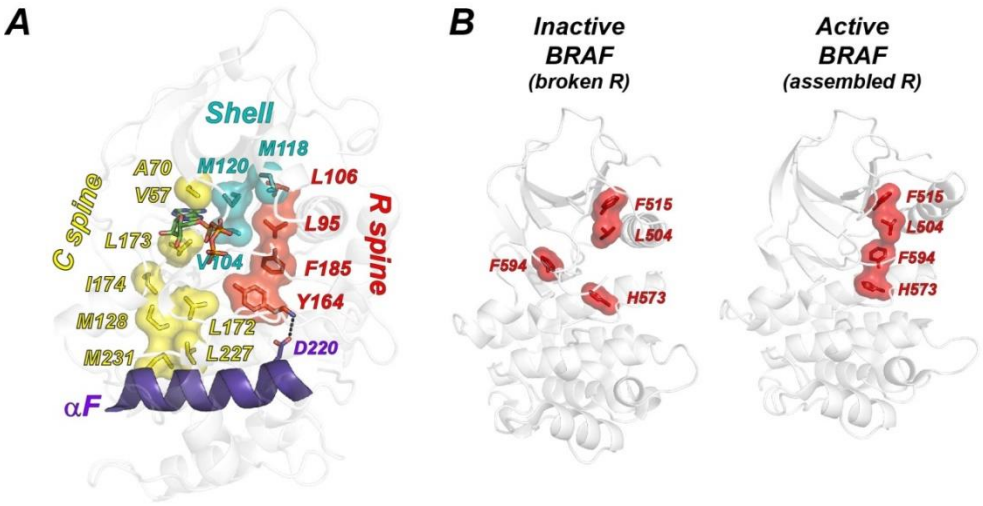

Figure 1.3. Hydrophobic spines and their role in the activity of eukaryotic protein kinases.
A. The hydrophobic side chains in PKA-C constituting the regulatory (R, red) and catalytic (C, yellow) spines. The adenine ring completes the C-spine. The shell residues (teal) stabilize the R-spine. Both spines are docked into the hydrophobic F-helix. B. The R-spine is broken in an inactive BRAF kinase (PDB: 1UWH) while it is assembled in active BRAF (PDB: 3C4C).

1.1.2 Conformational States and Dynamics

Active protein kinases toggle between different conformational states. X-ray crystallographic data of PKA-C identified three major conformational states: namely, open (apo form), intermediate (binary, or nucleotide-bound form), and closed (ternary, or both nucleotide and substrate/pseudosubstrate-bound form) [37-39] (**Figure 1.4A**). These states have been well-characterized structurally and dynamically [14]. NMR[40, 41] and fluorescence[42] measurements, as well as molecular dynamics simulations data[41], have demonstrated that the conformational landscape of kinases is modulated by the changes in the conformational dynamics of the enzyme induced by ligand binding. The apo state is in a dynamically uncommitted state, represented as an ensemble of interchanging conformations [41]. Nucleotide binding then activates the enzyme

dynamically and allosterically, shifting it into a dynamically committed state, where the two lobes of the kinase are engaged and primed for catalysis. While binding of the substrate shifts the equilibrium toward the closed state with persistent μs-ms dynamics that correlate with the catalytic turnover rate, binding of minimum pseudosubstrate sequence, PKI_{5-24}, greatly attenuated the dynamics of the enzyme, shifting it to a dynamically quenched state. This is corroborated by thermocalorimetric data showing that substrate binding is entropically-driven, while binding of pseudosubstrate inhibitor is enthalpically-driven [41]. In the dynamically committed state, the catalytically important loops exhibited synchronous motions in the microsecond-millisecond (μs-ms) timescale that correlate to the opening and closing of the active site cleft [40, 41]. The importance of synchronous dynamics in catalysis is further underscored in the case of the mutant Y204A, where mutation of Tyr204 that is distal from the active site, though X-ray crystallography has shown that it is structurally indistinguishable from the wild type enzyme, desynchronizes the motion of the two lobes of the kinase, reducing its catalytic efficiency [43]. Concomitant to its impairment of catalytic machinery is the loss of binding cooperativity [44].

1.1.3 Regulation

Due to the pivotal role that PKA plays in a number of crucial cellular processes, its activity and localization must be tightly regulated. In the cell, two proteins bind to the catalytic subunit of PKA with high affinity and specificity. They both inhibit and direct the localization of the PKA-C. First is PKA-R, which dimerizes and binds to PKA-C to form the inactive holoenzyme [14]. It contains the dimerization/docking domain at the N-terminus, which is not only involved in dimer formation of PKA-R, but also serves as the docking site for A-kinase anchoring proteins (AKAPs), which anchor the kinase to specific subcellular location [45]. The dimerization/docking domain is followed by a linker region, which contains the inhibitory sequence that is recognized by PKA-C, and then followed by two cAMP binding domains. Increased level of cAMP as a consequence of β-adrenergic stimulation results in cAMP binding to PKA-R that will induce conformational change, unleashing the catalytic subunit [10].

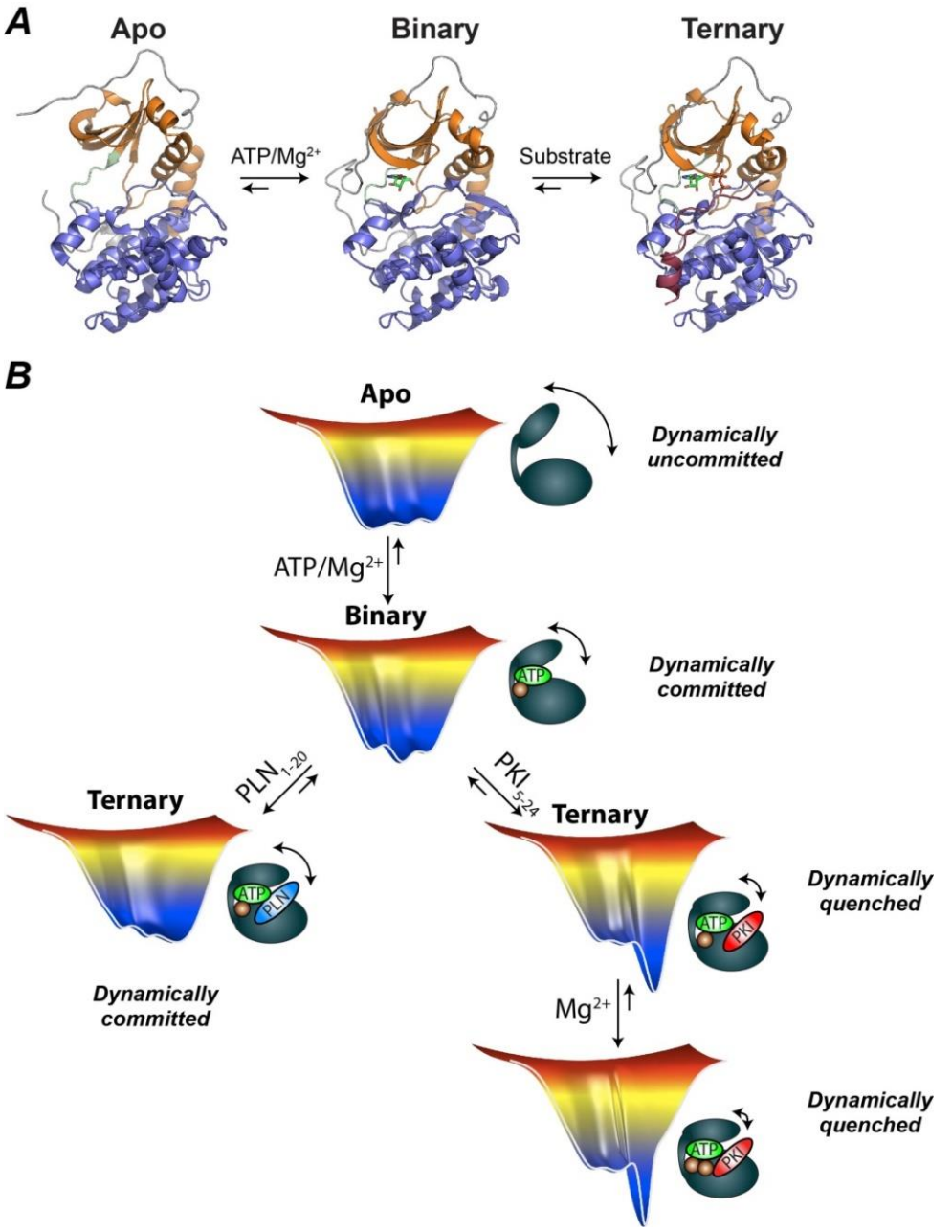

Figure 1.4. The conformational states and energy landscape of PKA-C.
(A) The three main conformational states of PKA-C that have been characterized structurally are open (apo, PDB: 1J3H), intermediate (binary, PDB: 1BKX), and closed (PDB: 1ATP). (B) The conformational energy landscape of PKA-C changes in response to ligand binding. The apo is dynamically uncommitted and samples a wide variety of conformations. Binding of ATP poised the enzyme for catalysis by synchronizing its dynamics (dynamically committed). Binding of substrate (such as phospholamban, PLN) forms the Michaelis complex with persistent dynamics, while binding of pseudosubstrate (such as PKI_{5-24}) or excess Mg^{2+} quenches the relevant dynamics (dynamically quenched). Adapted from [41]

On the other hand, protein kinase inhibitor (PKI) is another protein that performs similar regulatory functions as PKA-R, but is independent of cAMP concentration. PKI is a 75-residue heat-stable protein that binds PKA-C with high affinity (K_i ~0.2 nM) [46] and contains two important domains: the kinase inhibitory domain (residues 1-24) [47] and the nuclear export signal (NES) domain (residues 37-46) [48]. The kinase inhibitory domain consists of the high-affinity region at the N-terminus followed by the pseudosubstrate sequence that docks into the active site cleft of PKA-C, responsible for inhibiting the kinase; while the NES domain consists of a leucine-rich amphipathic helix that is responsible for shuttling the kinase out of the nucleus [49]. In its free form, PKI is mostly unstructured , with nascent helices in each of the two domains [48].

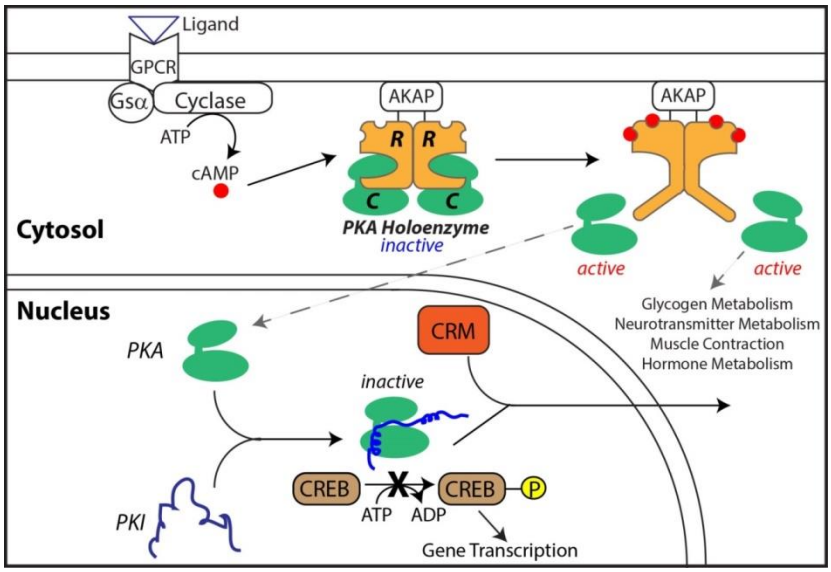

Figure 1.5. Regulation of activity and intracellular localization of PKA-C in the cell.
Both the regulatory subunit (R) and PKI inhibit and direct the localization of the catalytic (C) subunit of PKA-C. The R subunit binds with the C subunit to form an inactive tetramer (holoenzyme) that can be activated by binding of cyclic AMP (cAMP). The A-kinase anchoring protein (AKAP) directs the subcellular localization of the holoenzyme through its interaction with the R subunit. Meanwhile, PKI contains a pseudosubstrate sequence that binds with a nanomolar affinity to the C subunit to inhibit it, and a nuclear export signal to recruit exporting proteins such as Chromosomal Maintenance 1 (CRM) to help shuttle PKA-C out of the nucleus. GPCR: G-protein coupled receptor, CREB: cAMP response-element binding protein

1.2 NMR Spectroscopy to Probe Protein Dynamics

Proteins exist as ensembles of interchanging conformers displaying a wide array of motions spanning a large range of timescales from picosecond-nanosecond, such as bond librations and side chain rotations, to microsecond-millisecond, such as global conformational changes during ligand binding or protein folding. These conformational fluctuations are the driving forces for overcoming energy barriers in a free energy landscape (**Figure 1.6A**). The protein structures solved by X-ray crystallography usually represent the lowest energy or "ground state" conformations. Protein function, such as catalysis, allosteric regulation, folding, or ligand binding, often involves the transition to the higher-energy, lowly-populated states or "excited states". These transitions are chemical exchange processes. To fully understand protein function, one must study the kinetics and thermodynamics of the conformational dynamics undergone by proteins as they explore the high-energy states. A steadily increasing number of studies in the literature have demonstrated how protein dynamics are coupled to function [50-52]. NMR spectroscopy proves to be a powerful tool among many others in studying protein dynamics for a number of reasons. While both X-ray crystallography and NMR spectroscopy provide site-specific information of the protein under study, only NMR spectroscopy has the advantage of probing these protein motions or conformational dynamics over a wide range of timescales (from picosecond to kilosecond). A huge arsenal of NMR experiments is available to capture these motions at different ranges of timescales (**Figure 1.6B**). Furthermore, compared to other methods of spectroscopy used to measure protein dynamics (such as fluorescence, hydrogen-deuterium exchange mass spectroscopy, etc.), NMR has the advantage of being non-invasive and can interrogate multiple probes at various sites of the proteins simultaneously. The theory of chemical exchange will be presented first, followed by the three experiments used to measure protein dynamics in the microsecond-millisecond (μs-ms) timescale, namely, the Carr-Purcell-Meiboom Gill (CPMG)[53, 54] relaxation dispersion, Chemical Exchange Saturation Transfer (CEST)[55, 56], and TROSY Hahn-Echo [57]. This section concludes by describing the experiments used to measure the picosecond-nanosecond (ps-ns) timescale dynamics of the protein.

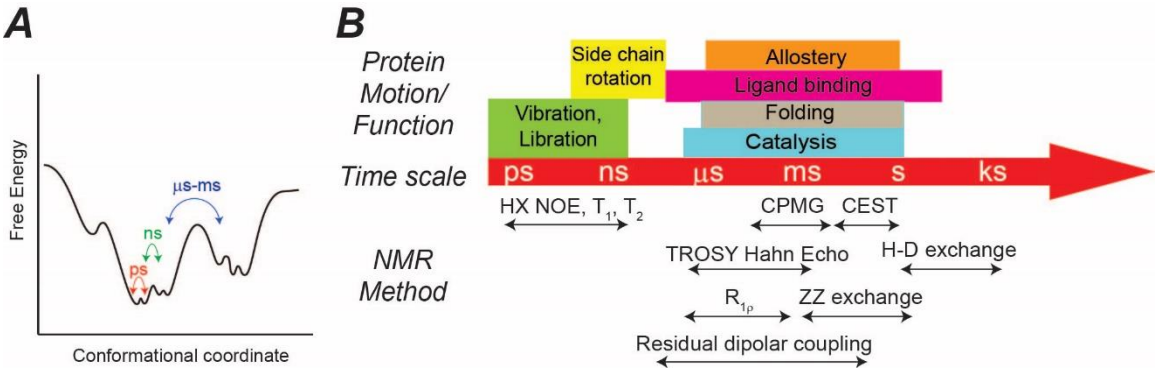

Figure 1.6. The different timescales of protein motions and the NMR techniques that cover these timescales.
A. The conformational fluctuations in a protein at different time scales can be viewed as an energy landscape. B. The different NMR experiments used to probe dynamics at different time scales and the relevant protein motions. Adapted from [50]

1.2.1 Chemical Exchange

A nuclear spin that is exchanging between at least two different chemical environments or states as a result of conformational change or chemical reaction is said to be undergoing chemical exchange [58]. Due to the difference in the chemical environment, its chemical shift or resonance frequency changes with time, resulting in increased transverse relaxation rate. Suppose that a nuclear spin is exchanging between two different environments A and B:

$$A \underset{k_{-1}}{\overset{k_1}{\rightleftharpoons}} B \tag{1.1}$$

where $k_1$and k_{-1} are the rate constants for the forward and reverse reactions, respectively. The rate equations that govern the time-dependence of the concentration of spins in the two states are given by [58]:

$$\frac{d}{dt}\begin{bmatrix}[A](t)\\ [B](t)\end{bmatrix} = \begin{bmatrix}-k_1 & k_{-1}\\ k_1 & -k_{-1}\end{bmatrix}\begin{bmatrix}[A](t)\\ [B](t)\end{bmatrix} \tag{1.2}$$

At equilibrium,

$$\frac{d[A]}{dt} = \frac{d[B]}{dt} = 0 \tag{1.3}$$

$$k_1[A]_{eq} = k_{-1}[B]_{eq} \tag{1.4}$$

$$K_{eq} = \frac{[B]_{eq}}{[A]_{eq}} = \frac{k_1}{k_{-1}} \tag{1.5}$$

The equilibrium population of spins in state A, p_A, is given by:

$$p_A = \frac{[A]_{eq}}{[A]_{eq} + [B]_{eq}} = \frac{k_{_1}}{k_1 + k_{-1}} = \frac{k_1}{k_{ex}} \tag{1.6}$$

where k_{ex} is the chemical exchange rate constant:

$$k_{ex} = k_1 + k_{-1} \tag{1.7}$$

and

$$p_A + p_B = 1 \tag{1.8}$$

The evolution of magnetization, **M**, in a magnetic field, **B**, is described by the Bloch equations[59]:

$$\frac{d\mathbf{M}}{dt} = \gamma \mathbf{M} \times \mathbf{B} - R[\mathbf{M} - M_0] \tag{1.9}$$

where γ is the gyromagnetic ratio, and R is the relaxation rate constant. The Bloch equations can be expressed alternatively as:

$$\frac{d}{dt}\begin{bmatrix} E \\ M_z \\ M^+ \\ M^- \end{bmatrix} = \begin{bmatrix} & & & \\ & R_1 M_{z0} - R_1 & & \\ & & i\omega - R_2 & \\ & & & -i\omega - R_2 \end{bmatrix} \begin{bmatrix} E \\ M_z \\ M^+ \\ M^- \end{bmatrix} \tag{1.10}$$

where E is the identity operator, R_1 and R_2 are the longitudinal and transverse relaxation rate constants, respectively, ω is the chemical shift, and M_{z0} is the equilibrium z magnetization. For spins in two states A and B, the Bloch equations for the transverse coherence in the absence of chemical exchange are given by:

$$\frac{d}{dt}\begin{bmatrix} M_A^+ \\ M_B^+ \end{bmatrix} = \begin{bmatrix} i\omega_A - R_{2A}^0 & \\ & i\omega_B - R_{2B}^0 \end{bmatrix} \begin{bmatrix} M_A^+ \\ M_B^+ \end{bmatrix} \tag{1.11}$$

In the presence of chemical exchange between states A and B, the Bloch equations will be modified as follows:

$$\frac{d}{dt}\begin{bmatrix} M_A^+ \\ M_B^+ \end{bmatrix} = \left\{ \begin{bmatrix} i\omega_A - R_{2A}^0 & \\ & i\omega_B - R_{2B}^0 \end{bmatrix} + \begin{bmatrix} -k_1 & k_{-1} \\ k_1 & -k_{-1} \end{bmatrix} \right\} \begin{bmatrix} M_A^+ \\ M_B^+ \end{bmatrix} \tag{1.12}$$

These equations are known as Bloch-McConnell equations [60], whose solution is given by:

$$\begin{bmatrix} M_A^+(t) \\ M_B^+(t) \end{bmatrix} = \begin{bmatrix} a_{11}(t) & a_{12}(t) \\ a_{21}(t) & a_{21}(t) \end{bmatrix} \begin{bmatrix} M_A^+(0) \\ M_B^+(0) \end{bmatrix} \tag{1.13}$$

with

$$a_{11}(t) = \frac{1}{2}\left[\left(1 - \frac{i\Delta\omega - \Delta R_2^0 + k_1 - k_{-1}}{\lambda_+ - \lambda_-}\right)e^{-\lambda_- t} + \left(1 + \frac{i\Delta\omega - \Delta R_2^0 + k_1 - k_{-1}}{\lambda_+ - \lambda_-}\right)e^{-\lambda_+ t}\right] \tag{1.14}$$

$$a_{22}(t) = \frac{1}{2}\left[\left(1 + \frac{i\Delta\omega - \Delta R_2^0 + k_1 - k_{-1}}{\lambda_+ - \lambda_-}\right)e^{-\lambda_- t} + \left(1 - \frac{i\Delta\omega - \Delta R_2^0 + k_1 - k_{-1}}{\lambda_+ - \lambda_-}\right)e^{-\lambda_+ t}\right] \tag{1.15}$$

$$a_{12}(t) = \frac{k_{-1}}{\lambda_+ - \lambda_-}\left[e^{-\lambda_- t} - e^{-\lambda_+ t}\right] \tag{1.16}$$

$$a_{21}(t) = \frac{k_1}{\lambda_+ - \lambda_-}\left[e^{-\lambda_- t} - e^{-\lambda_+ t}\right] \tag{1.17}$$

and eigenvalues λ_+ and λ_- equal to:

$$\lambda_\pm = \frac{1}{2}\left[\left(-i\omega_A - i\omega_B + R_{2A}^0 + R_{2B}^0 + k_{ex}\right) \pm \left\{\left(i\Delta\omega - \Delta R_2^0 + k_1 - k_{-1}\right)^2 + 4k_1k_{-1}\right\}^{1/2}\right] \tag{1.18}$$

where $\Delta\omega = \omega_B - \omega_A$ and $\Delta R_2^0 = R_{2B}^0 - R_{2A}^0$. The Fourier transform of $M_A^+(t)$ and $M_B^+(t)$ gives the resulting NMR spectrum.

On the basis of the relative values of k_{ex} and $\Delta\omega$, the chemical exchange process can be categorized into three regimes:

$k_{ex} < \Delta\omega$	Slow exchange
$k_{ex} \approx \Delta\omega$	Intermediate exchange
$k_{ex} > \Delta\omega$	Fast exchange

A simple illustration depicting two scenarios is shown in **Figure 1.7**. If the populations of the two states are equal ($p_A = p_B = 0.5$, **Figure 1.7A**), under slow exchange limit, i.e. $k_{ex} \ll \Delta\omega$, two peaks will be observed, each at their respective chemical shifts. From the Bloch-McConnell equations, we get:

$$\frac{d}{dt}\begin{bmatrix} M_A^+ \\ M_B^+ \end{bmatrix} = \begin{bmatrix} -R_{2A}^0 - k_1 & k_{-1} \\ k_1 & i\Delta\omega - R_{2B}^0 - k_{-1} \end{bmatrix} \begin{bmatrix} M_A^+ \\ M_B^+ \end{bmatrix} \tag{1.19}$$

Under slow exchange limit, the off-diagonal terms are negligible, so the Bloch-McConnell equations reduce to:

$$\frac{d}{dt}\begin{bmatrix} M_A^+ \\ M_B^+ \end{bmatrix} = \begin{bmatrix} -R_{2A}^0 - k_1 & \\ & i\Delta\omega - R_{2B}^0 - k_{-1} \end{bmatrix}\begin{bmatrix} M_A^+ \\ M_B^+ \end{bmatrix} \tag{1.20}$$

with solution equal to:

$$M^+(t) = M_A^+(0)e^{-(R_{2A}^0 + k_1)t} + M_B^+(0)e^{-(-i\Delta\omega + R_{2B}^0 + k_{-1})t} \tag{1.21}$$

The effect of chemical exchange is to broaden the linewidth or increase the transverse relaxation rate constant by a quantity, R_{ex}:

$$R_2 = R_2^0 + R_{ex} \tag{1.22}$$

where R_{ex} is the chemical exchange contribution to the transverse relaxation rate constant. Equation (1.21) indicates that the two peaks observed at ω_A and ω_B have linewidths that will be broadened by chemical exchange according to the following relations:

$$\begin{aligned} R_{2A} &= R_{2A}^0 + k_1 \\ R_{2B} &= R_{2B}^0 + k_{-1} \end{aligned} \tag{1.23}$$

Under slow exchange limit, R_{ex} is equal to k_1 or k_{-1} for state A and B, respectively. As the exchange rate increases, the resonance positions change and the peaks broaden until they coalesce when $k_{ex} \approx \Delta\omega$ (**Figure 1.7A**). At this regime, the nucleus is said to be in intermediate exchange. Further increase in exchange rate would result in the appearance of a single peak at the population-weighted average chemical shift, $\bar{\omega} = p_A\omega_A + p_B\omega_B$, whose linewidth becomes sharper as k_{ex} increases (**Figure 1.7A**) according to the following relation:

$$R_{2,ave} = p_A R_{2A}^0 + p_B R_{2B}^0 + \frac{p_A p_B \Delta\omega^2}{k_{ex}} \tag{1.24}$$

This is known as the fast exchange limit ($k_{ex} \gg \Delta\omega$) with:

$$R_{ex} = \frac{p_A p_B \Delta\omega^2}{k_{ex}} \tag{1.25}$$

If the populations are skewed (**Figure 1.7B**) such that, $p_A > p_B$, (as in the case of proteins in ground state exchanging with a lowly-populated excited state), in the slow exchange limit, the intensities of the two peaks are scaled according to their relative

populations. As k_{ex} increases, chemical exchange broadens the peaks to a different extent as dictated by their respective R_{ex} (eqn 1.23), with the minor peak being more preferentially broadened (since $p_A \gg p_B$, $k_1 \ll k_{-1}$) such that the minor peak becomes completely undetected. The major peak continues to broaden as k_{ex} increases and eventually sharpens as it enters the fast exchange regime (**Figure 1.7B**). Hence, the observation of a single peak does not necessarily mean fast exchange in the chemical shift time scale [61].

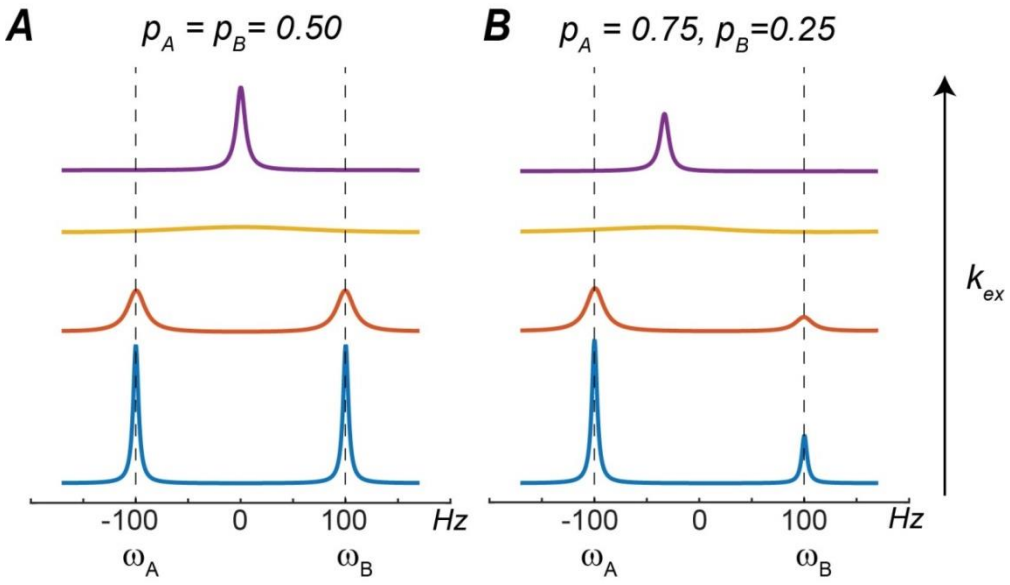

Figure 1.7. NMR spectrum of peaks undergoing two-state exchange at different regimes.
Simulated NMR spectra showing how the linewidths, intensities and peak positions change in different exchange regimes for spins undergoing two-state exchange (A) when the two states are equally populated ($p_A = p_B = 0.50$), and (B) when the population is skewed ($p_A > p_B$). In slow exchange limit, when $k_{ex} \ll |\Delta\omega|$, two peaks will be observed at their respective chemical shifts, with the relative intensities proportional to the populations. In the intermediate exchange regime, $k_{ex} \approx |\Delta\omega|$, the two peaks will be broadened and coalesce. In the fast exchange regime, $k_{ex} \gg |\Delta\omega|$, a single peak will be observed at the population-weighted average chemical shift. If the population is skewed, as k_{ex} increases, the minor peak gets more preferentially broadened that it could go undetected.

Alternatively, the static magnetic field, B_0, dependence of R_{ex} for the observed peak can determine the NMR chemical shift time scale in systems with $p_A > p_B$[62]. In slow exchange limit, R_{ex} is independent of B_0 since $R_{ex} = k_1 = p_B k_{ex}$ for the major peak, while in the fast exchange limit, $R_{ex} \propto B_0^2$ since $R_{ex} = \frac{p_A p_B \Delta\omega^2}{k_{ex}}$ and $\Delta\omega \propto B_0$. Therefore, a scaling factor, α, defined as follows [62]:

$$\frac{\delta R_{ex}}{R_{ex}} = \alpha \frac{\delta B_0}{B_0} \tag{1.26}$$

$$\alpha = \frac{d(\ln R_{ex})}{d(\ln \Delta\omega)} \tag{1.27}$$

can be used to determine the exchange regime in chemical shift time scale. Under the condition when $p_A > 0.7$ and $R_{2A}^0 = R_{2B}^0$,

$$\alpha = \frac{2\left(k_{ex}/\Delta\omega\right)^2}{1+\left(k_{ex}/\Delta\omega\right)^2} \tag{1.28}$$

with the following relations between α and exchange regime:

$0 \leq \alpha < 1$	Slow exchange
$\alpha \approx 1$	Intermediate exchange
$1 < \alpha \leq 2$	Fast exchange

1.2.2 Microsecond-millisecond Timescale Dynamics

Enzyme catalysis [52], allosteric regulation[51], ligand binding, and protein folding [63] are some of the important cellular processes that occur in the microsecond-millisecond time scale. These dynamic processes exemplify chemical exchange that will stochastically modulate the isotropic chemical shift, increasing the transverse relaxation rate constant and thereby broadening the linewidth.

A number of NMR relaxation experiments can be used to measure this chemical exchange contribution at the μs-ms timescale including $R_{1\rho}$ [64], Carr-Purcell-Meiboom-Gill [53, 54](CPMG) relaxation dispersion, Chemical Exchange Saturation Transfer (CEST) [55, 56], ZZ exchange[65], and TROSY Hahn-Echo [57]. Each method has its own strengths and limitations, but ultimately, the choice of method to use depends on the timescale of the exchange process, τ_{ex}, which is dictated by the exchange rate constant, k_{ex}: $\tau_{ex} = 1/k_{ex}$. While a brief description of each experiment will be given below, emphasis will be placed on CPMG, CEST, and TROSY Hahn-Echo. The readers are referred to the following references for an in-depth description of $R_{1\rho}$ [66] and ZZ-exchange experiments [67].

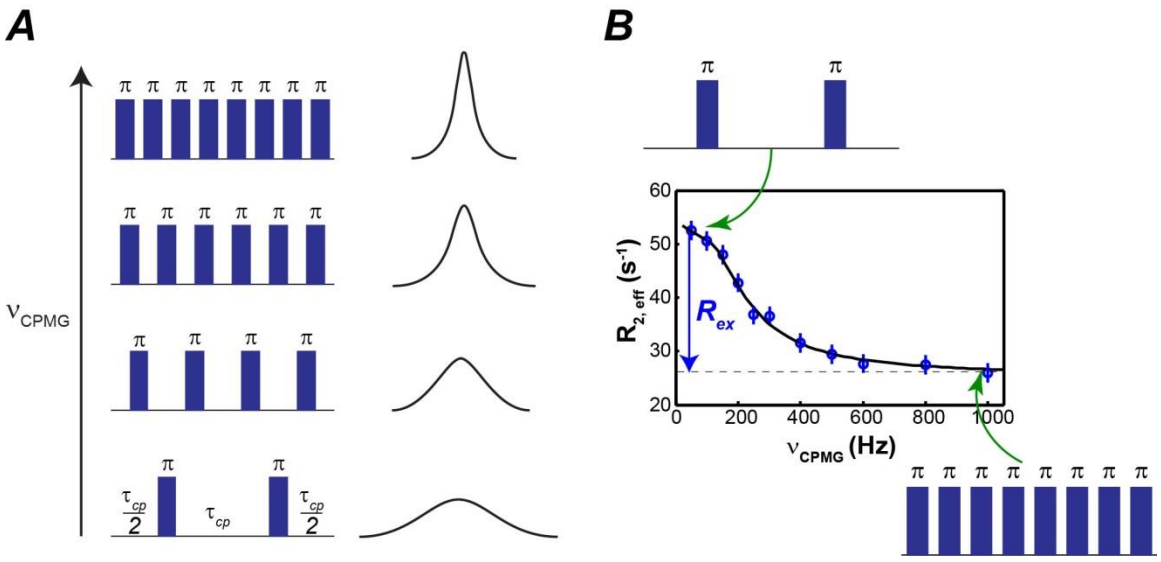

Figure 1.8. Principle of CPMG relaxation dispersion.
(A) A series of refocusing π pulses, or spin echoes, is systematically applied to suppress the effect of chemical exchange on the transverse relaxation rate. As the frequency of pulses, υ_{CPMG}, increases, the chemical exchange contribution is increasingly suppressed, so the linewidth becomes sharper. (B) The CPMG relaxation dispersion curve is obtained by plotting the effective transverse relaxation rate constant, R_{ex}, as a function of the frequency of pulses, υ_{CPMG}. The chemical exchange contribution to the transverse relaxation rate constant, R_{ex}, is then obtained from the difference between the observed R_2 at $\upsilon_{CPMG} \to 0$ and $\upsilon_{CPMG} \to \infty$.

CPMG, CEST, and $R_{1\rho}$ experiments are typically used to probe the chemical exchange process when the excited state is "invisible" or not detected by measuring the relaxation properties of the ground state. In CPMG, a series of π pulses, called spin-echoes, is applied and the effective transverse relaxation rate constant, $R_{2,eff}$, is measured as a function of the rate of radiofrequency field application, ν_{CPMG} [68] (**Figure 1.8**). The spin-echo sequence, $\frac{\tau_{cp}}{2} - 180^\circ - \frac{\tau_{cp}}{2}$, in which τ_{cp} is the spacing between successive 180° pulses, serves to refocus the transverse magnetization by the application of 180° pulse in the middle to invert the sense of precession. Chemical exchange will cause the transverse magnetization to diphase quickly. A train of spin echoes with varying τ_{cp} or ν_{CPMG} $(= \frac{1}{2\tau_{cp}})$ is hence systematically applied to progressively suppress the effect of chemical exchange to R_2 (**Figure 1.8**). In a constant-time CPMG experiment, the effective transverse relaxation rate constant at a particular ν_{CPMG} value is evaluated by comparing the intensity of the peak (I) with that of

the reference spectrum (I_0) that is recorded without the CPMG pulses, according to the following expression:

$$R_{2,eff} = -\frac{\ln \frac{I}{I_0}}{T_{CPMG}} \tag{1.29}$$

where T_{CPMG} is the total relaxation delay. The exchange contribution, R_{ex}, is then obtained from the difference in R_2 at infinite and no pulsing:

$$R_{ex} = R_2\left(1/\tau_{cp} \to 0\right) - R_2\left(1/\tau_{cp} \to \infty\right) \tag{1.30}$$

The relaxation dispersion curves are then typically fit to a two-state model to extract the kinetic (k_{ex}), thermodynamic (p_A, p_B) and structural ($\Delta\omega$) parameters. For a two-state exchange model, the Carver-Richards equation gives the general expression that applies to all exchange regimes[69-71]:

$$R_2\left(\frac{1}{\tau_{cp}}\right) = \frac{1}{2}\left(R_{2A}^0 + R_{2B}^0 + k_{ex} - \frac{1}{\tau_{cp}}\cosh^{-1}\left[D_+\cosh\left(\eta_+\right) - D_-\cos\left(\eta_-\right)\right]\right) \tag{1.31}$$

where:

$$D_\pm = \frac{1}{2}\left[\pm 1 + \frac{\Psi + 2\Delta\omega^2}{\left(\Psi^2 + \zeta^2\right)^{1/2}}\right] \tag{1.32}$$

$$\eta_\pm = \frac{\tau_{cp}}{\sqrt{2}}\left[\pm\Psi + \left(\Psi^2 + \zeta^2\right)^{1/2}\right]^{1/2} \tag{1.33}$$

$$\Psi = \left(R_{2A}^0 - R_{2B}^0 - p_A k_{ex} + p_B k_{ex}\right)^2 - \Delta\omega^2 + 4 p_A p_B k_{ex}^2 \tag{1.34}$$

$$\zeta = 2\Delta\omega\left(R_{2A}^0 - R_{2B}^0 - p_A k_{ex} + p_B k_{ex}\right) \tag{1.35}$$

In fast exchange limit, the Carver-Richard equation can be approximated as[72]:

$$R_2\left(\frac{1}{\tau_{cp}}\right) = R_2^0 + \left(\frac{p_A p_B \Delta\omega^2}{k_{ex}}\right)\left[1 - \frac{2\tanh\left(k_{ex}\tau_{cp}/2\right)}{k_{ex}\tau_{cp}}\right] \tag{1.36}$$

In addition, for highly skewed population between two states ($p_A \gg p_B$), a simple equation was derived by Ishima and Torchia[61]:

$$R_2\left(\frac{1}{\tau_{cp}}\right) = R_2^0 + \frac{p_A p_B \Delta\omega^2 k_{ex}}{k_{ex}^2 + \left(p_A^2\Delta\omega^4 + {144}/{\tau_{cp}^4}\right)^{1/2}} \quad (1.37)$$

The typical shapes of CPMG relaxation dispersion profiles for fast, intermediate, and slow exchange are shown in **Figure 1.9B**.

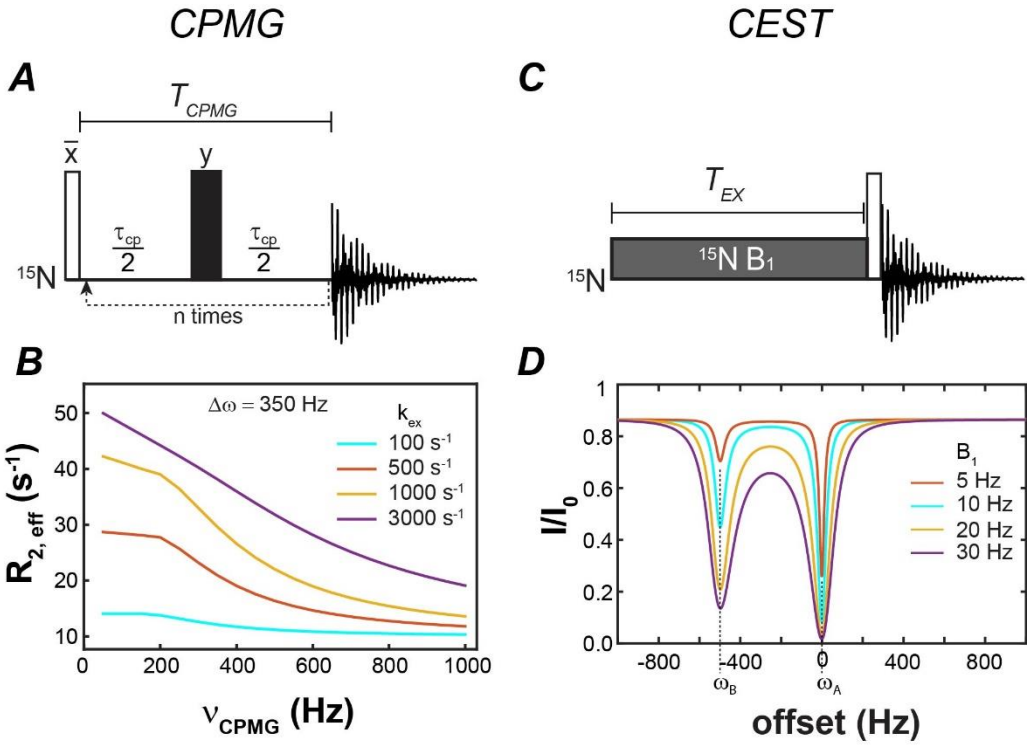

Figure 1.9. Comparison between CPMG and CEST.
(A) The CPMG pulse sequence is composed of a series of refocusing π pulses applied with different spacing, τ_{cp}, at a constant relaxation delay, T_{CPMG}, to suppress the chemical exchange contribution to the transverse relaxation rate constant. (B) Typical CPMG relaxation dispersion profiles showing how the shape of the curves changes as the exchange regime changes. (C) The CEST pulse sequence consists of the application of a weak B_1 field at different offset for a long time, T_{EX}, and the variation in the ground state peak intensity is monitored. (D) Typical CEST profiles showing how the widths of the dips change as B_1 is varied. Adapted from [56]

If the exchange rate is too fast, $k_{ex} > 10000\, s^{-1}$, one cannot use CPMG experiment and pulse at a rate comparable to the high k_{ex} because of the limitation of the hardware and the concomitant sample heating. In this case, the $R_{1\rho}$ rotating frame relaxation experiment can be used [66]. The $R_{1\rho}$ experiment is similar to CPMG except

that the radiofrequency field is applied to spin-lock the magnetization in the rotating frame. The relaxation rate constant of the component of magnetization that lies along the effective field in the rotating frame, called $R_{1\rho}$, is measured as a function of the applied effective field, ω_e, where $\omega_e = \sqrt{\Delta\Omega^2 + \omega_1^2}$, $\Delta\Omega$ is the resonance offset given by $\Delta\Omega = \omega - \omega_0$, ω_1 is the amplitude of the spin-lock field. The $R_{1\rho}$ for a two-state exchange in fast-exchange limit is given by:

$$R_{1\rho} = R_1 \cos^2\theta + (R_2^0 + R_{ex})\sin^2\theta \tag{1.38}$$

where:

$$R_{ex} = \frac{p_A p_B \Delta\omega^2 k_{ex}}{k_{ex}^2 + \omega_e^2} \tag{1.39}$$

On the other hand, if the exchange rate is too slow ($k_{ex} < 200s^{-1}$), the relaxation time must be kept long enough to observe and accurately quantify a significant change in intensity. In this case, chemical exchange saturation transfer (CEST) experiment is the more appropriate method to use. Unlike CPMG, CEST is based on the longitudinal magnetization [55, 56]. Since R_1 is almost always an order of magnitude smaller than R_2, the relaxation time can be extended for a long period of time to allow more exchange processes to happen, resulting in significant loss in intensity. **Figure 1.9** compares the two methods. In the CEST experiment, a weak radiofrequency B_1 field is applied at varying frequency offset for a long period of time, typically 300-500 ms, and the change in intensity of the ground state peak is monitored [56]. If the B_1 field is applied on resonance with the ground state resonance frequency, there will be saturation of the energy levels, leading to a loss in signal. Similarly, saturation of the excited state peak will occur when the applied field is on resonance with it, but in addition, due to chemical exchange, this saturation will be transferred to the ground state and will result in the decrease in signal intensity of the ground state peak. A typical CEST profile, shown in **Figure 1.9D**, is a plot of the relative intensity (I/I_0) of the ground state peak as a function of frequency offset. The data are fitted using the Bloch-McConnell equation and the parameters k_{ex}, p_B, $\Delta\omega$ can be obtained. For more reliable parameters, CEST is

carried out in at least two B_1 fields. The width of the dips broadens as the magnitude of B_1 increases (**Figure 1.9D**).

For larger proteins with MW > 50 kDa, the chemical exchange contribution, R_{ex}, can be determined using the TROSY Hahn-echo experiment [57]. TROSY Hahn-echo takes advantage of the different relaxation properties of the two components of the scalarly coupled ^{15}N doublet due to the interference between the dipole-dipole (DD) and chemical shift anisotropy (CSA) (discussed later):

$$R_2^{\alpha} = R_2^0 - \eta_{xy} + R_1^H/2 + R_{ex}$$
$$R_2^{\beta} = R_2^0 + \eta_{xy} + R_1^H/2 + R_{ex} \quad (1.40)$$

where R_2^{α} and R_2^{β} are the transverse relaxation rate constants for the slow relaxing and fast relaxing doublet components, respectively, R_2^0 is the intrinsic transverse relaxation rate constant for in-phase ^{15}N magnetization, η_{xy} is the cross-correlation rate constant between DD and CSA, and R_1^H is the longitudinal rate constant for the $^1H^N$ spin from interactions with neighboring ^{1}H spins. For spins undergoing exchange, R_2^0 is obtained from the ratio $\kappa = R_2^0/\eta_{xy}$, where κ is a proportionality constant that is independent of chemical exchange and internal dynamics in large proteins. The values of κ can be calculated theoretically [73, 74] or experimentally from the trimmed mean of $1 + \frac{(R_2^{\alpha} - R_1^{2H_zN_z})/2}{\eta_{xy}}$ over all nonexchanging residues, where $R_1^{2H_zN_z}$ is the longitudinal two-spin order relaxation rate constant. $R_1^{2H_zN_z}$ can be approximated as the sum of the longitudinal rate constants of $^1H^N$ and ^{15}N, i.e. $R_1^{2H_zN_z} \approx R_1^H + R_1^N$, where R_1^N is the longitudinal relaxation rate constant of ^{15}N. $R_1^N$is often negligible for proteins with MW > 30 kDa. Equations 1.40 can then be rearranged to solve for R_{ex} during the Hahn spin echo:

$$R_{ex} = R_2^{\alpha} - R_1^{2H_zN_z}/2 - \eta_{xy}(\kappa - 1) \quad (1.41)$$

To determine R_{ex}, three relaxation rate constants, R_2^{α}, R_2^{β}, and $R_1^{2H_zN_z}$, will be measured experimentally using the pulse sequence reported by Wang, et al. [57] During the spin echo period of time T, the slow and fast relaxing components of the ^{15}N doublet

relax independently if $T = n/J_{HN}$, where n is an integer, and J_{HN} is the scalar coupling constant [75]. The cross-correlation rate constant, η_{xy}, is calculated from the ratio of the intensities of the α and β spin states:

$$\eta_{xy} = -\frac{1}{2T}\ln\left[\frac{I^{\beta}}{I^{\alpha}}\right] \tag{1.42}$$

and $R_2^{\alpha} - {R_1^{2H_zN_z}}/{2}$ is calculated from:

$$R_2^{\alpha} - {R_1^{2H_zN_z}}/{2} = -\frac{1}{2T}\ln\left[\frac{I^{\alpha}}{I^{2H_zN_z}}\right] \tag{1.43}$$

The value of R_{ex} is then calculated using equation 1.41. For non-exchanging residues, there is a distribution in the values of R_{ex} about 0 s^{-1} due to variation in CSA throughout the protein.

1.2.3 Picosecond-Nanosecond Timescale Dynamics

Protein motions in the picosecond-nanosecond (ps-ns) timescale include backbone and side chain bond librations and rotations. These motions are faster than molecular tumbling, and hence they stochastically modulate the local magnetic fields resulting in spin relaxation. The two dominant mechanisms that influence relaxation of spins are the dipole-dipole (DD) and chemical shift anisotropy (CSA). Dipole-dipole interactions pertain to the through-space interaction between a pair of magnetic dipoles (**Figure 1.10A**). The magnitude of DD depends on the internuclear distance between the dipoles and their orientation with respective to the magnetic field. On the other hand, CSA refers to the anisotropic nature of the electronic environment surrounding the nucleus. This creates local magnetic fields, which also depends on the orientation of the bond vector relative to the static magnetic field (**Figure 1.10B**). Molecular tumbling and/or internal motions will cause the local fields created by DD and CSA to fluctuate with time. These oscillations contain frequency components that are equivalent to the transition frequencies involved in spin relaxation. The probability by which a bond vector oscillates at a specific frequency is given by the spectral density function, $J(\omega)$. The three NMR relaxation parameters: the longitudinal relaxation rate constant (R_1), the transverse relaxation rate constant (R_2), and the steady-state heteronuclear nuclear Overhauser

effect (HX NOE), are linear combinations of the spectral density functions at different transition frequencies according to the following relations:

$$R_1 = \frac{1}{4} d^2 \left[J\left(\omega_H - \omega_X\right) + 3J\left(\omega_X\right) + 6J\left(\omega_H + \omega_X\right) \right] + c^2 J\left(\omega_X\right) \tag{1.44}$$

$$R_2 = \frac{1}{8}\left[4J\left(0\right) + J\left(\omega_H - \omega_X\right) + 3J\left(\omega_X\right) + 6J\left(\omega_H\right) + 6J\left(\omega_H + \omega_X\right) \right] + \frac{1}{6} c^2 \left[4J\left(0\right) + 3J\left(\omega_X\right) \right] + R_{ex} \tag{1.45}$$

$$NOE = 1 + \frac{1}{4} d^2 T_1 \left(\frac{\gamma_H}{\gamma_X} \right) \left[6J\left(\omega_H + \omega_X\right) - J\left(\omega_H - \omega_x\right) \right] \tag{1.46}$$

where

$$d = \left(\frac{\mu_0 h \gamma_H \gamma_X}{8\pi^2} \right) \left\langle \frac{1}{r_{HX}^3} \right\rangle \tag{1.47}$$

$$c = \frac{\omega_X \Delta\sigma}{\sqrt{3}} \tag{1.48}$$

where μ_0 is the permeability of free space, h is the Planck's constant, $\gamma_H$and $\gamma_X$are the gyromagnetic ratios of X and ^{1}H nuclei, respectively, r_{HX} is the length of the H-X bond vector, and $\Delta\sigma$ is the chemical shift anisotropy of the X spin.

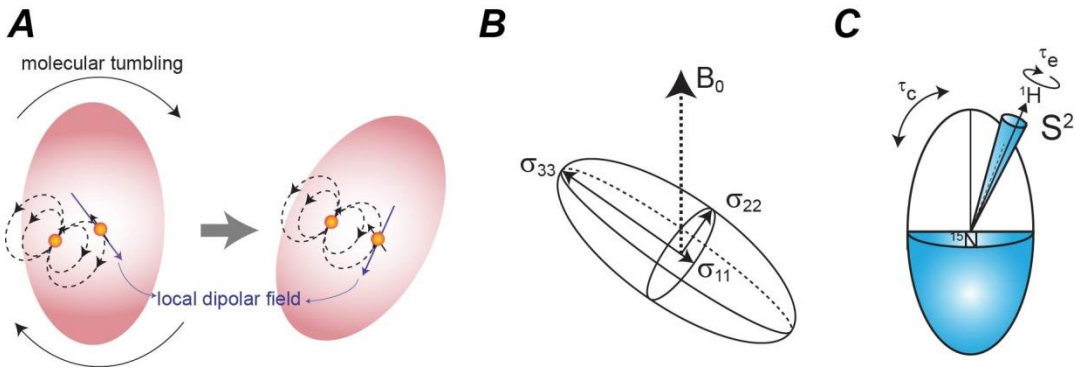

Figure 1.10. Dominant relaxation mechanisms and the Lipari-Szabo model-free formalism.
(A) Dipole-dipole interaction between two magnetic dipoles creates time-fluctuating local magnetic field affecting the neighboring spin. (B) Chemical shift anisotropy refers to the unequal electronic environment that shields the nucleus from the static magnetic field. Molecular motion creates an oscillating field based on the orientation of the bond vector relative to the static magnetic field B_0. (C) The Lipari-Szabo model-free formalism assumes that the internal motions (τ_e) are independent of the global correlation time (τ_c). A generalized order parameter, S^2, that indicates the degree of restriction of the bond vector can be determined.

The three NMR relaxation parameters are measured to probe the ps-ns timescale dynamics of the amide (or side chain) bond vector according to the pulse sequence reported by Farrow, et al. [76]. Briefly, R_1 is measured by inversion recovery experiment [77], where the return of the longitudinal magnetization back to the equilibrium value is monitored as a function time. The transverse relaxation rate constant, R_2, is determined using spin echo sequences, as in CPMG, where the decay of transverse magnetization is followed as a function of time. The steady-state heteronuclear NOE measures the enhancement of the longitudinal magnetization of the X spin when its dipolar coupled proton is irradiated by a weak radiofrequency field. This is carried out by getting the ratio of the intensities (i.e. $NOE = \frac{I_{sat}}{I_{unsat}}$) from two spectra: one acquired with (I_{sat}) and one acquired without (I_{unsat}) saturation of proton. These three parameters are then fitted to obtain the spectral density function, $J(\omega)$ using a variety of approaches. The most common is the Lipari-Szabo model-free formalism [78, 79]. According to the Lipari-Szabo model free approach, the internal motions of the bond vectors are independent of the overall global molecular tumbling. Assuming isotropic tumbling, $J(\omega)$ can be expressed as:

$$J(\omega) = \frac{S^2\tau_c}{1+\omega^2\tau_c^2} + \frac{(1-S^2)\tau}{1+\omega^2\tau^2} \tag{1.49}$$

where τ_c is the global correlation time of the molecule, S^2 is the generalized order parameter, and $\frac{1}{\tau} = \frac{1}{\tau_c} + \frac{1}{\tau_e}$ where τ_e is the effective internal correlation time of the bond vector. The order parameter represents the spatial restriction of motion of the bond vector, where a value of 1.0 denotes highly restricted motion, and a value of 0 denotes unrestricted motion [78, 79] (**Figure 1.10C**).

1.3 Allostery and Cooperativity

Allostery underlies almost all aspects of regulation of biological processes including signal transduction, catalysis, metabolism, and gene regulation [80, 81]. It is the phenomenon by which binding of a ligand at one site affects a distant site by a change in conformation and/or dynamics. Allostery also gives rise to cooperativity where a perturbation at one site can either enhance (positive cooperativity) or reduce (negative

cooperativity) the affinity of a binding site toward a substrate. It can either be *homotropic* (where the allosteric effector and substrate are identical) or *heterotropic* (where the two ligands are different) [82]. In the case of enzyme catalysis, allosteric ligand can either alter the binding interaction between the enzyme and the substrate or K_M (*K-type allostery*), or the turnover kinetics of the enzyme or V_{max} (*V-type allostery*). The classic example of allosteric cooperativity is hemoglobin [83, 84] where oxygen binding in one subunit increases the oxygen binding affinity of the other subunits. Since the discovery of allostery, people have been baffled for decades as to how allostery works at the atomic level.

There were two main classical models of allostery, namely, the Monod-Wyman-Changeux [82] (MWC, or the concerted model) and the Koshland-Nemethy-Filmer [85] (KNF, or the sequential model). Both models assume a conformational change accompanying allostery in oligomeric proteins. Each subunit can exist in either the tense (T) state or the relaxed (R) state, where the R state favors ligand binding. In the MWC model, all the subunits adopt the same state, and binding of a ligand can shift the equilibrium between the two states [82]. On the other hand, in the KNF model, not all subunits have to be in the same state, and binding of a ligand causes a local conformational change, which in turn induces the conformational change of nearby subunit [85]. This is often termed as “induced fit” mechanism. Although the two models prevailed for a long period time, they are phenomenological and they fail to explain at the atomic level how the long-range communication is transmitted between two distant sites [86].

Experimental and computational advances have reshaped the definition of allostery through the years. Allostery can be driven solely by dynamics, without having a conformational change [87-89]. Allosteric regulation is not restricted to oligomers only [90], but to almost all dynamic proteins [91]. One of the modern view of allostery involves the shift of the populations of the conformers in an ensemble [92]. A precise mechanism of allosteric control at the atomic level is important in understanding protein regulation.

1.4 Objectives and Organization of Thesis

Given that protein kinases are dynamic and allosteric molecular switches, the overall goal of this work is to elucidate the mechanism by which allostery is propagated

in protein kinase A and the manner by which different ATP analogs and ATP-competitive inhibitors influence the kinase's allostery and binding cooperativity. Specifically, the study aims to address the following questions: How do changes in hydrogen bond network in a protein correlate with allostery? How do different nucleotides and ATP-competitive inhibitors influence the binding cooperativity of kinases? What are the dynamic effects of the binding of different ATP-competitive inhibitors? What role do conformational dynamics play in allosteric regulation and binding cooperativity in protein kinase A?

Mapping the chemical shift perturbation by NMR spectroscopy is one of the most common experimental method in tracing protein allostery. In Chapter 2, we present a complementary method where allosteric changes can be monitored by measuring the changes in the strength of the hydrogen bonds between the residues in the protein.

NMR spectroscopy is usually limited by the size of the protein, but with the development of more efficient labeling strategy, coupled with the advancement in pulse sequence methodology, this limitation can be circumvented and more powerful experiments can be performed to study the structure and dynamics of large proteins. Chapter 3 outlines the labeling method and the semi-automated assignment for the methyl groups of large proteins.

Recent kinase literature has introduced the dual functions of kinases, where it is possible to perform one function while deprived of the other. Moreover, there are ATP-competitive inhibitors that can paradoxically activate a kinase [35]. Motivated by these findings, Chapter 4 dissects the effect of various nucleotides and ATP-competitive inhibitors in uncoupling the dual functions of kinases.

While structural studies are the most predominant routes in understanding ligand binding and inhibition of kinases, increasing number of evidences point to the crucial role that dynamics play in which excursion to excited states enable proteins to perform their function [52]. Chapter 5 probes in detail the role of conformational dynamics in modulating the binding cooperativity of kinases.

By understanding how allostery operates in protein kinase A and how the chemical groups of ligands in ATP-binding site can tune the binding cooperativity of protein kinase A, we can explore alternative ways to gain better control of the function of kinases.

CHAPTER 2 MAPPING THE HYDROGEN BOND NETWORKS IN THE CATALYTIC SUBUNIT OF PROTEIN KINASE A USING H/D FRACTIONATION FACTORS

Geoffrey C. Li[1], Atul K. Srivastava[2], Jonggul Kim[1], Susan S. Taylor[3] and Gianluigi Veglia[1,2]*

[1]Department of Chemistry– University of Minnesota, Minneapolis, MN 55455.
[2]Department of Biochemistry, Molecular Biology, and Biophysics- University of Minnesota, Minneapolis, MN 55455;
[3]Howard Hughes Medical Institute, Department of Chemistry and Biochemistry, University of California at San Diego, CA 92093

Reprinted with permission from:
Biochemistry (2015) Vol. 54, pp. 4042-4049.

Can be accessed at: http://pubs.acs.org/doi/full/10.1021/acs.biochem.5b00387

2.1 Conspectus

Protein kinase A is a prototypical phosphoryl transferase, sharing its catalytic core (PKA-C) with the entire kinase family. PKA-C substrate recognition, active site organization, and product release depend on the enzyme's conformational transitions from the open to the closed state, which regulate its allosteric cooperativity. Here, we used equilibrium NMR hydrogen/deuterium (H/D) fractionation factors (φ) to probe the changes in the strength of hydrogen bonds within the kinase upon binding the nucleotide and a pseudo-substrate peptide (PKI_{5-24}). We found that the φ values decrease upon binding both ligands, suggesting that the overall hydrogen bond networks in both the small and large lobes of PKA-C becomes stronger. However, we observed several important exceptions, with residues displaying higher φ values upon ligand binding. Notably, the changes in φ values are not localized near the ligand binding pockets; rather, they are radiated throughout the entire enzyme. We conclude that, upon ligand and pseudo-substrate binding, the hydrogen bond networks undergo extensive reorganization, revealing that the open-to-close transitions require global rearrangements of the internal forces that stabilize the enzyme's fold.

2.2 Introduction

Cyclic AMP-dependent protein kinase A (PKA) is a ubiquitous signaling enzyme that catalyzes the phosphoryl transfer from ATP to the serine or threonine residues of their protein substrates. First crystallized in 1991 [8, 9], it served as a prototype for the kinase family. The catalytic subunit of PKA (PKA-C) is a 350-residue protein consisting of a conserved bilobal core flanked by an N-terminus helical segment, known as the A-helix, and a 50-residue C-terminal tail that wraps around the kinase [9] (**Figure 2.1 A**). The small lobe of the kinase is rich in β-strands with only two short helical segments, while the large lobe is mostly helical. The active site cleft is positioned at the interface of the two lobes and harbors the nucleotide binding site. A glycine-rich loop acts as a lid, protecting the nucleotide's phosphates that protrude from the binding cleft toward the substrate from hydrolysis. A short helix (C-helix) positioned by the activation loop contributes to the organization of the active site. The peptide positioning loop registers the substrate with respect to the nucleotide, aligning the P-site toward the γ-phosphate, with two Mg^{2+} ions participating in the active site organization for phosphoryl transfer. While the catalytic regions of PKA-C are responsible for the chemistry at the active site, signaling involves the core of the protein [31] with two hydrophobic spines (C- and R-spines) that contribute to the definition of active and inactive states of the enzyme. The C-spine is assembled upon nucleotide binding, while the R-spine is assembled upon phosphorylation of the activation loop.[16, 23] Structural studies on other protein kinases suggest that the spines are responsible for both allosteric signaling [93] and regulation [94, 95].

During the catalytic cycle, the kinase is thought to undergo extensive structural rearrangements. High-resolution crystal structures revealed at least three main conformational states: apo, intermediate (nucleotide-bound), and closed (ternary complex) [14]. NMR relaxation experiments have shown that the conformational dynamics of the enzyme drive the structural transitions from the open to closed conformation and play a key role in substrate recognition and turnover [40, 41]. The nucleotide acts as an allosteric effector, completing the catalytic spines [23, 40, 44] and shifting the kinase toward a structurally and dynamically committed state.[41] Reaching the committed state may require the rearrangement of the internal forces that stabilize each conformational state, such as hydrophobic, electrostatic, van der Waals, and

hydrogen bonding interactions. Although to a lesser extent, hydrogen bonds are thought to play an important role in protein stability and in fine-tuning their tertiary structure [96].

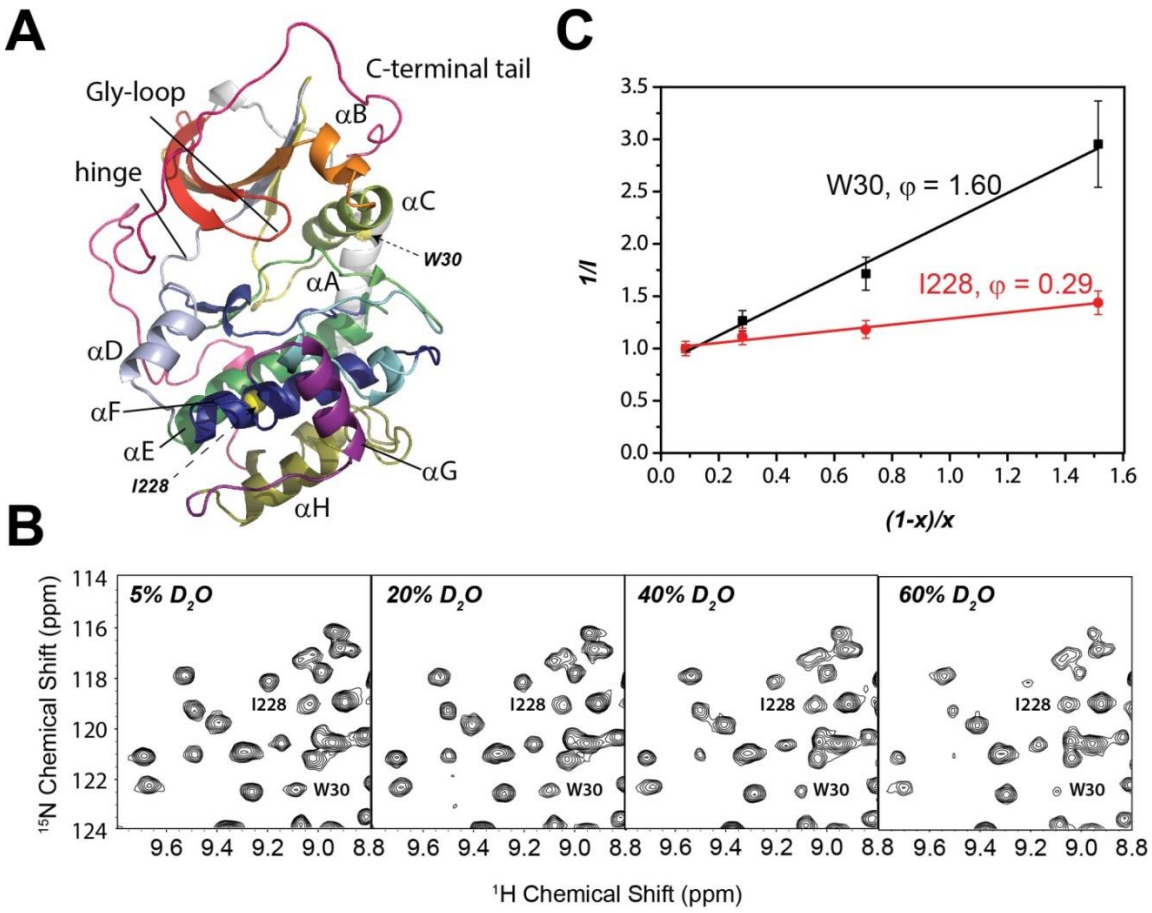

Figure 2.1. Determination of fractionation factors.
(A) Structural motifs mapped onto the ternary complex of PKA-C (PDB ID: 1ATP). (B) Representative portions of the [^{1}H, ^{15}N]-TROSY-HSQC spectra for apo PKA-C at various concentrations of D_2O, highlighting W30 and I228 located in helical domains of the kinase. (C) Linear least-squares fit of the inverse of intensities for W30 and I228 versus (1-x)/x, where x is the mole fraction of H_2O.

In this paper, we studied the changes in the kinase hydrogen bond strengths across the three major conformational states. To obtain residue-specific information in the hydrogen-bond strengths, we measured the hydrogen/deuterium (H/D) fractionation factors (φ) using solution NMR spectroscopy [97, 98]. The φ values report on the preference of each amide site to take up deuterium over protium from a mixed H_2O/D_2O solution. Initially developed to probe hydrogen bond strengths in dicarboxylic acids [99], φ values have been widely utilized to investigate low-barrier hydrogen bonds in enzymes [100] and in evaluating the contribution of hydrogen bonds to protein stability [101, 102].

Recently, Cao and Bowie revisited issue of hydrogen/deuterium fractionation providing a revised energetic scale for the φ values and underscoring the importance of analyzing φ values to determine the changes in hydrogen bond strength for ligand binding to proteins [103].

Generally, a φ value of unity indicates equal distribution of deuterium and protium between protein and bulk solvent. The amide sites involved in strong hydrogen bonds prefer protium over deuterium with $\varphi < 1$; whereas amides involved in weak hydrogen bonds have $\varphi > 1$ [101]. In proteins, amide hydrogens have φ values ranging from 0.3 to 2.0, with the latter measured for very weak hydrogen bonds.[101] We measured the φ values for the backbone amides of PKA-C in three different forms: apo, ADP-bound (binary complex), and ADP-PKI peptide bound (ternary complex). Our results show that the overall φ values decrease as the kinase binds ADP and a pseudo-substrate peptide (PKI_{5-24}), indicating that the strength of hydrogen bonds gradually increases from the free to the ternary forms. Importantly, the changes in hydrogen bond strengths are not localized to the binding site but are pervasive throughout the entire protein. Whereas the majority of the hydrogen bonds increase their strengths, several other hydrogen bonds away from the ligand binding sites become weaker, suggesting a redistribution of the protein free energy. From this study, φ measurements emerge as an important complement to other NMR parameters such as chemical shifts [104-107], H/D protection factors [108, 109], residual dipolar couplings [110, 111], and nuclear spin relaxation measurements [112-116] to characterize protein conformational dynamics and to identify long-range allosteric changes upon ligand binding or mutations.

2.3 Experimental Procedures

NMR sample preparation. Uniformly ^{15}N-labeled PKA-C was expressed in *E. coli* bacteria and purified as reported previously [117]. A single protein stock solution was used for each set of the experiments for each form of the kinase. Each NMR sample contained ~200 μM PKA, 20 mM KH_2PO_4, 90 mM KCl, 10 mM $MgCl_2$, 10 mM MEGA-8 (Octanoyl-N-methylglucamide), 5% Glycerol, 20 mM dithiothreitol (DTT), 1 mM NaN_3. The pH of the buffer solutions in both protonated and deuterated water was adjusted to 6.5 (without correction for the isotope effect). For the nucleotide-bound form, PKA-C was

saturated with 12 mM ADP, while for the ternary complex, the enzyme was saturated with 12 mM ADP and 350 μM of a peptide corresponding to the recognition sequence of the protein kinase inhibitor (PKI_{5-24}), and 60 mM $MgCl_2$ was used. The samples containing varying concentrations of D_2O (5%, 20%, 40%, and 60% by volume for the apo and ternary forms; 5%, 20%, 40%, 50%, and 60% by volume for the binary form) were prepared by mixing buffer solutions of protonated and deuterated water. A maximum of 60% D_2O mole fraction was chosen to minimize errors due to the increase of T_1 values at high deuteration levels.

Determination of H/D fractionation factors. The H/D equilibrium fractionation factor (φ) is defined as the equilibrium constant of the following reaction:

$$NH : B + \frac{1}{2} D_2O \Leftrightarrow ND : B + \frac{1}{2} H_2O \tag{2.1}$$

$$\phi = \frac{\left([D]/[H]\right)_{protein}}{\left([D]/[H]\right)_{water}} \tag{2.2}$$

where NH represents the weak acid and B the weak base.

To determine the fractionation factors, a series of [^{1}H,^{15}N]-TROSY-HSQC[118] spectra were acquired using the CLEAN-TROSY version of the original pulse sequence [119] were recorded on all of the forms of the kinase for all of the D_2O concentrations. The spectra were acquired on an 850 MHz Bruker spectrometer equipped with a triple resonance probe at 27°C with either 128 scans (for both the binary and ternary forms) or 64 scans (for the apo form) and 60 increments and a recycle delay of 1.5 seconds. The spectra were processed using NMRPipe [120]. The peak intensities were determined using Sparky [121] with assignments previously determined for PKA-C [122]. Fractionation factors are obtained by the linear least-squares analysis of

$$\frac{1}{y} = C\left[\phi\frac{1-x}{x} + 1\right] \tag{2.3}$$

where *y* is the peak intensity, x is the mole fraction of water and C is the normalization parameter, which is the inverse peak intensity at 100% H_2O. Note that for high D_2O concentrations, it is advisable to use non-linear fitting as the linear fitting amplifies the errors [123].

2.4 Results

H/D fractionation factors and structural transitions of PKA-C. Fractionation factors (φ) were measured by incubating PKA-C in aqueous solutions with D_2O concentrations ranging from 5 to 60%. Under these conditions, the intensities of the amide resonances in the [^{1}H,^{15}N]-TROSY-HSQC spectrum decrease according to their relative propensity to incorporate deuterium, reflecting the strength of the hydrogen bonds in which they are involved [97, 101]. To ensure that the exchange reached equilibrium, we incubated the samples and kept them at 25°C for 24 hours prior to acquiring the [^{1}H,^{15}N]-TROSY-HSQC spectra (**Figure 2.2**) [118]. Indeed, we found that the amide resonance intensities were unchanged after a 7 day incubation period (**Figure 2.3**). To calculate the φ values, we fit the trend of the amide peak intensities as a function of the mole ratio of D_2O. To mimic the three major conformational states of PKA-C, we performed our experiments on the apo, ADP-bound, and ADP/PKI_{5-24}-bound kinase. ADP was used in place of the common ATP mimic, ATPγN, because of the very slow hydrolysis on the timescale of weeks that was observed with ATPγN [124]. The [^{1}H,^{15}N]-TROSY-HSQC spectra of PKA-C saturated with either ADP or ATPγN are almost superimposable (**Figure 2.2**), indicating that the average conformations of the kinase are very similar. As for the binary complexes, the spectra of the ternary complexes formed with either ADP/PKI_{5-24} or ATPγN/PKI_{5-24}-bound are similar. Only small chemical shift perturbations are observed nearby the active site, reflecting the effect of the γ-phosphate group. Upon ligand binding, PKA-C undergoes linear chemical shift changes between the apo and closed form of the enzyme, [43, 122, 125] indicating that ligand binding shifts a pre-existing conformational equilibrium from *open* and *closed* state in the fast exchange regime on the chemical shift time scale [125]. To estimate the average conformational state of the kinase free and bound undergoing fast exchange equilibrium, we used CONCISE (COordiNated ChemIcal Shifts beHavior) [125]. As reported in **Figure 2.4**, the probability densities of the complexes with ADP and ATPγN are essentially overlapped. A small but significant difference is observed for the probability densities for the ternary complexes, which reflect the differences in the observed chemical shifts (**Figure 2.4 panel A**). Nonetheless, the average positions of the distributions on the average principal

component (PC) score indicate that these complexes recapitulate both the intermediate and the closed states (**Figure 2.4 panel C**).

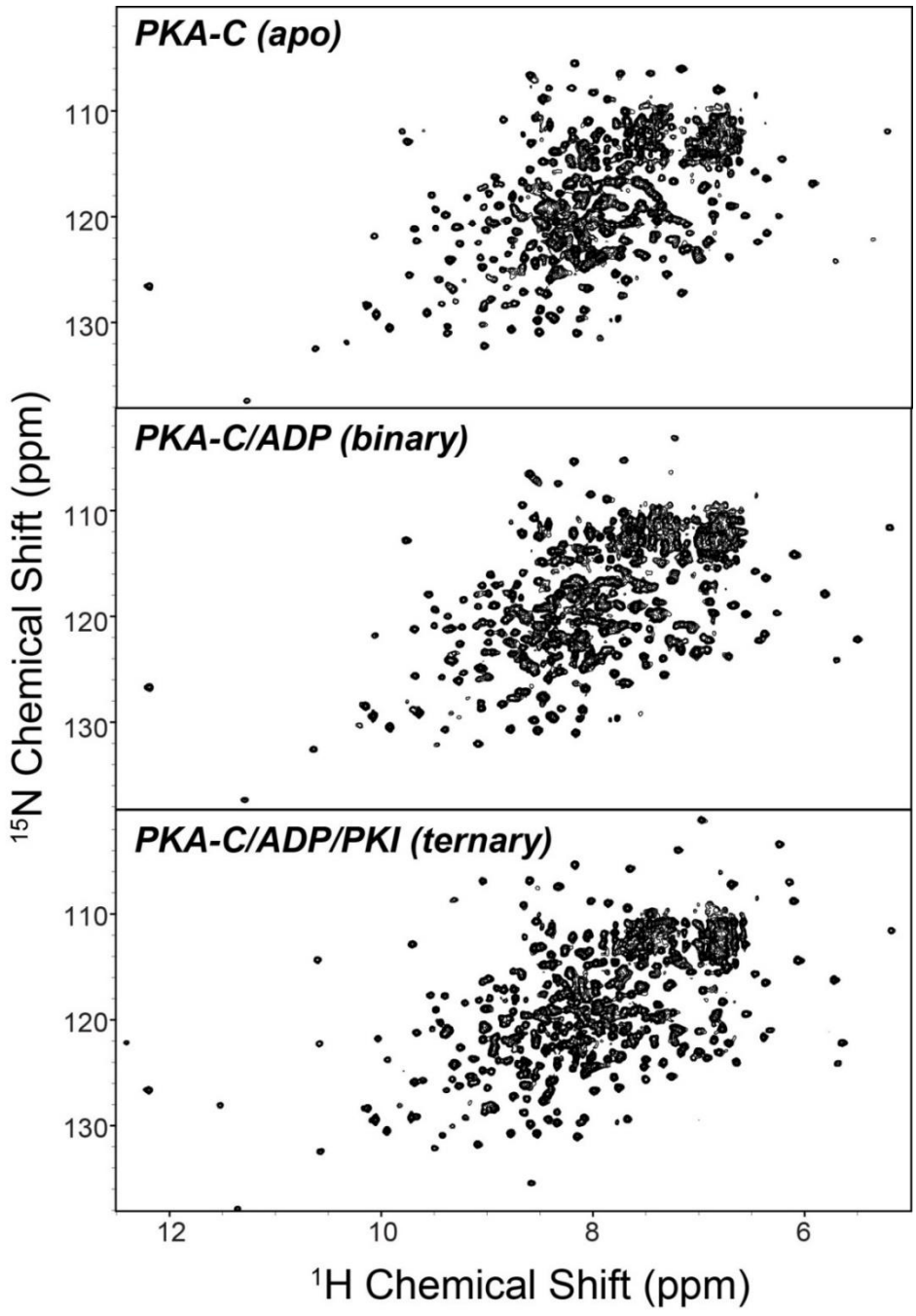

Figure 2.2. [^{1}H,^{15}N]-TROSY-HSQC spectra of the three major conformational states of PKA-C used in this study.

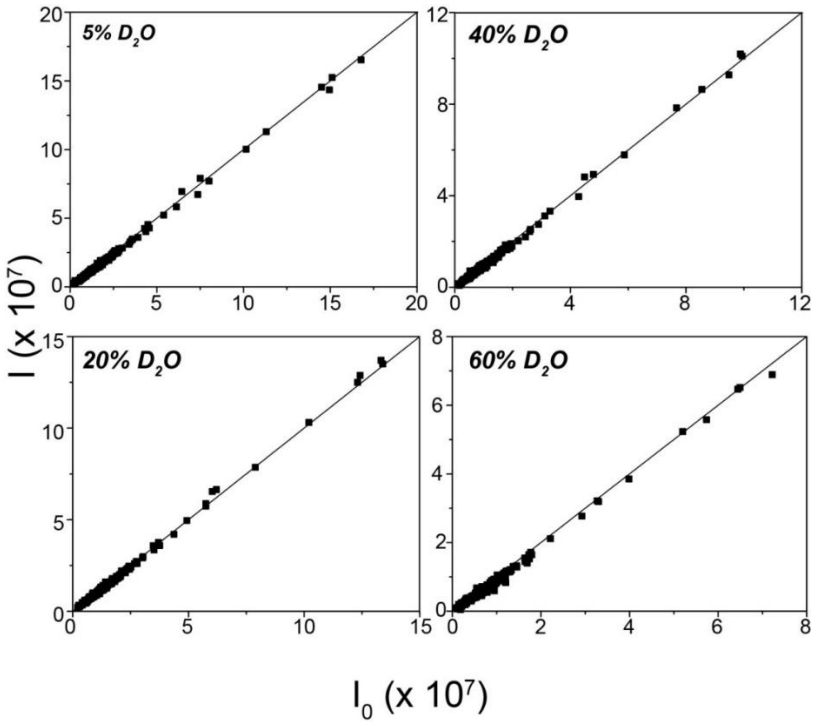

Figure 2.3. Plots showing the correlation of the peak intensities used in the analysis of the fractionation factors of the amide resonances of the ternary form of PKA-C at the day of actual measurement (I0) and 7 days after (I).
The linear correlation suggests that the 24-hour incubation time is enough for sufficient isotope exchange.

When ADP is bound, the enzyme's resonances undergoes significant line broadening originating from conformational dynamics on the μs-ms timescale similar to those experienced with ATPγN or ATP (**Figure 2.5**) [40, 43]. Therefore, several resonances in the intermediate states are not available for analysis. Overall, 211, 201, and 243 resonances for the apo, binary, and ternary forms of PKA-C, respectively, were available for the calculations of the φ values (**Figure 2.6**). Of the calculated φ values, we eliminated those exceeding the value of 2.0, which are affected by rapid exchange and T_1 values [101] as well as those residues showing poor correlation coefficients (R^2 < 0.70). Note that in a few instances we measured φ values slightly lower than 0.20. Although included in the plots, those residues are considered not exchanging with the solvent in the time scale we analyzed. These observation are in agreement with previous work by Taylor and co-workers, who found similar non-exchanging residues in the hydrophobic core of PKA-C using deuterium exchange mass spectrometry (DXMS) [22].

The overall mean fractionation factor values for the apo, binary, and ternary complexes were 1.06 ± 0.52, 1.04 ± 0.52 and 0.96 ± 0.55, respectively.

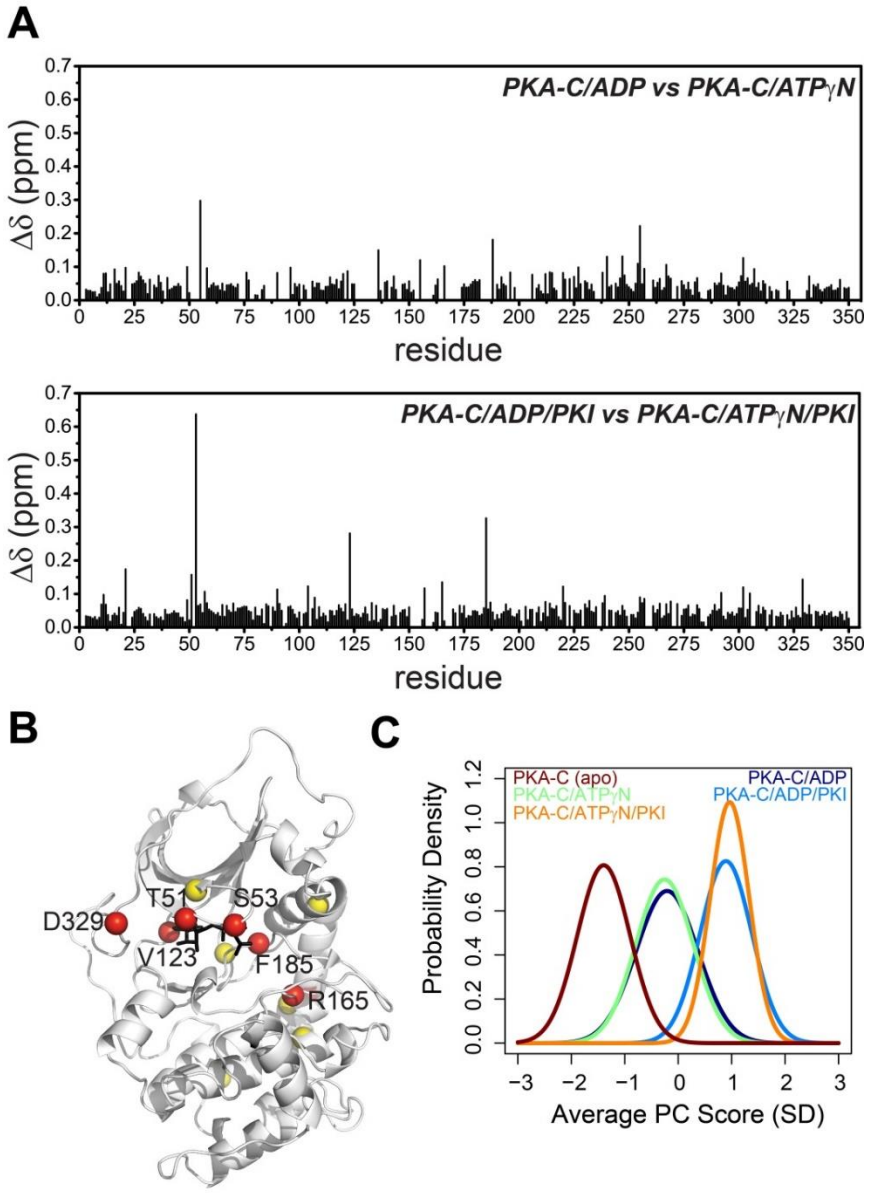

Figure 2.4. Chemical shift changes upon addition of ADP and ATPγN.
A. Plots of the chemical shift changes upon addition of ADP and ATPγN. **B.** Most significant chemical shift differences mapped onto the structure of PKA-C, PDB: 1ATP. Red spheres indicate residues with Δδ greater than one standard deviation from the mean (i.e. Δδ > 0.12); yellow spheres are residues with Δδ > 0.10. **C.** CONCISE analysis [125] of the amide chemical shifts showing that the average conformations of the binary and ternary complexes using ADP as nucleotide are similar to their ATPγN counterparts.

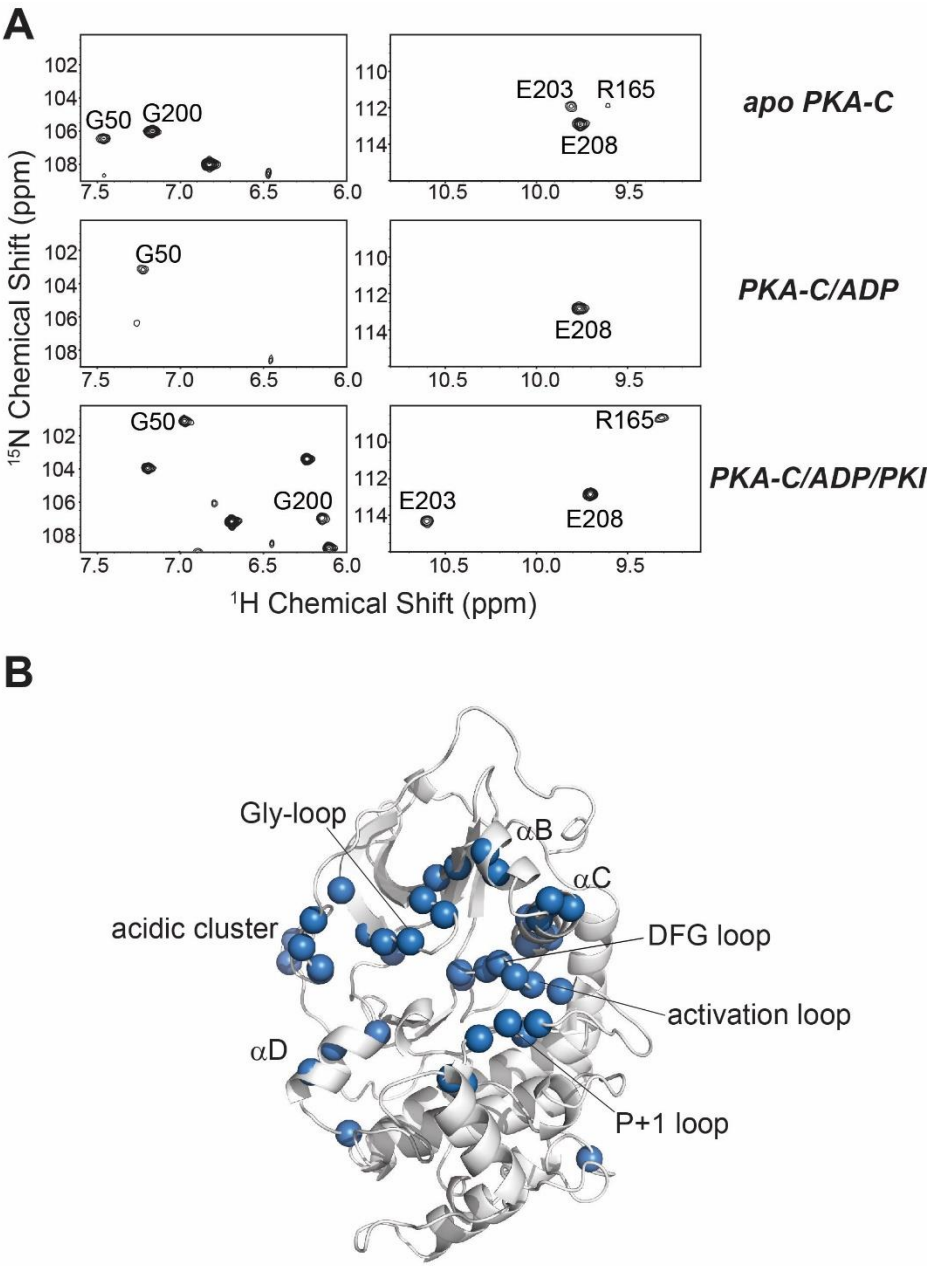

Figure 2.5. Residues that are exchange-broadened in the spectrum of PKA-C/ADP.
(A) Portions of [^{1}H,^{15}N]-TROSY-HSQC spectra of the three states, showing the exchange broadening in the binary form. (B) These residues include Gly-rich loop, B-, C-, and D-helices, DFG loop, activation loop, P+1 loop and the acidic cluster in C-terminal tail. Gly50 and Gly55 are parts of the Gly-rich loop, Arg165 is part of the catalytic loop, Gly200 and Asp203 are parts of the P+1 loop.

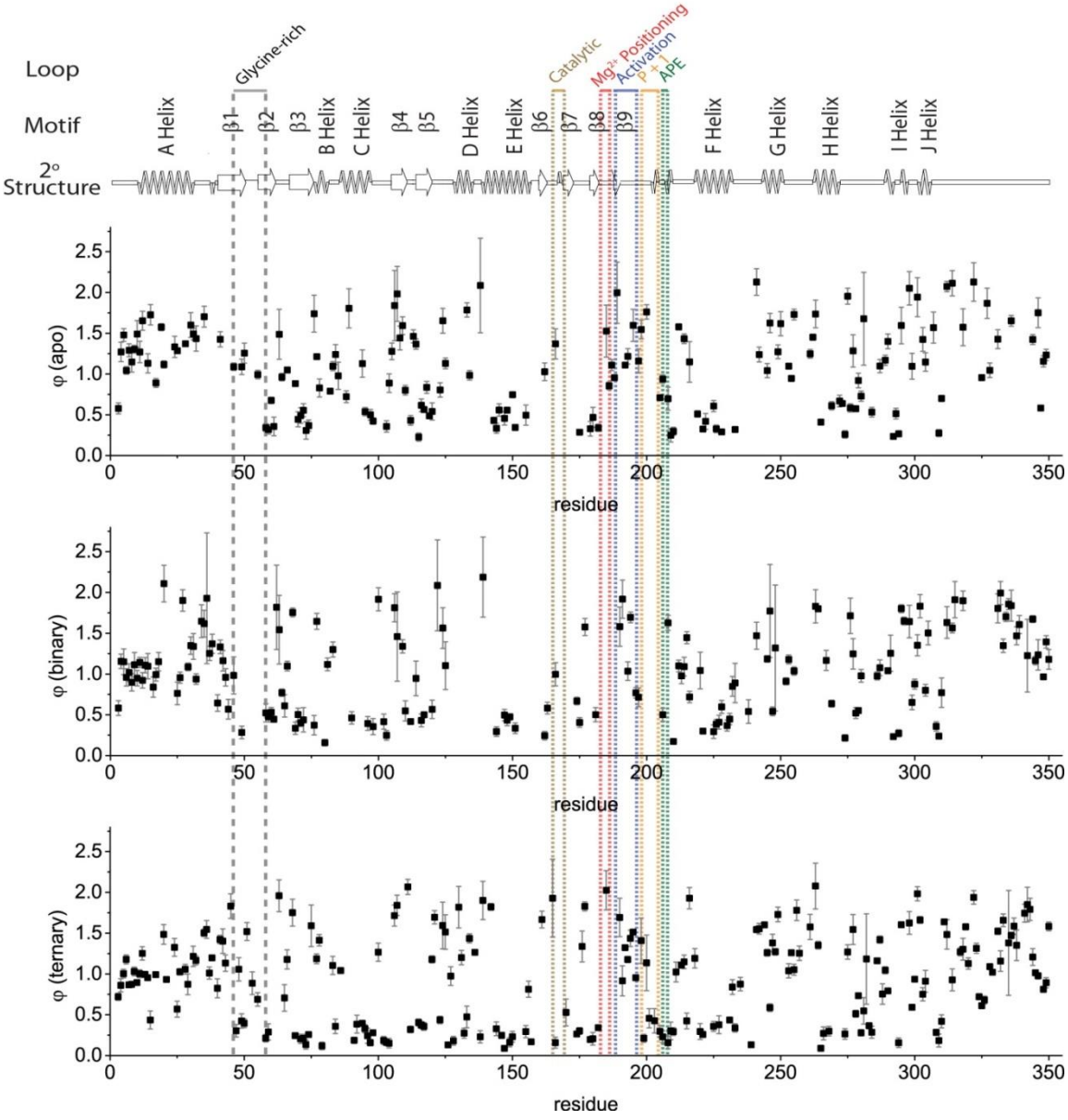

Figure 2.6. . Fractionation factors of the amide resonances of PKA-C in three different states. Fractionation factors of the amide resonances of PKA-C in three different states: apo, binary (ADP-bound), and ternary (ADP- and PKI-bound) are plotted versus residue number.

Although the overall strength of the hydrogen bonds increases in agreement with the thermostability of the protein [14], there is variability of the φ values across the enzyme, reflecting local changes in hydrogen bond strength upon ligand binding (**Figure 2.7**). In fact, the plots describing the number of occurrences versus φ values for all three forms of PKA-C show broad distributions of φ values (**Figure 2.8**). This contrasts with

the tight bell-shaped distribution of φ in staphylococcal nuclease that was centered at 0.85 [101]. The variability of φ is apparent in all of the structural motifs for all of the states (**Table 2.1)**. In the apo state, high φ values (<φ> greater than 1.2) were measured for the N-terminus (αA and β1) and C-terminal tail; while the helices in the large lobe, namely along αE and αF, display very low φ values (<φ> less than 0.5, **Table 2.1**). These results, in qualitative agreement with the DXMS experiments, suggest that these hydrogen bonds make a significant contribution to the stability of the large lobe.[22] Unlike previous fractionation studies,[101, 126-128] there is no correlation between φ values and secondary structure in PKA-C. For instance, W30 and I228, both located in α-helices, exhibit rather different hydrogen bond strengths (**Figures 2.1B and C**). We also observed that most residues with φ values >> 2 (**Figure 2.9A**) are located in the solvent-exposed, unstructured regions of the enzyme undergoing significant motions[40, 41, 43, 122]. Due to exchange broadening on the μs-ms timescale upon ADP binding, we were unable to measure φ in the active site, including the Gly-rich, DFG, activation, and peptide positioning loops. However we observed several changes in φ values radiating away from the nucleotide binding pocket to more peripheral domains of the enzyme (**Figures 2.8 and 2.10**). In the small lobe these changes include β strands 1, 4-5 ($<\Delta\varphi^{binary\text{-}apo}> = -0.27$), the αA-β linker ($<\Delta\varphi^{binary\text{-}apo}> = -0.23$), and αA ($<\Delta\varphi^{binary\text{-}apo}> = -0.16$) (**Figure 2.10**). Interestingly, the loops connecting the αE, αF, and αH helices in the large lobe display lower φ values than in the apo state ($<\Delta\varphi^{binary\text{-}apo}>= -0.25$, **Table 2.1**). Previous research has shown that the nucleotide in PKA-C functions as an allosteric effector [40, 44]. These results suggest that nucleotide binding may affect short- and long-range intermolecular forces through altering in part the hydrogen bonding network.

Binding of PKI_{5-24} increases the compactness of the enzyme as it adopts a closed, solvent-protected conformation [14], with 54 out of 231 resonances displaying φ values around 0.3 (**Figure 2.8**), including residues in β strands 2 and 3, C-helix, αC-β4 loop, hinge, αD, αE, the segment from the P+1 loop until the F helix, αF, αH, and the αH-αI loop. Most of these residues are buried in the interior of the kinase (**Figure 2.9B**). Overall, we observed a decrease of the average φ values ($<\Delta\varphi^{ternary\text{-}binary}> = -0.10 \pm 0.38$), particularly for residues localized in the large lobe and C-terminal tail (**Figure 2.10**), except for a few residues in the αA helix ($<\Delta\varphi^{ternary\text{-}binary}> = -0.09 \pm 0.21$) and the

small lobe (<$\Delta\varphi^{ternary\text{-}binary}$> = -0.09 ± 0.24) (**Figure 2.10**). In contrast, the hinge region shows a positive change of <$\Delta\varphi$> (0.35 ± 0.30, **Figure 2.10 and Table 2.1**), which may result from a reorientation of the hinge region that enables the active site cleft to close. Additionally, $PKI_{5\text{-}24}$ binding increases the hydrogen bond strength in the inner core of the kinase for helices αE, αF and αH (**Table 2.1**) as well as for several residues in the C-terminal tail (**Figure 2.10),** consistent with the crystallographic data[14, 37, 129]. Specifically, the acidic patch (residues 330-334) has been hypothesized to recruit the basic substrate into the active site cleft, where Y330 is poised to interact with the substrate's P-3 arginine residue [122, 130]. Substrate binding primarily strengthens the hydrogen bonds in the large lobe of the enzyme, and also those in the C-terminal tail, recruited to assemble the active site for catalysis.

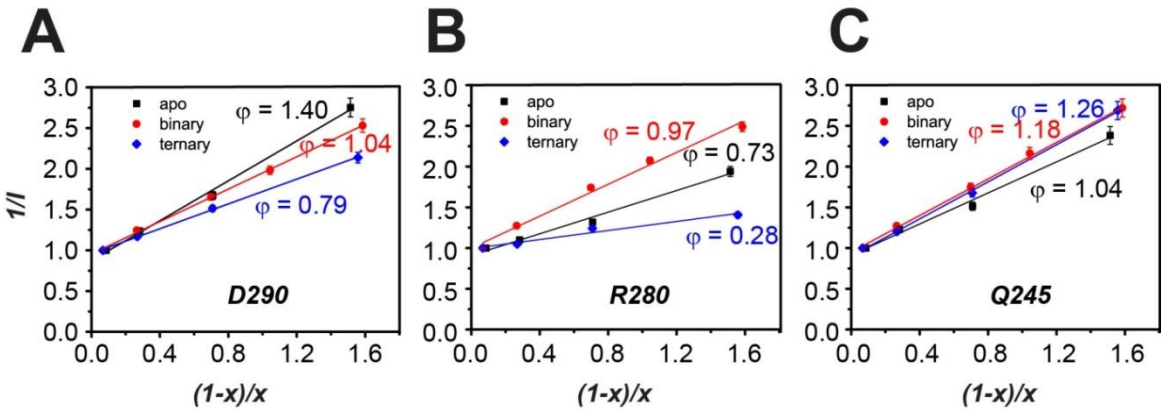

Figure 2.7. Representative least-squares fitting of residues showing different types of changes in hydrogen bond strengths upon binding nucleotide and pseudo-substrate.

To account for the changes in catalytically important motifs (i.e. Gly-rich, DFG loop, peptide positioning loops, etc.), we considered only the φ values for the apo and ternary forms (**Figure 2.11**). The majority of the catalytic motifs experienced strengthening of hydrogen bonds, including the Gly-rich loop (<$\Delta\varphi^{ternary\text{-}apo}$> = -0.61 ± 0.28), αC (<$\Delta\varphi^{ternary\text{-}apo}$> = -0.43 ± 0.27), and the peptide positioning loop (<$\Delta\varphi^{ternary\text{-}apo}$> = -0.39 ± 0.24). In contrast, the only reporter of the DFG loop (Phe185) shows a higher φ value for the ternary complex ($\Delta\varphi^{ternary\text{-}apo}$ = 0.50). Its propensity to incorporate deuterium could result from the increased conformational fluctuations caused by nucleotide binding. Taken together, these results show that nucleotide and pseudo-substrate

binding assembles the active site, strengthening the hydrogen bonds in the active site and coordinating catalysis in PKA-C.

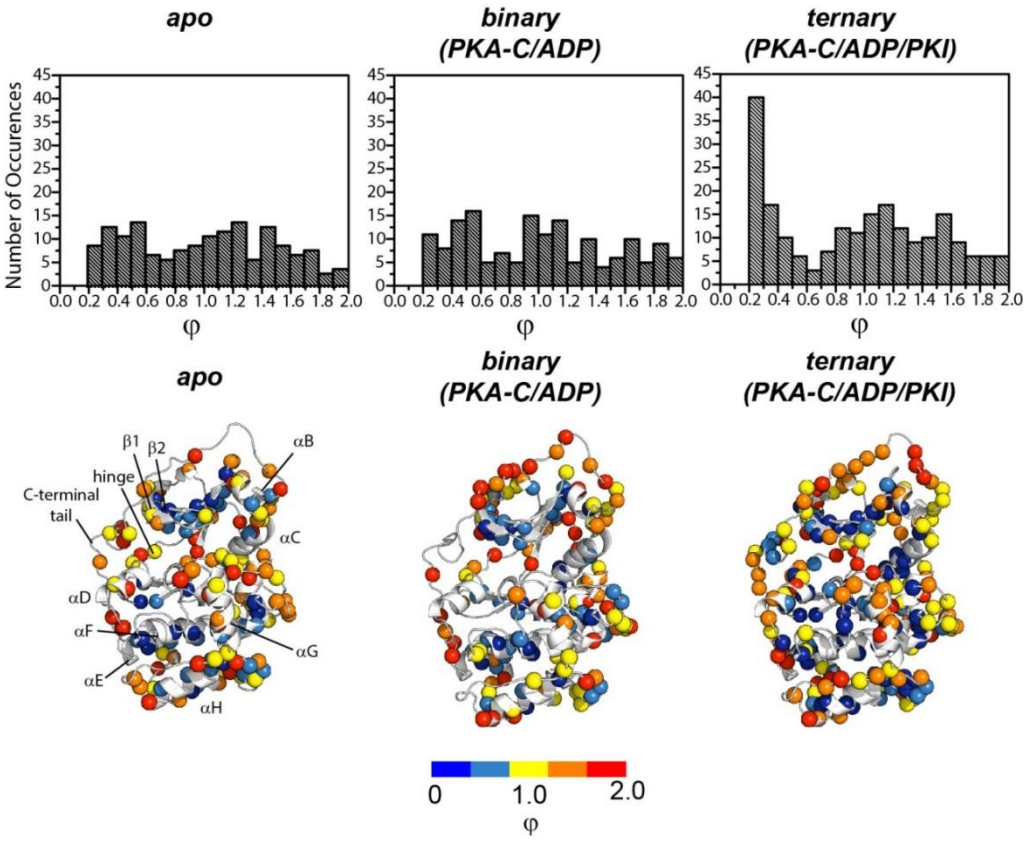

Figure 2.8. Distribution of the amide fractionation factors in three major states of PKA-C.
Histogram of the occurrences vs fractionation factor values (top panel). Mapping of the fractionation factors on the PKA-C structure (lower panel, PDB ID: 1ATP). The amide groups are represented as spheres and color-coded according to the spectrum bar (Blue: strong hydrogen bonds, high φ values; Red: weak hydrogen bonds, low φ values).

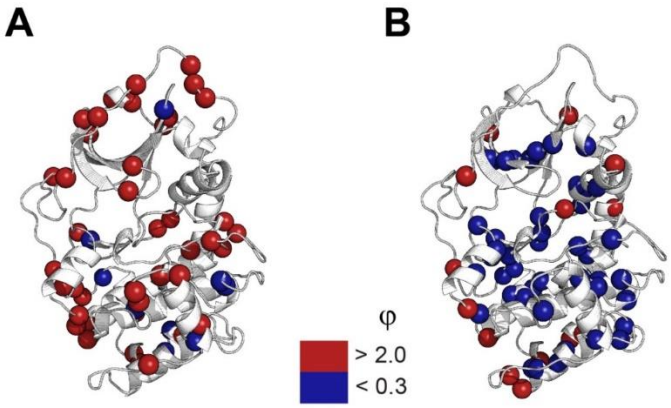

Figure 2.9. Mapping of the residues with fractionation factors greater than 2.0 and less than 0.3 on the X-ray structure (1ATP).
(A) Apo form, (B) ternary form. The H-bond strengths of several residues in the apo form are significantly weaker than the corresponding ternary complex. Also, residues with $\varphi > 2.0$ are mostly situated on the solvent-exposed, unstructured region of the kinase; while those with $\varphi < 0.3$ are buried within the enzyme.

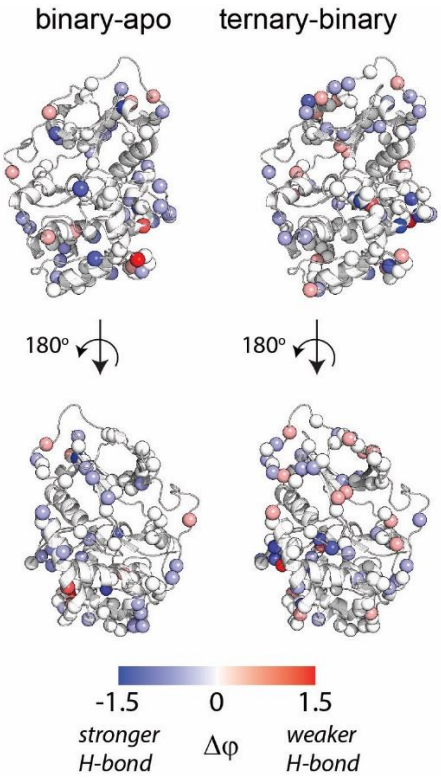

Figure 2.10. Differences in the fractionation factor between states of PKA-C mapped onto the PKA-C structure.
Differences in the fractionation factor between apo and binary (left), and binary and ternary complexes (right) of PKA-C mapped onto the PKA-C structure.

Table 2.1. Average φ values for the various structural motifs of PKA-C in the difference conformational states

Motifs	<φ>			<Δφ>	
	apo	binary	ternary	$\varphi^{binary} - \varphi^{apo}$	$\varphi^{ternary} - \varphi^{binary}$
A-helix	1.30 ± 0.27	1.12 ± 0.34	0.98 ± 0.23	-0.16 ± 0.37	-0.08 ± 0.21
αA-β linker	1.52 ± 0.16	1.32 ± 0.39	1.26 ± 0.25	-0.23 ± 0.24	-0.13 ± 0.20
hinge (res 120-127)	1.03 ± 0.48	1.33 ± 0.65	1.23 ± 0.47	-0.03 ± 0.06	0.35 ± 0.30
E-helix	0.49 ± 0.13	0.41 ± 0.09	0.51 ± 0.57	-0.03 ± 0.07	-0.16 ± 0.23
F-helix	0.40 ± 0.12	0.56 ± 0.27	0.51 ± 0.33	0.12 ± 0.34	-0.19 ± 0.32
G-helix	1.39 ± 0.28	1.15 ± 0.46	1.31± 0.40	0.14 ± 0.002	-0.08 ± 0.84
H-helix	0.86 ± 0.60	1.36 ± 0.57	1.00 ± 0.88	0.06 ± 0.05	-0.10 ± 0.49
C-terminal tail					
Res 298-314	1.44 ± 0.63	1.10 ± 0.55	1.03 ± 0.59	-0.34 ± 0.22	-0.11 ± 0.33
Res 315-345	1.51 ± 0.39	1.65 ± 0.27	1.32 ± 0.37	0.28 ± 0.08	-0.25 ± 0.47
Res 346-350	1.18 ± 0.48	1.19 ± 0.18	1.07 ± 0.35	-0.18 ± 0.34	-0.13 ± 0.38

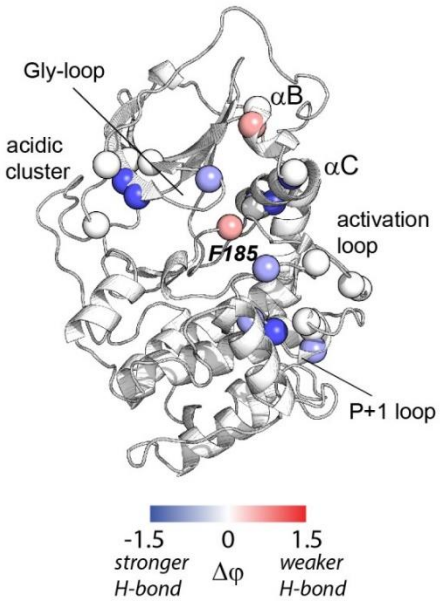

Figure 2.11. The difference in fractionation factor between apo and ternary complexes for the residues that were exchange-broadened upon ADP binding.

2.5 Discussion

In recent years, PKA-C has emerged as a model system to understand both kinase function as well as intramolecular allosteric signaling [14, 23]. The transitions of PKA-C between different states involve both conformational and dynamic (protein flexibility) changes that propagate from the ligand binding sites to remote parts of the molecule [40, 44]. Therefore, a complete understanding of this allosteric signaling necessitates the analysis of intra- and inter-molecular interactions that hold the protein together.[131] Among those, hydrogen bonds play a key role in allosteric regulation[84] and recent reports have demonstrated their importance in enzymatic catalysis and inhibition.[132, 133] DXMS techniques have been used to analyze hydrogen bond networks of proteins to identify domains that might be involved in allosteric transitions.[22, 134] Unlike DXMS, NMR spectroscopy monitors H/D exchange in a site-specific manner, making it possible to track hydrogen bonds throughout the protein at the atomic level. On the other hand, the NMR H/D exchange technique reports on the kinetic protection factors, monitoring the decay of the amide signals versus time.[108, 109] However, this technique, with a few exceptions for selected systems,[135-140] usually requires the lyophilization of the protein under examination. In contrast, the

equilibrium φ measurements can be accomplished by incubating the proteins in H_2O/D_2O solutions without lyophilization and report directly on the strength of the hydrogen bonds. These measurements are carried out under equilibrium conditions, which avoid the freezing-drying procedures required for the H/D protection factor measurements. This is crucial for PKA-C, an enzyme that is partially or completely inactivated upon lyophilization. Previous studies using H/D fractionation factors focused on the enzyme's active sites [102, 141] and did not fully exploit the potential of this approach for identifying local and long-range changes in the hydrogen bond network and allosteric communication. In fact, only marginal changes were detected for the φ values upon ligand binding to the proteins analyzed [97, 101, 128, 141]. These proteins, however, possess relatively rigid and compact structures with uniform values of φ. In contrast, the structure of PKA-C is highly dynamic, undergoing substantial conformational changes upon ligand binding.[142, 143] As a result, the φ values we measured for PKA-C have a much broader distribution than those measured for staphylococcal nuclease [101], ubiquitin [126], histidine-containing proteins [127], and immunoglobulin G binding domain of protein G [127]. As PKA-C transitions from the open to closed conformations upon binding the nucleotide and the pseudo-substrate inhibitor, the average φ values decrease, suggesting that the intramolecular hydrogen bonds become stronger. Globally, these results correlate well with X-ray crystallography [14], NMR spectroscopy [44], florescence studies [42, 144], thermodynamic [145] as well as DXMS analysis[22, 134] that show PKA-C's structure becoming more compact and thermostable in the closed conformation. Structurally, nucleotide binding allosterically couples the two lobes of the kinase, causing positive binding cooperativity between the nucleotide and the pseudo-substrate [44, 122]. Binding of the pseudo-substrate further stabilizes the complex, as is also evident in the increased strengths of hydrogen bonds in the large lobe as measured by the fractionation factors. Overall, nucleotide binding affects the strength of hydrogen bonds both in the small and large lobes, while pseudosubstrate binding affects mostly the residues in the large lobe. This is consistent with the view that the nucleotide is an allosteric effector, organizing the active site, while the large lobe provides a docking surface for the substrate to bind [14, 44]. These detailed effects of the nucleotide binding went undetected in the previous DXMS measurements [134] either for lack of data points or intrinsic limitations of the technique.

Recent community maps analysis of molecular dynamics simulations [93] predicted that the motions of the different secondary structural elements of the small lobe are highly correlated. The β1, β4, β5 and the αA-β linker were attributed to community A (responsible for nucleotide binding), while the A-helix, portion of αA-β linker, and αC-β4 linker were ascribed to community C (**Figure 2.12**)**,** a central hub that controls the functions of the other communities [93]. The increase in the strength of the hydrogen bond networks in the small lobe upon nucleotide binding supports the communication between these communities that may act in concert for the enzyme's closure. [93] Moreover, the φ values show that, from the apo to the ternary complex, the hydrogen bonds in the αC helix become stronger, indicating that perhaps strengthening these interactions is essential for proper organization of the active site. From the X-ray structure, the side chains in each turn of the αC helix interact with the different domains of the enzyme (**Figure 2.13**). Specifically, Arg93 forms a cation-π interaction with the aromatic side chains of Trp30 and Phe26 of the αA helix. Glu91 forms a conserved dyad with Lys72 of β-strand 3, while His87 forms an ion pair with the phosphate group of Thr197 in the closed conformation [14]. The H/D fractionation factors also show an extensive rigidification of the hydrophobic core in the enzyme upon ligand binding as previously highlighted by DXMS studies, with the αE, αF, and αH helices involved in the intra-molecular communication are more resistant to deuterium exchange [22].

Nucleotide binding also increases the hydrogen bond strengths of residues in the region that caps the bottom of the large lobe. The allosteric coupling between the catalytic loop and the large lobe was also observed using DXMS experiments [22]. In particular, the interactions between the conserved residues Glu208 of the APE motif and Arg280 are evident in our data, where these residues show lower φ values upon PKI binding to the binary form of the enzyme. This ion pair connects the P+1 loop and the loop between the G and H helices. The C-terminal tail undergoes significant domain movement when the enzyme transitions from open to closed conformation, as observed in the crystal structure (**Figure 2.14**) [37]. While DXMS data suggest that the nucleotide binding increase the amide protection factors for the entire C-terminal tail [134], our data show that residues 315-345, which contains the gate controlling the nucleotide access, display hydrogen bonds weaker than in the apo form. These weak hydrogen bonds

concur to the increased flexibility of the intermediate state, but eventually become stronger upon formation of the ternary complex, with the interactions between the acidic cluster and the basic residues of the pseudo-substrate [130].

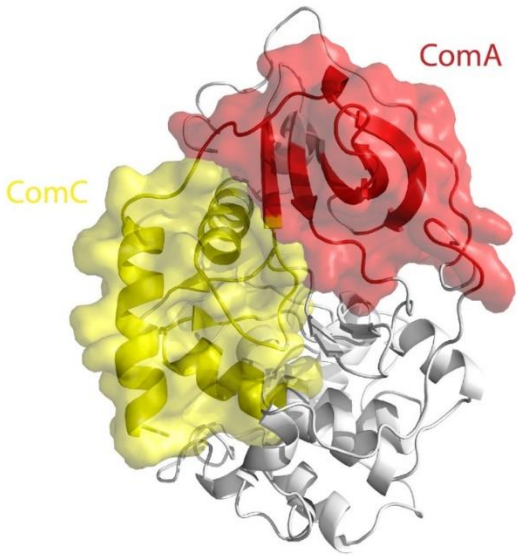

Figure 2.12. Regions showing the A and C communities.
Regions showing the A and C communities, red and yellow, respectively. Illustration adapted from McClendon *et al.* [93]

Overall, this study demonstrates that the changes in the allosteric network of the kinase are manifested through variations in hydrogen bond strengths. These changes are not unidirectional: while several hydrogen bonds become stronger upon ligand binding, other interactions become weaker, underscoring a redistribution of the free energy of binding occurring throughout the whole enzyme. As NMR methodology progresses toward understanding the mechanisms of allosteric transmission at the atomic level, the measurement of equilibrium H/D fractionation factors emerges as a complementary method to other NMR techniques to trace allosteric communications within proteins and enzymes.

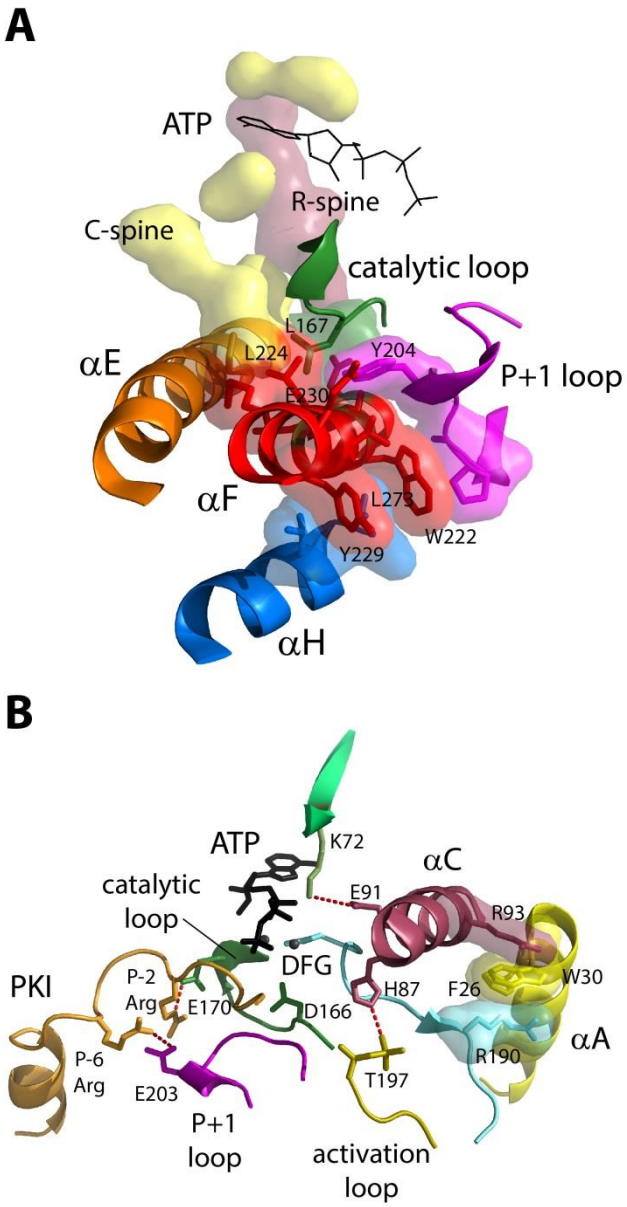

Figure 2.13. Signal integration motifs in PKA-C.
(A) The F-helix (red) is a central scaffold where the catalytic and regulatory spines are tethered. It also forms hydrophobic packing with the H-helix (blue) and catalytic loop (green). It also forms a salt bridge and hydrophobic packing with the P+1 loop (magenta). (B) The C-helix (dark pink) integrates the important catalytic elements in the active site with the small lobe and A-helix (yellow).

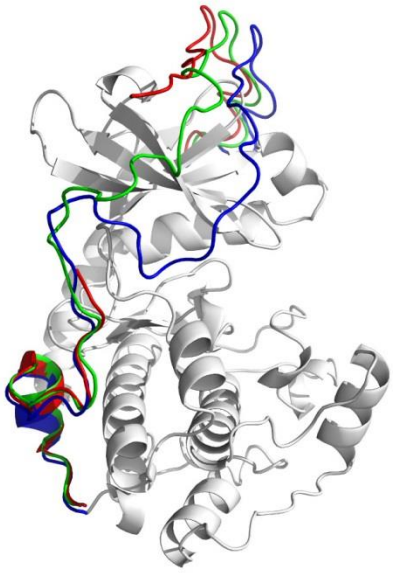

Figure 2.14. The orientations of the C-terminal tail in three different conformations of PKA as observed in the crystal structures.
PDB ID: 1J3H (apo, red), 4NTT (binary, green), 1ATP (ternary, blue).

2.6 Acknowledgements

The NMR spectra were acquired at the Minnesota NMR Center. We would like to thank Youlin Xia for assistance with the NMR experiments and Prof. A. Cembran for assistance with the CONCISE scripts.

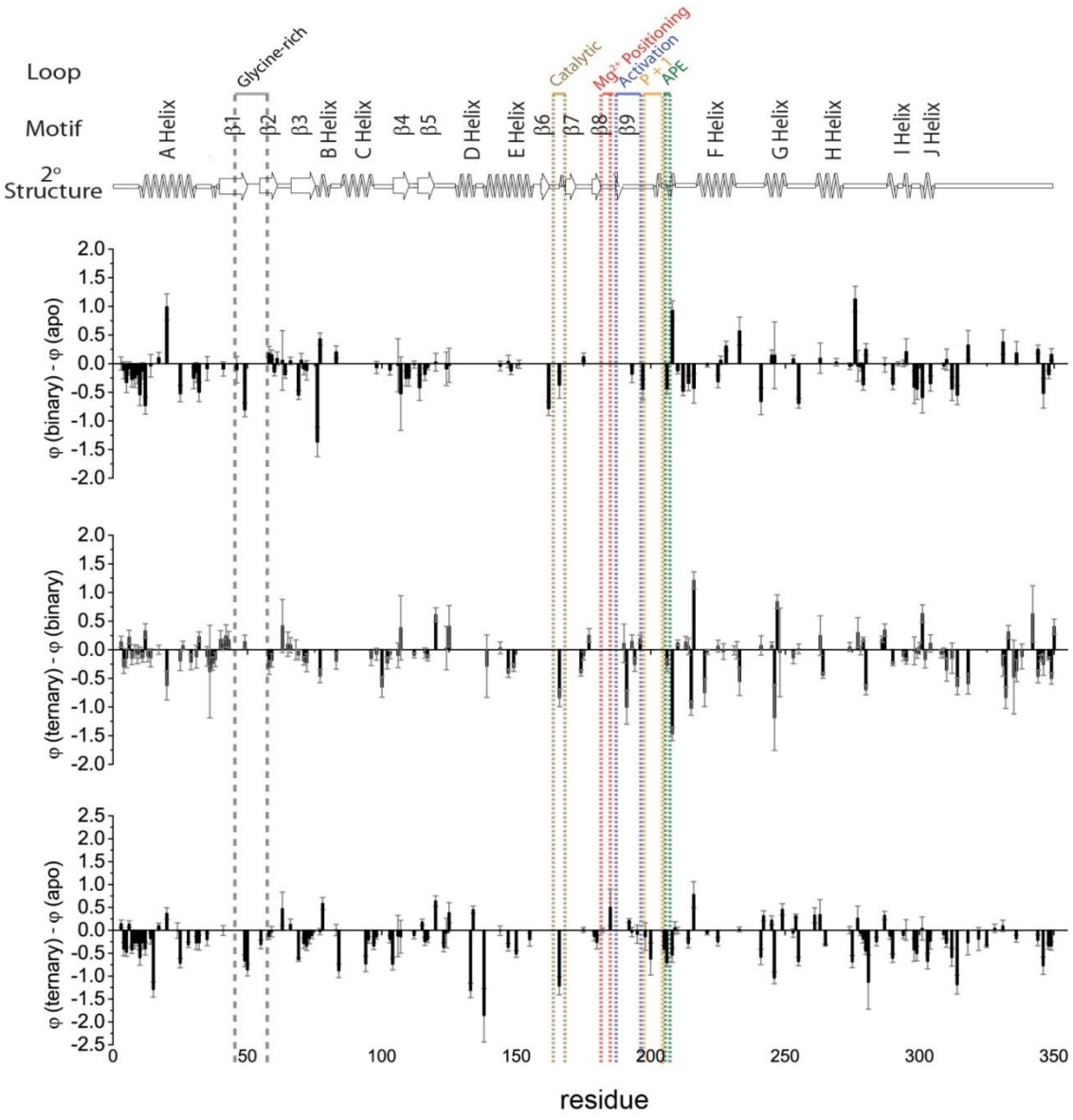

Figure 2.15. Fractionation factors differences for the amide resonances of PKA-C among the different states.

Table 2.2. Equilibrium H/D Fractionation Factors of the Residues in Three Major States of PKA-C

Residue	Apo	Binary (PKA:ADP)	Ternary (PKA:ADP:PKI)
3	0.58 ± 0.07	0.58 + 0.09	0.72 + 0.04
4	1.27 ± 0.12	1.16 + 0.09	0.86 + 0.08
5	1.48 ± 0.08	1.15 + 0.16	1.00 + 0.05
6	1.04 ± 0.05	0.96 + 0.11	1.18 + 0.06
7	1.29 ± 0.08	1.02 + 0.11	0.87 + 0.01
8	1.15 ± 0.12	0.90 + 0.11	0.87 + 0.03
9	1.30 ± 0.05	1.11 + 0.15	1.03 + 0.05
10	1.49 ± 0.16	0.95 + 0.09	0.89 + 0.02
11	1.27 ± 0.13	1.14 + 0.06	1.00 + 0.05
12	1.65 ± 0.12	0.92 + 0.10	1.25 + 0.08
13	-	1.11 + 0.09	0.99 + 0.04
14	1.13 ± 0.12	1.10 + 0.16	0.95 + 0.02
15	1.73 ± 0.13	-	0.44 + 0.11
16	-	0.84 + 0.12	-
17	0.89 ± 0.05	0.99 + 0.08	0.99 + 0.01
18	-	1.15 + 0.11	-
19	1.57 ± 0.04	-	-
20	1.12 ± 0.04	2.11 + 0.22	1.49 + 0.12
21	-	-	0.93 + 0.02
24	1.33 ± 0.13	-	1.33 + 0.11
25	1.29 ± 0.03	0.76 + 0.14	0.57 + 0.10
26	-	0.96 + 0.07	1.03 + 0.04
27	-	1.90 + 0.13	*ND*
28	1.37 ± 0.02	-	1.06 + 0.06
29	-	1.09 + 0.05	0.87 + 0.13
30	1.60 ± 0.15	1.35 + 0.11	-
31	1.49 ± 0.07	1.34 + 0.16	1.22 + 0.12
32	1.44 ± 0.15	0.94 + 0.06	1.17 + 0.05
34	-	1.65 + 0.20	-
35	1.70 ± 0.13	1.62 + 0.16	1.50 + 0.04
36	-	1.93 + 0.80	1.55 + 0.11
37	*ND*	1.25 + 0.09	1.01 + 0.07

38	-	1.37 + 0.12	1.20 + 0.03
40	*ND*	0.64 + 0.10	0.82 + 0.12
41	1.43 ± 0.09	1.33 + 0.08	1.42 + 0.05
42	*ND*	1.16 + 0.12	1.40 + 0.15
43	-	0.96 + 0.11	1.13 + 0.10
44	-	0.57 + 0.12	-
45	*ND*	-	1.83 + 0.15
46	1.09 ± 0.05	0.98 + 0.23	-
47	-	-	0.30 + 0.08
48	-	-	1.06 + 0.14
49	1.09 ± 0.10	0.28 + 0.08	0.42 + 0.09
50	1.26 ± 0.12	*ND*	0.40 + 0.05
51		-	1.52 + 0.11
52	*ND*	-	-
53	-	-	0.89 + 0.14
55	0.99 ± 0.05	-	0.69 + 0.08
56	*ND*	-	-
58	0.34 ± 0.05	0.52 + 0.11	0.21 + 0.05
59	0.32 ± 0.05	0.47 + 0.06	0.29 + 0.10
60	0.68 ± 0.04	0.53 + 0.06	-
61	0.36 ± 0.11	0.45 + 0.01	-
62	*ND*	1.82 + 0.52	*ND*
63	1.49 ± 0.31	1.54 + 0.42	1.96 + 0.19
64	0.96 ± 0.05	0.77 + 0.05	-
65	-	0.61 + 0.14	0.71 + 0.16
66	1.05 ± 0.02	1.10 + 0.06	1.18 + 0.12
68	-	1.75 + 0.05	1.75 + 0.16
69	0.88 ± 0.02	0.33 + 0.07	0.24 + 0.03
70	0.45 ± 0.09	0.50 + 0.08	ND
71	0.49 ± 0.10	0.40 + 0.04	0.21 + 0.06
72	0.56 ± 0.08	0.44 + 0.15	0.21 + 0.05
73	0.31 ± 0.11	-	*ND*
74	0.37 ± 0.07	-	0.26 + 0.02
75	-	-	1.59 + 0.26

76	1.74 ± 0.23	0.37 + 0.12	-
77	1.21 ± 0.03	1.65 + 0.10	1.19 + 0.06
78	0.83 ± 0.11	-	1.41 + 0.07
79	-	-	*ND*
80	-	0.16 + 0.04	-
81	-	1.12 + 0.08	-
82	0.79 ± 0.01	-	-
83	1.10 ± 0.05	1.30 + 0.09	1.10 + 0.11
84	1.24 ± 0.12	-	0.36 + 0.09
85	0.98 ± 0.17	-	*ND*
86	-	-	1.04 + 0.02
88	0.72 ± 0.07	-	-
89	1.81 ± 0.24	-	-
90	-	0.46 + 0.08	-
91	-	-	0.19 + 0.04
92	-	-	0.38 + 0.11
94	1.13 ± 0.17	-	0.40 + 0.03
95	0.54 ± 0.05	-	0.33 + 0.05
96	-	0.39 + 0.08	0.24 + 0.09
97	0.50 ± 0.07	-	0.16 + 0.04
98	0.42 ± 0.04	0.36 + 0.10	0.28 + 0.03
99	*ND*	-	-
100	*ND*	1.92 + 0.14	1.27 + 0.11
102	-	0.42 + 0.09	0.19 + 0.05
103	0.36 ± 0.07	0.25 + 0.06	0.16 + 0.04
104	0.89 ± 0.11	-	0.15 + 0.06
105	1.28 ± 0.10	-	-
106	1.84 ± 0.43	1.81 + 0.17	1.72 + 0.13
107	1.98 ± 0.34	1.46 + 0.55	1.84 + 0.12
108	1.44 ± 0.15	ND	ND
109	1.59 ± 0.11	1.34 + 0.08	-
110	0.80 ± 0.06	0.55 + 0.12	ND
111	*ND*	*ND*	2.07 + 0.09
112	0.43 ± 0.06	0.42 + 0.02	0.32 + 0.04

113	1.46 ± 0.08	*ND*	-
114	1.37 ± 0.06	0.95 + 0.21	-
115	0.23 ± 0.05	ND	0.41 + 0.04
116	0.62 ± 0.08	0.43 + 0.08	0.37 + 0.04
117	0.56 ± 0.03	0.50 + 0.02	0.36 + 0.05
118	0.84 ± 0.07	-	-
119	0.49 ± 0.03	-	-
120	0.54 ± 0.11	0.57 + 0.11	1.18 + 0.04
121	-	-	1.70 + 0.08
122	-	2.09 + 0.56	-
123	0.81 ± 0.09	-	0.44 + 0.05
124	1.65 ± 0.15	1.56 + 0.25	1.59 + 0.29
125	1.13 ± 0.07	1.10 + 0.29	1.51 + 0.21
126	-	-	*ND*
127	-	-	0.97 + 0.11
128	-	-	0.18 + 0.05
129	-	-	ND
130	-	-	1.82 + 0.25
131	-	-	1.20 + 0.09
132	-	-	0.27 + 0.06
133	1.79 ± 0.09	-	0.47 + 0.13
134	0.99 ± 0.06	-	1.44 + 0.06
136	-	*ND*	1.27 + 0.03
137	-	*ND*	*ND*
138	2.09 ± 0.58	-	0.23 + 0.07
139	*ND*	2.19 + 0.49	1.90 + 0.23
140	*ND*	*ND*	*ND*
142	*ND*	*ND*	1.82 + 0.04
143	0.43 ± 0.04	ND	-
144	0.33 ± 0.06	0.29 + 0.06	0.33 + 0.08
145	0.56 ± 0.08	-	-
146	-	-	0.25 + 0.03
147	0.46 ± 0.08	0.50 + 0.07	*ND*
148	0.56 ± 0.02	0.43 + 0.07	-

149	*ND*	0.47 + 0.04	0.16 + 0.06
150	0.75 ± 0.03	ND	0.23 + 0.07
151	0.35 ± 0.03	0.33 + 0.07	-
155	0.50 ± 0.12	ND	0.29 + 0.07
156	-	-	0.81 + 0.10
157	-	-	0.17 + 0.03
160	ND	-	-
161	*ND*	-	1.67 + 0.10
162	1.03 ± 0.11	0.24 + 0.05	-
163	-	0.58 + 0.07	-
165	*ND*	-	1.93 + 0.48
166	1.37 ± 0.18	1.00 + 0.14	0.16 + 0.07
170	-	-	0.53 + 0.16
174	-	0.67 + 0.05	0.26 + 0.03
175	0.29 ± 0.03	0.41 + 0.06	0.30 + 0.04
176	*ND*	*ND*	1.34 + 0.19
177	-	1.58 + 0.10	1.83 + 0.06
178	ND	ND	-
179	0.33 ± 0.09	ND	0.20 + 0.03
180	0.47 ± 0.12	ND	0.21 + 0.08
181	-	0.50 + 0.09	-
182	0.34 ± 0.05	-	0.34 + 0.02
184	-	-	ND
185	1.53 ± 0.32	-	2.03 + 0.24
186	0.86 ± 0.05	-	ND
187	1.11 ± 0.07	-	ND
188	0.96 ± 0.02	ND	ND
189	2.00 ± 0.38	-	-
190	*ND*	1.58 + 0.24	1.69 + 0.24
191	*ND*	1.92 + 0.23	0.92 + 0.18
192	1.11 ± 0.03	-	1.32 + 0.03
193	1.22 ± 0.09	1.03 + 0.11	1.18 + 0.04
194	-	1.69 + 0.07	1.44 + 0.10
195	1.60 ± 0.20	-	1.51 + 0.03

196	-	0.77 + 0.06	0.95 + 0.03
197	1.16 ± 0.15	0.71 + 0.11	-
198	1.55 ± 0.11	*ND*	1.41 + 0.28
199	*ND*	-	0.21 + 0.05
200	1.76 ± 0.09	-	1.14 + 0.34
201	ND	-	0.46 + 0.12
203	*ND*	-	0.43 + 0.15
205	0.71 ± 0.01	-	0.30 + 0.07
206	0.94 ± 0.05	0.50 + 0.08	0.23 + 0.07
208	0.70 ± 0.14	1.63 + 0.09	0.16 + 0.07
209	0.25 ± 0.08	-	0.30 + 0.11
210	0.30 ± 0.05	*ND*	0.29 + 0.05
211	-	-	1.02 + 0.12
212	1.58 ± 0.03	1.10 + 0.07	-
213	-	0.98 + 0.09	1.11 + 0.04
214	1.43 ± 0.06	1.09 + 0.12	1.15 + 0.08
215	-	1.45 + 0.07	0.42 + 0.10
216	1.15 ± 0.25	0.72 + 0.07	1.93 + 0.13
218	-	-	1.19 + 0.12
219	0.51 ± 0.04	-	-
220	-	1.04 + 0.23	0.29 + 0.10
221	0.33 ± 0.02	0.30 + 0.03	0.26 + 0.03
222	0.42 ± 0.10	-	-
225	0.61 ± 0.07	0.29 + 0.08	0.36 + 0.06
226	0.33 ± 0.05	0.39 + 0.06	-
227	-	0.41 + 0.08	0.38 + 0.11
228	0.29 ± 0.03	0.60 + 0.08	-
230	-	0.37 + 0.07	-
231	-	0.45 + 0.07	0.44 + 0.03
232	-	0.85 + 0.12	0.84 + 0.09
233	0.32 ± 0.01	0.89 + 0.24	0.34 + 0.05
235	-	-	0.88 + 0.08
238	-	0.54 + 0.14	-
239	-	-	*ND*

240	*ND*	ND	ND
241	2.13 ± 0.16	1.47 + 0.16	1.54 + 0.04
242	1.24 ± 0.09	*ND*	1.55 + 0.07
244	*ND*	*ND*	1.60 + 0.03
245	1.04 ± 0.09	1.19 + 0.04	1.26 + 0.04
246	1.63 ± 0.12	1.77 + 0.57	0.59 + 0.05
247	-	0.54 + 0.05	1.38 + 0.11
248	-	1.32 + 0.77	1.27 + 0.04
249	1.27 ± 0.08	-	1.73 + 0.09
250	1.62 ± 0.15	-	-
251	*ND*	-	-
252	-	0.91 + 0.04	-
253	1.10 ± 0.03	1.18 + 0.06	1.04 + 0.09
254	0.95 ± 0.02	ND	1.26 + 0.03
255	1.73 ± 0.07	1.04 + 0.05	1.05 + 0.07
256	*ND*	*ND*	1.78 + 0.13
257	-	-	1.25 + 0.09
261	1.25 ± 0.05	*ND*	1.58 + 0.15
262	1.45 ± 0.03	*ND*	*ND*
263	1.74 ± 0.17	1.83 + 0.20	2.08 + 0.28
264	-	1.80 + 0.02	1.35 + 0.05
265	0.41 ± 0.01	ND	*ND*
266	-		0.27 + 0.08
267	-	1.17 + 0.12	0.30 + 0.06
268	-	-	-
269	0.61 ± 0.05	0.64 + 0.04	-
272	0.67 ± 0.07	-	-
273	0.64 ± 0.03	-	-
274	0.26 ± 0.05	0.22 + 0.04	0.26 + 0.07
275	1.95 ± 0.10	*ND*	1.27 + 0.09
276	0.58 ± 0.05	1.71 + 0.22	-
277	1.28 ± 0.20	1.25 + 0.19	1.55 + 0.18
278	0.58 ± 0.03	0.52 + 0.07	0.51 + 0.04
279	0.92 ± 0.09	0.55 + 0.03	0.73 + 0.02

280	0.73 ± 0.06	0.98 + 0.08	0.28 + 0.04
281	1.68 ± 0.57	*ND*	0.55 + 0.16
282	-	-	1.18 + 0.55
283	-	-	0.37 + 0.03
284	0.53 ± 0.06	-	0.29 + 0.07
286	-	0.98 + 0.05	1.16 + 0.02
287	1.10 ± 0.08	1.08 + 0.10	1.42 + 0.04
288	-	-	0.75 + 0.13
289	1.17 ± 0.06	-	1.05 + 0.04
290	1.40 ± 0.09	1.04 + 0.03	0.79 + 0.02
291	*ND*	1.25 + 0.22	*ND*
292	0.24 ± 0.03	0.23 + 0.02	-
293	0.51 ± 0.07	-	*ND*
294	0.27 ± 0.03	0.27 + 0.04	0.16 + 0.06
295	1.60 ± 0.22	1.80 + 0.05	1.60 + 0.01
296	*ND*	1.65 + 0.05	*ND*
297	ND	ND	ND
298	2.05 ± 0.21	1.64 + 0.20	1.63 + 0.14
299	1.10 ± 0.16	0.65 + 0.09	0.59 + 0.01
300	-	0.88 + 0.06	0.94 + 0.02
301	1.94 ± 0.24	1.35 + 0.13	1.98 + 0.09
302	*ND*	1.83 + 0.14	1.66 + 0.04
303	1.42 ± 0.15	-	0.75 + 0.08
304	1.15 ± 0.11	0.80 + 0.07	0.91 + 0.13
305	-	1.50 + 0.14	-
307	1.57 ± 0.19	*ND*	-
308	-	0.36 + 0.06	0.28 + 0.04
309	0.28 ± 0.04	0.24 + 0.03	0.18 + 0.08
310	0.70 ± 0.03	0.77 + 0.18	0.42 + 0.08
311	*ND*	*ND*	1.64 + 0.01
312	2.07 ± 0.06	1.63 + 0.19	1.48 + 0.18
314	2.11 ± 0.15	1.56 + 0.06	0.93 + 0.13
315	*ND*	1.91 + 0.22	*ND*
317	-	*ND*	1.27 + 0.05

318	1.57 ± 0.23	1.90 + 0.12	1.30 + 0.13
319	-	-	1.58 + 0.04
320	-	-	1.13 + 0.07
322	2.13 ± 0.24	*ND*	1.94 + 0.08
323	-	-	1.31 + 0.06
324	-	-	0.72 + 0.02
325	0.96 ± 0.02	-	0.61 + 0.02
326	-	-	0.68 + 0.05
327	1.87 ± 0.18	-	ND
328	1.05 ± 0.09	-	1.09 + 0.01
329	-	-	1.02 + 0.02
330	*ND*	-	*ND*
331	1.43 ± 0.12	1.80 + 0.18	1.52 + 0.04
332	-	1.99 + 0.14	1.16 + 0.13
333	-	1.35 + 0.08	1.66 + 0.08
334	*ND*	1.70 + 0.06	-
335	-	1.86 + 0.07	1.38 + 0.64
336	1.65 ± 0.07	1.84 + 0.19	1.47 + 0.04
337	*ND*	-	1.59 + 0.10
338	-	1.47 + 0.11	1.35 + 0.19
339	-	1.61 + 0.11	-
341	*ND*	*ND*	1.74 + 0.11
342	*ND*	1.22 + 0.45	1.85 + 0.21
343	*ND*	*ND*	1.79 + 0.14
344	1.42 ± 0.06	1.67 + 0.04	1.21 + 0.10
345	-	1.16 + 0.05	1.02 + 0.02
346	1.75 ± 0.18	1.23 + 0.19	0.98 + 0.04
347	0.58 ± 0.03	-	ND
348	1.16 ± 0.07	0.97 + 0.02	0.81 + 0.02
349	1.23 ± 0.07	1.39 + 0.08	0.89 + 0.06
350	-	1.18 + 0.12	1.58 + 0.05

CHAPTER 3 A SEMI-AUTOMATED ASSIGNMENT PROTOCOL FOR METHYL GROUP SIDE-CHAINS IN LARGE PROTEINS

Jonggul Kim[1], Yingjie Wang[1], Geoffrey Li[1], and Gianluigi Veglia[1,2*]

[1]Department of Chemistry- University of Minnesota, Minneapolis, MN 55455; [2]Department of Biochemistry, Molecular Biology, and Biophysics– University of Minnesota, Minneapolis, MN 55455

Reprinted with permission from:
Methods of Enzymology (2015) Vol. 566 pp. 35-57.

3.1 Conspectus

The developments of biosynthetic specific labeling strategies for side-chain methyl groups have allowed structural and dynamic characterization of very large proteins and protein complexes. However, the assignment of the methyl-group resonances remains an Achilles' heel for NMR, as the experiments designed to correlate side chains to the protein backbone become rather insensitive with the increase of the transverse relaxation rates. In this chapter, we outline a semi-empirical approach to assign the resonances of methyl group side chains in large proteins. This method requires a crystal structure or an NMR ensemble of conformers as an input, together with NMR data sets such as NOEs and PREs, to be implemented in a computational protocol that provides a probabilistic assignment of methyl group resonances. As an example, we report the protocol used in our laboratory to assign the side chains of the 42-kDa catalytic subunit of the cAMP-dependent protein kinase A. Although we emphasize the labeling of isoleucine, leucine, and valine residues, this method is applicable to other methyl group side chains such as those of alanine, methionine, and threonine, as well as reductively-methylated cysteine side chains.

3.2 Introduction

Isotopic labeling is at the heart of NMR spectroscopy. After the pioneering work in the early '60s by several research groups [146-149], more complex labeling schemes have been used to attenuate transverse relaxation and push the boundaries of NMR analysis of large macromolecular complexes [150-152]. A significant step forward was made when non-labile protons in proteins were substituted by deuterons, ameliorating the dipolar relaxation due to ^{1}H-^{13}C, ^{1}H-^{15}N, and ^{1}H-^{1}H interactions, increasing sensitivity and resolution, thereby rendering proteins larger than 20 kDa amenable to structural NMR studies [153, 154]. Although complete deuteration has been used for backbone assignments in conjunction with transverse relaxation optimized spectroscopy (TROSY) [118], NOESY-based experiments benefit from incomplete (or fractional) deuteration, which preserves some protons for distance measurements [154]. Another quantum leap in the NMR structure determination of large complexes was made by Kay and co-workers, who developed a biosynthetic strategy for ^{1}H,^{13}C methyl group labeling in a highly deuterated background [155, 156]. Since then, this labeling strategy has expanded to include selective methyl group labeling such as isoleucine, valine, leucine, methionine [157], threonine [158], and alanine [159]. Although selective labeling schemes for aromatic side chains will certainly have an impact both in structure determination and dynamic characterization of large proteins [152], here we will focus on the use of methyl groups for the spectroscopy of large systems [160] akin to the TROSY method developed for backbone amides [118]. Following these methyl labeling schemes, quantitative studies on binding, structure, and conformational dynamics of proteins that are several hundred kDa are emerging, such as large molecular machinery [161-163], allosteric enzymes [164], chaperones [165], and protein thermodynamics [112].

The first methyl labeling scheme was published in 1997 by Gardner and Kay [156], who obtained a selective protonation of amino acids in which the direct biosynthetic precursor to isoleucine, 2-ketobutyrate, was enzymatically and chemically prepared with selective $^{13}CH_3$ labeling in a highly deuterated background. Exploiting the Escherichia coli (*E. coli)* biosynthetic pathway, this protocol enables the specific $^{13}CH_3$ labeling of the Cδ of Ile, while the remaining non-labile protons are replaced by deuterons. The incorporation of 2-ketoisovalerate, in a similar fashion, leads to selective

labeling on the Cδ and Cγ of leucine and valine, respectively [155], resulting in the so-called “ILV labeling” scheme (**Figure 3.1**). Nowadays, these biosynthetic precursors are commercially available in a variety of labeling schemes for assignment, structure determination, and dynamics studies. Selective labeling of the Cγ methyl of isoleucine has also been devised [166], but is uncommon due to the superior spectral qualities of the Cδ methyl group. Usually, selective labeling of other amino acids is achieved through direct addition of the amino acid to the growth medium during cell growth. For alanine and methionine, this is most commonly accomplished by directly incorporating the amino acid prior to induction (30 minutes to 1 hour) at final concentrations of 100-250 mg/L [112, 165] for Met and from 100-800 mg/L for alanine [112, 159]. An alternate approach is to engineer cysteine and react with ^{13}C-methyl-methanethiosulfonate (^{13}C-MMTS) to produce a methionine mimic [167]. Kay and coworkers have also developed an *in vitro* biosynthetic method to produce U-[^{2}H],Thr-γ2[$^{13}CH_3$] ($^{13}CH_3$ labeled threonine in a deuterated background) [158]. Threonine is a direct biosynthetic precursor to 2-ketobutyrate, leading to isoleucine methyl (Cδ) labeling. Since threonine is converted to glycine either from threonine aldolase or threonine dehydrogenase/2-amino-3-ketobutyrate ligase, the authors used 100 mg/L of d_5-glycine along with 50 mg/L of U-[^{2}H] Thr-γ2[$^{13}CH_3$] and 50 mg/L of 2-ketobutyrate for specific threonine and isoleucine labeling (**Figure 3.1**).

3.3 Methyl labeling protocol for the cAMP-dependent Protein Kinase A (PKA-C)

In this outline, we highlight a method to label the ^{13}C isoleucine (Cδ), leucine, and valine methyl groups for the catalytic subunit of cAMP-dependent Protein Kinase A (PKA-C) (**Figure 3.2**). Specific labeling of side-chain methyl groups is achieved using the M9 minimal medium typically used for ^{15}N labeling of proteins with the addition of appropriate amounts of methyl labeling precursors. As the protocols for overexpression and purification of PKA-C have been described extensively [28, 168, 169], here we report only the main steps of the protocol (**Figure 3.3**). Note that for binding titrations studies we used fully protonated kinase and 2D NMR experiments; however, for methyl group assignment experiments (i.e., 3D [^{13}C,^{13}C]-methyl NOESY experiments) we

utilized fractionally deuterated kinase expressed in 80% D_2O. In our hands, the utilization of fully perdeuterated media resulted in a scarce expression of the kinase. Nonetheless, for larger proteins with molecular weights greater than 100 kDa, high levels of deuteration are often necessary. In the latter case, over-expression of proteins in 100% D_2O is highly strain-, vector-, and protein-dependent and requires optimization for each of these variables. Several tips for the optimization of perdeuterated growths have been provided by Gardner *et al.* [170].

Materials

Note: All stocks should be sterile before usage.

LB Media (1L)

10.0 g Tryptone

5.0 g Bacto-Yeast

10.0 g NaCl

M9 Media (1L)

3.0 g KH_2PO_4

12.8 g $Na_2HPO_4 \cdot 7H_2O$

1.0 g NH_4Cl (for ^{15}N labeling use $^{15}NH_4Cl$)

0.5 g NaCl

Vitamins (50mL)

5.0 mg Ca D(+)-panthothenate

5.0 mg Biotin

5.0 mg Folic Acid

5.0 mg Niacinamide USP

5.0 mg Pyridoxal 5-phosphate monohydrate

1000 mg Thiamin

Trace Metals (1x, 100mL)

50 mM $FeCl_3$

20 mM $CaCl_2$

10 mM $MnCl_2$

10 mM $ZnSO_4$

2 mM $CoCl_2$

2 mM $CuCl_2$

2 mM $NiCl_2$

2 mM Na_2MoO_4

2 mM Na_2SeO_3

2 mM H_3BO_3

Note: More details in the preparation of Trace Metal solution is provided at Studier et. al.[171]

Keto-acid Stock (10 mL, water)

2-ketobutyric acid-4-^{13}C sodium salt (70mg/L of media)

2-keto-3-(methyl-^{13}C)-butyric acid-4-^{13}C sodium salt (90mg/L of media)

Calcium Chloride

Magnesium Sulfate

D-glucose

Ampicillin

Isopropyl β-D-1-thiogalactopyranoside (IPTG)

1. Place 500 mL of M9 media into baffled flasks and autoclave.
2. Grow BL21 (DE3) cells containing the pRSET plasmid with PKA-C overnight in LB media (with Ampicillin).
3. In the morning the culture should be in log phase growth. Then pellet the BL21 (DE3) cells under 2200xg for 10 minutes. During this time prepare add the following per 500 mL flask containing M9 media:
    a. 10 ml of 20% w/v glucose
    b. 5 mL of Vitamin stock
    c. 1 mL of 1 M $MgSO_4$.
    d. 1 mL of 50 mM $CaCl_2$
    e. 500 μL of 1000x Trace Metals
    f. 500 μL of 10% w/v Ampicillin stock
4. Resuspend the cell pellet in M9 media and allow to grow for at least an hour to allow for the culture to adapt to the adjusted metabolism. We usually have an initial OD_{600} of ~0.8.
5. Once the cells reach log phase growth, lower the temperature to 24°C and add in the appropriate concentration of keto-acids into each flask (70 mg/L of 2-

ketobutyric acid-4-^{13}C sodium salt and 90 mg/L of 2-keto-3-(methyl-^{13}C)-butyric acid-4-^{13}C sodium salt).

6. After one hour, induce with 0.4 mM IPTG for at least 5 hours. Harvest under 8000xg for 25 minutes at 4°C.

Purification of PKA-C

Buffer A (1L)

- 30 mM MOPS (3-(N-morpholino)propanesulfonic acid) (6.28g)
- 15 mM $MgCl_2$ (3.05g)
- 5 mM β-mercaptoethanol (352μl/L of buffer)
- pH 8.0

Buffer B (1L)

- 30 mM MOPS (6.28g)
- 15 mM $MgCl_2$ (3.05g)
- 25 mM KCl (1.86g)
- 5 mM β-mercaptoethanol (352μl/L of buffer)
- pH 8.0

Elution Buffer (100mL)

- 30 mM MOPS (628 mg)
- 15 mM $MgCl_2$ (305 mg)
- 25 mM KCl (186 mg)
- 1 mM cAMP (33 mg)
- 5 mM β-mercaptoethanol (35.2μl/100 mL of buffer)
- pH 8.0

Cell Lysis

1) Re-suspend PKA and the His_6-RIIβ(R213K) overexpressed cells in Buffer A. Make sure the pellet containing RIIα was grown in at least 1/3 of the volume of your PKA.
2) Grind the cells in ice for approximately 10 minutes then lyse using a French press using 1000 psi of pressure.
3) Spin down the solution at 20,000 rpm for 40 minutes at 4°C. Mix with 10 mL of NiNTA slurry and batch bind at 4°C for a minimum of 3 hours.

Elution

1) Run the slurry through the column (make sure the resin does not dry).
2) Wash with Buffer B (~200 mL). If preferred the wash buffer can also include 20 mM Imidazole to remove some non-specific binding proteins. This will not affect the PKA:RIIα interaction.
3) Elute PKA-C using 150 mL of elution buffer.

To remove RIIα wash with ~50 mL of Buffer B with 250 mM imidazole.

Although mass spectrometry is a viable method to assess the labeling of proteins with stable isotopes, the most straightforward way to determine the correct isotopic incorporation is to acquire the [^{1}H,^{13}C]-HMQC spectra of the system of interest. The characteristic chemical shift patterns allow one to easily identify isoleucine (Cδ), leucine, and valine methyl groups as they resonate in distinct regions of the ^{1}H/^{13}C correlated spectra. Due to the high sensitivity of methyl groups, 2D spectra of large proteins (~40 kDa) with reasonable sensitivity (S/N ratio 200-400) can be measured with modern spectrometers (700-900 MHz) with relatively modest concentrations (~200 μM). A [^{1}H,^{13}C]-HMQC spectrum of apo PKA-C shows the labeling and spectral quality of ILV-methyl groups labeling (**Figure 3.4**). Below, we outline the NMR sample preparation that we use for *apo* form of PKA-C:

Materials

Potassium Phosphate Monobasic

Potassium Chloride

Dithiothreitol

Magnesium Chloride

Sodium Azide

10kDa Centrifugal Concentrator

99+% Deuterium Oxide

Long-tip Pipet, 13-1/4”

5 mm Shigemi Tube

1. Dialyze purified PKA-C under NMR buffer (20 mM KH_2PO_4, 90 mM KCl, 10 mM DTT, 10 mM $MgCl_2$, 1mM NaN_3 at pH 6.5) overnight at 4°C. Initial concentration of PKA-C should < 5 μM.
2. Concentrate PKA-C at 2400xg using a 10kDa cutoff centrifugal concentrator at 4°C until the enzyme is concentrated to ~200 μM. The protein concentration can reliably be measured by absorbance measurement at 280 nm using an extinction coefficient of 52060 $M^{-1}cm^{-1}$.
3. Pipette 250 μL (for Agilent spectrometers) or 300 μL (for Bruker spectrometers) and add 12.5 or 15 μL of D_2O (~5% v/v), respectively. Transfer the protein solution into a shigemi tube using a long-tip pipet. Place the plunger inside the tube until the plunger is evenly covered with no visible bubbles in the solution.

After spectrometer set up (spectrometer details are dependent on model and spectrometer) acquire an [^{1}H,^{13}C]-HMQC spectrum.

3.4 Semi-Automated Methyl Group Resonance Assignment Strategies

For backbone studies, the assignment is carried out by walking through the peptide backbone through a series of triple resonance NMR experiments [172-175]. For the assignment of methyl groups resonances, the classical approach requires TOCSY-based spectroscopy with the magnetization starting on the methyl groups and transferred *via* ^{13}C-^{13}C couplings to the protein backbone [176]. This approach, however, is not applicable to methyl group side-chains of large proteins, such as the 82 kDa malate synthase G with a correlation time of ~46 ns [177]. In the latter case, the branched amino acids present a bifurcation of the magnetization pathways with a significant loss of transfer. Although several experiments have been tailored to correlate

backbone Cα, Cβ and C' chemical shifts to methyl groups [178-180], the relatively fast transverse relaxation rates of these nuclei for larger proteins or conformational exchange phenomena (see the case of PKA-C [43]) do not allow to carry out sequential backbone assignments. A possible solution is to use a *divide and conquer* approach in which proteins are dissected into several smaller domains and the assignments are pieced together [165, 181]. However, there are many large monomeric proteins that are unamenable to this approach. An alternative strategy is to use site-specific mutations to exchange amino acids with methylated side chains for glycine or other amino acids. The latter method, however, is very cumbersome and time-consuming, particularly for very large systems. In response to this need, Matthews and co-workers proposed an automatic method that uses both NMR and X-ray structural data to back calculate methyl side chain assignments [182]. This automated procedure was designed to rapidly assign methyl groups using full-length proteins and without mutagenesis [182]. This approach requires a crystal structure as a starting point to calculate methyl group chemical shifts and synthetic NOEs. An algorithm is then used to rank the scores of the initial (seed) assignment against the experimental NMR data. The latest version of this method features an improved algorithm with no manual intervention in NOESY spectra peak picking.

Inspired by this work, we developed an approach that uses a similar philosophy, but utilizes a probabilistic method to tackle assignment problem. Specifically, we improved the efficiency of the phase space search using *fuzzy logic* coupled with Monte Carlo sampling. This approach, named FLAMEnGO (Fuzzy Logic Assignment of Methyl Groups), utilizes NOESY data as the primary input in concert with other data sets, such as methine-methyl TOCSY data, as well as paramagnetic relaxation enhancements (PREs). In our newer version of this software, FLAMEnGO 2.0 [183], we introduced a graphic interface that enables the interactive assignment of the methyl group resonances with the option of including secondary constraints, such as mutagenesis or supplemental NMR data.

In the following synopsis, we describe the construction and usage of FLAMEnGO 2.0, as well as its application to the side-chain methyl groups of PKA-C.

3.5 Semi-Automated Assignment Protocol using FLAMEnGO 2.0

All of the available methyl auto-assignment algorithms share the same philosophy: searching for the best assignments by comparing experimental NOE connectivities and chemical shifts to back-calculated data from the X-ray coordinates [182-186]. Starting from the available crystal structure or NMR structural bundle, FLAMEnGO 2.0 back-calculates a 3D/4D NOESY spectrum from the internuclear methyl-methyl distances and compares synthetic data to an experimental NOESY spectrum (**Figure 3.5**). The algorithm iteratively swaps the resonance assignments until the scoring function is maximized. This process is repeated iteratively for an array of different simulated NOE distances until no further improvement is found. Given the probabilistic nature of this algorithm, multiple runs are performed in parallel to provide a statistical weight to the resonance assignments. Although FLAMEnGO is designed to handle sparse NOE data sets, sufficient coverage of the NOE network and other restraints (i.e., methine-methyl TOCSY or methyl-HN COSY, PREs or site-directed mutagenesis) are required for a confident assignment. The outline of the procedure for using FLAMEnGO GUI is shown in **Figure 3.6**.

Below, we detail the experimental data and data formatting, as well as brief instructions on usage of FLAMEnGO 2.0

Materials

- 3D C,C,H ^{13}C-HMQC NOESY ^{13}C-HMQC data set (These pulse sequences are part of the TOPSPIN release for Bruker spectrometers, and are downloadable from the NMRFAM website http://pine.nmrfam.wisc.edu/download_pulseprogs.html for Agilent spectrometers).
- 2D [^{1}H,^{13}C]-HMQC data set (required)
- Predicted chemical shift table (required, sources listed below)
- Paramagnetic Relaxation enhancement data (optional)
- Methine-methyl TOCSY data (optional)
- Assigned amide chemical shifts (optional, if amide-methyl NOESY data are incorporated)

- PDB file for protein. Note that hydrogen atoms need to be added to the PDB. Molprobity (http://molprobity.biochem.duke.edu/) is a resource to perform this function.

System Requirements and Specifications

The python-based FLAMEnGO 2.0 program includes two main components: 1) the frontend GUI program flame.py, and 2) the backend engine FLAMEnGO.py. The former provides a convenient interface for configuring the setup and displaying the results, while the latter is the driver for a Monte-Carlo search. The software is ready to run under Python 2.7, and requires wxPython and matplotlib modules for GUI and plotting. An integrated scientific python package, such as Enthought Canopy (https://www.enthought.com/products/canopy/) or Anaconda Python (https://store.continuum.io/cshop/anaconda/) are needed for full functionality.

Input File Formats

FLAMEnGO 2.0 uses a Monte Carlo search algorithm to swap resonance assignments from given input data and computes the *fitness* of the resonance assignments based on a score function. The details of the scoring function are discussed in Chao *et al.* [183, 186].

Initial Random Assignment

The algorithm needs an *arbitrary* initial assignment to start the swapping process associated with the Monte Carlo algorithm. This *seed* assignment must be consistent with PDB numbering and included in all input data. The data are formatted in a series of columns by <assignment #> <amino acid type> <resonance atom ID> -> <assignment #> <amino acid type> <resonance atom ID>. Note that there is no change in residue, rather this indicates to the program which residues to assign. To constrain a specific resonance assignment (*e.g.*, found using site-directed mutagenesis), the user should place an asterisk at the beginning of the line:

```
296 VAL HG2 -> 296 VAL HG2
* 301 ILE HD1 -> 301 ILE HD1
```

```
321 ILE HD1 -> 321 ILE HD1
323 VAL HG1 -> 323 VAL HG1
323 VAL HG2 -> 323 VAL HG2
325 ILE HD1 -> 325 ILE HD1
```

3D C,C,H ^{13}C-HMQC-NOESY-^{13}C-HMQC

The 3D C,C,H ^{13}C-HMQC-NOESY-^{13}C-HMQC data need to be formatted in a series of columns in the following order: <^{13}C (ω2) chemical shift> <^{1}H (ω3) chemical shift> <^{13}C (ω1) chemical shift> <^{13}C (ω2) linewidth> <^{1}H (ω3) linewidth> <^{13}C (ω1) linewidth>

```
18.32 1.28  27.41 0.4   0.025 0.4
22.76 0.88  19.53 0.4   0.025 0.4
22.76 0.88  15.69 0.4   0.025 0.4
22.76 0.88  21.55 0.4   0.025 0.4
22.76 0.88  18.66 0.4   0.025 0.4
20.97 0.78  17.77 0.4   0.025 0.4
25.05 0.68  23.33 0.4   0.025 0.4
```

[^{1}H,^{13}C]-HMQC/^{15}N Amide

The data is formatted in a series of columns by <assignment #> <amino acid type> <resonance atom ID> <chemical shift value>. Note that the assignment reported in this file at the beginning of the calculation is arbitrary for the [^{1}H,^{13}C]-HMQC. The amide chemical shifts are optional and only required if one is using amide to methyl NOE data. The amide chemical shifts must be assigned based on previous experiments.

```
  7 LEU HD1     0.34
  7 LEU HD2     0.56
  7 LEU CD1    25.39
  7 LEU CD2    24.56
 20 LEU HD1     0.88
 20 LEU HD2     0.64
 20 LEU CD1    25.10
 20 LEU CD2    27.22
```

Paramagnetic Relaxation Enhancement Data (PREs)

Although the PRE data are listed as an option, we demonstrated that the inclusion of these constraints in the computation dramatically increases both the speed and accuracy of the resonance assignments [183, 186]. In particular, PRE data are crucial to solve the ambiguities caused by partial peak overlap (**Figure 3.7**). PRE data

are included as distances using the semi-quantitative approach described by Battiste and Wagner [187], in which the ratios of the peak intensities in the presence of the oxidized versus the reduced spin label are converted into three different categories: weakly affected (< 20% of signal is lost through the PRE effect), moderately affected (20-80% of the signal is lost) or strongly effected (<20% of the signal is lost). These categories are flagged as W, M, and S in the input file. If a resonance is unobserved regardless of the PRE effect, then a flag of 999 is used in the 4th column of the input file. The data are formatted in four columns, including <assignment #> <amino acid type> <resonance atom ID> <Flag (W, M, S, 999)>:

```
 89   HD1   LEU    999
 92   HD2   LEU    999
102   HD1   LEU    M
102   HD2   LEU    M
 71   HD1   ILE    S
 92   HD1   LEU    S
138   HD1   LEU    W
 13   HD1   LEU    W
```

Prediction of Methyl group chemical shifts from the PDB file

Various algorithms are used to predict the side chain chemical shift values. Output from any commonly used program, such as CH3SHIFT [188] (http://www-sidechain.ch.cam.ac.uk/CH3Shift/), SHIFTX2 [189], (http://www.shiftx2.ca/) and PPM [190] (http://spin.ccic.ohio-state.edu/index.php/ppm) can be implemented in FLAMEnGO 2.0. Since the output is not uniform between programs, data must be reformatted as follows: <residue #> <amino acid type> resonance atom ID> <predicted chemical shift value> <error of prediction>

```
1 VAL CG2 19.992 1.128
1 VAL HG2 0.828 0.173
5 LEU CD1 25.747 1.412
5 LEU HD1 0.969 0.176
```

Residue Type

Amino acid-type assignments can be included as constraints in the search algorithm. The data format is identical to that of the initial assignment file.

Instructions to run FLAMEnGO 2.0 GUI

1. Open FLAMEnGO
   "`python flame.py`"
2. Specify the location of each input file on the main window.
3. To set up FLAMEnGO go under **File** > **SetUp** (**Figure 3.8A**). Set the NOE range between 5.0-10.0 with step size of 0.5. The sampling number is the number of Monte Carlo calculations run at each point and should be over 100k (**Figure 3.8B**).
4. Select the **Run** button. Please note that calculations take a considerable amount of time.
5. Once the runs are finished a plot of the score with respect to the NOE distance will appear (**Figure 3.8C**). To minimize the uncertainty of the assignment, click on the point where the NOE value with the maximum score is first reached.
6. Select the number of calculations you wish to run (≥10). The final output will give the assignment and the statistical weight of each assignment.

Output Files

FLAMEnGO provides two types of output files. The first is the assignment file, which provides the calculated assignment at each given calculation at a specified NOE cutoff distance. Once the aggregate calculations are performed at a cutoff distance, the probability of each assignment is calculated. The probability of each assignment from the calculations is what is used to determine the *fitness* of the assignment.

Score and Assignment

The output file provides the user with the percent of the residues assigned, the assignment score and the assignment from the single calculation. The assignment is provided as the following <initial assignment> -> <calculated assignment. On the first line the first two columns provide the <final scoring value> <% of residues assigned>.

```
(205.2936878260806, 93.079554272662747, 193, 17.844744345905379)
    ############################
    158   LEU   HD1 ->    148   LEU   HD1
    237   VAL   HG1 ->     90   VAL   HG2
    321   ILE   HD1 ->    196   ILE   HD1
    259   LEU   HD2 ->    191   LEU   HD2
    197   LEU   HD1 ->     75   LEU   HD1
```

Summary

The summary file will provide the assignment, as well as the number of times the particular assignment was made across all the calculations. A confident assignment is defined in this case as one that is consistent through all calculations at least 80% of the time; a reliable statistic for this assessment requires ≥10 calculations. For each assignment the output is as follows: <initial assignment> -> <calculated assignment> <number of times the assignment was calculated>.

```
105   VAL   HG1 ->    137   VAL   HG1    10
254   LEU   HD1 ->     68   LEU   HD1    10
 75   LEU   HD2 ->    263   LEU   HD2     6
143   LEU   HD2 ->     45   LEU   HD2     7
 13   LEU   HD1 ->    259   LEU   HD1    10
241   VAL   HG2 ->    137   VAL   HG2    10
```

3.6 Conclusions and Perspectives

Selective labeling of the methyl group side-chains has extended the application of NMR methods to the analysis of both structure and dynamics of proteins up to 1 MDa. However, as the systems become larger, classical methods for resonance assignments fail. In this chapter, we reported a semi-empirical approach that enables the assignment of methyl group resonances in large proteins. This structure-based approach requires the X-ray or the NMR ensemble of structures to generate a probability-based assignment. Inclusion of NOEs, PRE, site-specific mutagenesis data, methine-methyl TOCSY, and partial assignment from methyl-HN COSY data dramatically improves both the accuracy and the speed of the assignment procedure. This method promises to extend biomolecular NMR studies beyond the MDa limit.

3.7 Acknowledgements

This work was supported in part by the NIH (GM100310 and GM72701 to GV and T32 AR007612 to JK). NMR experiments were carried out at the Minnesota NMR Center and FLAMEnGO 2.0 calculations at the Minnesota Supercomputing Institute.

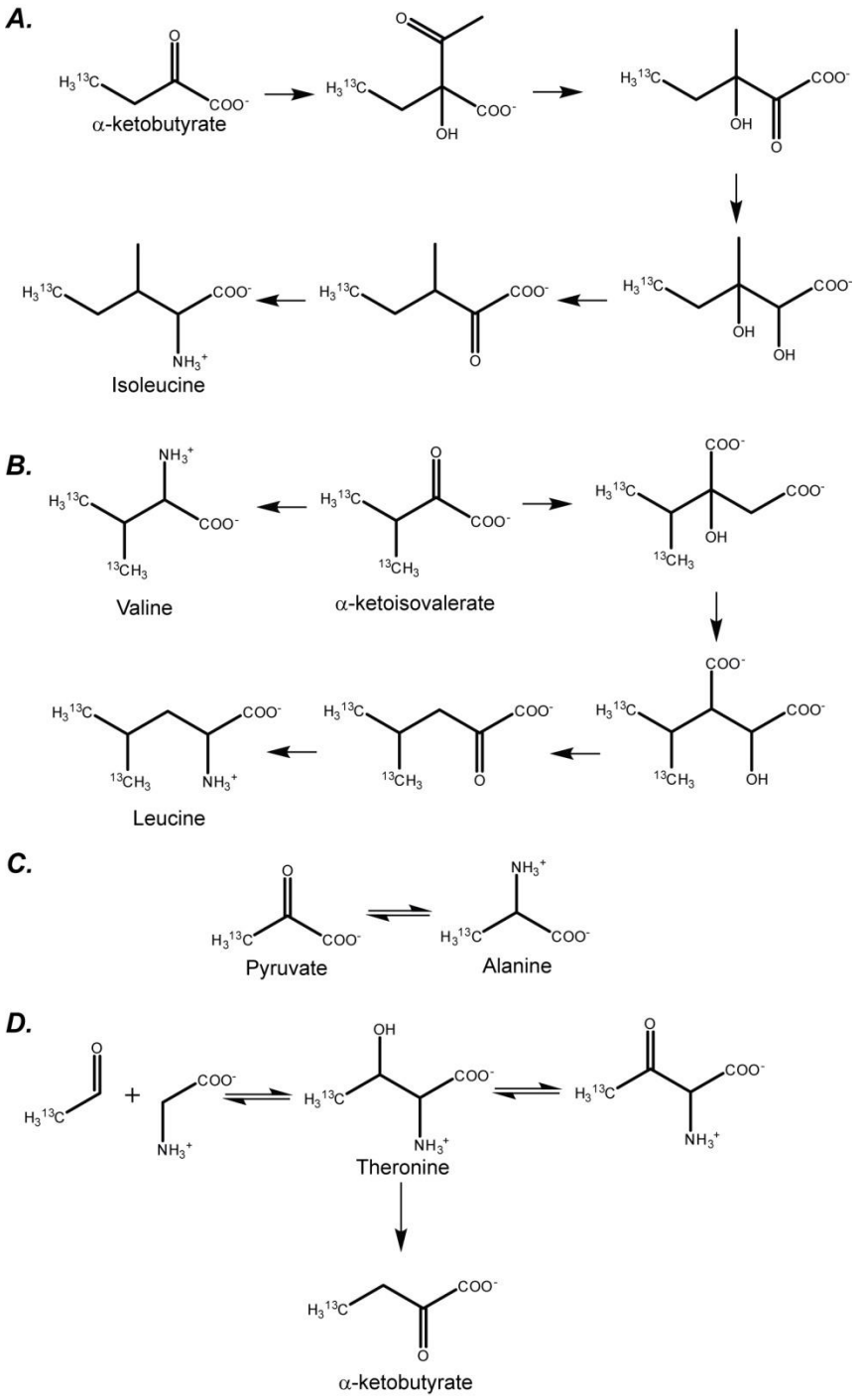

Figure 3.1. Biosynthetic pathways for the specific labeling of A) isoleucine, B) leucine and valine, C) alanine, D) methionine and E) threonine.
Note the off-pathway dilution of alanine and threonine amino acids.

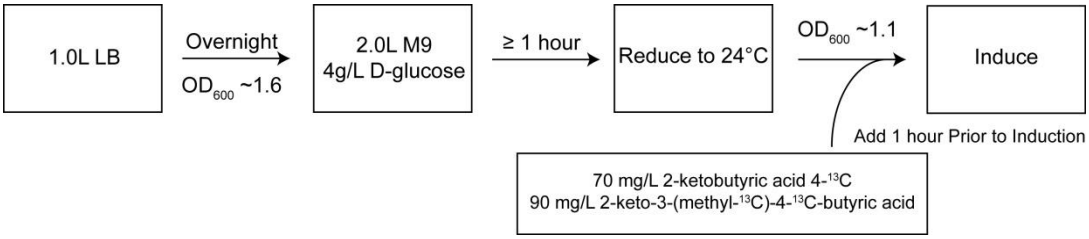

Figure 3.2. General growth scheme used to express ^{15}N ^{13}C-ILV labeled PKA-C.
All cultures are grown in 32°C with induction occurring at 24°C. This is to prevent the formation of inclusion bodies during expression [169]. In M9 media, $^{15}NH_4Cl$ (1 g/L) and D-glucose (4 g/L) are used as the only nitrogen and carbon sources respectively.

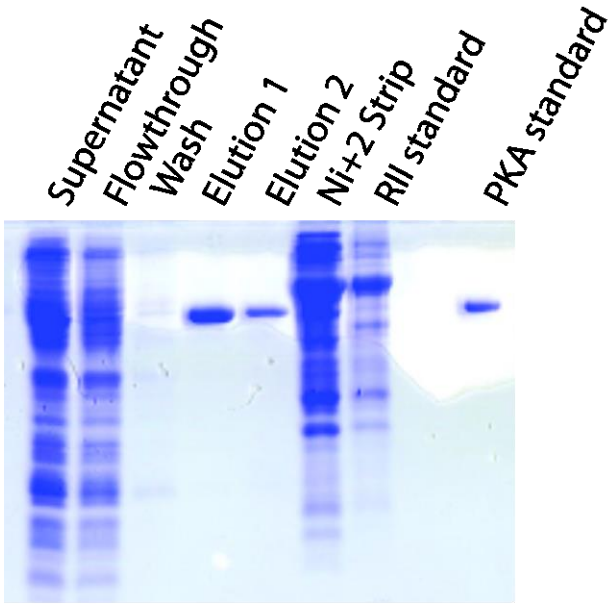

Figure 3.3. SDS-PAGE of the purification of PKA-C using a His_6-RIIα immobilized construct.

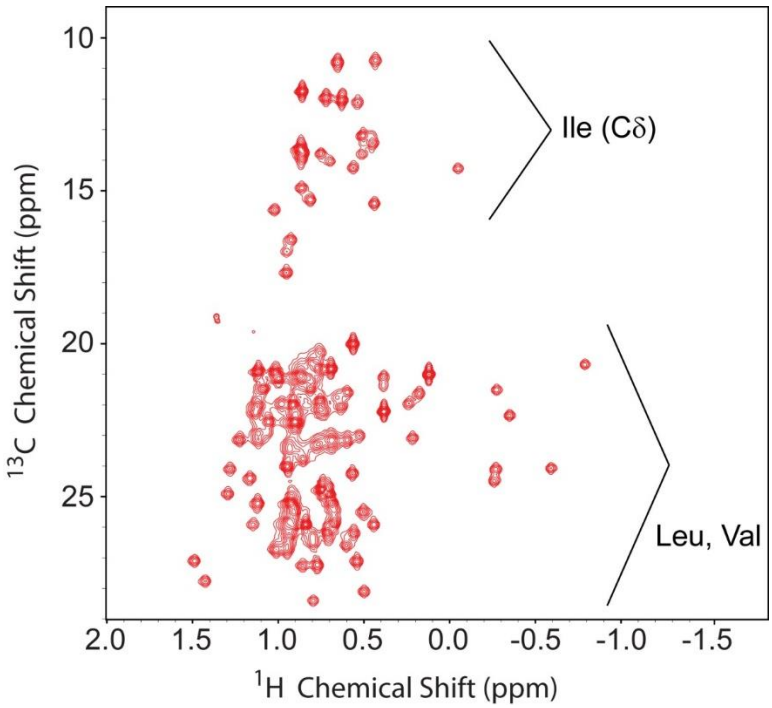

Figure 3.4. [^{1}H,^{13}C]-HMQC of Apo PKA-C acquired with a 220 μM sample on an Avance III 900 MHz Bruker spectrometer.
The spectrum was acquired with 2048 x 200 complex points and 16 transients at 27°C for a total acquisition time of approximately 1 ½ hours.

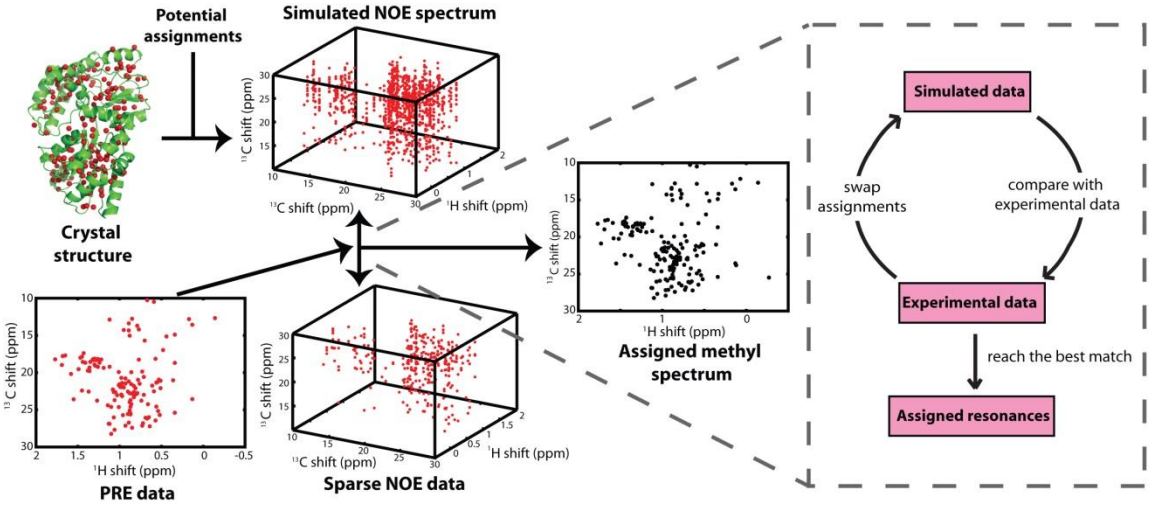

Figure 3.5. Overview of the FLAMEnGO algorithm.
An input structure and the [^{1}H,^{13}C]-HMQC spectrum are used to simulate a NOE spectrum. This spectrum is compared with the experimental NOE data, the assignments swapped and the process is repeated until a best match is found. Other experimental restraints, such as PRE data, are used. Figure adapted from Chao, et al. [186]

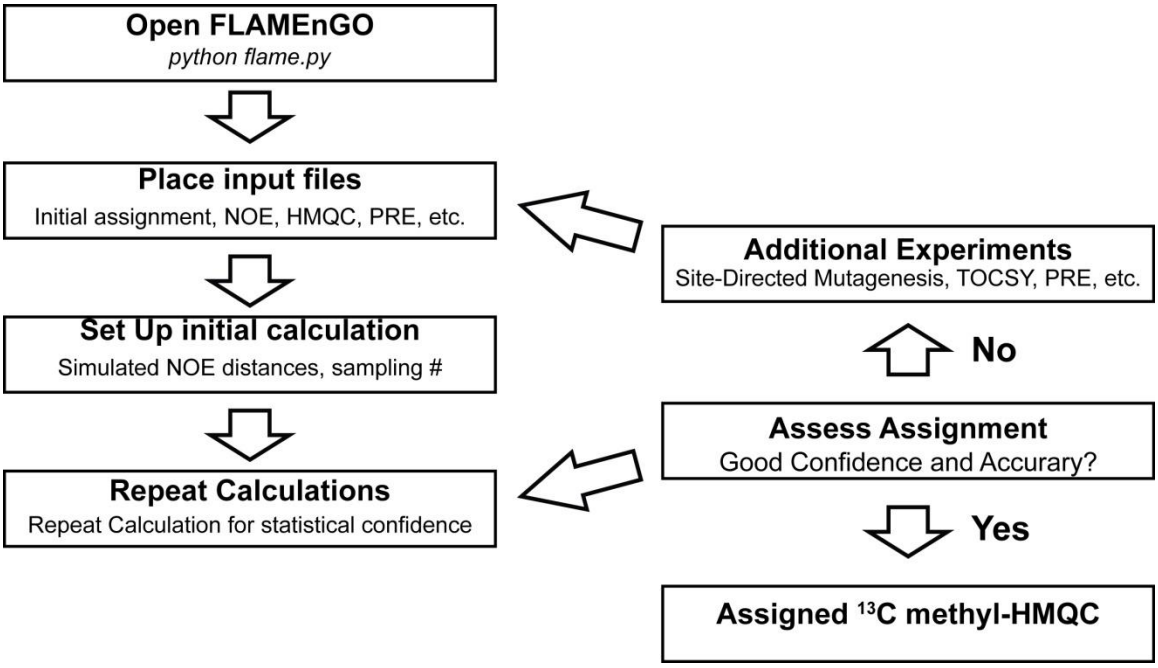

Figure 3.6. Outline for running FLAMEnGO GUI.

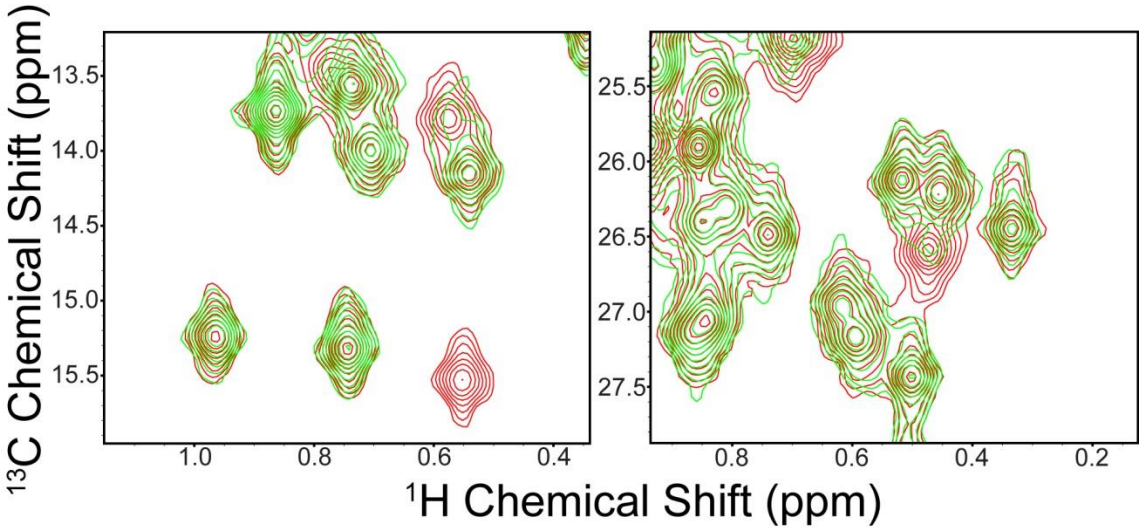

Figure 3.7. Spectra of oxidized (green) and reduced (red) PKA-C with a spin label on residue 244. Note the spectrum should be nearly identical before and after the reduction of the spin label.

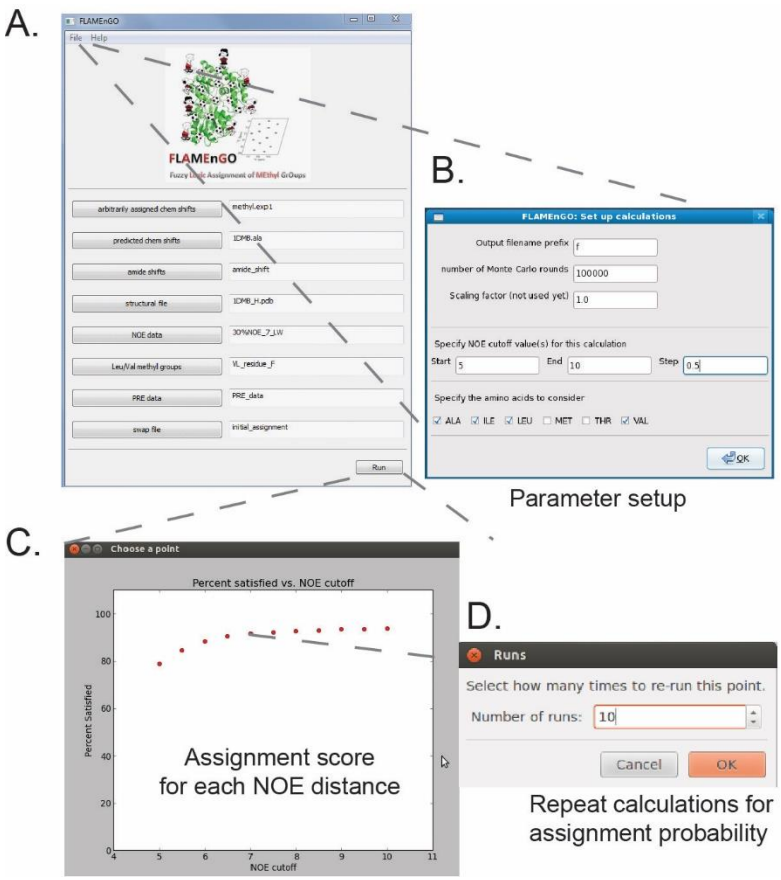

Figure 3.8. Graphical Interface for FLAMEnGO.
(A) Main menu of FLAMEnGO. Input files are directly placed inside the selection. (B) Parameter set up for the NOE distances, amino acid types you wish to assign, and the number of Monte Carlo steps. (C) Output from the run. Note that the program performs the calculation at each NOE distance. (D) Once the score has plateaued from increasing the NOE distance, select the point and repeat the calculation at this distance to provide a statistical assignment of each residue. Figure adapted from [183]

CHAPTER 4 UNCOUPLING CATALYTIC AND BINDING FUNCTIONS IN THE CAMP-DEPENDENT PROTEIN KINASE A

Jonggul Kim[1], Geoffrey Li[1], Michael A. Walters[3], Susan S. Taylor[4] and Gianluigi Veglia[1,2]*

[1] Department of Chemistry, University of Minnesota, Minnesota, 55455 United States.

[2] Department of Biochemistry, Molecular Biology and Biophysics, University of Minnesota, MN, 55455 United States.

[3] Institute for Therapeutics Discovery and Development, Department of Medicinal Chemistry, University of Minnesota, Minnesota, 55455 United States.

[4] Department of Chemistry and Biochemistry, University of California at San Diego, La Jolla, CA 92093, USA

Reprinted with permission from:
Structure (2016) Vol. 24, pp. 353-363.

4.1 Conspectus

The *canonical* function of kinases is to transfer a phosphoryl group to substrates, initiating a signaling cascade; while their *non-canonical* role is to bind other kinases or substrates, acting as scaffolds, competitors, and signal integrators. Here, we show how to uncouple kinases dual function by tuning the binding cooperativity between nucleotide (or inhibitors) and substrate allosterically. We demonstrate this new concept for the C-subunit of protein kinase A (PKA-C). Using thermocalorimetry and NMR, we found a linear correlation between the degree of cooperativity and the population PKA-C's closed state. The non-hydrolysable ATP analog (ATPγC) does not follow this correlation, suggesting that changing the chemical groups around the phosphoester bond can uncouple kinases dual function. Remarkably, this uncoupling was also found for two ATP-competitive inhibitors, H89 and balanol. Since the mechanism for allosteric cooperativity is not conserved in different kinases, these results may suggest new approaches for designing selective kinase inhibitors.

4.2 Introduction

Protein kinases are ubiquitous phosphoryl transferases that regulate many cellular signaling processes [191]. Due to their primary role in cell physiology and pathology, protein kinases have become major drug targets to counteract human diseases, such as heart failure and cancer [192, 193]. Kinases *canonical function* is to transfer the γ-phosphate of ATP to Ser/Thr/Tyr residues of substrates, thereby activating or deactivating various signaling pathways [3, 193-195]. About a decade ago, Manning and co-workers identified a *non-canonical function* for kinases that, in several instances, do not carry out any catalytic function; rather they provide binding scaffolds to modulate, integrate, or compete in signaling cascades, the so-called pseudo-kinases [194]. While kinases mediate signaling through phosphoryl transfer and scaffolding (dual function), pseudo-kinases' function is independent from catalysis [33, 196]. To date, approximately 10% of the 518 members of the mammalian kinases have been identified as pseudo-kinases, with reduced or completely obliterated ability to catalyze phoshoryl transfer [32, 33]. Recent site-directed mutagenesis studies suggest that it is possible to uncouple the canonical from the non-canonical function of kinases [36, 95, 197]. Also, it has been found that small molecules that inhibit kinase phosphorylation *in vitro* are able to activate kinase pathways in cell [35, 198, 199]. The latter suggests that kinases depleted of their catalytic functions still work as scaffolds and play an active role in cell signaling. Therefore, uncoupling canonical and non-canonical functions of protein kinases with small molecules would enable one to achieve a higher level of control over the kinase-mediated signaling pathways [32].

Although substantial progress has been made for the development of allosteric inhibitors [200-202], small molecules that bind the ATP binding site (ATP-competitive inhibitors) remain the most common kinase inhibitors [203]. However, none of these drugs have been engineered to uncouple the dual functions of kinases, rendering them either pseudo-kinases (devoid of catalytic activity) or dead kinases (non-catalytic and non-scaffolding). So, how can we uncouple canonical and non-canonical kinase functions? Since allosteric binding cooperativity (*K*-type cooperativity, *i.e.*, nucleotide binding affects substrate affinity) is a hallmark for several kinases [44, 143], we reasoned that by modulating the chemical moieties of nucleotides and nucleotide-analogs it would be possible to control allosteric binding cooperativity. The latter will

make it possible to design inhibitors able to steer kinases' function toward pseudo-kinases or dead kinases.

As a model system, we chose the catalytic subunit of the cAMP-dependent protein kinase A (PKA-C). This enzyme is one of the most studied and has represented the benchmark for the entire kinase family [14]. PKA-C is organized into two lobes, an N-terminal small lobe with 5 β-strands and one helix (αC helix), and a C-terminal large lobe mostly helical that harbors the substrate binding cleft [8] (**Figure 4.1A**). The nucleotide (ATP) binds at a critical junction of the kinase core, which is embedded between the small and large lobes [8]. Through coordination of two Mg^{2+} ions, the nucleotide positions several amino acids from various catalytic motifs such as the DFG loop, glycine-rich loop, and catalytic loop for phosphoryl transfer (**Figure 4.1C**) [93]. Structurally, the nucleotide's adenine ring completes the architecture of the catalytic spine (C-spine), an array of hydrophobic residues that play a key role in intramolecular allosteric signaling and kinase activation [23]. The substrate binds the C-lobe, laying on the peptide positioning loop, which provides high-binding affinity for registering the recognition sequence. It has been hypothesized that ATP acts as an allosteric effector priming the kinase structure for substrate binding [23, 41, 204]. The dynamic apo enzyme toggles between three major conformational states along the free energy reaction coordinate (open, intermediate, and closed, **Figure 4.1B**). ATP binding shifts the enzyme conformational ensemble from an open to an intermediate state, increasing substrate affinity through a *K*-type binding cooperativity [205-207]. Binding of substrate further shifts the ensemble toward the enzyme's closed state. In spite of a plethora of structural [14] and biophysical data [208], it is still unclear how the different chemical moieties of ATP confer positive *K*-type cooperativity for substrates.

By combining isothermal titration calorimetry (ITC) with NMR spectroscopy we show how small molecules (nucleotides or small molecule inhibitors, **Figure 4.1D**) are able to modulate the degree of the binding cooperativity for the pseudo-substrate peptide derived from the endogenous protein kinase inhibitor (PKI_{5-24}). For the nucleotide analogs, we found a linear correlation between the degree of cooperativity and the population of the closed state of the enzyme. The highest degree of cooperativity is reached with ATP, where the phosphate groups pre-organize the active site for phosphoryl transfer and prime the substrate binding site for high binding affinity

(catalytically competent state). The degree of cooperativity is substantially reduced for ATPγN and completely abrogated for ATPγC. In addition, ATPγC drastically decreases the binding affinity of PKA-C for phospholamban, a natural substrate of this kinase in the heart muscle. For H89 and balanol, two chemically different ATP-competitive inhibitors of PKA-C, we found negative and positive binding cooperativity, respectively. These results demonstrate that it is possible to modulate substrate binding cooperativity by changing the chemical nature of small molecule inhibitors that can decouple the dual functions of kinases, opening new directions for manipulating protein kinases functions in a specific manner.

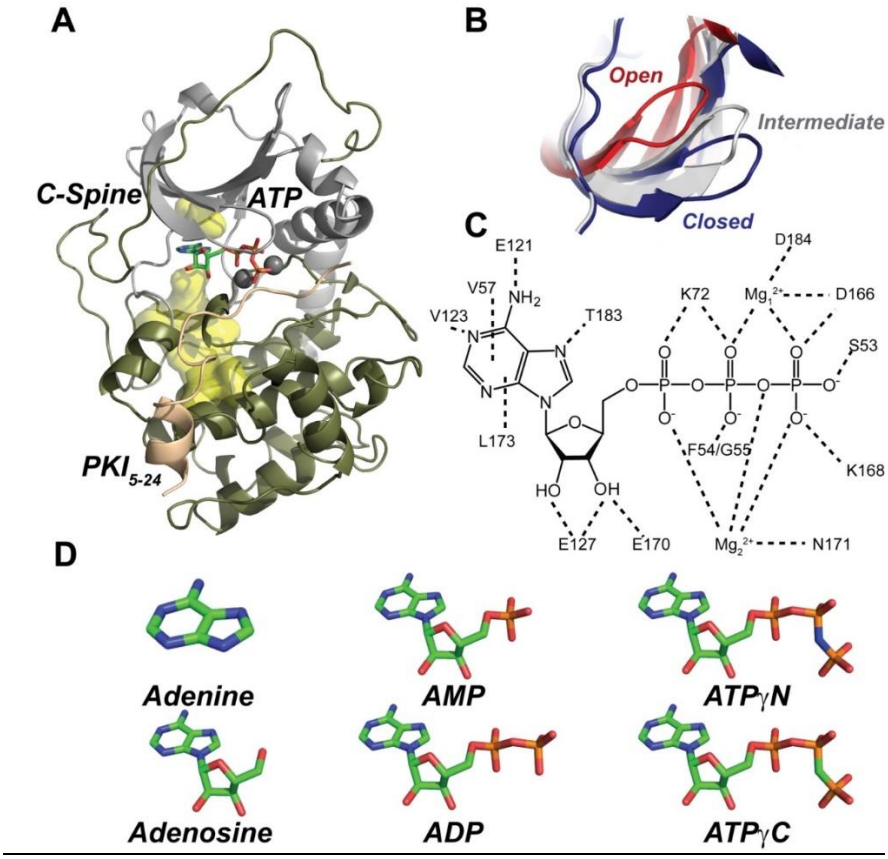

Figure 4.1. Three-dimensional fold and conformational states of PKA-C.
(A) Ribbon diagram of the catalytic subunit of protein kinase A (PDB: 1ATP) shown with the C-spine scaffold (yellow surface), sandwiching the adenine moiety of ATP, and the peptide fragment of the heat stable protein kinase inhibitor (PKI_{5-24}). (B) Overlay of the glycine-rich loop of the open (PDB: 1J3H), intermediate (PDB:1BKX) and closed (PDB:1ATP) forms of PKA-C. (C). Electrostatic and hydrophobic contacts with ATP deduced from the 1ATP structure of PKA-C. (D) Chemical structures of the nucleotide analogues used in this study.

4.3 Results

Different nucleotides provide varying degree of binding cooperativity.

To measure substrate binding cooperativity of PKA-C, we utilized ITC to measure the binding affinity of PKA-C for the heat stable protein kinase A inhibitor peptide (PKI_{5-24}). Since PKI_{5-24} contains the substrate recognition motif for PKA-C (with Arg residues on the P-2 and P-3 positions and an Ala instead of a Ser at the P-site), it is considered a pseudo-substrate[14], recapitulating the high binding affinity of the R-subunits[8, 9, 41, 209]. The degree of binding cooperativity between PKI_{5-24} and the nucleotide was assessed by saturating the kinase with a series of nucleotide analogs: adenine, adenosine, AMP, ADP, ATPγN, ATPγC, and ATP (**Figure 4.2-4.4**). Under the time scale of our experiments, we did not detect any hydrolysis of ATPγN, which has been detected in the crystallized PKA-C/ATPγN/SP20 complex (SP20 is a substrate peptide derived from PKI_{5-24} with Asn20Ala and Ala21Ser mutations [124]). The different nucleotides were chosen to dissect the contribution of each chemical moiety (*i.e.*, adenine ring, ribose, and phosphates) to the *K*-type cooperativity. All of these nucleotides display very similar binding affinities for the enzyme [43, 210, 211], with K_d values between 20-50 μM. Note that under our experimental conditions, two Mg^{2+} ions occupy the binding site, which are required for the high binding affinity of PKI_{5-24} [212]. To quantify the extent of cooperativity, the binding thermodynamics were interpreted using a classical heterotropic linkage model (**Figure 4.2A**), where the binding of one ligand enhances or reduces the affinity of the second ligand. The degree of cooperativity (σ), which is independent of the order of ligand binding, quantifies the extent of *K*-type cooperativity [44, 213]. Saturation with most nucleotides increases the binding affinity toward PKI_{5-24}. The highest affinity and degree of cooperativity ($\sigma = 400$) was measured for ATP. Specifically, we found a gradual increase of affinity of PKI_{5-24} and binding cooperativity for the following series: adenine < adenosine < ADP < ATPγN << ATP (**Figure 4.2B**). These data indicate that the adenine ring, the ribose and the three phosphates contribute incrementally to the enzyme's binding affinity for PKI_{5-24}. As previously observed [210], the adenine moiety (**Figures 4.2-4.4**, and **Table 4.1**) is especially important for the binding affinity, since its ring, sandwiched between residues Val57 in the N-Lobe and Leu173 in the C-Lobe, is stabilized by hydrophobic interactions. The

ribose moiety and phosphate groups further increase PKI_{5-24} binding affinity, with a significant increase in cooperativity correlated with the number of phosphate groups. Notice that the affinity of the pseudo-substrate peptide is much greater when the enzyme is bound to ATP than ADP, indicating that ADP facilitates the exit of the enzymatic product. An anomalous behavior is observed for AMP, which has been shown to have a lower binding affinity for PKA compared to other nucleotide analogs [210]. In agreement with these previous data, we found a substantially weaker affinity with AMP (K_d ~ 250 μM). These binding experiments were repeated at higher AMP concentrations to saturate the kinase; however, we did not observe significant changes in the pseudo-substrate affinity (**Figure 4.5**). Since the structure of the kinase in complex with AMP is not available, we speculate that the absence of the β and γ phosphates prevents the closure of the binding cleft, reducing the affinity for the substrate. Interestingly, two non-hydrolysable nucleotide mimics that are commonly used for structural studies, ATPγN and ATPγC, show a decrease in PKI_{5-24} binding cooperativity. In fact, the presence of a nitrogen atom in place of oxygen at the γ position of the ATP phosphoester dramatically reduces the binding cooperativity (σ = 53). This phenomenon is accentuated for ATPγC, where a methylene group replaces the bridging oxygen. In this case, the binding cooperativity between the non-hydrolysable nucleotide and pseudo-substrate is completely abolished (σ = 1.0).

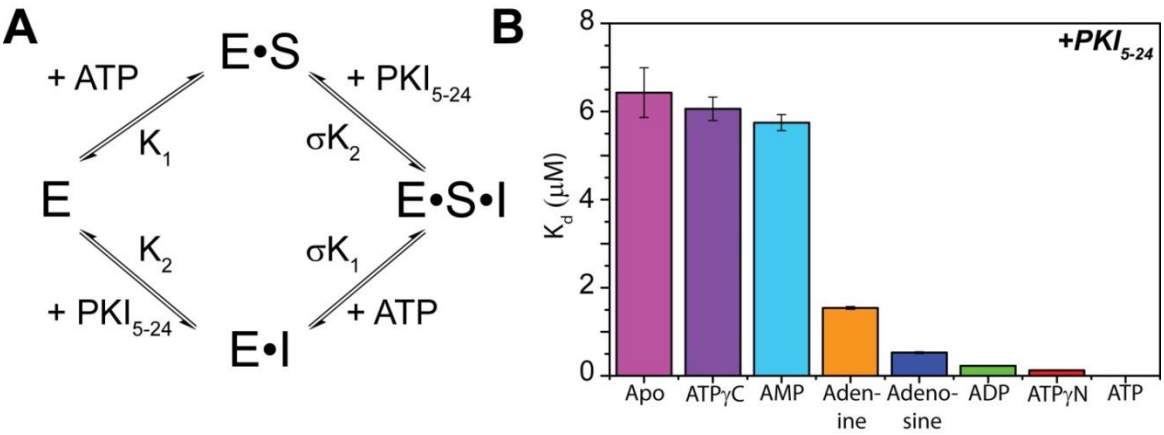

Figure 4.2. Binding cooperativity between nucleotide and pseudo-substrate.
(A) Two-state heterotropic linkage model for nucleotide and pseudo-substrate binding. CB) Plot of the K_d of PKI_{5-24} to PKA-C in the presence of various nucleotides (See also Figures 4.9-4.12).

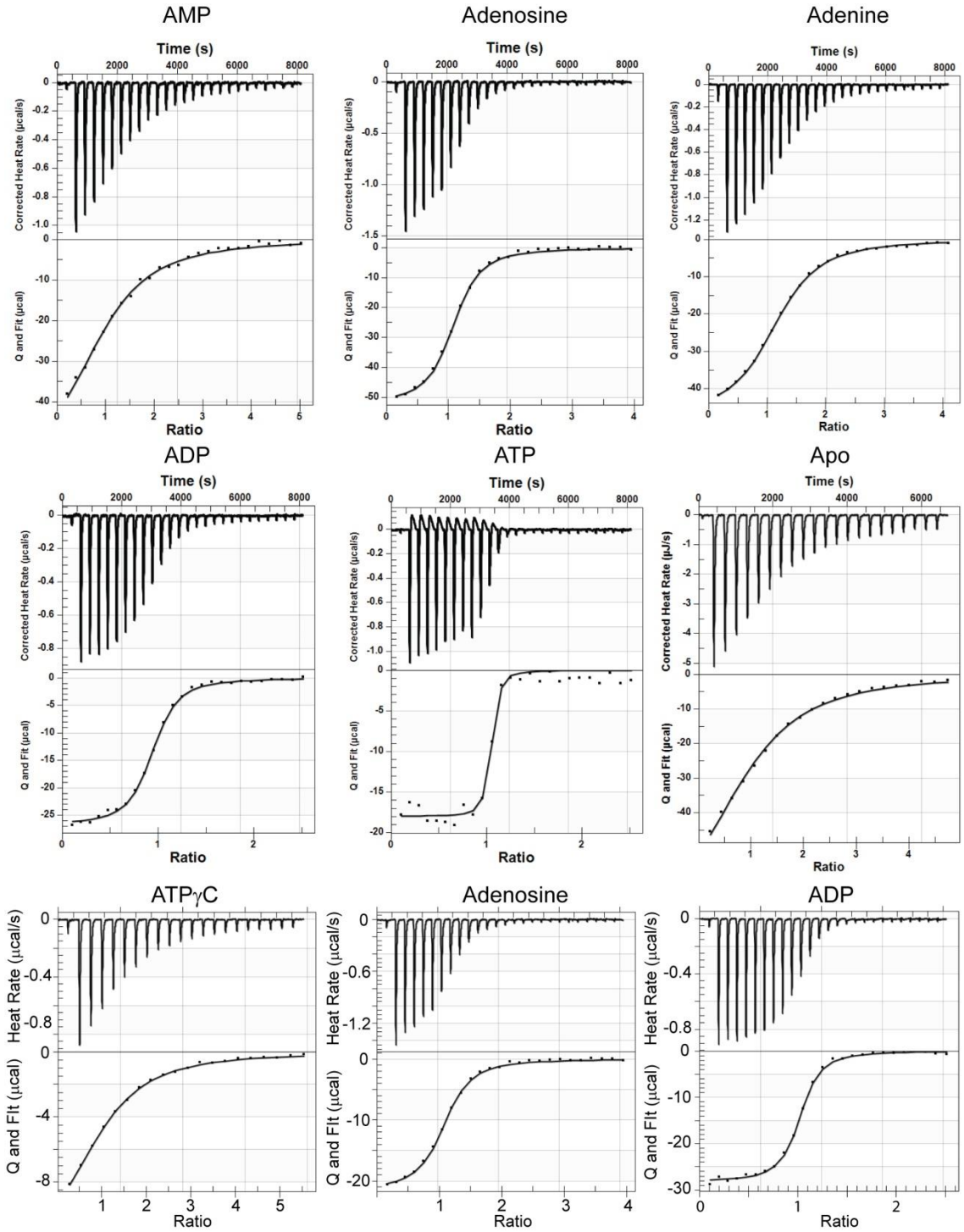

Figure 4.3. The ITC isotherms and their fits of PKI_{5-24} titrating to PKA-C under different nucleotide saturating conditions (2 mM).
(related to Figure 4.2)

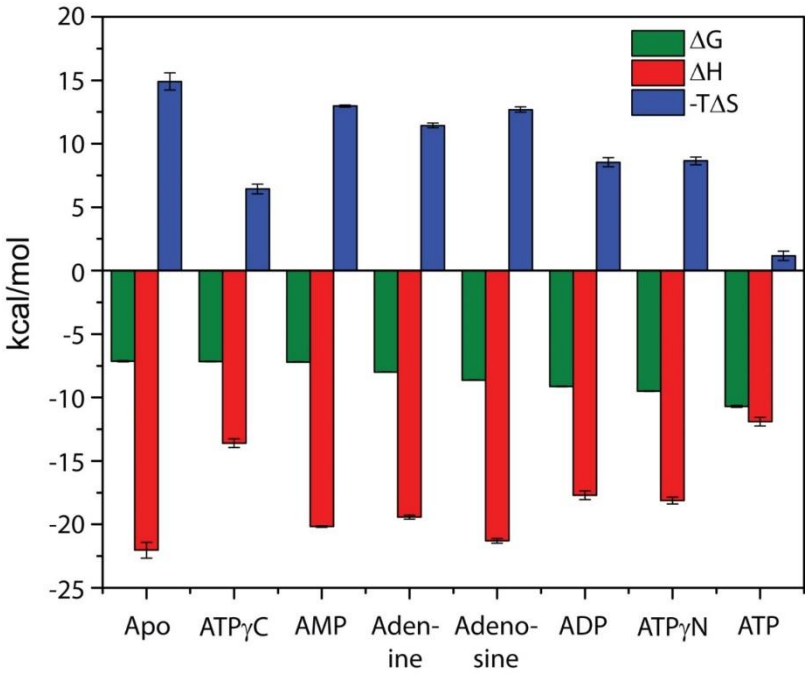

Figure 4.4. Full thermodynamic profile of PKI_{5-24} binding in the presence of various nucleotides. The entropic contribution was calculated as described in the methods section. (related to Figure 4.2)

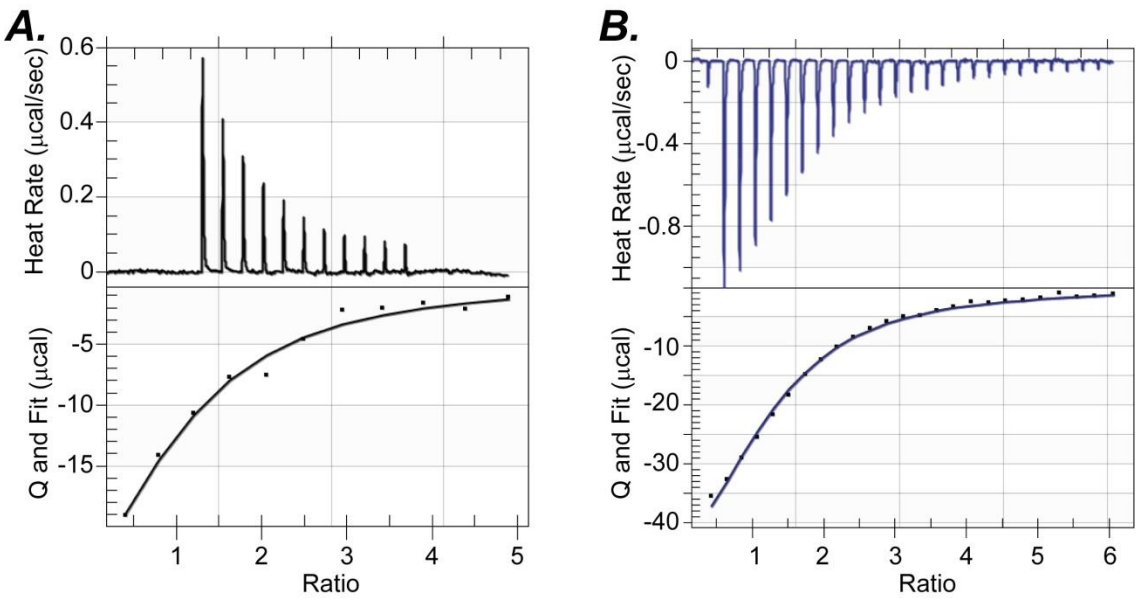

Figure 4.5. ITC isotherm of AMP binding to PKA-C and PKI_{5-24} binding at 6 mM AMP. (A) ITC isotherm of AMP binding to PKA-C. A K_d value of 250 ± 57 μM was found. (B) ITC isotherm of PKI_{5-24} binding at 6 mM AMP. Fit to a single-site binding model gave a K_d value of 6.2 μM (related to Figure 4.2).

Table 4.1. The affinity, degree of cooperativity (σ), and thermodynamics of PKI_{5-24} binding with respect to the kinase saturated with the nucleotide determined from ITC.

Note that some of the binding isotherms (See also Figure 4.3, 4.14) do not have a sharp inflection point and the ΔH and ΔS terms are less reliable.

	K_d (μM)	σ	ΔG (kcal/mol)	ΔH (kcal/mol)	*TΔS (kcal/mol)*
Apo	6.4 ± 0.56	1	-7.14 ± 0.05	-22.03 ± 0.63	-14.90 ± 0.68
ATPγC	6.1 ± 0.27	1.0	-7.17 ± 0.02	-13.61 ± 0.36	-6.43 ± 0.38
AMP	5.7 ± 0.18	1.1	-7.20 ± 0.02	-20.17 ± 0.07	-12.97 ± 0.08
Adenine	1.5 ± 0.03	4.3	-8.00 ± 0.01	-19.43 ± 0.16	-11.43 ± 0.18
Adenosine	0.53 ± 0.02	12	-8.63 ± 0.02	-21.32 ± 0.18	-12.69 ± 0.20
ADP	0.23 ± 0.0097	29	-9.13 ± 0.03	-17.67 ± 0.35	-8.54 ± 0.37
ATPγN	0.12 ± 0.0050	53	-9.49 ± 0.02	-18.12 ± 0.27	-8.64 ± 0.30
ATP	0.016 ± 0.0019	400	-10.72 ± 0.07	-11.90 ± 0.34	-1.17 ± 0.38

ATPγC prevents substrate binding.

To further understand the role of the bridging oxygen of the β and γ phosphates on the binding cooperativity of more realistic substrates that display much lower affinity than the pseudo-substrate, we utilized a 19-amino acid peptide corresponding to the cytoplasmic domain of phospholamban (PLN_{1-19}), a signaling target for PKA-C that regulates cardiac contractility [40, 214, 215]. Although phospholamban contains a transmembrane domain, the cytoplasmic domain alone is recognized and phosphorylated by PKA-C [214]. Remarkably, the binding titrations carried out in the presence of saturating concentration of ATPγC showed a dramatic reduction of the binding affinity. Previous binding studies show that the dissociation constant of PLN_{1-19} in the ternary complex PKA-C/ATPγN/ PLN_{1-19} is approximately 28 μM [122]. In stark contrast, for the PKA-C/ATPγC complex the PLN_{1-19} peptide has a K_d > 1 mM (**Figure 4.6A**). Accordingly, NMR titrations of the PLN_{1-19} peptide on the PKA-C/ATPγC complex do not show any detectable chemical shift changes in both the amide and methyl group

fingerprints (**Figure 4.6B**). Although PLN_{1-19} and PKI_{5-24} share the same recognition sequence, PKI_{5-24} contains a high affinity region [209] that is not found in other substrates. Both ITC and NMR titrations indicate that the loss of binding affinity by ATPγC observed in the pseudo-substrate is not only confirmed using PLN_{1-19}, but is accentuated with natural substrates.

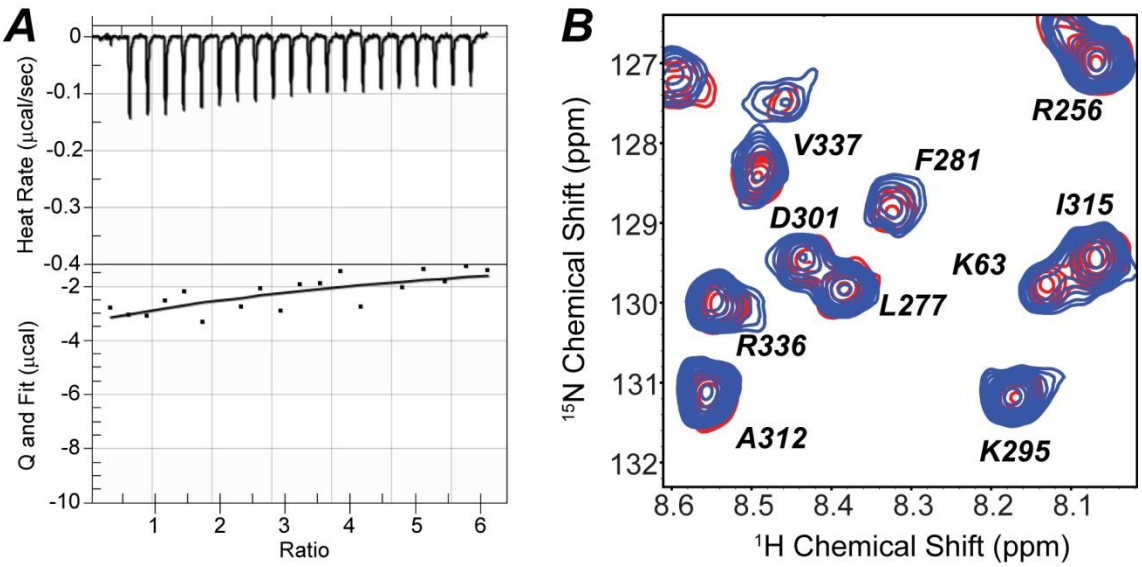

Figure 4.6. ATPγC abrogates native substrate binding.
(A) ITC isotherm of PLN_{1-19} binding to ATPγC saturated PKA-C. (B) Overlay of [^{1}H,^{15}N]-TROSY-HSQC spectra of the complexes PKA-C/ATPγC (green) and PKA-C/ATPγC/PLN_{1-19} (red) showing no detectable chemical shift changes (related to Figure 4.2).

Linkage between structural transitions and binding cooperativity.

To probe the conformational transitions of the enzyme with the different nucleotides, we mapped the enzyme's amide fingerprint using [^{1}H,^{15}N]-TROSY-HSQC experiments [118] as the amide chemical shifts are sensitive reporters of allosteric transitions (**Figure 4.7**) [104, 125, 216]. Although previous crystallographic structures of these complexes were reported to be identical [14], small changes in chemical shifts have been demonstrated to report on subtle changes in conformation and allostery [105, 106, 217]. Resonance assignments for the different free and ligated states of the kinase were previously obtained using triple-resonance experiments [122] and transferred to the spectra of the kinase saturated with the different nucleotides, as well as in the ternary complexes. We found that the addition of the pseudo-substrate to nucleotide-saturated

PKA-C shifts the amide resonances of the enzyme along linear chemical shift trajectories (**Figure 4.8A**). This indicates that the enzyme predominately interconverts between two states and pseudo-substrate binding shifts the populations of the enzyme toward the closed state to different extents.

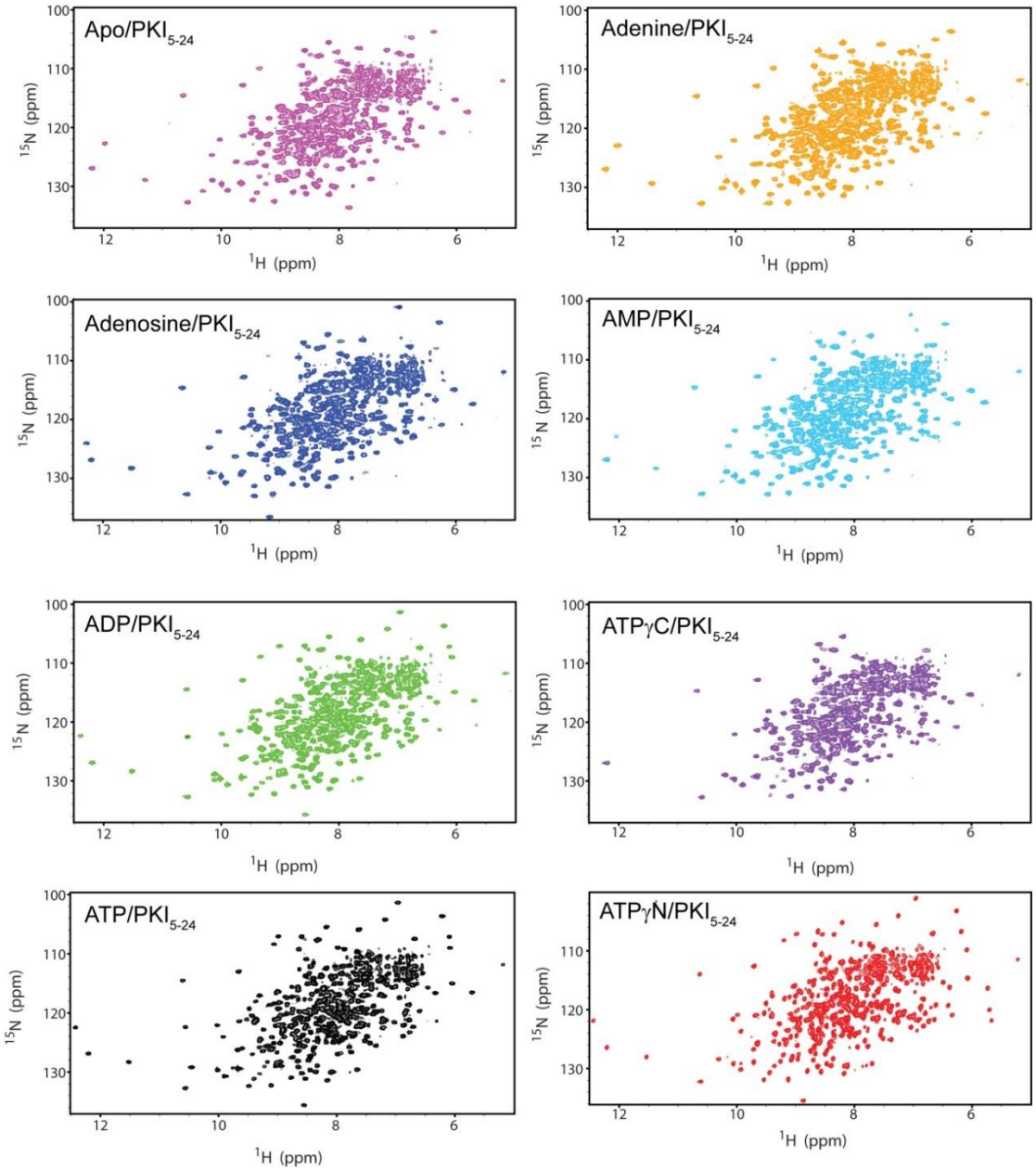

Figure 4.7. ^{1}H-^{15}N TROSY-HSQC of all the binary (PKA-C and PKI_{5-24}) and ternary complexes of PKA-C with PKI_{5-24}.

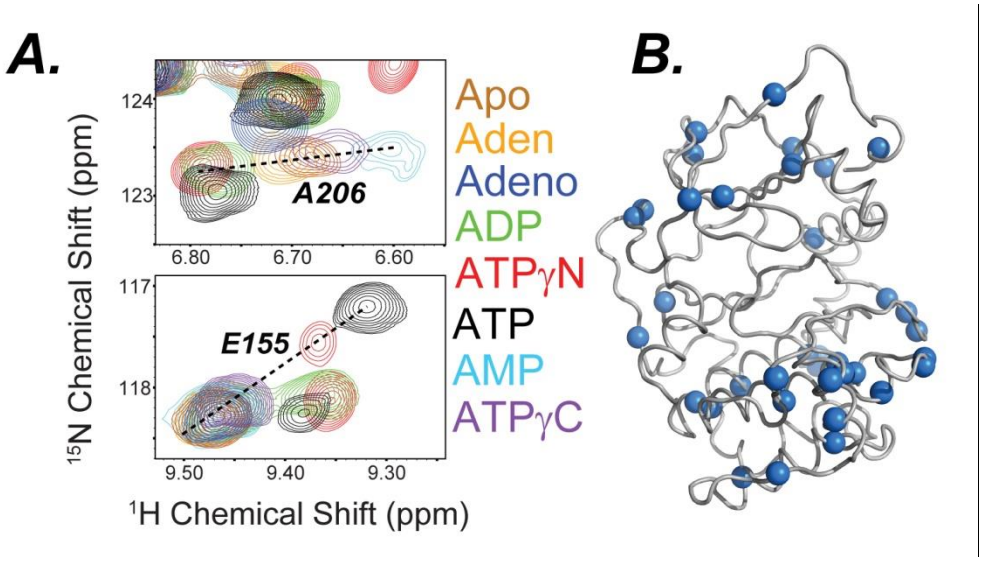

Figure 4.8. CONCISE analysis of the chemical shift changes with nucleotide.
(A) [^{1}H,^{15}N]-TROSY-HSQC spectra showing the backbone amide chemical shift changes of PKA-C saturated with different nucleotides upon binding PKI_{5-24} (See also Figures 4.13, 4.14 and 4.16) (B) Residues following linear trajectories (blue spheres) plotted on the cartoon representation of the PKA-C crystal structure (PDB: 1ATP).

A succinct view of the process is offered by the analysis of the amide chemical shifts using CONCISE [125], a statistical approach that utilizes principal component analysis to quantify the global coordinated response of the amide chemical shifts upon ligand binding. This method identifies the predominant linear trajectory of all the chemical shifts and the aggregate amide chemical shifts for each state is grouped together by their average position along the linear trajectory (PC score). These changes are displayed as probability density distributions defining a specific conformational state of the kinase along the conformational equilibrium [125]. The chemical shifts of each of the three major conformational states (open, intermediate, and closed) were previously defined by performing triple resonance experiments to assign the backbone chemical shifts or the apo, nucleotide bound and PKI bound forms of the enzyme [122]. Addition of PKI_{5-24} to all of the nucleotide-bound forms of the kinase shifts the conformational equilibrium toward the closed state (**Figures 4.8**, **4.9**, **and Table 4.2 and 4.3**), reflected in the higher PC score from CONCISE, but to different degrees (**Figure 4.10**). In particular, a gradual shift of the probability density distributions of the amide chemical shifts is apparent going from adenine, adenosine, and ADP up to ATP, indicating that the presence of the ribose and the increased number of phosphates gradually shifts the

conformational equilibrium toward the kinase closed state. To link the binding thermodynamics of PKI_{5-24} with the conformational transition, we first compared the free energy of binding of PKI_{5-24} under saturating conditions of nucleotide with the PC score (**Figure 4.11**) and did not find a firm correlation. However, a comparison between the free energy of binding for PKI_{5-24} and the PC score of the enzyme's ternary complexes with PKI_{5-24} (**Figure 4.12B**) shows a linear correlation between the extent of the closed state and the free energy of binding (|R| = 0.95, **Figure 4.12B**), indicating that the degree of cooperativity of substrate binding strongly depends on the extent of the closed state.

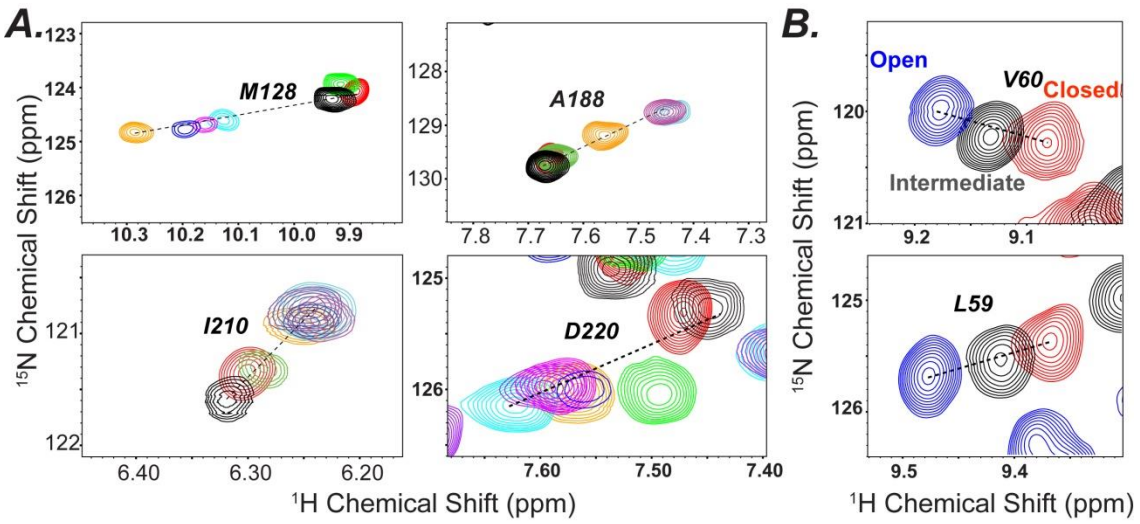

Figure 4.9. Linear chemical shift trajectories of PKA-C.
(A) Linear chemical shift trajectories that either have some states missing or demonstrate some deviation around the linear trajectory due to local chemical changes. (B) Trajectory for the Open, Intermediate and Closed state in PKA-C (related to Figure 4.3 and 4.5).

Table 4.2. List of residues that defined linear trajectories for the 12 states analyzed with CONCISE.

8	16	17	35	37	44	58	62	97	117
143	144	155	177	191	192	193	206	208	213
214	220	226	241	245	249	256	265	274	315
322	323	331	337	338	348				

Table 4.3. PCA and standard deviation of the CONCISE analysis of all ten structural states.

	PCA 1	Standard Deviation
Apo	-2.14	0.68
ATPγN	-0.96	0.81
AMP/PKI$_{5-24}$	-0.01	0.48
ATPγC/PKI$_{5-24}$	0.19	0.43
Apo/PKI$_{5-24}$	0.03	0.49
Adenine/PKI$_{5-24}$	0.38	0.48
Adenosine/PKI$_{5-24}$	0.48	0.62
ADP/PKI$_{5-24}$	0.52	0.49
ATPγN/PKI$_{5-24}$	0.64	0.59
ATP/PKI$_{5-24}$	0.77	0.66
H89/PKI$_{5-24}$	0.05	0.96
Balanol/PKI$_{5-24}$	0.04	0.78

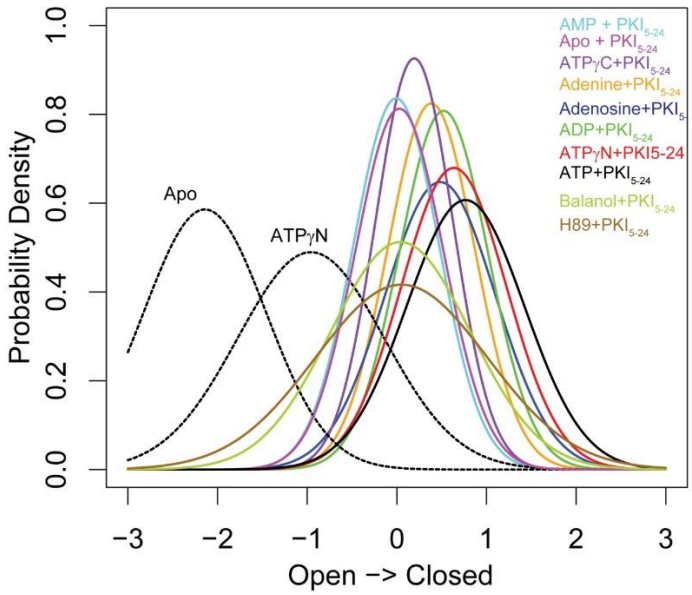

Figure 4.10. CONCISE analysis of the ^{1}H-^{15}N TROSY-HSQC of all the binary (PKA-C and PKI$_{5-24}$) and ternary complexes of PKA-C with PKI$_{5-24}$.

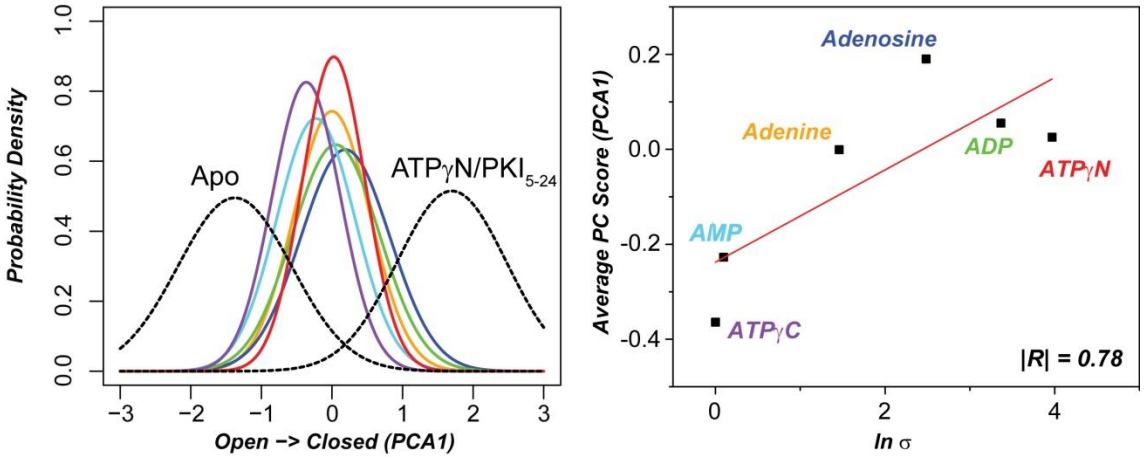

Figure 4.11. CONCISE analysis performed on the nucleotide bound states of PKA-C (without PKI_{5-24}) and a comparison of the PC score of the nucleotide bound states with the cooperativity of PKI_{5-24} binding.

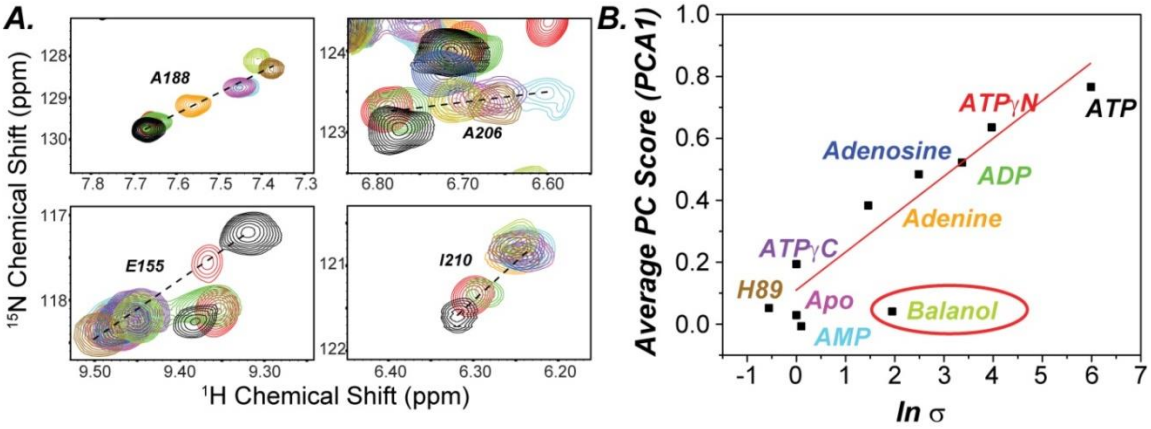

Figure 4.12. Chemical Shift Trajectories with Nucleotides and ATP-competitive inhibitors.
(A) [^{1}H,^{15}N]-TROSY-HSQC spectra showing the backbone amide chemical shift changes of PKA-C saturated with different ATP-competitive inhibits and nucleotides upon binding PKI_{5-24}. (B) Linear correlation between PC1 score and degree of cooperativity of the aggregate chemical shifts including the ATP-competitive inhibitors (see also Figures 4.7, 4.9-4.11 and Table 4.2-4.3).

The CONCISE analysis yields insights into the global opening and closing transitions following only those residues with linear trajectories. Therefore, we followed the chemical shift trajectories of the Ile, Val, and Leu methyl groups. Methyl group chemical shifts also report on allosteric networks particularly in large proteins [164, 218, 219]. Upon ligand binding most of the methyl group chemical shifts follow predominately linear trajectories along the open to close conformational states, reporting on a two state equilibrium in the fast exchange regime (**Figure 4.13**). However, several methyl groups

in the PKA-C/ATPγC/PKI$_{5-24}$ complex located near the binding site as well as in distal regions follow non-linear chemical shift trajectories, with many resonances exhibiting substantial line broadening even at ligand saturation conditions. These features suggest that ATPγC shifts the enzyme into another conformational state that is outside the open-to-closed reaction coordinates traceable with the other nucleotides and that binds substrates with lower affinity.

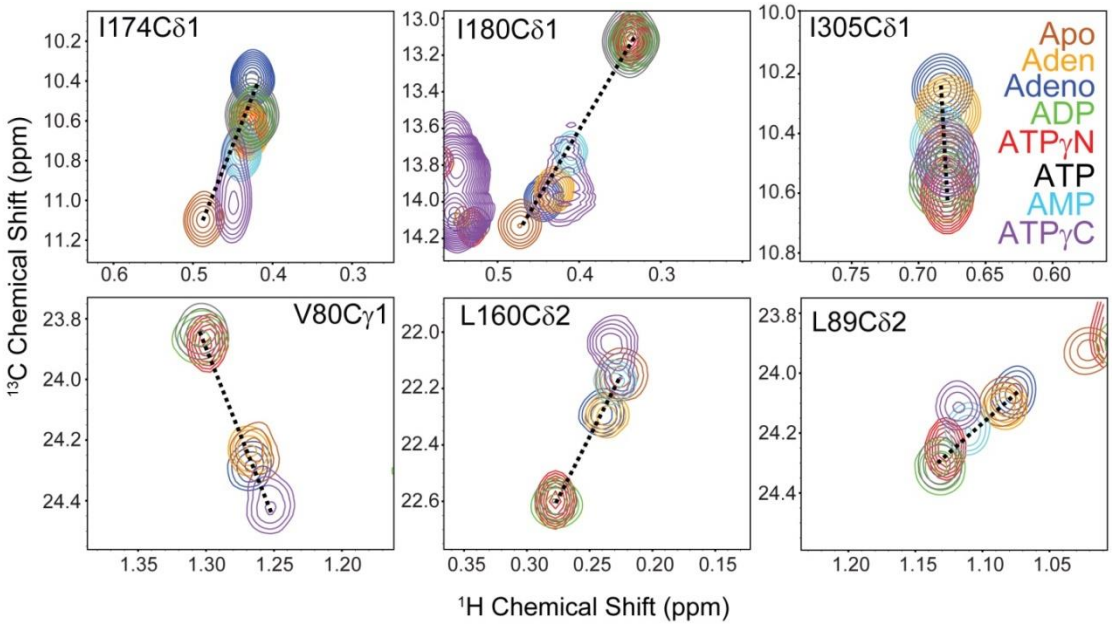

Figure 4.13. Effects of the ligand binding on the kinase side chains.
Methyl-TROSY spectra of ^{13}C methyl-labeled PKA-C saturated with different nucleotides. Most of the resonances follow linear chemical shift trajectories. Several resonances for ATPγC do not lay the shared linear trajectory

ATP-competitive inhibitors exhibit positive and negative cooperativity.

To understand the allosteric response of commonly used high affinity ATP-competitive inhibitors, we analyzed the binding cooperativity of H89 and balanol (**Table 4.4 and Figure 4.14**). H89 is an isoquinoline sulfonamide-based inhibitor designed to achieve higher selectivity for PKA-C and is commonly used to block PKA-C activity in cells [220]. Balanol is a natural occurring small molecule isolated from *Verticillium balanoides* with high inhibitory potency for PKC [221] and PKA-C [222]. We found that balanol displays a positive cooperativity (σ = 7.0) for PKI$_{5-24}$. In contrast, H89, displays negative binding cooperativity (σ = 0.55). Our ITC results reveal that high affinity ATP-

competitive inhibitors can modulate allosteric binding cooperativity in a manner similar to the nucleotides.

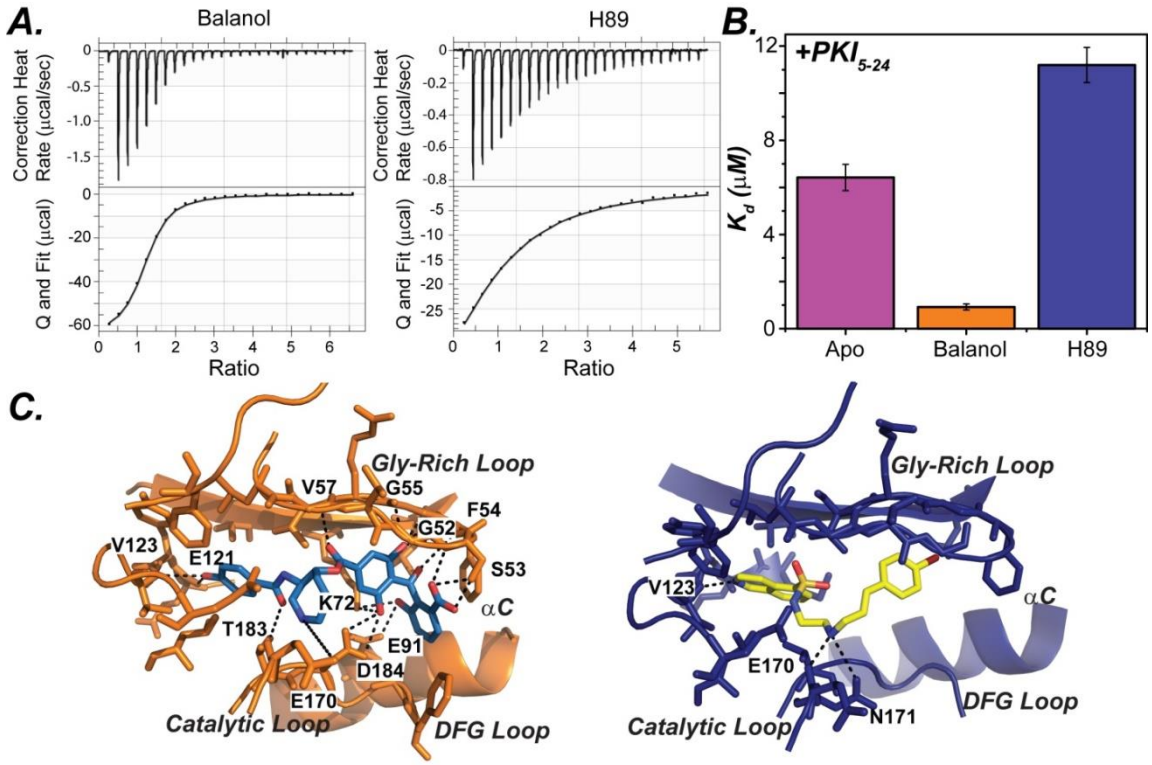

Figure 4.14. Binding cooperativity between ATP-competitive inhibitors and pseudo-substrate. (A) ITC isotherms for PKI_{5-24} binding to PKA-C saturated with Balanol (left), and H89 (right). (B) Plot of the K_d of PKI_{5-24} to PKA-C in the presence and absence of ATP-competitive inhibitors. (C) Structure of PKA-C with balanol (PDB:1BX6, orange) and H89 (PDB: 1YDT, blue) with key electrostatic interactions.

Table 4.4. The affinity, degree of cooperativity (σ), and thermodynamics of PKI_{5-24} binding with respect to the kinase saturated with the ATP-competitive inhibitor determined from ITC.

	K_d (µM)	σ	ΔG (kcal/mol)	ΔH (kcal/mol)	*TΔS (kcal/mol)*
Balanol	0.92 ± 0.13	7.0	-8.30 ± 0.09	-16.14 ± 0.56	-7.83 ± 0.65
H89	11.2 ± 0.75	0.57	-6.81 ± 0.04	-18.46 ± 0.62	-11.65 ± 0.60

To map the conformational state of PKA-C complexes with H89 or balanol and the pseudo-substrate PKI_{5-24}, we used [^{1}H,^{15}N]-TROSY-HSQC experiments and performed similar analysis (**Figure 4.12**). Several residues of the amide backbone followed linear trajectories along the two-state equilibrium. Several other residues, however, showed marked deviations from these trends and were excluded from the CONCISE analysis (**Figures 4.12 and 4.17**). Many of these non-linear trajectories result in the unique chemical environment around each ligand and not accurately report on the global conformational transition [106]. The probability distribution curves show that these ternary complexes are only partially closed and occupy intermediate position in the conformational equilibrium. When plotted as a function of the degree of binding cooperativity, the ternary complex with H89 falls within the linear correlation, displaying negative cooperativity, while the ternary complex with balanol, which shows a positive binding cooperativity, deviates from this relationship (**Figure 4.12B**). Although balanol shows cooperativity with pseudo-substrate binding, it fails to drive the entire enzyme toward a substrate competent state as in the case of ATP.

Analysis of the crystal structures and the NMR spectral signatures of the binary complexes with H89 and balanol explain the differences between their cooperative behaviors. The hydroxybenzophenone moiety together with the ester linkage of balanol form several hydrogen bonds with residues in the Gly-rich loop, i.e., Val57, Gly55, Phe54, Ser53, and Gly52, as well as the side chain groups of the conserved ion pair Lys72 and Glu91, and Asp184 (a residue in the DFG loop), while the bromocinnamoyl group of H89 does not make such electrostatic interactions (**Figure 4.14C**). This electrostatic interactions from balanol enable the Gly-rich loop to be clamped down and be coupled to the residues in the C-helix and large lobe. The NMR spectra show that, while both inhibitors caused apparent chemical shift changes in the small lobe, hinge and C-terminal residues, balanol perturbs the chemical shifts of the residues in the catalytically important motifs more significantly than H89 (**Figures 4.15 and 4.16**). These residues include Gly186, Ala188 (DFG loop), Thr197 (activation loop) and Glu203 (residue in the peptide positioning loop which interacts with the P-6 Arg). This allosteric interaction between the residues in the small lobe and substrate binding site may be responsible for the observed contrasting cooperativity effect with the two ATP-competitive inhibitors.

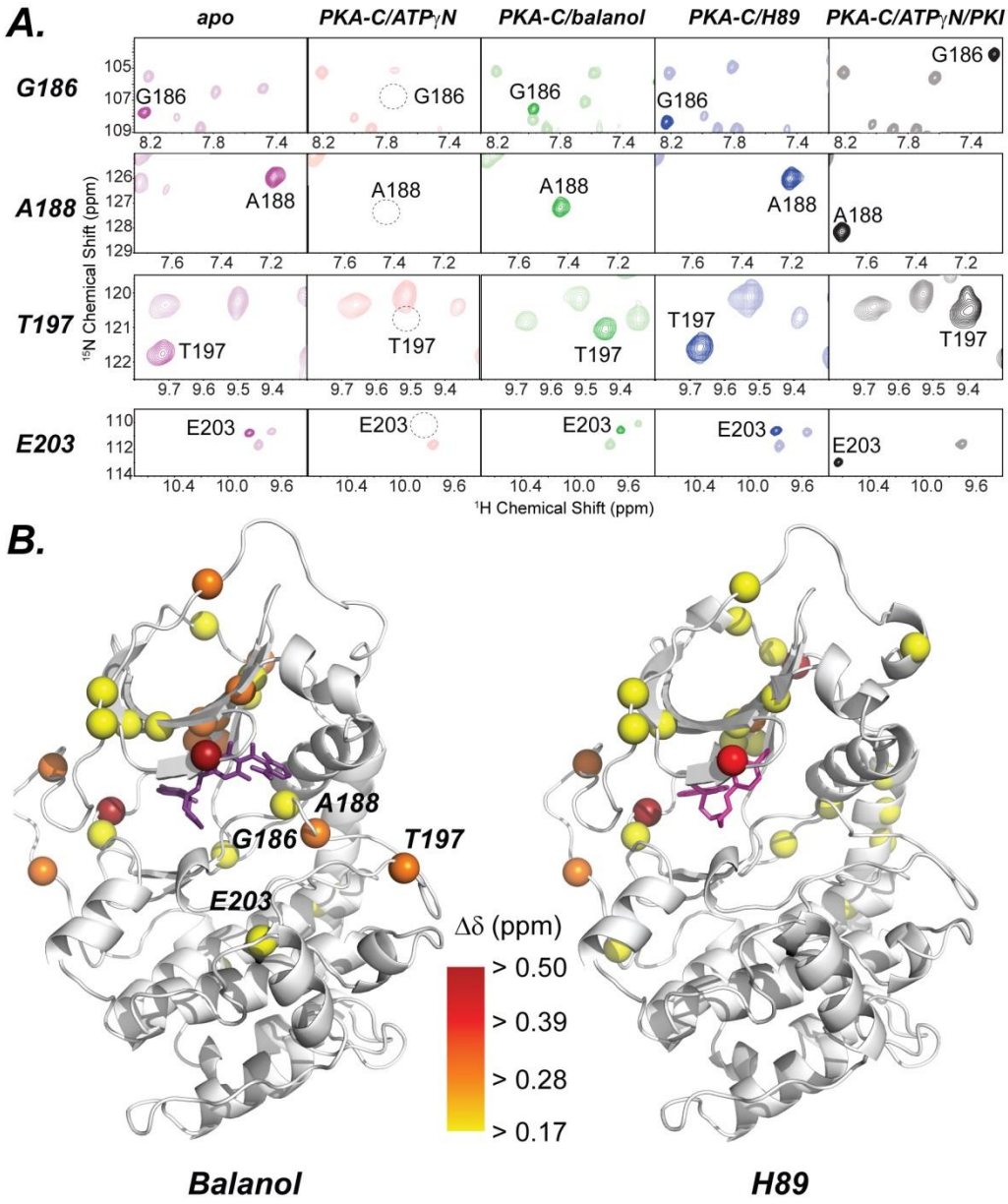

Figure 4.15. Chemical Shift Changes in the Active Site.
(A) [^{1}H,^{15}N]-TROSY-HSQC spectra of the backbone chemical shifts of active site residues in PKA-C. In the ATPγN bound state, many of these resonances experience exchange so they are unobservable (dotted circle). (B) Significant chemical shift changes upon binding of balanol and H89. Note that balanol induces more significant chemical shift changes in the active site compared to H89.

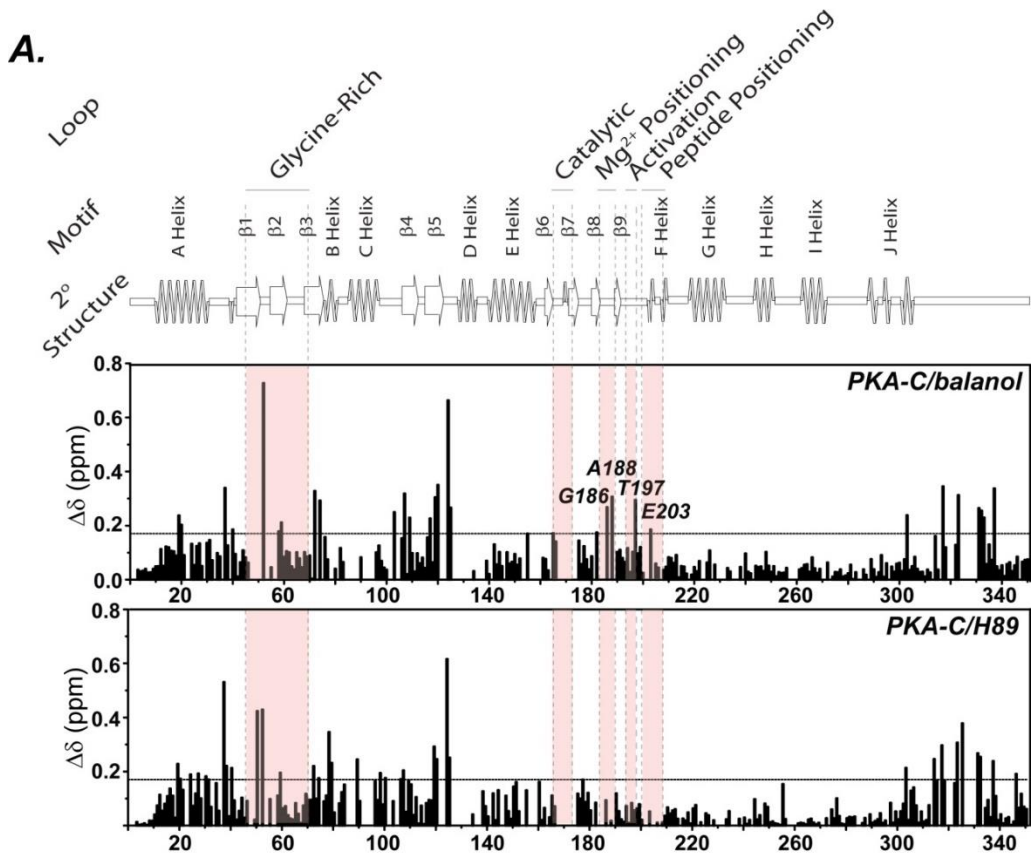

Figure 4.16. Chemical shift perturbation of PKA upon balanol or H89 binding.

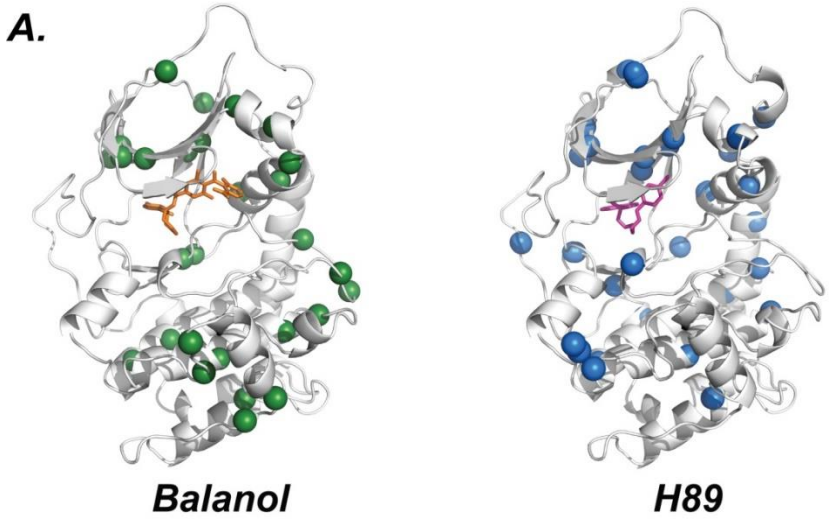

Figure 4.17. Residues of PKA-C that do not follow the open to closed linear trajectory upon ATP-competitive inhibitor binding.

4.4 Discussion

Although it has been known that PKA-C exhibits K-type allosteric cooperativity [44, 223], this work illuminates the structural basis for this phenomenon. The correlation we found between the conformational state of the ternary complex and the free energy of binding for the pseudo-substrate has many implications for kinase substrate recognition and function. The nucleotide emerges not only as carrier of the phosphate group for chemistry at the active site, but also having a structural role for mediating allosteric binding cooperativity. Importantly, high binding affinity of the substrate and pseudo-substrate can only be achieved when the appropriate nucleotide brings together the small and the large lobes, shifting the population of the enzyme toward the intermediate state [125], pre-organizing the active site such that it is complementary for substrate binding and enabling the ternary complex to reach a catalytically competent state [224, 225]. This conformational transition is most closely obtained with native substrates and ATP, leading to the most favorable free energy of binding. Removal of the β- and γ-phosphate or ribose does not significantly alter the nucleotide binding affinity, but results in an enzyme conformation progressively less complementary for substrate binding.

Interestingly, for both AMP and ATPγC, they did not fall within the linear relationship between free energy of pseudo-substrate binding and extent of the closed state, showing that these nucleotides do not exhibit positive *K*-type cooperativity (**Figures 4.2B and 4.12**). Not only AMP has a lower binding affinity, but it is also unable to drive the conformation of the glycine-rich loop in a competent state, abrogating binding cooperativity. Interestingly, the non-hydrolysable nucleotide mimic ATPγC has a similar effect (**Figure 4.2**). Our data could be explained by comparing the crystal structures of the kinase in the presence of SP20 and ATPγC (PDB entry 4IAC[226]) with that in complex with PKI_{5-24} and ATP (PDB entry 1ATP). Overall, the backbone structures of the two complexes are identical. However, in the 4IAC structure ATPγC does not interact with the backbone amide groups of Phe54 and Gly55, preventing the glycine-rich loop from closing and resulting in a more open conformation (**Figure 4.18**). Furthermore, in the presence of ATPγC, the second Mg^{2+} ion adopts a bi-pyramidal coordination geometry rather than the octahedral geometry found with both ATP and ATPγN [226]. Therefore, the coordination of the metal ion plays a key role in positioning

the γ-phosphate and the substrate for productive phosphoryl transfer. Moreover, the chemical shifts of the methyl groups suggest that the ternary complex PKA-C/ATPγC/PKI$_{5-24}$ occupies a different state in the conformational landscape of the enzyme, with a loss of binding cooperativity for the pseudosubstrate and complete obliteration of binding for phospholamban. Although all chemical moieties are important for binding cooperativity, our data underscore the central role of the oxygen atom bridging the β and γ phosphate. Structurally, this atom provides the coordination geometry for the second Mg^{2+} ion, clamping down the glycine-rich loop and shifting the conformational equilibria for the formation of a productive ternary complex with substrates. In fact, the degree of cooperativity is significantly attenuated when nitrogen replaces the oxygen (ATPγN). The latter was also predicted but not proven in the published work by Walsh and coworkers [227]. If the degree of cooperativity is attenuated by the substitution of the oxygen with nitrogen (ATPγN), it is completely lost with ATPγC, a widely used non-hydrolysable ATP analog for both kinases and ATPases [228]. In the case of PKA-C, this compound appears to prevent the formation of a catalytically competent complex with endogenous substrates.

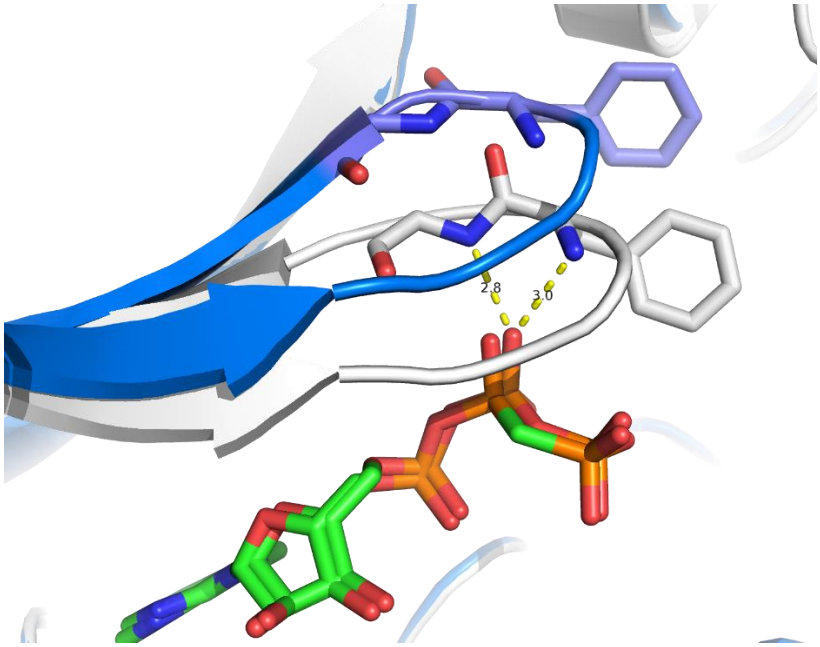

Figure 4.18. Structure of the glycine rich loop of PKA-C/ATP/PKI$_{5-24}$ and PKA-C/ATPγC/PKS$_{5-24}$. PKA-C/ATP/PKI$_{5-24}$ (PDB:1ATP, white) and PKA-C/ATPγC/PKS$_{5-24}$ (PDB: 4IAC, blue)

Based on the above considerations, we conclude that the oxygen bridging the β and γ phosphate is a *hot spot* for modulating binding cooperativity. By changing the chemistry around this hot spot, it is possible to convert a kinase into a completely dead kinase abrogating both its canonical and non-canonical functions. These results may have important implications in the design of new inhibitors of kinases. It is possible to anticipate that newly designed inhibitors may be directed to either the catalytic function (*i.e.*, phosphoryl transfer) or both catalytic and binding functions. In the former case, the kinase would still function as a pseudo-kinase preserving its signaling role as scaffolds, anchors, spatial modulators, traps, and ligand-driven regulators of canonical kinases [36, 196]. In fact this case has previously been observed with small molecular inhibitors of RAF kinase, activating kinase signaling pathways in a dose dependent manner [35, 199] or in the more recent finding that ATP-competitive inhibitors can block protein kinase recruitments to the Hsp90-Cdc37 system[229]. In the latter case, the kinase would be totally dead and removed from its signaling pathways (**Figure 4.19**). Mutations have been reported to convert active kinases into pseudo-kinases, preserving their non-catalytic functions [95, 197]. In the case of PKA-C, residual catalytic activity enables yeast to survive[230]. On the other hand, a catalytically dead PKA-C fails to be autophosphorylated, but it can still bind ATP as well as the regulatory subunits and is recognized and phosphorylated by PDK-1 [197]. Another notable case is with a mutation that fuses the C-spine, blocks ATP binding and allows for dimerization of RAF kinase domains [36]. ATPγC renders the kinase dead, abolishing both catalysis and binding of substrates, despite assembly of the C-spine.

In fact, widely used ATP-competitive inhibitors such as balanol and H89 are able to render PKA-C a pseudo-kinase and a dead kinase, respectively. Although both inhibitors contain aromatic rings that intercalate with the C spine residues, balanol possesses several polar groups that form hydrogen bonds with side-chain groups critical for substrate recognition and catalysis, including the conserved Lys72 and Glu91 in the active site [231], the conserved Asp184 in the DFG loop, and the Gly-rich loop. H89 lacks these hydrophilic groups and the interaction within the binding site is almost exclusively through hydrophobic contacts. The polar interactions in balanol bring down the Gly-rich loop in a quasi-competent state. This is further supported by the crystal structure where the Gly-rich loop in the H89-bound complex is directed away from the

catalytic loop, resulting in the loss of interaction between the pseudosubstrate and the Gly-rich loop, resulting in a negative cooperativity. In the committed complex, the movement of the Gly-rich loop coordinated by the nucleotide corresponds to allosteric rearrangements of the residues in the substrate binding site [40, 44]. Interestingly, both balanol and H89's electrostatic interactions with the critical Mg^{2+} ion are not observed in the X-ray structures. Future design of inhibitors exploiting the *hot spot* for binding cooperativity may lead to greater control of kinase function *in vivo* and tune the kinase binding cooperativity.

In a recent work on Src kinase, Foda *et al.* show a negative binding cooperativity between ATP and substrates [232]; while a positive cooperativity was measured for ADP and phosphorylated substrate. These authors found that the negative cooperativity is mediated by an allosteric network of contacts initiated by a protonation event occurring at the DFG loop [232]. This contrasts the positive *K*-type binding cooperativity found for PKA-C [44], where a high degree of cooperativity was observed for ATP with the endogenous protein kinase inhibitor (PKI), regulatory subunits (R-subunits) [46], and substrates [122]. These findings suggest that the mechanism for cooperativity is not uniform throughout the kinome and that cooperativity hot spots may become a target for designing inhibitors able to fine-tune specific signaling pathways.

In conclusion, our study identifies a hot spot for tuning binding cooperativity and decoupling canonical and non-canonical functions in kinases, introducing the concept of a possible higher level of control achievable by high affinity competitive inhibitors. By modulating the extent of closure of the Gly-rich loop, newly designed kinase inhibitors would then be able to convert a kinase into a pseudokinase, *i.e.*, creating a scaffold that it is still involved in signaling, or alternatively, subtract kinases from their signaling pathways altogether, impairing both enzymatic activity and substrate binding (dead kinases) [32, 196].

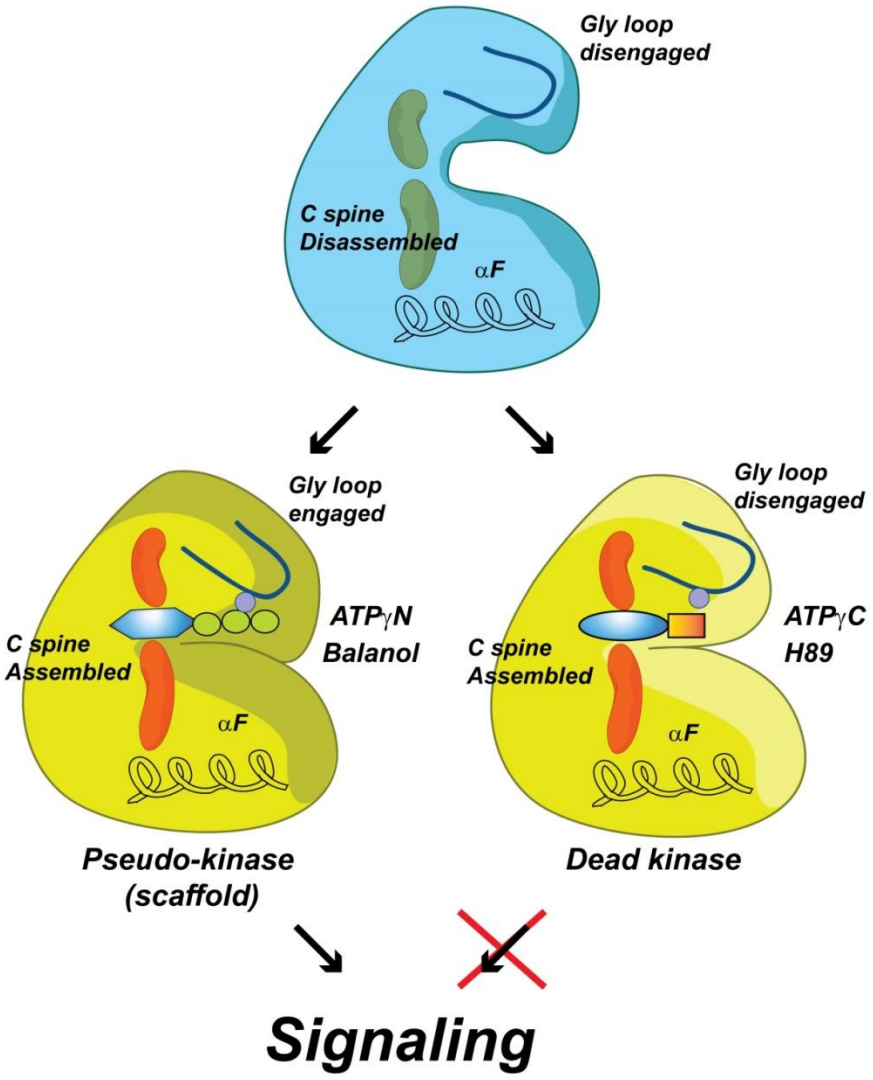

Figure 4.19. Uncoupling canonical and non-canonical function of kinases.
The apo enzyme (blue) displays both disassembled C spine and disengaged Gly-loop. Binding of non-hydrolyzable ATP analogs or good ATP mimic drug inhibitors (i.e., able to engage Gly-rich loop via coordination of Mg^{2+} ion) produce a pseudokinase that is unable to carry out phosphoryl transfer but is able to bind substrates cooperatively (yellow). Binding of drug inhibitors that are unable to properly coordinate the Mg^{2+} ion to engage the Gly-loop (i.e., ATPγC, H89, see also Figure 4.19) obliterates both catalytic and scaffolding function (dead kinase).

4.5 Experimental Procedures

Adenosine 5'-triphosphate (ATP), adenosine 5'-monophosphate (AMP), γ-β-methyleneadenosine 5'-triphosphate (ATPγC), adenine, and N-[2-(p-bromocinnamylamino)ethyl]-5-isoquinolinesulfonamide (H89) were purchased from Sigma Aldrich (St. Louis, MO, USA). Adenosine 5'-diphosphate (ADP) and adenosine were purchased from Research Products International (Mt. Prospect, IL, USA). Adenosine 5'-(β,γ-imido)triphosphate (ATPγN) was purchased from Roche Diagnostics (Indianapolis, IN, USA). Balanol was purchased from AnalytiCon Discovery, LLC (Rockville, MD, USA).

Sample Preparation. Recombinant catalytic subunit of PKA was expressed in BL21 (DE3) cells as previously described by Studier[171] at 24 °C. Purification of PKA-C was performed as previously described using the His_6-RIIα(R213K)[168] subunit and a second purification step was performed using the HiTrap SP cation exchange column as previously described[183]. The most abundant isoform, corresponding to phosphorylation at S338, T197 and S10, was used for all experiments. Peptide synthesis was performed on a CEM Liberty microwave synthesizer as described previously[41]. Kinase activity was tested with a gel shift assay and quantified using A_{280} = 52060 $M^{-1}cm^{-1}$.

ITC measurements. All ITC measurements were performed with a Microcal VP-ITC instrument or TA NanoITC instrument at 300K. Samples were buffer exchanged into 20 mM MOPS, 90 mM KCl, 10 mM DTT, 10 mM $MgCl_2$, 1 mM NaN_3, pH 6.5. Approximately 1.7 mL of 11.4-32μM of PKA-C was used for each experiment and 280 μL of 140-350μM of PKI_{5-24} in the titrant syringe. For the AMP binding experiment 300 μL of 238μM of PKA-C was used with 50 μL of 3.3mM of AMP. Final concentration of 2mM of nucleotide was used for nucleotide saturated experiments and a concentration of 50 μM for the inhibitor saturated experiments. All experiments were performed in triplicate. The heat of dilution of the ligand to the buffer was taken into account by measuring the heat of dilution of the ligand to the buffer and was subtracted from the experiment accordingly. Binding was assumed to be 1:1 and was analyzed using the NanoAnalyze software (TA instruments New Castle, DE, USA), with the Wiseman Isotherm [233]:

$$\frac{d[MX]}{d[X_{tot}]} = \Delta H^{\circ} V_0 \left[\frac{1}{2} + \frac{1-(1+r)/2-R_m/2}{\left(R_m^2 - 2R_m(1-r)+(1+r)^2\right)^{1/2}} \right] \quad (4.1)$$

where the change of the total complex, d[MX] with respect to the change of the ligand concentration, d[X_{tot}] is dependent on r, the ratio of the K_d with respect to the total protein concentration, and R_m, the ratio between the total ligand and total protein concentration. The free energy of binding was determined using the following:

$$\Delta G = RT \ln K_d \quad (4.2)$$

where R is the universal gas constant and T is the temperature at measurement (300 K). The entropic contribution to binding was calculated using the following:

$$T\Delta S = \Delta H - \Delta G \quad (4.3)$$

Calculations for the cooperativity constant (σ) were calculated as follows:

$$\sigma = \frac{K_{d,Apo}}{K_{d,nucleotide} \; or \; K_{d,inhibitor}} \quad (4.4)$$

where $K_{d,Apo}$ is the K_d of PKI_{5-24} binding to the apo enzyme and $K_{d,nucleotide}$ or $K_{d,inhibitor}$ is the K_d of PKI_{5-24} to the nucleotide- or inhibitor-bound enzyme, respectively.

NMR Experiments. Samples for ^{13}C IVL ^{15}N labeled PKA-C were expressed and purified as previously described[44, 183]. Effective final sample concentrations were 0.2-0.25 mM in 20 mM KH_2PO_4, 90 mM KCl, 10 mM DTT, 10 mM $MgCl_2$ 1 mM NaN_3 at pH 6.5 with 12 mM of nucleotide. Adenosine and adenine lack solubility in aqueous solution and concentrations of 10 mM and 6mM respectively were used. For ATP-competitive inhibitors concentrations of 0.8 mM of Balanol and 3 mM of H89 were used. Samples with ATP and ATPγN were performed with 60 mM $MgCl_2$ for MgATP. Additions of 4, 8, 12, 18, 24, and 32 µL of 4.0 mM of PKI_{5-24} were used for a minimum final two fold molar excess of ligand. NMR assignments on the apo, nucleotide bound (ATPγN) and ternary (ATPγN and PKI_{5-24}) were carried out on an 850 MHz Bruker Avance III spectrometer and described elsewhere [234]. ^{1}H-^{15}N TROSY-HSQC experiments and ^{1}H-^{13}C HMQC experiments for nucleotide-bound PKA-C were carried out on a Varian Inova 600 MHz spectrometer equipped with a Cold HCN probe operating at 300 K. [^{1}H-^{15}N] TROSY-

HSQC experiments of PKA-C with ATP-competitive inhibitors were performed on a Bruker Avance 700 MHz spectrometer equipped with a TXI probe.

Analysis of Chemical Shift Perturbations. We employed the COordiNate ChemIcal Shift bEhavior (CONCISE)[125] method to monitor trajectories of chemical shifts and measure the change in equilibrium position associated with each PKA-C construct (apo, ATPγN, adenosine/PKI_{5-24}, adenine/PKI_{5-24}, Apo/PKI_{5-24}, AMP/PKI_{5-24}, ADP/PKI_{5-24}, ATPγC/PKI_{5-24}, ATPγN/$PKI_{5-24,}$ balanol/PKI_{5-24} and H89/PKI=). In short, through Principal Component Analysis (PCA), the method identifies a set of residues whose chemical shifts respond linearly to the conformational transition. Each one of these residues provides a measure of the equilibrium position for every PKA-C construct in form of scores along the first principal component. The equilibrium position for a given construct is given by the average of the PC-scores over all linear residues. To identify the residues whose chemical shifts follow a linear pattern, a threshold of 1.0 to 3.0 for the ratio of the standard deviations of PC1 over PC2 was used, and residues that were affected by chemical shifts perturbations below 0.05 ppm were also discarded (see [125]for details on the threshold calibration). After this threshold was applied, a total of 36 residues formed the subset that was used to trace the equilibrium position of each state (see **Table 4.3-4.4**).

4.6 Acknowledgements

This work is supported by the NIH (GM100310 and GM72701 to GV and T32AR007612 to JK). We thank Prof. Alessandro Cembran (University of Minnesota-Duluth) and Prof. Larry Masterson (Hamline University) for helpful discussions, and Prof. Robert Geraghty (University of Minnesota) for access to the VP-ITC instrument. NMR Experiments were carried out at the Minnesota NMR Center.

CHAPTER 5 DIFFERENTIAL SUPPRESSION AND FORMATION OF CONFORMATIONALLY EXCITED STATES BY ATP-COMPETITIVE INHIBITORS MODULATES KINASE BINDING COOPERATIVITY

Geoffrey C. Li[1], Jonggul Kim[2], Manu V.S.[2], Susan S. Taylor[3] and Gianluigi Veglia[1,2]*

[1]Department of Chemistry– University of Minnesota, Minneapolis, MN 55455.
[2]Department of Biochemistry, Molecular Biology, and Biophysics- University of Minnesota, Minneapolis, MN 55455;
[3]Department of Chemistry and Biochemistry and Pharmacology, University of California at San Diego, CA 92093

Submitted

5.1 Conspectus

ATP-competitive compounds are the most potent drugs developed for protein kinases, and to date constitute the only clinically approved kinase inhibitors. By targeting the ATP binding pocket, these molecules block the catalytic or canonical function of kinases, preventing substrate phosphorylation. Paradoxically, a few ATP-competitive inhibitors activate down-stream kinase pathways *in vivo* through poorly understood mechanisms. Here, we utilized the catalytic subunit of cyclic AMP-dependent protein kinase (PKA-C) as a benchmark to determine how its inhibited forms recognize substrates. As the X-ray structures of the inhibited kinases are very similar, we analyzed the dynamic response of PKA-C upon binding to two high-affinity ATP competitive inhibitors, balanol and H89, and compared it with the nucleotide mimic, ATPγN. When bound to either inhibitor, PKA-C is still able to recognize the pseudo-substrate, PKI_{5-24}, although with opposite *K-type* allosteric cooperativity. Multi-timescale NMR relaxation experiments show that balanol and H89 differentially alter the conformational landscape of the kinase, shifting the timescale of its motions and influencing the allosteric binding cooperativity. While both inhibitors attenuate the microsecond-millisecond timescale dynamics of the enzyme, balanol engages the two lobes, preserving the coordinated motions. Our results provide a new paradigm for exploring the chemical nature of ATP-competitive inhibitors, showing how they can differently modulate allosteric binding cooperativity and other non-catalytic functions.

5.2 Introduction

Eukaryotic protein kinases (EPKs) populate ~2% of the genome and control vital cellular processes such as development and differentiation, metabolism, and stress response by catalyzing the transfer of the γ-phosphate from ATP to serine, threonine, or tyrosine residues in their protein substrates[2]. Aberrant phosphorylation is linked to diseases such as cancer [235], autoimmune disorders [236], cardiac disease [6], and diabetes [7]. To date, there are at least 60 diseases associated with kinases, and this number is likely to increase, making protein kinases major drug targets [237-239]. Although allosteric drugs for kinases have been discovered [240], the majority of small molecules targeting kinases are ATP-competitive inhibitors (Type I or II). These molecules abolish the canonical or catalytic function of kinases by blocking the ATP-binding site, and thus prevent phosphorylation of substrates [240]. Interestingly, several ATP-competitive inhibitors display paradoxical activation of kinase pathways *in vivo* [241]. Although inhibited, kinases can still participate in signaling pathways, suggesting these competitive inhibitors may induce alternative ways to control kinases' signaling [32, 33, 196]. Specifically, how ATP-competitive inhibitors influence the substrate binding affinity remains unexplored.

ATP-competitive inhibitors bind in a pocket located between the two lobes of the structurally conserved catalytic cores. This bilobal fold is preserved among EPKs and was first revealed when the structure of the catalytic subunit of PKA (PKA-C) was solved [8]. The small N-lobe includes a 5-stranded β-sheet that controls nucleotide-binding and a highly conserved αC-helix, whose positioning is dynamically regulated and crucial for active kinases [242]. The larger C-lobe is mostly α-helical and includes the substrate-binding site and the catalytic residues that are essential for phosphoryl transfer [14, 243]. Two stacks of hydrophobic residues, referred to as Regulatory (R)- and Catalytic (C)-spines, span the two lobes of the kinase core and are docked onto the αF-helix in the C-lobe [23, 31]. Other conserved structural elements include the linker region and four loops (the Gly-rich, DFG, activation, and catalytic loops)[14]. ATP binding connects all of these elements and couples both lobes structurally and dynamically (**Figure 5.1**)[40, 41]. While phosphorylation of the activation loop typically contributes to assembly of the R-spine, the adenine ring of ATP is necessary to complete the C-spine, intercalating

between A70 and Val57 in the N-lobe and L173 in the C-lobe, synchronizing the motions in the hydrophobic core, and linking the two lobes[244].

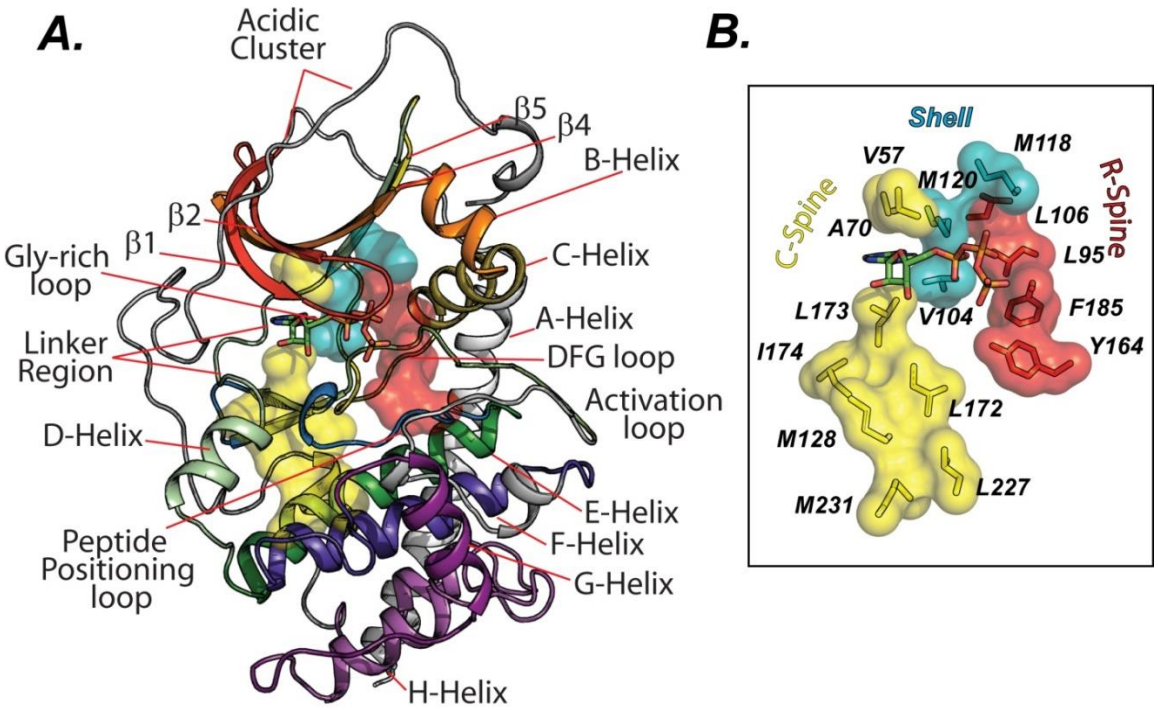

Figure 5.1. Architecture of the catalytic subunit of cAMP-dependent protein kinase A (PKA-C). A. The canonical kinase subdomains as identified by Hanks and Hunter [245] mapped onto the structure of PKA-C (PDB: 1ATP) B. The conserved hydrophobic core architecture of protein kinases as described by Kornev and Taylor [23] mapped onto the structure of PKA-C highlighting the C- spine (yellow), R-spine (red) and Shell (teal) residues (PDB ID: 1ATP)

To understand how ATP-competitive inhibitors modulate the substrate binding cooperativity of kinases, we chose PKA-C as a benchmark and analyzed its binding response to balanol and H89, two high affinity ATP-competitive inhibitors widely used for studying both PKA and PKC signaling pathways [222, 246]. Balanol is a fungal metabolite from *Verticillium balanoides* [247], while H89 (or N-[2-(p-bromocinnamylamino)ethyl]-5-isoquinoline sulfonamide) is a synthetic, H-series inhibitor used to study PKA signaling in cardiac and smooth muscle [248](**Figure 5.2A**). Both balanol and H89 inhibit PKA-C with low nM affinity, *i.e.*, K_i ~ 4 [247] and 48 nM [220], respectively, but surprisingly, they display opposite *K-type* cooperativity $\left(\sigma =\right.$

$\left(\frac{K_D of\ PKI_{5-24} binding\ to\ Apoenzyme}{K_D of\ PKI_{5-24} binding\ to\ inhibitor-bound\ enzyme}\right)$ with respect to the pseudo-substrate, protein kinase inhibitor (PKI_{5-24}), with a cooperativity value (σ) of 7 for balanol, and 0.6 for H89 [249]. As the X-ray structures of PKA-C/balanol and PKA-C/H89 are very similar (overall RMSD < 0.7 Å, **Figure 5.2B**) with significant differences only in the ATP binding pocket, we reasoned that the divergent cooperative behavior might correlate with the different conformational dynamics of the two complexes and the existence of alternate high-energy conformational states. To test this hypothesis, we used multi-timescale NMR relaxation measurements (from ps to ms timescale) and compared the dynamic response of PKA-C to both balanol and H89 binding with that of the nucleotide. We found that these inhibitors alter the structural coupling between the two lobes of the kinase in a completely different manner. Notably, they differentially alter the kinase's conformationally excited states responsible for the allosteric binding cooperativity, shifting the timescale of the enzyme's motions. While in the previous paper, we reported the thermodynamics for the binding of pseudosubstrate to the inhibitor-bound kinase, here we present the underlying mechanism for the observed opposite K-type cooperativity. We conclude that the divergent cooperativity observed for these ATP-competitive inhibitors is due to their different ability to steer the enzyme through energy basins of the conformational landscape that can be more or less committed to substrate binding. Our results suggest that it is possible to modulate the binding cooperativity of the kinases by tuning the chemical nature of the ATP-competitive inhibitor, introducing a new way to fine-tune kinase function.

5.3 Results

ATP-competitive inhibitors alter the structural coupling between the kinase's lobes.

To monitor the kinase's structural response to the binding of balanol and H89, we mapped both the amide and methyl group fingerprints (**Figure 5.3**), obtaining the distinct signatures for competent and incompetent states of PKA-C [41]. A hallmark for the kinase's competent (or *committed*) state (ATP-bound) is the dramatic broadening of the amide resonances associated with catalytically important loops such as the Gly-rich, DFG, activation and peptide-positioning loops, and the αC-helix [43]. This is correlated

with increased conformational dynamics in the intermediate timescale[43, 44]. In contrast, we found that binding either balanol or H89 to the kinase did not cause any line broadening in the amide or methyl fingerprint resonances; rather they induce distinct chemical shift perturbations (CSPs) throughout the enzyme (**Figures 5.4 and 5.5**). While both inhibitors cause substantial CSPs involving amide residues in the Gly-rich loop, linker region, and C-terminal tail, balanolcaused appreciable chemical shift changes that are localized within the catalytically important loops: DFG (G186, A188), activation (T197), and P+1 loop (E203) (**Figure 5.5**). Balanol binding also affects the resonances in the methyl fingerprint, with pronounced changes throughout the hydrophobic core (Leu173, Leu95 and Val104) and the hydrophobic PIF binding pocket where the C-terminal tail docks (Leu116, Val80). On the other hand, H89 binding perturbs mostly the side chains of the N-lobe and linker that line the binding site (I46, Val104, Leu106, Val123), with sparse long-range effects involving mostly L132 and I150 (**Figures 5.5 and 5.6**). The CSPs for both inhibitors follow linear trajectories along the open-to-closed conformational equilibrium of the kinase, with the exception of a few resonances for the balanol-bound complex. To quantify the structural transitions of PKA-C/inhibitor complexes, we analyzed the coordinated behavior of the chemical shifts along the open-to-closed conformational transition using apo, ADP-bound, ATPγN/PLN$_{1\text{-}19}$-bound and ATPγN/PKI$_{5\text{-}24}$-bound as reference states [125]. We found that on average the probability density of the fingerprint resonances for both balanol- and H89-bound complexes shifts toward an intermediate or nucleotide-bound state (**Figure 5.7**). This behavior is similar for both amide and methyl side chain resonances, indicating that the two lobes of the enzyme are close together upon binding these inhibitors in agreement with the X-ray structures [231, 250, 251]. To dissect the allosteric intramolecular network of communication, we performed covariance analysis on the CSPs [104]. Indeed, we noticed dramatic differences in the coordinated chemical shift changes of both amide and methyl resonances between nucleotide and inhibitors that report on the open-to-closed transition of the kinase. In fact, ATPγN binding causes globally coordinated changes of chemical shifts, with highly correlated residues across the N- and C- lobes (**Figures 5.8 and 5.9**). Specifically, the chemical shifts of the resonances associated with the αA (residues 17-30), αA-β1 linker (residues 31-41), β4 and β5 (residues 107-112, 117-119), activation loop (residues 190-96), APE motif (residues 206-210), αE helix

(residues 142, 147-152), and the C-terminal tail (residues 314, 318, 322, 323, 331, 332, 337, 348-350) show highly correlated changes (coefficients $|r_{ij}| > 0.98$). Interestingly, several correlations can also be observed between the N-lobe and the substrate binding cleft (activation loop, P+1, and APE) with both the αF and αG helices. The correlations found for the αG helix are especially important, as this motif constitutes a docking site for many substrates and regulatory subunits. The extent of the network of correlated chemical shifts observed for the ATPγN-bound kinase is largely underestimated, since several residues in the Gly-rich, αC helix, activation loop *etc.* are broadened beyond detection and cannot be monitored. A similar scenario is found for the methyl groups resonances in the ATPγN-bound, where extensive correlations cross the core of the enzyme, involving the αC helix, activation loop, peptide-positioning loop, C-terminal tail, αE, αF, αG, and αH helices (**Figures 5.8C-D, 5.12**). However, the methyl groups of the ATPγN-bound kinase are less affected by exchange broadening. The correlations found for the αF helix support the structural role of this element in anchoring the hydrophobic spines to the large lobe, constituting a signaling conduit that couples the two lobes structurally [23]. Overall, we observe a remarkable number of correlations between the N- lobe and the activation loop, suggesting cross talk between the ATP binding pocket and the activation loop of the kinase, an allosteric communication recently identified for Src kinase as well [252]. In contrast, the number and the extent of the correlations are much lower in the inhibitor-bound complexes (**Figures 5.8, 5.10-5.11**). Although the activation loop in the balanol-bound complex preserves most of its correlations with the αA helix, αA-β1 loop, and αE helix, these correlations are no longer present in the H89-bound complex (**Figure 5.15**). Analogously, in the inhibitor-bound complexes both the extent and the number of correlations for the methyl-bearing side chains from the ATP-binding pocket to the peripheral regions of the kinase are dramatically attenuated, with H89 displaying the least number of correlations (**Figures 5.8C-D, 5.13-5.14**). These coordinated changes in the CSPs caused by the nucleotide binding between the hydrophobic core of the enzyme and peripheral catalytic motifs of the kinase emphasize the central role that both the C- and R- spines, and their neighboring residues[244], have in reaching a catalytically committed state with higher binding affinity for the substrate. While binding either ATP-competitive inhibitor disrupts this allosteric network, they do so

in different manner, with balanol having more persisting allosteric communication between the two lobes.

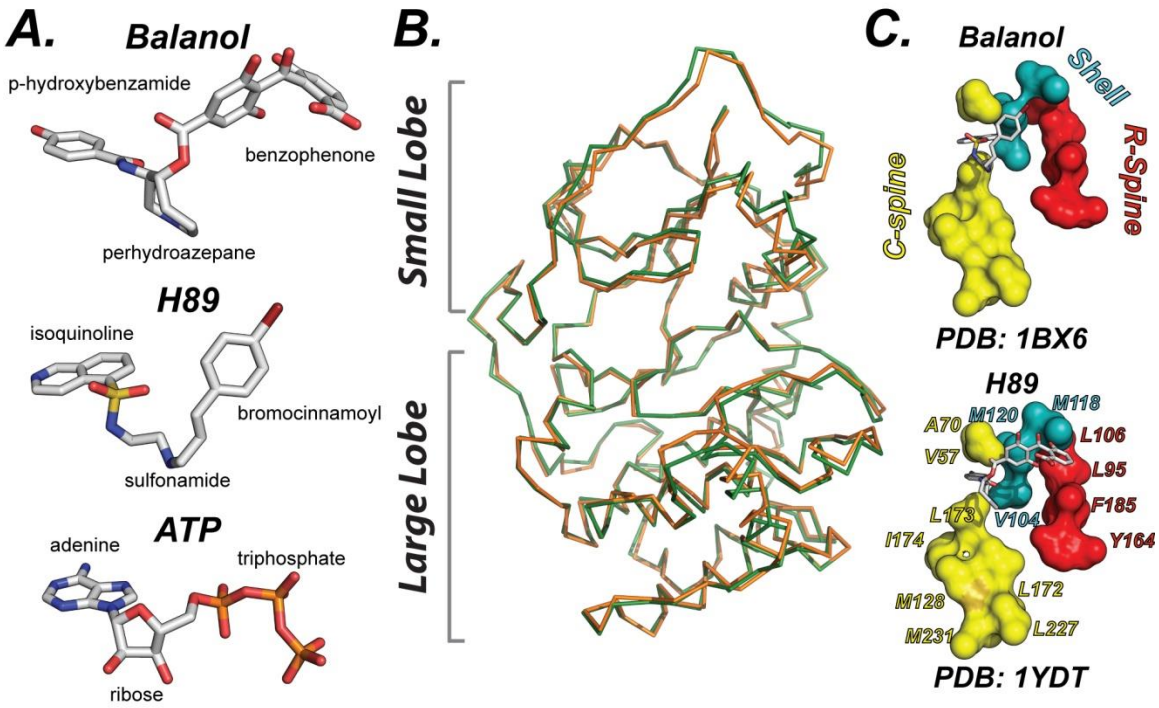

Figure 5.2. X-ray structure of PKA-C with ATP-competitive inhibitors.
A. Chemical structures of balanol, H89, and ATP. The *p*-hydroxybenzamide group in balanol (or isoquinoline ring in H89) mimics the adenine moiety of ATP, the perhydroazepane ring in balanol (or sulfonamide in H89) occupies the ribose subsite, while the benzophenone group in balanol (or bromocinnamoyl group in H89) takes the place of the triphosphate of ATP. B. Overlay of the crystal structures of PKA-C when bound to balanol (green, PDB: 1BX6) or H89 and PKI_{5-24} (orange, PDB:1YDT) with an RMSD < 0.7 Å. C. Architecture of the hydrophobic core of PKA-C is identical when bound to balanol or H89: the C- and R- spines are rendered in yellow and red, respectively, the shell residues are reported in teal.

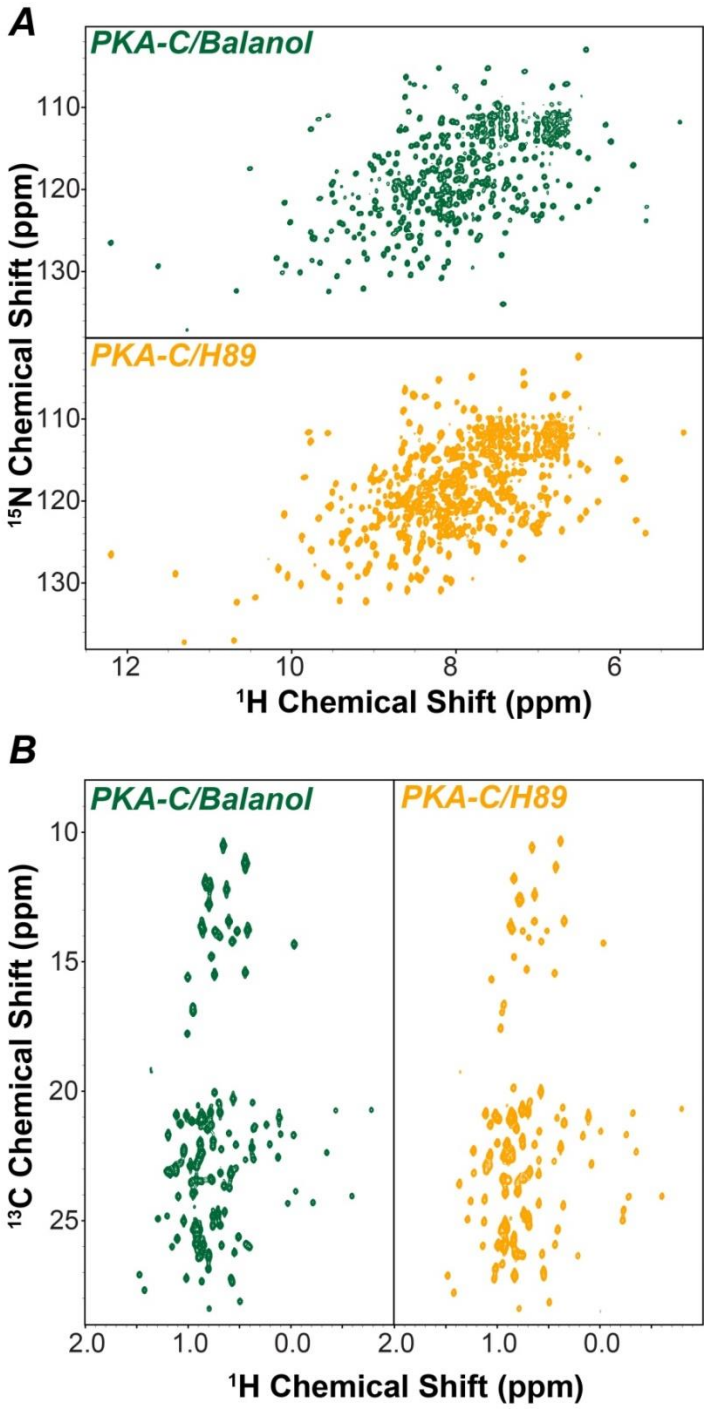

Figure 5.3. Backbone and methyl side chain fingerprints of the inhibited kinase.
(A) [^{1}H,^{15}N]-TROSY-HSQC spectrum of the amide fingerprints of PKA-C bound to balanol (green) or H89 (gold). (B) [^{1}H,^{13}C]-TROSY-HMQC spectra showing of the corresponding methyl fingerprint of the Ile, Leu, and Val residues.

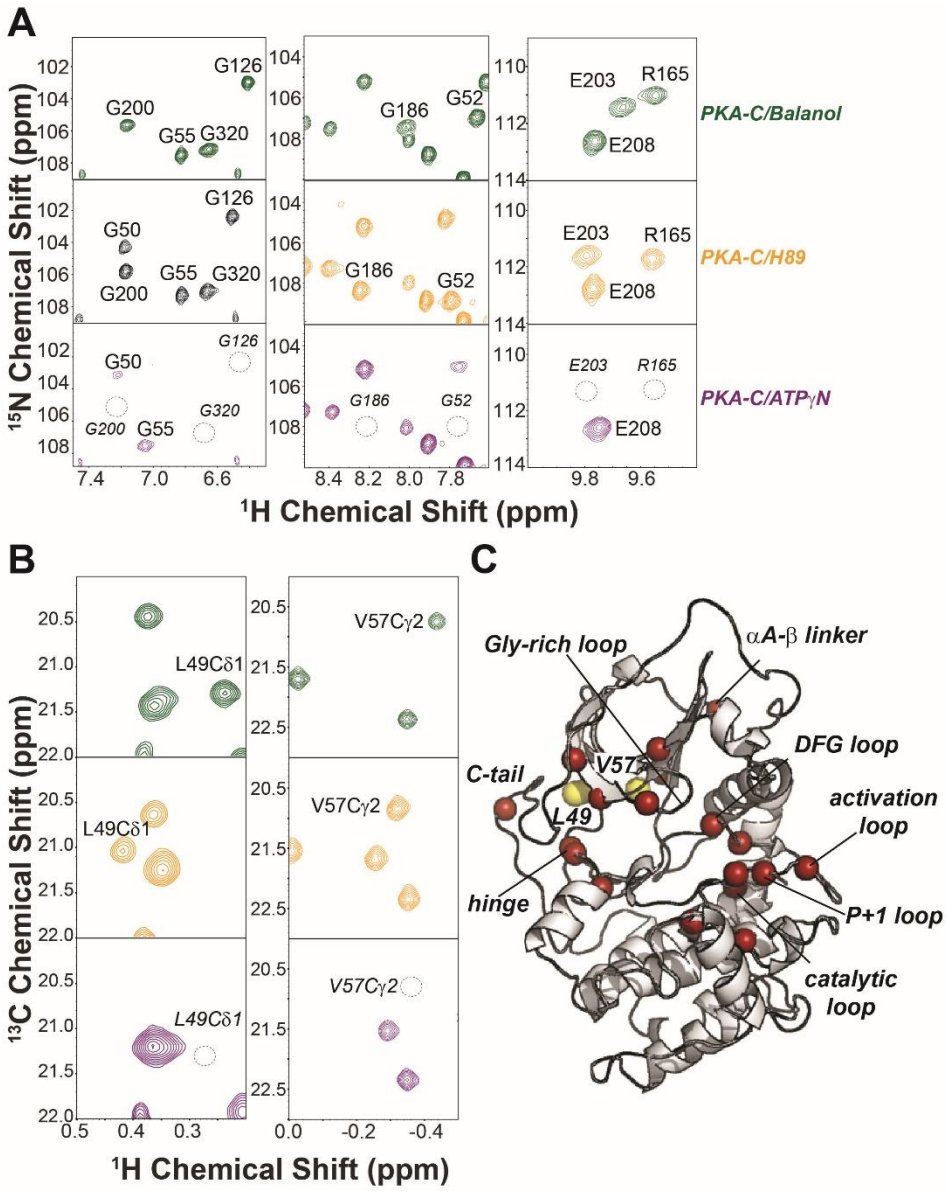

Figure 5.4. Inhibitor bound complexes do not adopt a dynamically committed state.
(A) Portions of the [^{1}H,^{15}N] TROSY-HSQC spectra showing the line broadening of several amide groups in the PKA-C/ATPγN complex (bottom) and corresponding narrow resonances in the balanol (top) and H89 (middle) complexes. (B) Corresponding portions of the [^{1}H,^{13}C] TROSY-HMQC spectra showing the methyl resonance fingerprints. As for the amide, several methyl resonances broaden out in the PKA-C/ATPγN, but they are sharp for inhibitor bound complexes. (C) Mapping of the exchange broadened residues in the 1ATP structures. All of these residues become sharper in the inhibitor bound complex and include the αA-β linker, Gly-rich loop, hinge, catalytic loop, DFG loop, activation loop, P+1 loop, and C-terminal tail.

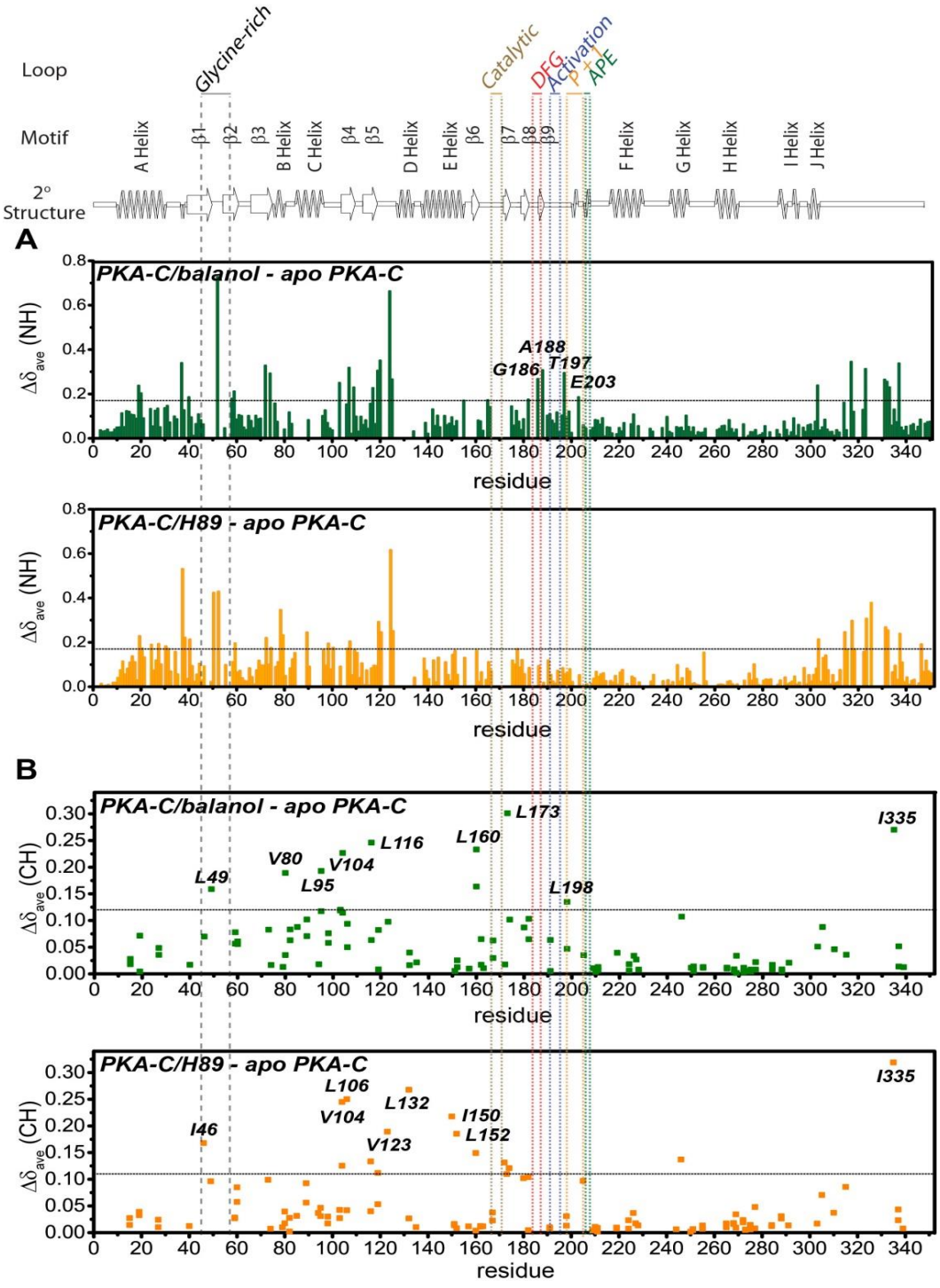

Figure 5.5. Chemical shift perturbations of of PKA-C upon binding balanol and H89.
Combined CSPs for (A) amide backbone and (B) methyl side chain resonances of PKA-C versus residue upon binding of balanol (green) or H89 (orange). The dashed line represents one standard deviation from the mean CSP.

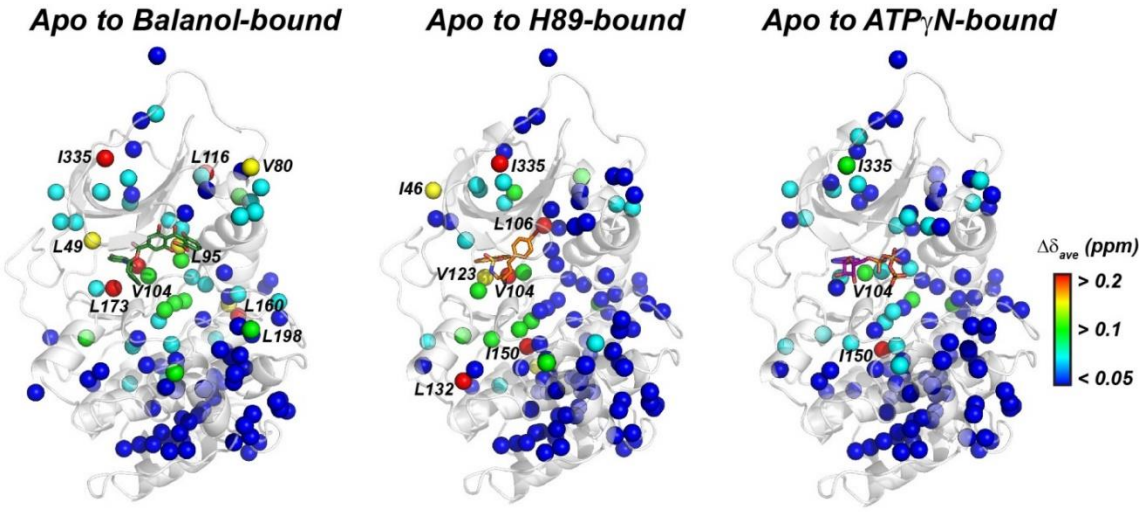

Figure 5.6. Mapping of the $^{1}H/^{13}C$ combined CSPs of the balanol, H89, and ATPγN states.

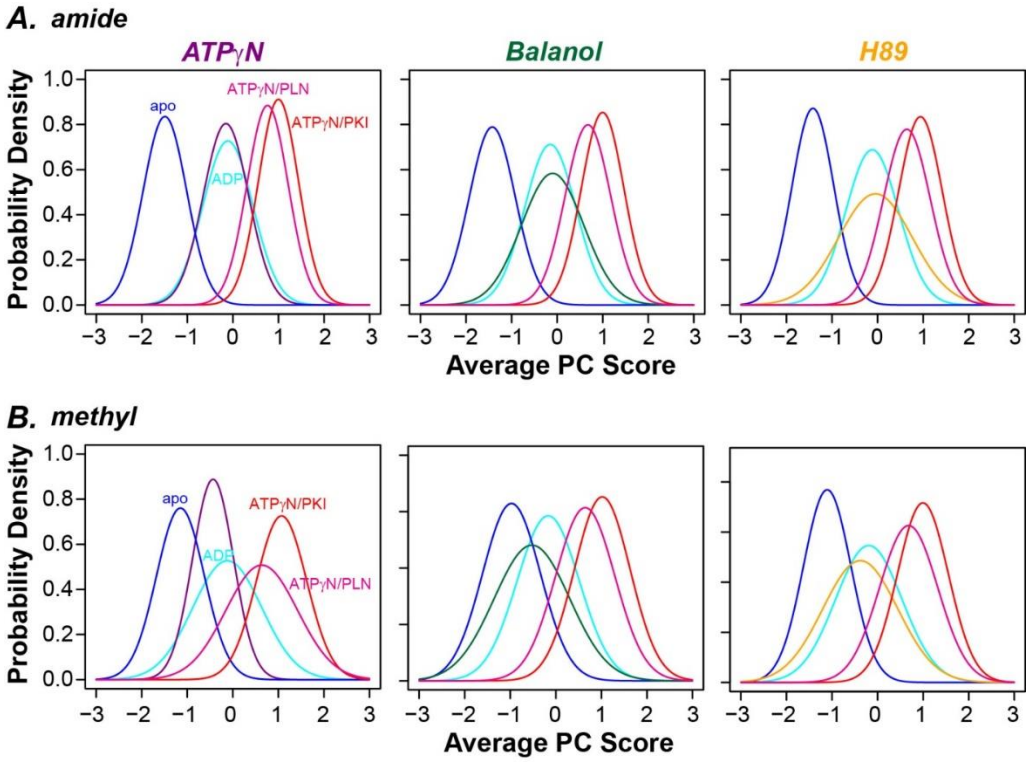

Figure 5.7. Probability densities of Inhibited states along the open to closed equilibrium.
Comparison of the probability distributions for the different states of PKA-C analyzed with CONCISE using the chemical shifts of (A) amide backbone and (B) methyl side chains. The reference states used in all of these analyses are apo (blue), ADP-bound (cyan), ATPγN/PLN-bound (magenta) and ATPγN/PKI_{5-24} bound (red).

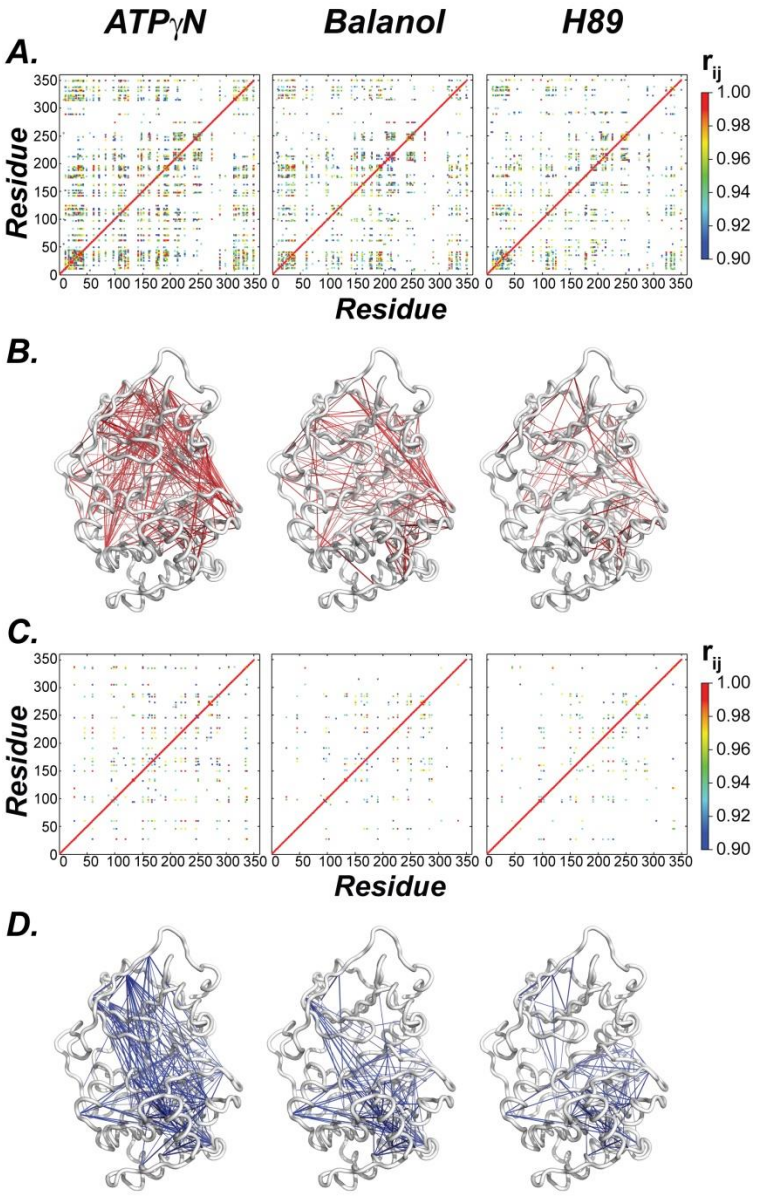

Figure 5.8. Allosteric network of communication as mapped by the chemical shift covariance analysis (CHESCA).

(A) CHESCA maps for the amide residues upon binding ATPγN, balanol, and H89. The different colors indicate the extent of correlations. (B) Allosteric network of the correlations among amide groups mapped onto the X-ray structure of PKA-C using the Xpyder utility [253]. Only correlations with r_{ij} > 0.98 are mapped for clarity. (C) CHESCA maps for the methyl groups of ILV side chains. (D) Allosteric correlations among methyl groups mapped onto the X-ray structures of the kinase. Only correlations with r_{ij} > 0.90 are indicated. The ATPγN-bound complex has the highest degree of correlation involving residues between the two lobes. The number and extent of correlation were lower in the inhibitor-bound complexes, with H89 showing the least number of correlations.

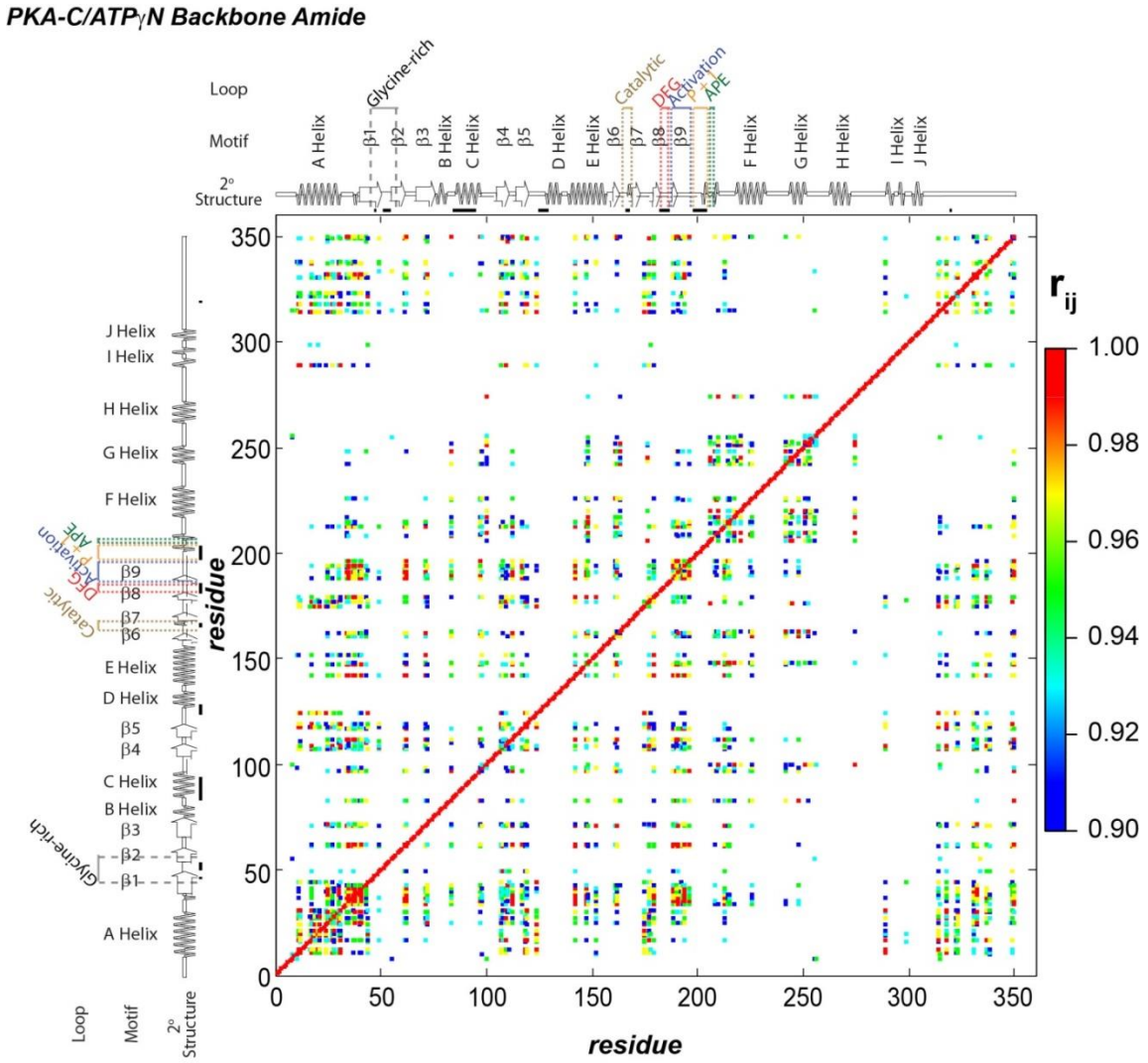

Figure 5.9. Correlated backbone chemical shift changes upon ATPγN binding.
CHESCA correlation matrix for the backbone amide resonances for the PKA-C/ATPγN complex (see also Figure 5.2). The backbone residues that were exchange-broadened (gly-rich, C-helix, DFG, P+1 loop, etc.) are indicated by black lines in the secondary structure plot.

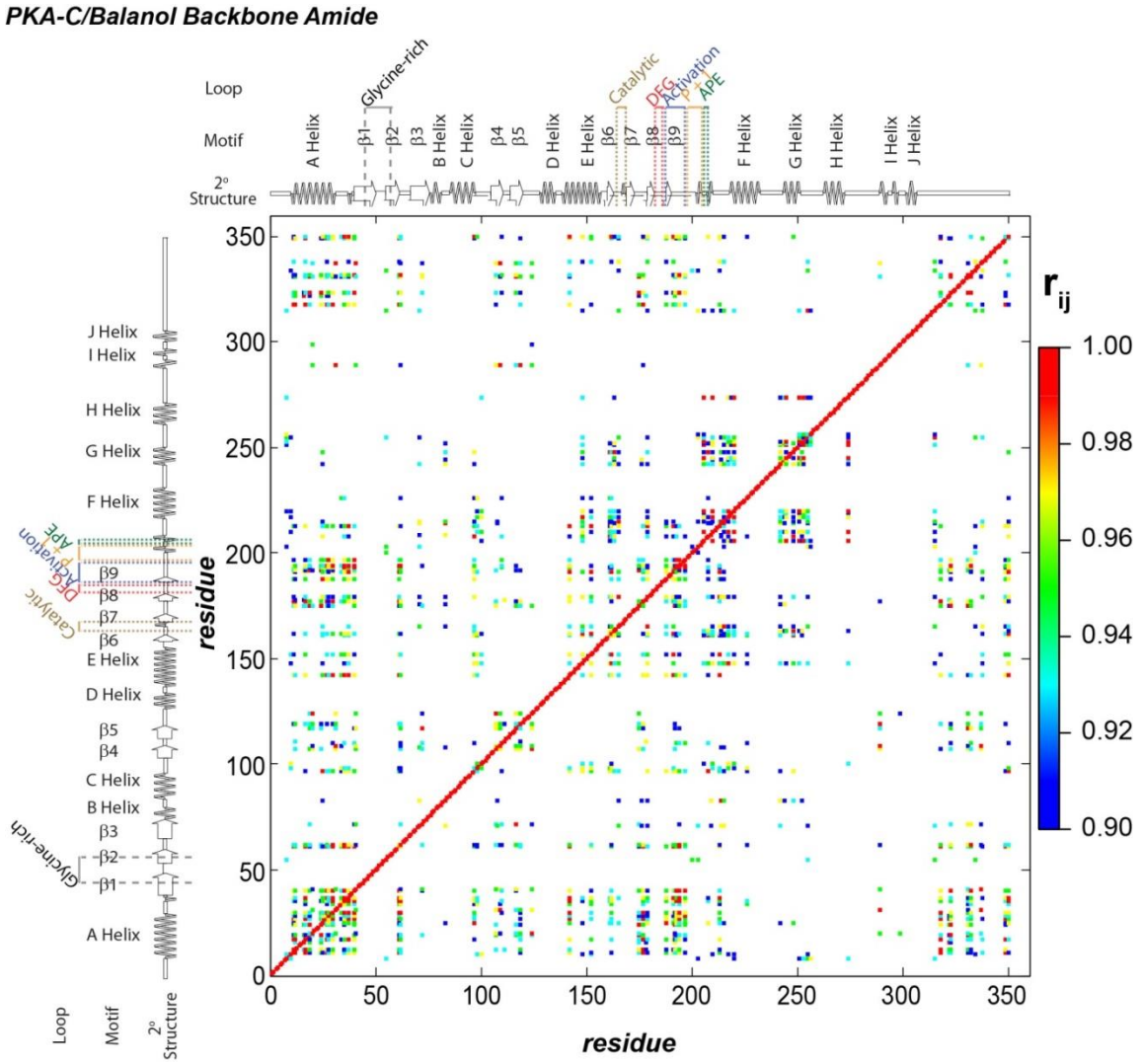

Figure 5.10. Correlated backbone chemical shift changes upon balanol binding.
CHESCA correlation matrix for the backbone amide resonances of the PKA-C/balanol complex (see also Figure 5.8).

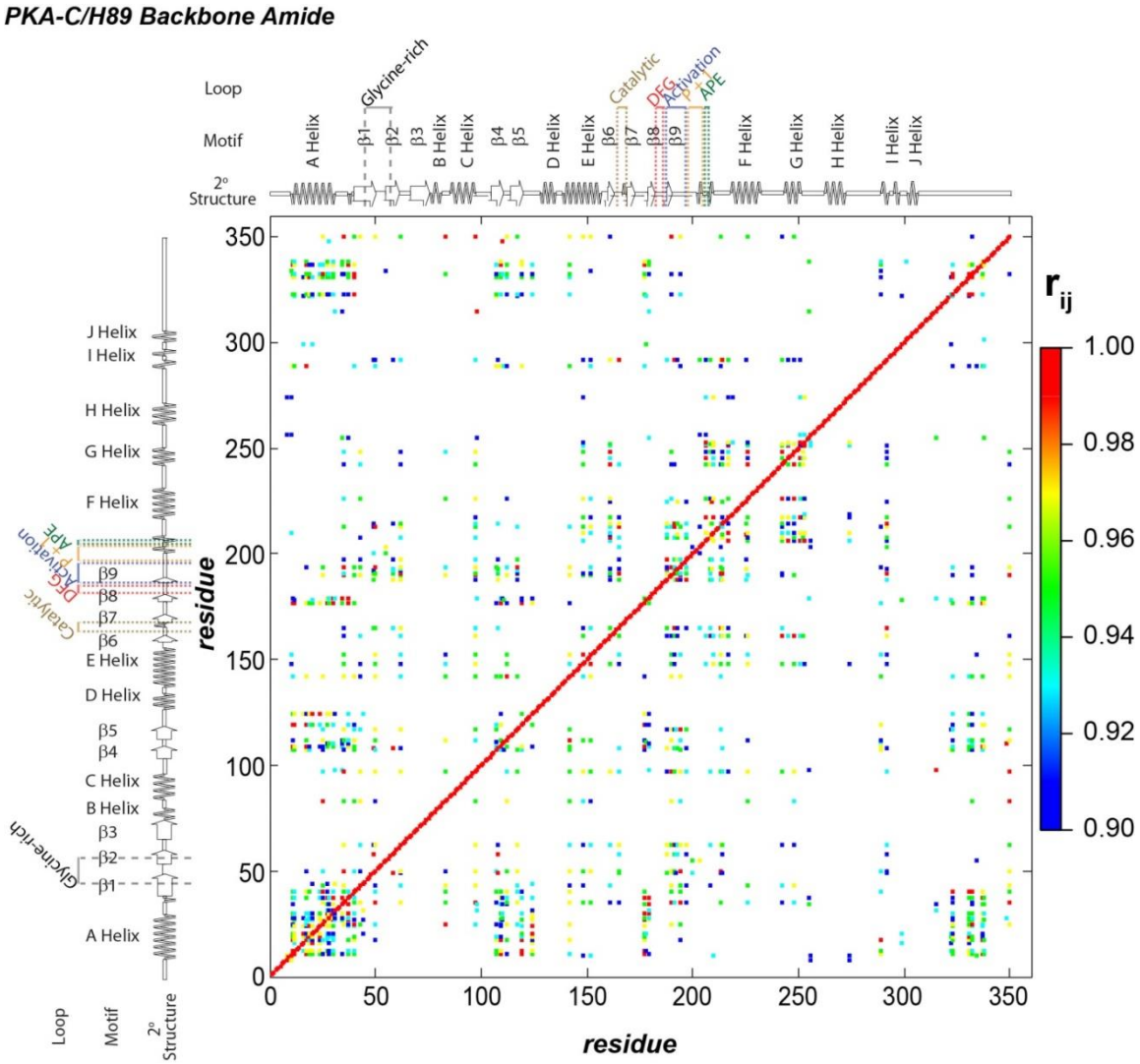

Figure 5.11. Correlated backbone chemical shift changes upon H89 binding.
CHESCA correlation matrix for the backbone amide resonances for the PKA-C/H89 complex (see also Figure 5.8).

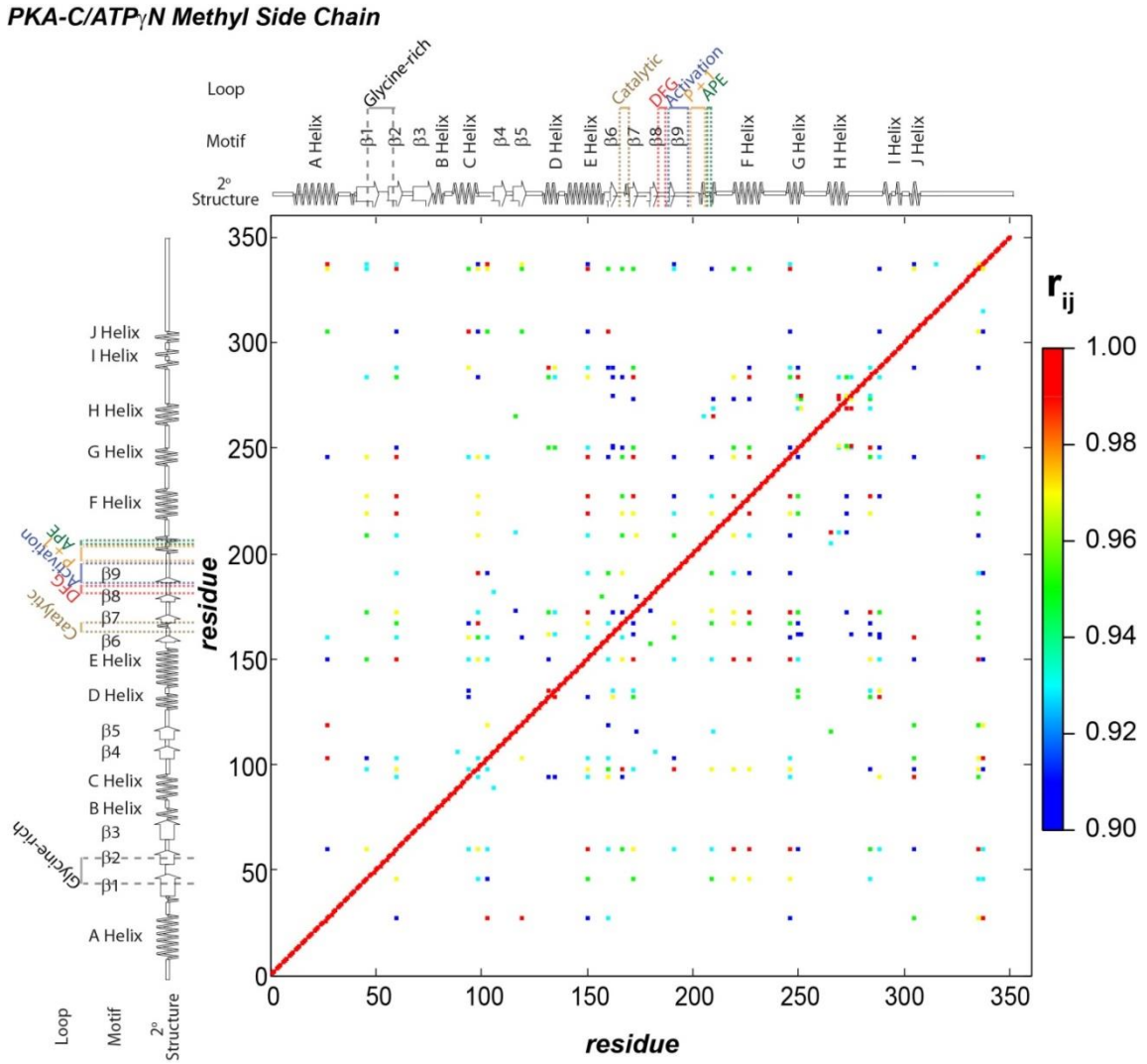

Figure 5.12. Correlated methyl side-chain chemical shift changes upon ATPγN binding.
CHESCA correlation matrix for the methyl side chain resonances for the PKA-C/ATPγN (see also Figure 5.2).

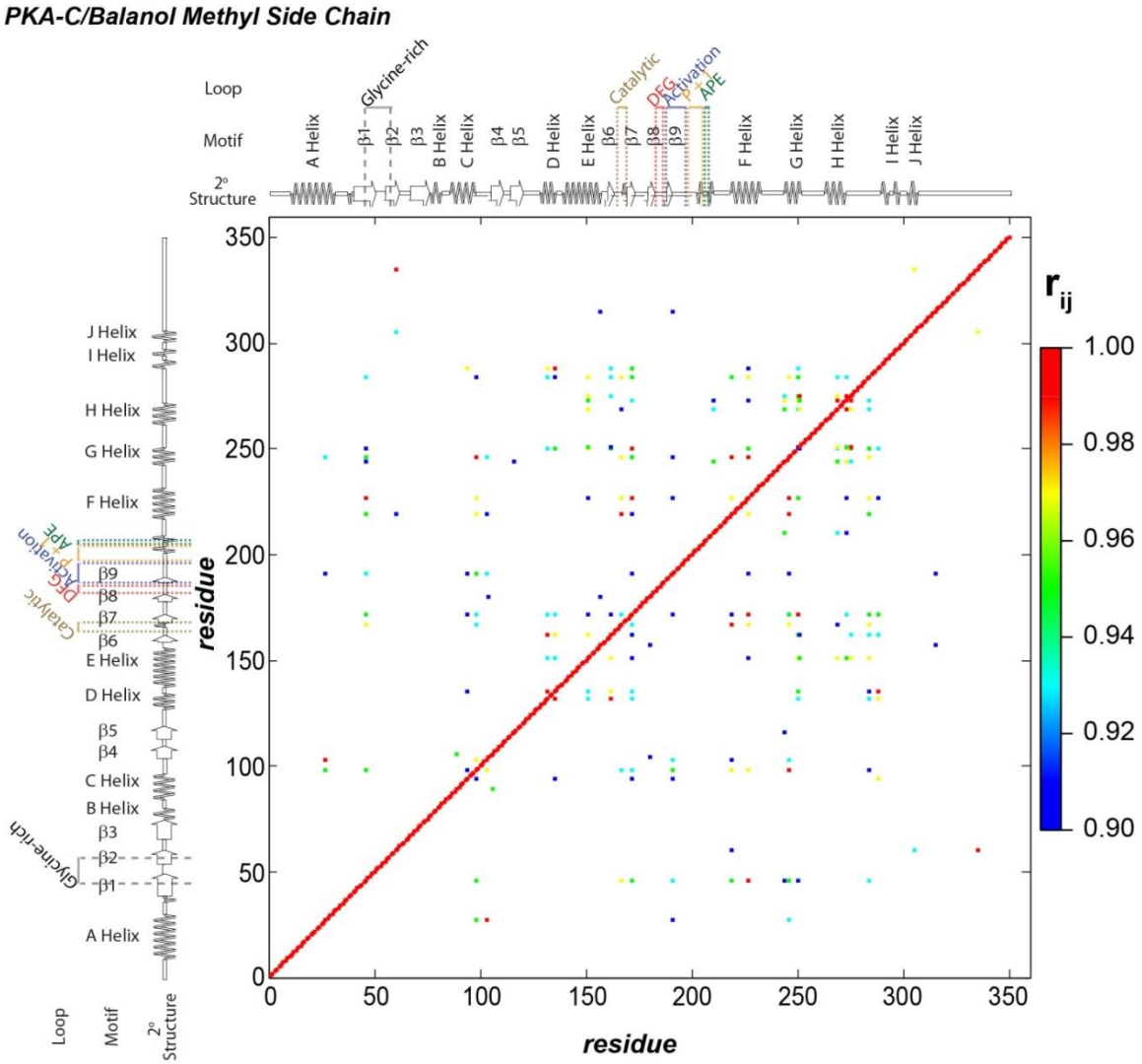

Figure 5.13. Correlated methyl side-chain chemical shift changes upon balanol binding.
CHESCA correlation matrix for the methyl side chain resonances for the PKA-C/balanol complex (see also Figure 5.2).

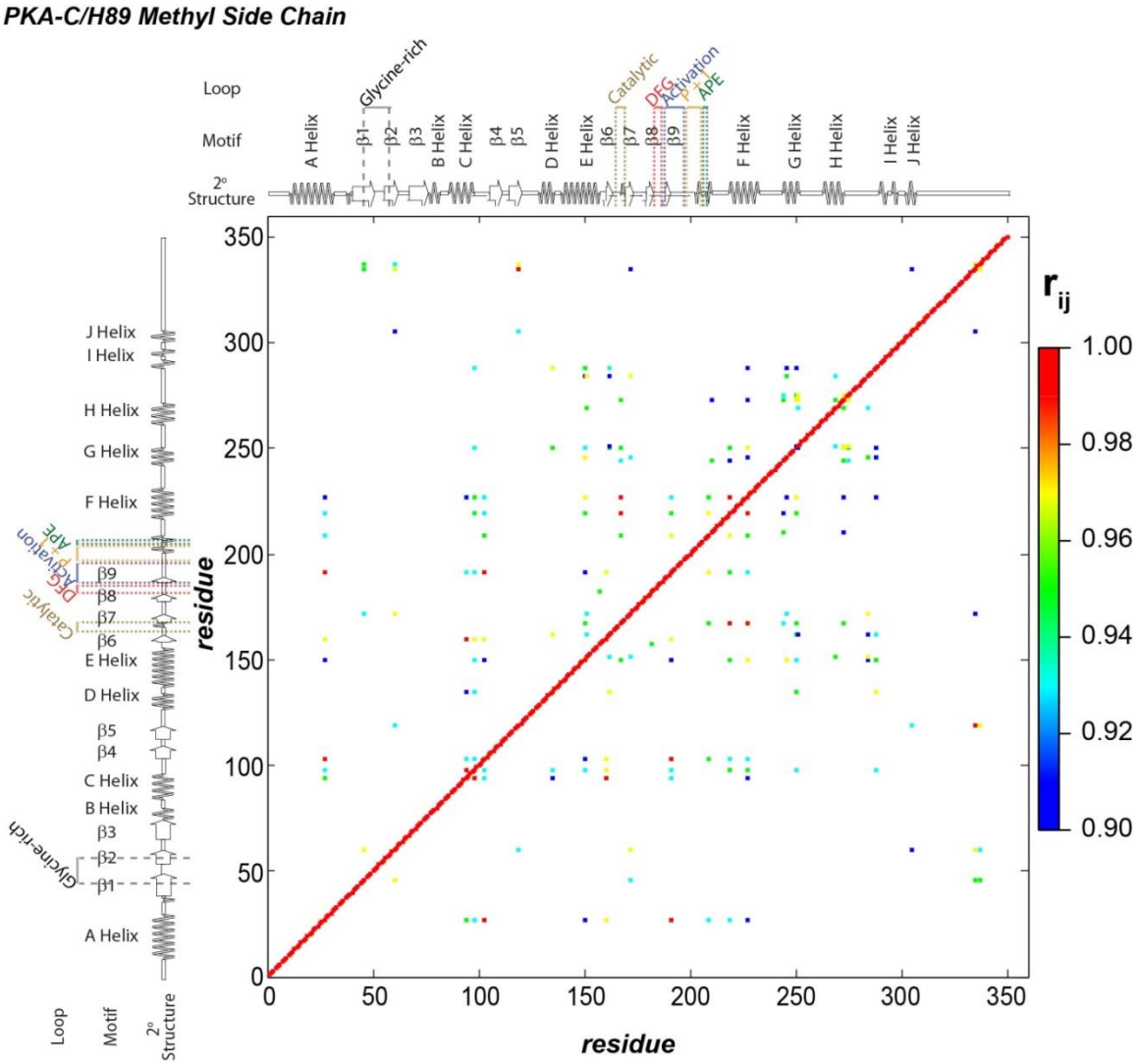

Figure 5.14. Correlated methyl side-chain chemical shift changes upon H89 binding.
CHESCA correlation matrix for the methyl side chain resonances of PKA-C/H89 complex (see also Figure 5.2).

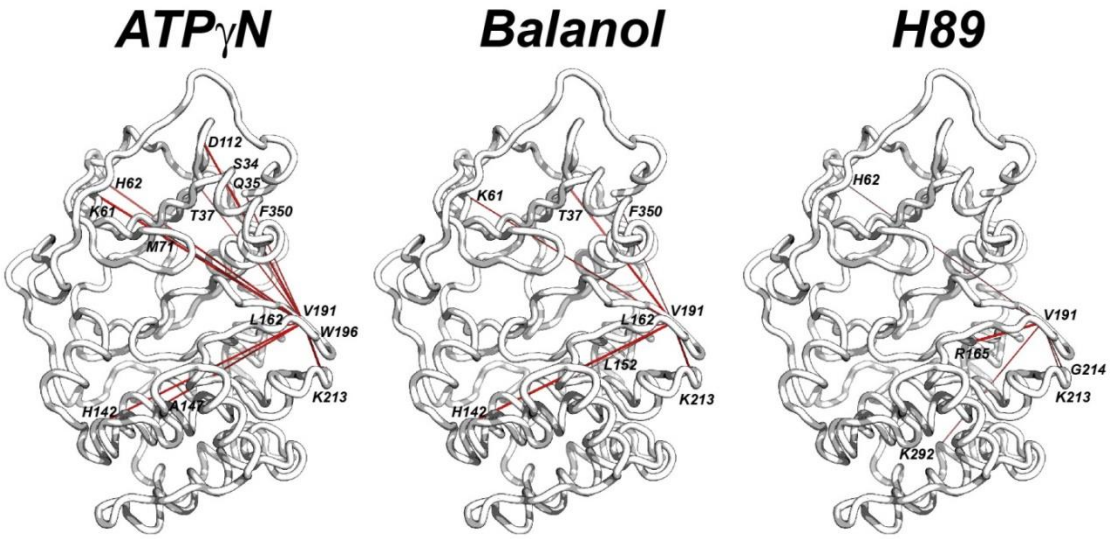

Figure 5.15. Allosteric communications between V191 and other residues in three different states. The number of correlations (r_{ij} > 0.98) between the amide resonance of V191 and the other residues of the protein decreases from ATPγN-bound to balanol-bound to H89-bound.

ATPγN, balanol and H89 differentially alter the microsecond-millisecond timescale dynamics of the kinase.

The coordinated CSPs suggest that changes in the conformational landscape and the dynamic state of the enzyme may lead to differences in its substrate binding cooperativity. To monitor the effects of the nucleotide and inhibitor binding on the conformational dynamics in the μs-ms timescale, responsible for changes in free energy landscape, we quantified the exchange contribution to the transverse relaxation rate (R_{ex}) using Carr-Purcell-Meiboom-Gill (CPMG) relaxation dispersion experiments [58, 254]. We found that the apo kinase is the most malleable state [40, 255], with several backbone amide residues exhibiting significant conformational exchange (**Figure 5.16A**). The most dynamic regions include the linker (residues 124-125), the αA-β1 (T37) and the αD-αE (residues 138-139) loop, β8 (residues 180-182), αD (residues 133-134), the catalytic loop (residues 165-166), and C-terminal tail (residues 314-315). Nucleotide binding further increases the μs-ms dynamics of these residues with the exception of the αD-αE loop (**Figure 5.17A**). In addition, the Gly-loop (L49, M58, L59), activation loop (W196), peptide-positioning loop (L198), portions of αF (residues 216-

221) as well as the acidic cluster (residues 331-334) displayed significant conformational exchange (i.e., high R_{ex}values). In contrast, upon binding either balanol or H89, the average μs-ms timescale conformational exchange is dramatically diminished across the entire enzyme (**Figure 5.17A**). However, there are significant differences in the dynamic behavior of PKA-C in complex with the two inhibitors. Specifically, the vast majority of the residues in the PKA-C/H89 complex show almost no conformational exchange for the amide resonances (R_{ex} ≤ 4 s^{-1}). In contrast, we found significant conformational exchange in the PKA-C/balanol complex for the Gly-rich, DFG, and activation loops, as well as the C-terminal tail (**Figure 5.17A**).

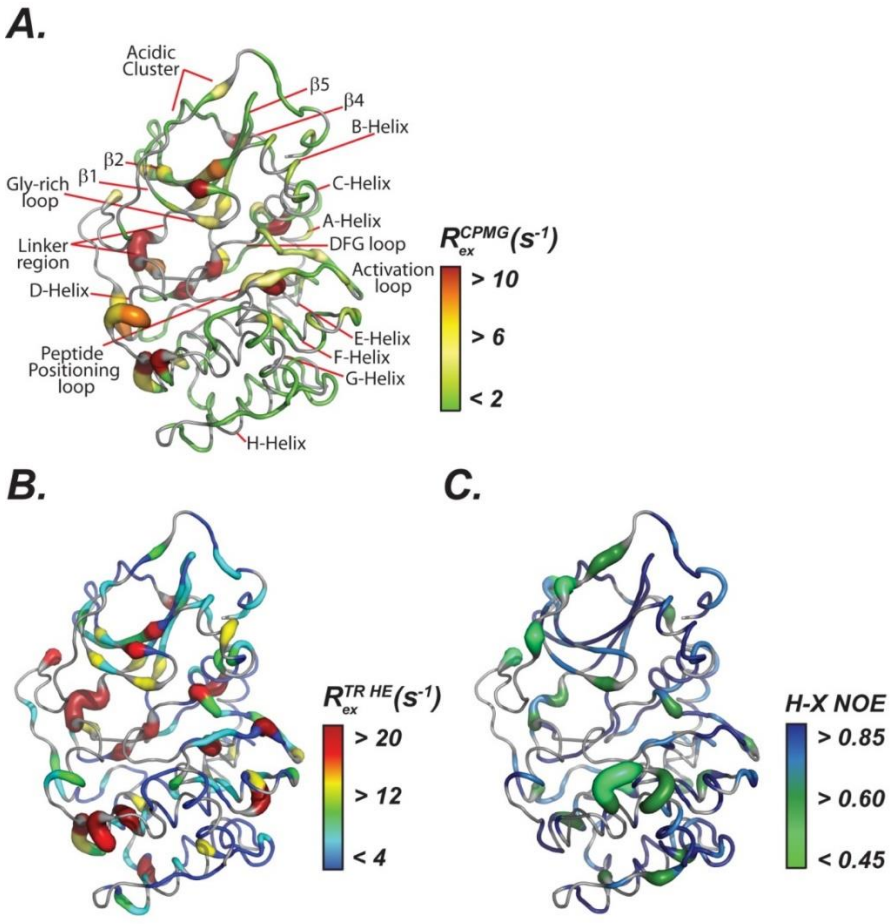

Figure 5.16. Multi-timescale conformational dynamics of apo PKA-C amide backbone.
Mapping of the (A) conformational exchange, R_{ex}^{CPMG}, measured using CPMG relaxation dispersion, (B) conformational exchange, R_{ex}^{TR-HE}, measured using TROSY Hahn-Echo experiments, and (C) HX-NOE, on the X-ray structure of PKA-C all measured on a 850 MHz spectrometer for the apo form of the kinase.

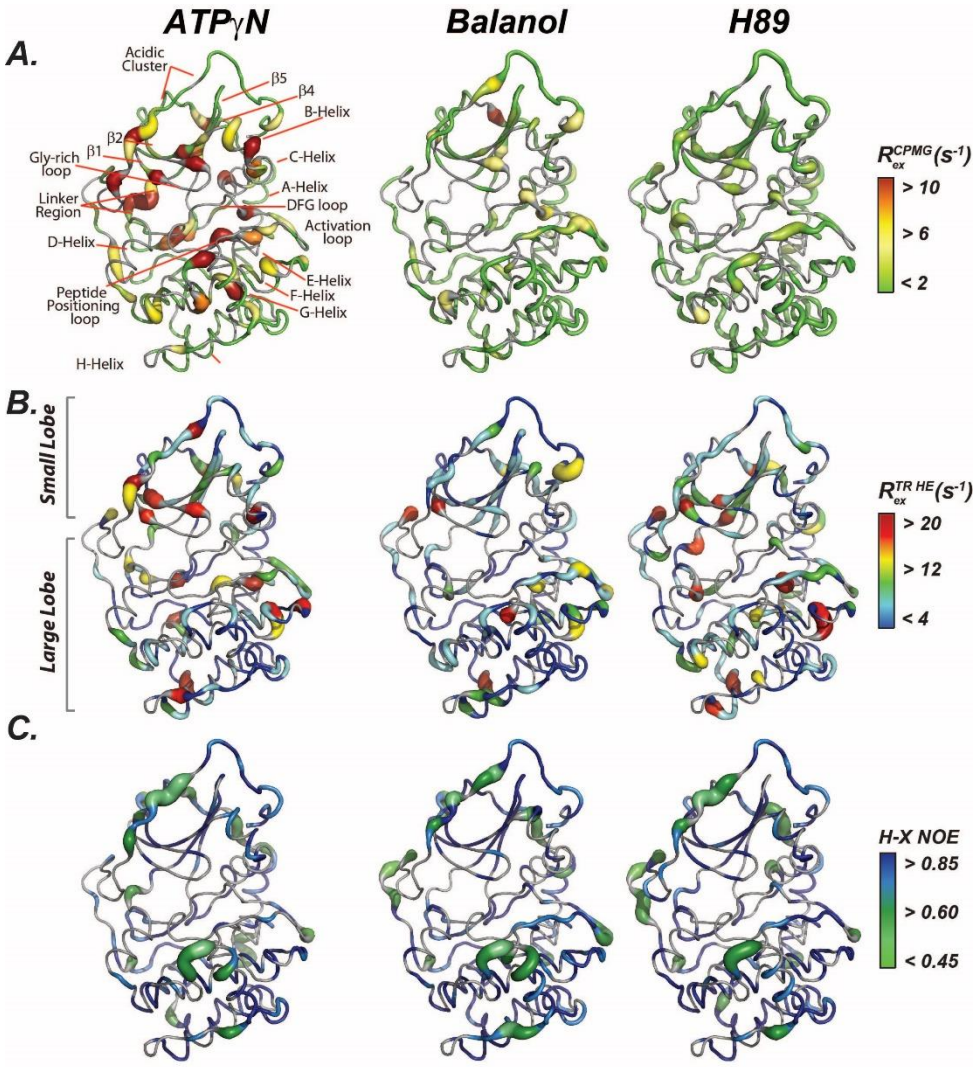

Figure 5.17. Multi-timescale conformational dynamics of PKA-C amide backbone upon binding ATP-competitive inhibitors.
(A) Mapping of the conformational exchange, R_{ex}^{CPMG}, on the X-ray structure of PKA-C measured using CPMG relaxation dispersion on a 850 MHz spectrometer for the ATPγN-bound, balanol-bound, and H89-bound forms of the kinase. (B) Corresponding mapping of the conformational exchange, R_{ex}^{TR-HE}, measured using TROSY Hahn-Echo experiments on a 850 MHz spectrometer. For comparison, the previously published data for the dynamics of ATPγN-bound state are shown[250]. (C) HX-NOE measured on a 900 MHz spectrometer of backbone amide residues as proxy for the fast timescale conformational dynamics (ps-ns).

To monitor the conformational dynamics of the highly conserved hydrophobic core, *i.e.*, the C- and R-spines, we analyzed the ^{13}C CPMG relaxation dispersion [255] of the methyl bearing side chains of Val, Ile, and Leu, with 125 total probes interspersed

throughout the enzyme. The apo PKA-C displays a wide range of conformational dynamics throughout the hydrophobic core that extend through the peripheral side chains. Binding of nucleotide dynamically activates many methyl side chain residues, particularly those lining the active site (C-spine, R-spine, shell, and allosteric hotspot (I150)). These motions are attenuated upon binding balanol and completely quenched with H89 (**Figure 5.18**). The only residues exhibiting significant R_{ex} in both inhibited complexes are located in the hydrophobic core in the ATP binding cleft (L49, V57, L95, L103, V104, L160). In general, the R_{ex} values found for the balanol-bound kinase are higher than those of the PKA-C/H89 complex. In addition to the core, the PKA-C/balanol complex displays substantial μs-ms motions for the methyl side chains located in the αB (V80), αC (I85, L89, and I94) helices, as well as in the peptide positioning loop (L198) (**Figures 5.18, 5.19, and 5.21**). Upon fitting the CPMG dispersion curves with a two-state model, we obtained the kinetic (k_{ex}) and thermodynamic (p_A) parameters of the exchange process [256]. For the ATPγN-bound kinase, several residues in the C-spine (L172, L173), R-spine (L106) and surrounding bridging residues (I150, I180, V182) fit to a single global two-state exchange process with a rate constant (k_{ex}) of 2400 ± 200 s^{-1} and a ground-state population (p_A) of 92.8 ± 0.4% **(Figures 5.19, 5.20 and Table 5.5)**. The rate and residues which undergo synchronous motions are consistent with other studies with nucleotide bound to PKA-C, suggesting these synchronous motions are critical for catalysis[255]. Meanwhile, a number of residues in the hydrophobic core and αB and αC helices of the balanol-bound kinase also fit into a global two-state exchange process, but in a much slower exchange regime (k_{ex} = 90 ± 50 s^{-1} and p_A = 90.9 ± 3.9%, **Figure 5.19** and **Table 5.6**). In contrast, we were unable to perform group fitting for the H89-bound complex due to the limited number of side chains showing R_{ex} > 2 s^{-1} and the relatively low k_{ex} values obtained from the fit of individual residues. Moreover, a k_{ex} < 200 s^{-1} obtained from the CPMG experiments suggests that the ground state of the kinase is in slow conformational exchange with its conformationally excited state. Therefore, to better characterize these slow chemical exchange process, we used ^{13}C CEST experiments on methyl group resonances, which are able to detect states exchanging in the range of 20-200 s^{-1} [56, 257]. For the apo kinase, we found that three residues in the conserved hydrophobic core, L95, V104 and I150, exhibit slowly-exchanging excited states with significant chemical shift difference (Δω) from the ground

state (**Figure 5.22A**). The exchange kinetics (k_{ex}), population (p_A), and chemical shift difference ($\Delta\omega$) obtained from CEST are in close agreement with those obtained from fitting the CPMG dispersion curves [244]. Remarkably, binding of either ATPγN or ATP-competitive inhibitor suppresses the excited state of L95 (broadened upon ATPγN binding), V104, and I150 (peak overlapped in the balanol complex), which are positioned in the hydrophobic core of the kinase. Their motions become coordinated and move at a faster timescale for ATPγN-bound complex. Furthermore, both nucleotide and inhibitors generate new slowly-exchanging excited states with significant $\Delta\omega$ for selected residues. Remarkably, both the ATPγN-bound and balanol-bound kinase displays new slowly-exchanging excited states for V80 and I85 (**Figure 5.22B**) with comparable chemical shift difference values ($\Delta\omega$) that are outside the trajectories delineating the open-to-closed conformational equilibrium (**Figure 5.23**). This demonstrates that balanol preserves similar slow millisecond dynamics of the αB-helix residues (V80 and I85) exhibited by ATPγN-bound kinase. In addition, L173 also exhibits slower exchange kinetics in the balanol-bound kinase (faster in the corresponding nucleotide-bound kinase, **Figure 5.22B**). L173 is located in the C-spine and is buried in the core of the enzyme, interacting with the adenine ring in the 1ATP structure and with the hydroxybenzamide moiety in the 1BX6 structure [231]. Two residues, L49 and L172, also show alternate states for the H89-bound kinase (**Figure 5.23**), with L172 being an integral part of the C-spine. Fitting the CEST profiles obtained for the inhibited kinases into a two-site exchange equation, we found that residues in the PKA-C/balanol complex interconvert with a k_{ex} spanning from 40 to 200 s^{-1} (**Table 5.7**), while slower exchange kinetics were found for the PKA-C/H89 complex (k_{ex} = 40-50 s^{-1}, **Table 5.7**). The differential suppression of μs-ms timescale dynamics, the formation of new alternate conformations, and the difference in exchange kinetics suggest that these ATP-competitive inhibitors exert different effects on the enzyme's populations. These molecules shift the enzyme to conformational states that are poised (committed) for substrate binding (as manifested by positive cooperativity) in the case of balanol, and less poised for substrate binding in the case of H89.

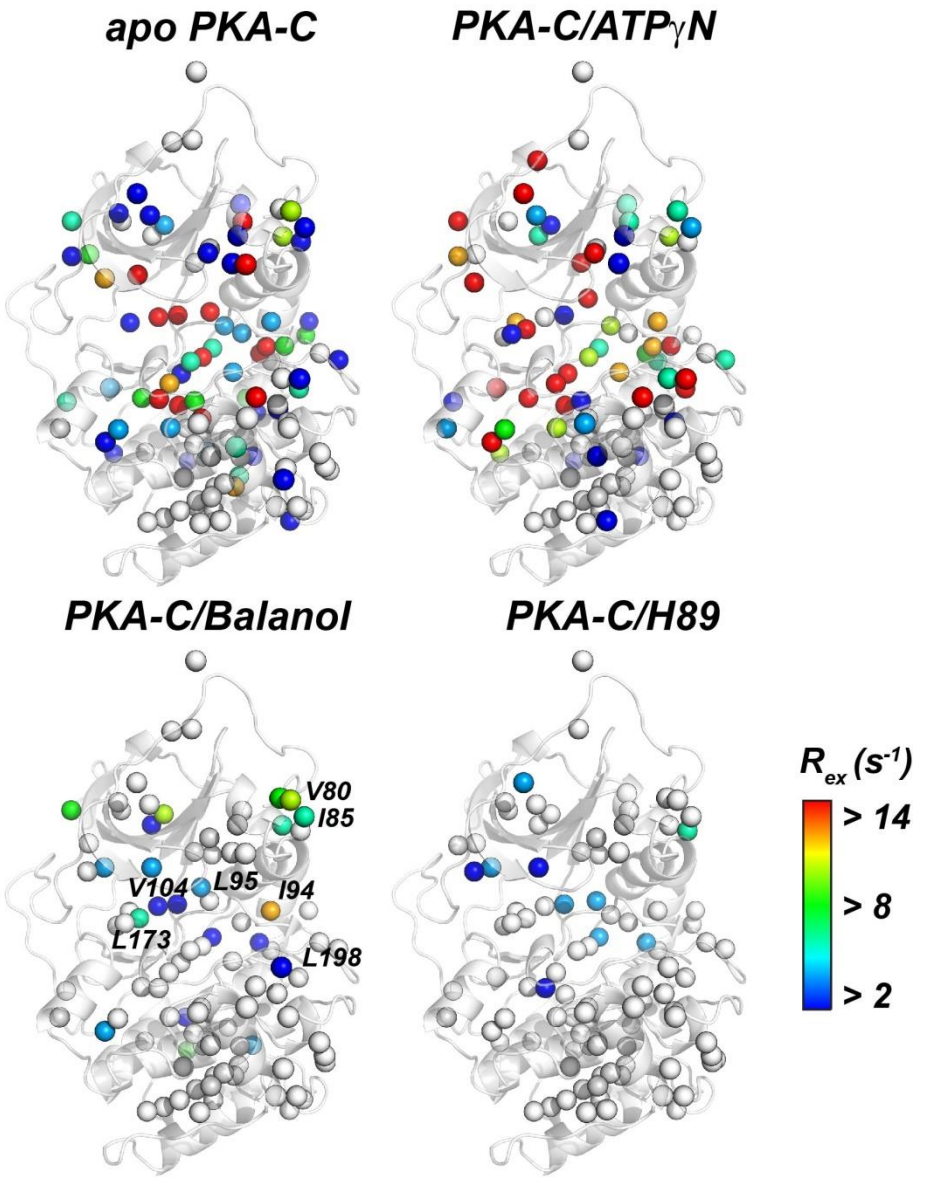

Figure 5.18. Slow conformational dynamics of the hydrophobic core measured by CPMG experiments.
Mapping of the R_{ex} of the methyl groups from ILV measured by ^{13}C SQ CPMG relaxation dispersion for the PKA-C/ATPγN, PKA-C/Balanol, and PKA-C/H89 complexes. The spheres are color-coded according to the spectrum bar on the right. White spheres denote side chains that did not exhibit chemical exchange. For comparison the previously published data for the apo form are shown [244]. All data were measured at 850 MHz spectrometer and 27°C.

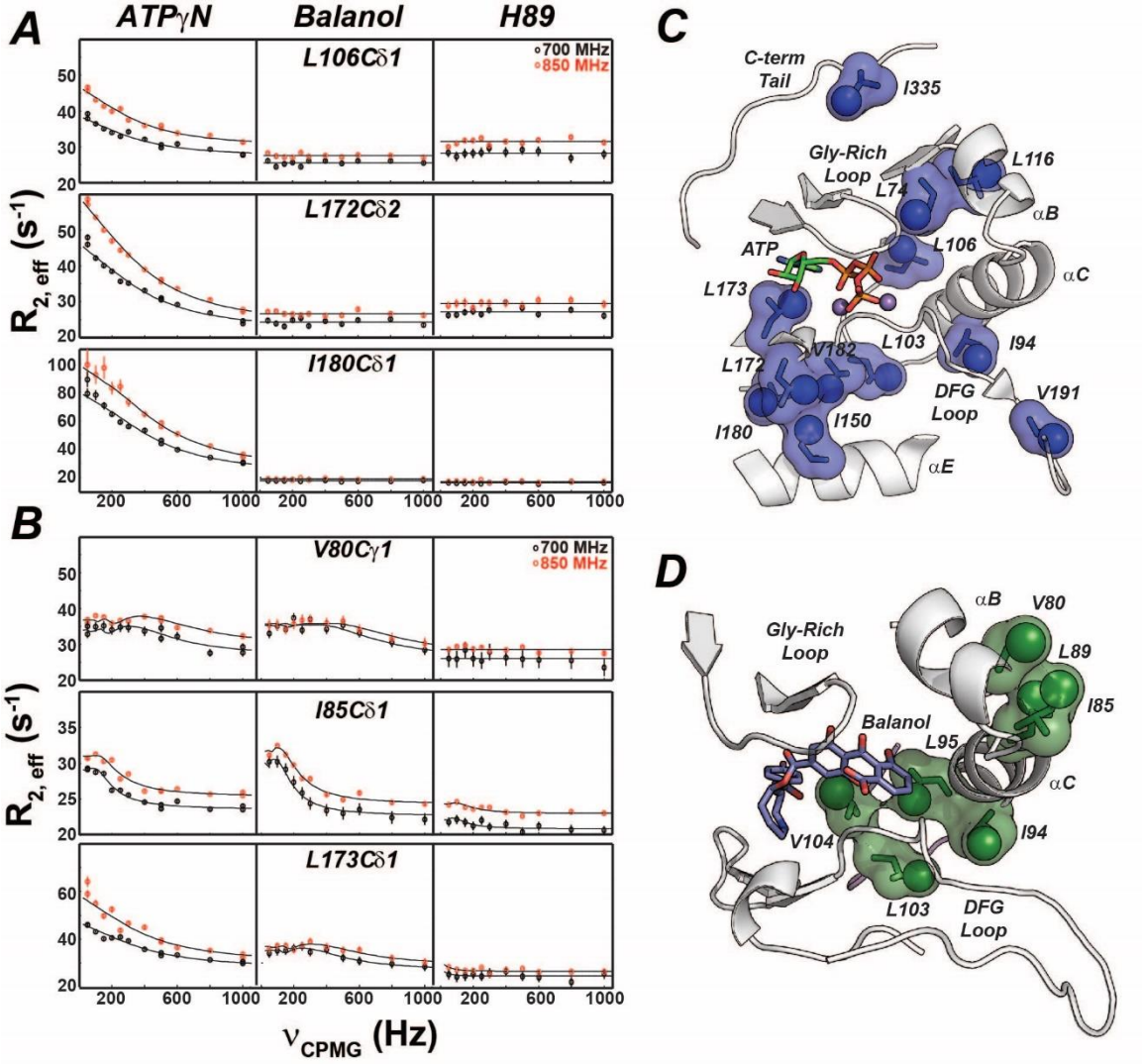

Figure 5.19. Dynamic response of the core residues of PKA-C upon binding ATPγN or ATP-competitive inhibitors.

(A) Relaxation dispersion curves of the methyl side chain groups measured on a 700 MHz (black) and 850 MHz (red) spectrometer, showing significant exchange in the PKA-C/ATPγN complex and no exchange in the inhibitor-bound complexes. (B) Relaxation dispersion curves of the methyl side chain groups (same as in A) that show significant exchange in both PKA-C/ATPγN and PKA-C/balanol complexes, but no exchange in PKA-C/H89. Duplicate measurements were carried out at ν_{CPMG}values of 50, 500 and 1000 Hz. Errors were propagated and reported as error bars. The methyl groups of PKA-C/ATPγN (C) and PKA-C/balanol (D) fitting a two-state exchange process are mapped into their respective structures.

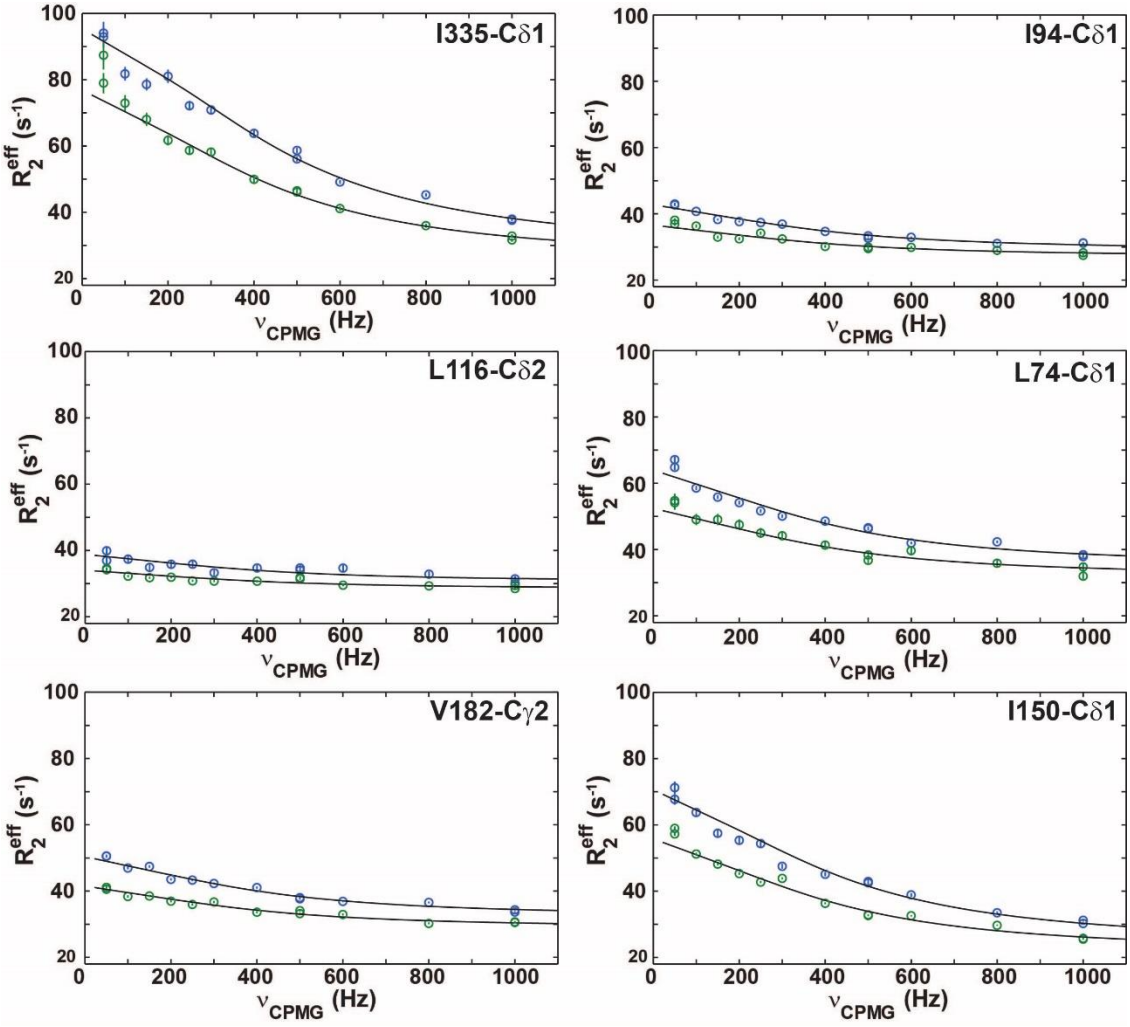

Figure 5.20. ^{13}C Dispersion curves of PKA-C bound to ATPγN under high Mg^{2+} conditions.
Dispersion curves (R_{ex} > 2 s^{-1}) for the PKA-C/ATPγN complex as measured using ^{13}C SQ CPMG relaxation dispersion at 850 (blue) and 700 MHz (green). The curves are fitted using the GUARDD[258] program. Errors were propagated from duplicate measurements at ν_{CPMG} values of 50, 500, and 1000 Hz.

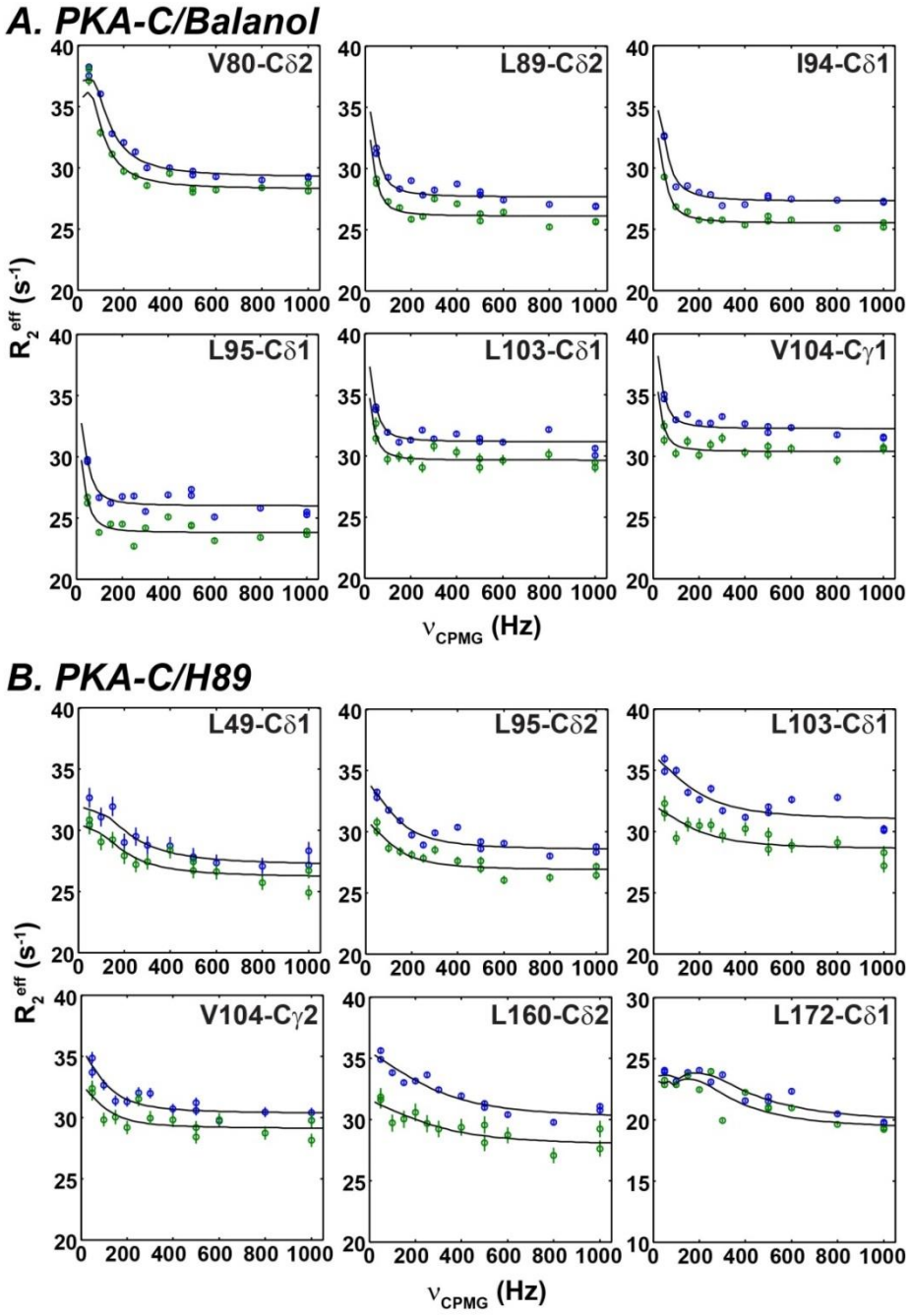

Figure 5.21. ^{13}C CPMG dispersion curves for the side chain methyl groups in PKA-C bound to ATP-competitive inhibitors.

Dispersion curves (R_{ex} > 2 s^{-1}) for the (A) PKA-C/balanol complex and (B) PKA-C/H89 complex as measured using ^{13}C SQ CPMG relaxation dispersion at 850 (blue) and 700 MHz (green). The curves are fitted using the GUARDD[258] program. Errors were propagated from duplicate measurements at ν_{CPMG} values of 50, 500 and 1000 Hz.

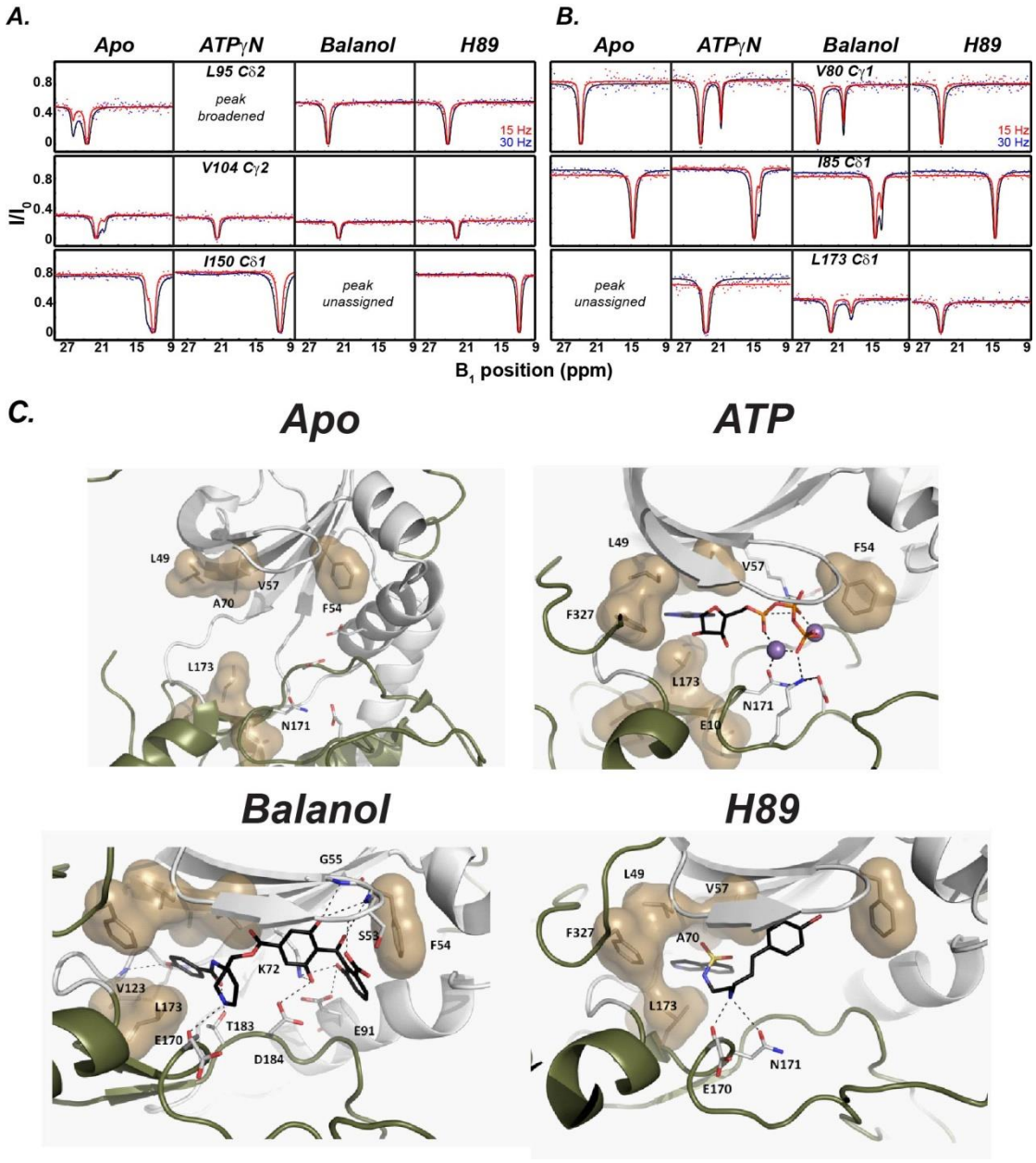

Figure 5.22. Differential suppression and formation of conformationally excited states of PKA-C upon binding of nucleotide and ATP-competitive Inhibitors.
(A) ^{13}C CEST measured on a 900 MHz spectrometer using a B_1 field of 15 MHz (red) and 30 Hz (blue). The side chain methyl groups for L95 (R-spine), V104 (shell), and I150 (allosteric hot spot) show distinct conformationally excited states in the apo form. Binding of ATPγN, balanol or H89 suppresses the conformationally excited states for these core residues. (B) Formation of new excited states for V80 and I85 (αB helix) for both ATPγN-bound and balanol-bound complex, and L173 (C-spine) for balanol-bound complex. The CEST profiles, as well as the chemical shift difference, for V80 and I85 for the ATPγN-bound and balanol-bound complexes are very similar. C. Hydrophobic and hydrogen bond interactions within the adenine and phosphate binding sites of PKA in the apo form, and when bound to ATP, balanol, and H89.

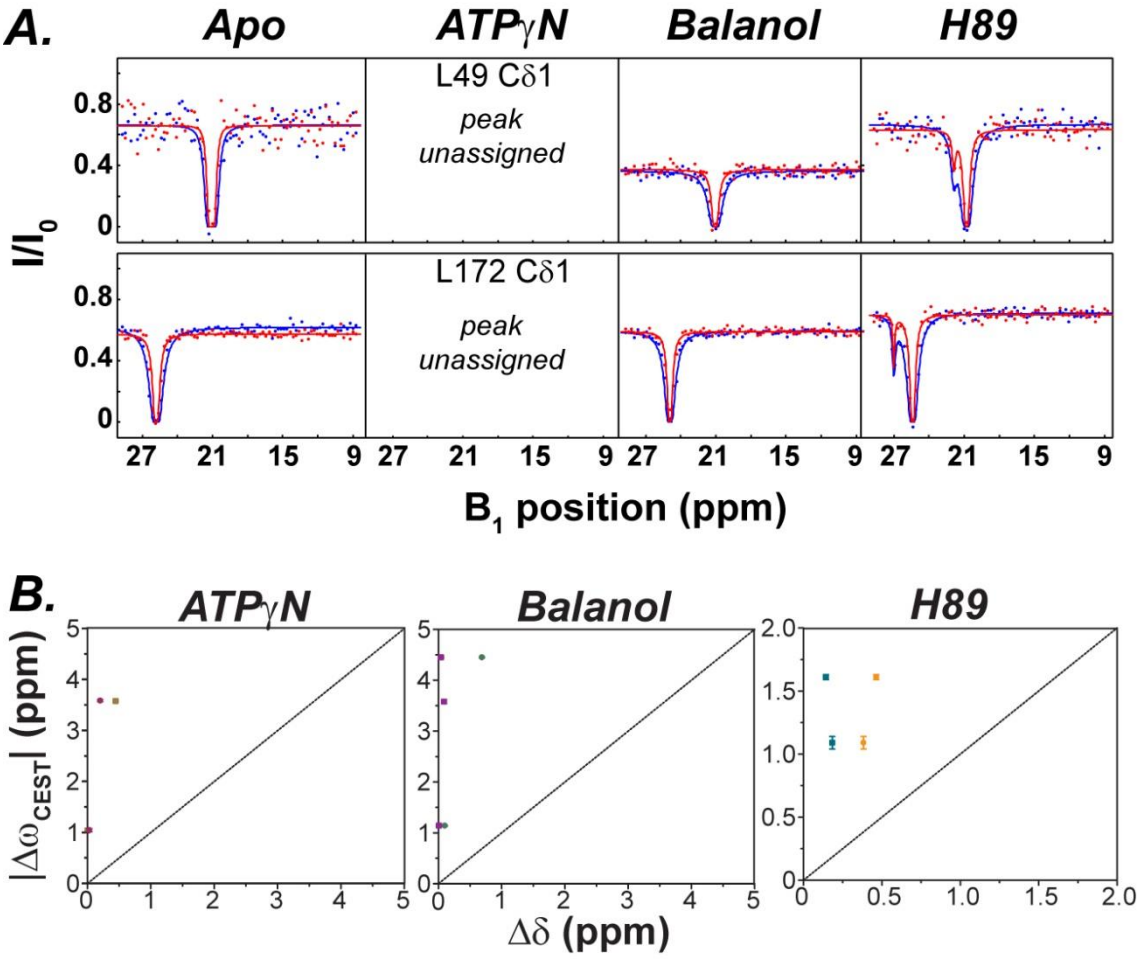

Figure 5.23. ^{13}C CEST profiles for the different PKA-C complexes.
(A) ^{13}C CEST profiles measured at 900 MHz using a B_1 field of 15 Hz (red) and 30 Hz (blue) that shows the formation of new excited states for L49 and L172 in H89-bound complex that were not observed in either ATPγN- or balanol-bound complexes. (B) Comparison of the chemical shift difference obtained from the CEST experiments (Δω) with the chemical shift difference between the nucleotide-bound or inhibitor-bound complex and the apo or the nucleotide-bound or inhibitor-bound complexes and the corresponding ternary complex.
Circle:$\Delta\delta = \delta_{nucleotide-bound} - \delta_{apo} (or\ \delta_{inhibitor-bound} - \delta_{apo})$;
Square: $\delta = \delta_{nucleotide-bound} - \delta_{nucleotide\ and\ PKI-bound}\ (or\ \delta_{inhibitor-bound} - \delta_{inhibitor\ and\ PKI-bound})$. The diagonal line shows the 1:1 correlation. The chemical shift difference from the CEST experiment does not correlate with the chemical shift difference between the binary and either apo or ternary forms.

ATP-competitive inhibitors shift the timescale of the kinase motions.

To monitor the conformational exchange on a faster time scale, we carried out [^{1}H,^{15}N]-TROSY Hahn echo (TR-HE) experiments on the different kinase forms [57]. This experiment is complementary to CPMG and is able detect conformational dynamics

closer to the μs timescale [259]. The dynamically uncommitted apo kinase displays extensive conformational exchange (R_{ex}^{TR-HE}), located in residues of the linker, the αA-β1 and αD-αE linkers, β3, β8, Gly-rich, catalytic, DFG and activation loop, as well as in the APE motif (**Figures 5.17B and 24**). Although the binding of the inhibitors causes an overall attenuation of the R_{ex}^{CPMG} across most residues, both inhibited complexes show several regions with significant R_{ex}^{TR-HE}, an effect that is more accentuated for the PKA-C/H89 complex (**Figures 5.17B and 24**). In the H89-bound complex, the αA-β linker, gly-rich loop, β3 and β5 strands, catalytic loop, αE and αH helices, the APE motif, and the acidic cluster in the C-terminal tail displayed higher R_{ex}^{TR-HE} values than those of the PKA-C/balanol complex. This suggests that these motions are shifted in a faster timescale, and probably preventing the kinase from sampling conformations that possess high binding affinity for the pseudo-substrate. Finally, we measured [^{1}H,^{15}N] heteronuclear NOEs as a proxy for backbone amide motions occurring in the ps-ns time scale. Upon inhibitor binding, we did not observe a significant change in overall backbone flexibility (average HX-NOE changed from 0.84 ± 0.14 to 0.86 ± 0.14 or 0.87 ± 0.13 in going from apo to inhibitor-bound) (**Figures 5.17C and 25**). Except for a few residues, we did not observe significant differences in the ps-ns timescale dynamics between the two inhibitor-bound complexes (**Figure 5.25**). Overall, these data suggest that the backbone ps-ns dynamics did not change significantly upon ligand binding and it does not play a major role in allosteric binding cooperativity.

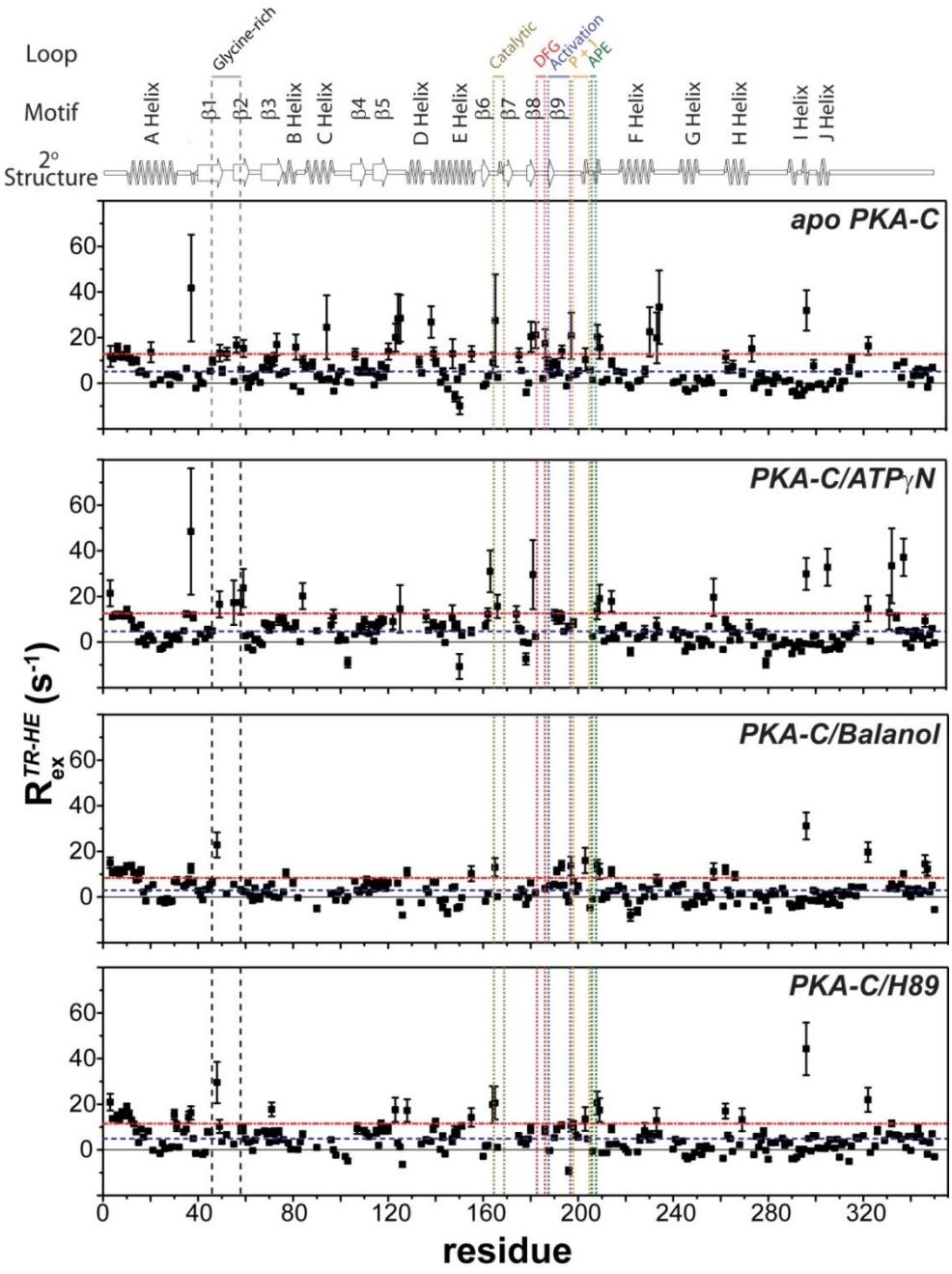

Figure 5.24. Slow conformational dynamics of the backbone as measured by TROSY Hahn-Echo experiments.

R_{ex} values versus residue for apo PKA-C, PKA-C/ATPγN, PKA-C/balanol, and PKA-C/H89 complexes as measured by ^{15}N TROSY Hahn-Echo experiments at 27°C on a 850 MHz spectrometer. The trimmed mean and a standard deviation from the trimmed mean are indicated by dashed line and dash dotted line, respectively. The uncertainties were calculated using error propagation of the root mean square noise of the spectra. For comparison, the previously published data for the ATPγN-bound state were shown [122].

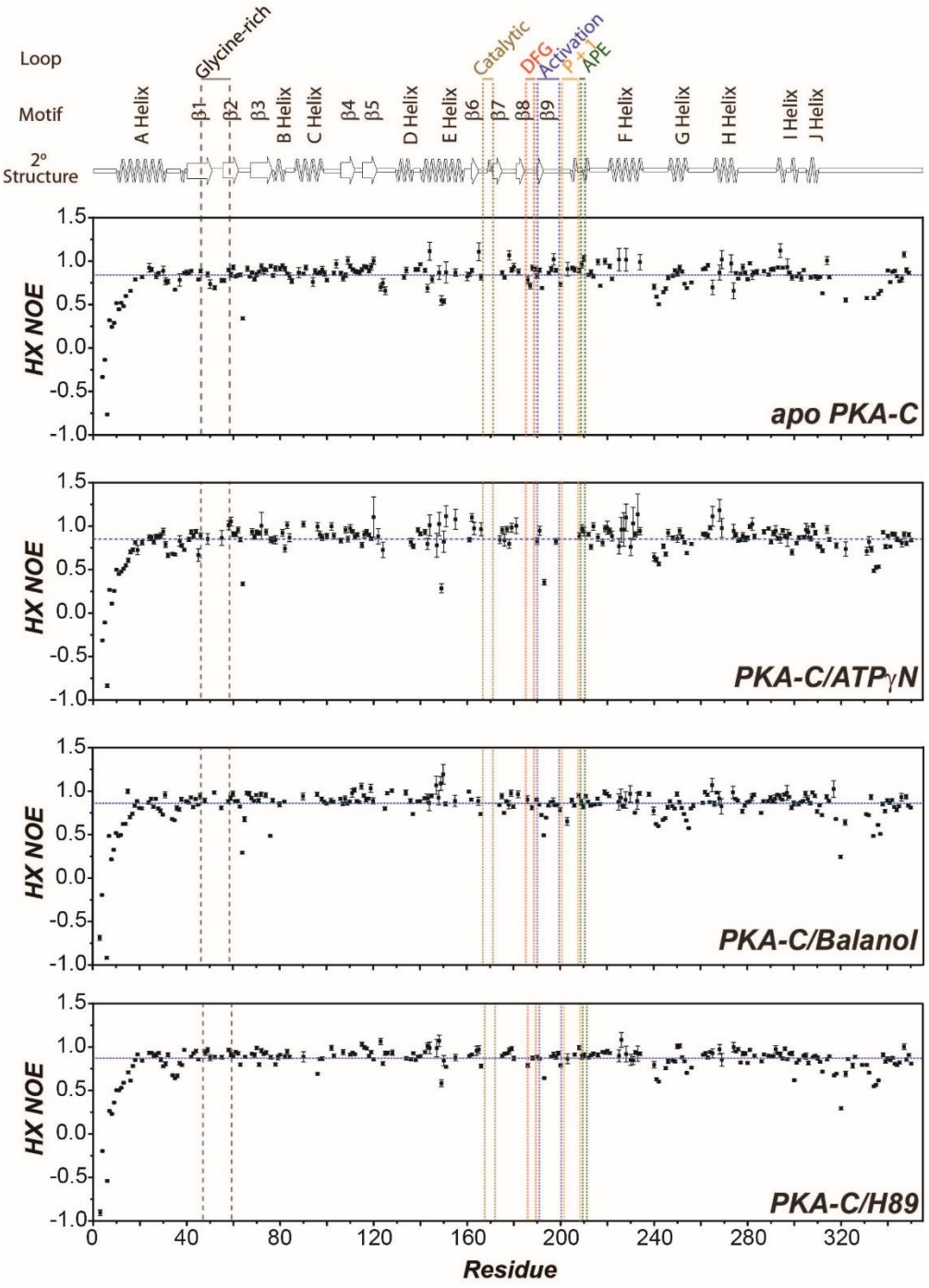

Figure 5.25. Fast backbone dynamics as measured by HX-NOE experiments.
HX-NOE values versus residue for (from top to bottom) apo PKA-C, PKA-C/ATPγN, PKA-C/Balanol , PKA-C/H89 complexes measured at 27°C and 900 MHz. The trimmed mean HX-NOE (indicated by dashed line) for apo PKA-C, PKA-C/ATPγN, PKA-C/Balanol, and PKA-C/H89 were 0.84 ± 0.14, 0.85 ± 0.29, 0.86 ± 0.14, and 0.87 ± 0.13, respectively. The uncertainties were calculated using error propagation of the root mean square noise of the spectra.

5.4 Discussion

The majority of the kinase literature focuses on the optimization of both potency and selectivity of ATP-competitive inhibitors. To the best of our knowledge, there are no publications reporting on the effects of these inhibitors on the binding cooperativity for substrate that is preserved when the ATP-binding pocket is occupied. Yet, it is emerging that both canonical and non-canonical functions of kinases are essential to cellular signaling [32, 33, 260]. Pseudo-kinases, for instance, are devoid of catalytic function, but they are still pivotal for the regulation of several cellular events by acting as scaffolds or substrates for binding other kinases [33]. As for the pseudo-kinases, inhibited kinases that are unable to phosphorylate substrates may still act as scaffolds or substrates for other kinases. A notable example is the activation of the RAF kinase *in vivo* using the ATP-competitive inhibitor PLX4270 [35, 238]. In this case, PLX4270 under sub-saturating conditions converts B-RAF into a pseudo-kinase, catalyzing dimerization and activation of C-RAF [261]. More recently, conformation-selective ATP-competitive inhibitors have been shown to control the regulatory interactions and non-canonical function of MAP kinases [262]. These examples support the wide spread phenomenon of paradoxical activation or off-target effects elicited by several kinase inhibitors [241, 263], and at the same time, generate a growing interest toward manipulating catalytic and non-catalytic kinase functions using small molecules [260].

Our data show that two chemically distinct inhibitors with comparable potency modulate the *K-type* cooperativity of PKA-C differently. The backbone of the inhibited complexes are very similar and do not explain the differential behavior of these compounds. In contrast, NMR reveals a direct correspondence between the extent of coordinated behavior of the chemical shifts and allosteric cooperativity in ATPγN, balanol, and H89. Specifically, we found that the gradual loss of cooperativity (degree of cooperativity, σ, going from 53 for ATPγN to 7 for balanol, and 0.6 for H89 [249]) is concomitant with the loss of chemical shift correlation throughout the entire enzyme. This indicates that small, but functionally significant, structural rearrangements must occur to allosterically couple the nucleotide pocket with the substrate binding site for cooperativity. The two inhibitors also exemplify the bivalent nature of the ATP binding site. Both share the hydrophobic adenine binding pocket as do almost all kinase inhibitors, however the way in which these two inhibitors complement the phosphate

binding part of the ATP binding pocket is completely different, and reveal dramatic differences in the dynamic features of the kinase Moreover, relaxation dispersion and CEST measurements show that the opposite binding cooperativity displayed by these ATP-competitive inhibitors is linked to the differential alteration and formation of lowly populated conformational states, or excited states, suggesting that they might be responsible for substrate recognition.

In fact, the ATPγN-bound, or intermediate, state of PKA-C is quite dynamic with synchronous motions for catalytically important loops [43] and the hydrophobic core [244]. The C- and R-spines, thought to be inert scaffolding for the enzyme's catalytic loops, are indeed highly dynamic and play a key role for propagating allostery and render the kinase committed to catalysis [244]. The PKA-C/balanol complex retains some of the correlated motions in the catalytic loops, the αB-helix (I85, V80), R-spine (L95), and C-spine (L173) found in the intermediate state, indicating that dynamics in the hydrophobic core contributes to allosteric control of positive cooperativity. H89 binding, on the other hand, quenches the dynamics in the majority of these residues, reflecting its negative *K-type* cooperativity due to the lack of the hydrophilic interactions with the active site eliminating the bi-valent nature of the ATP-binding pocket (**Figure 5.22C**). While both inhibitors attenuate the overall μs-ms timescale dynamics, balanol was able to engage the two lobes of the enzyme as a result of the interactions in the bivalent ATP-binding site. In addition to the hydrophobic interaction between the C spine residues, when balanol is bound, the benzophenone moiety forms a number of polar interactions with the Gly-rich loop of PKA-C, as well as with Asp184 of the conserved DFG loop [231], driving the kinase toward an intermediate-like state, displaying coordinated chemical shift behavior similar to the ATP-bound form (**Figure 5.22C**). Though balanol is not as cooperative as the natural ligand ATP, the opening and closing of the enzyme is still synchronous for some of the residues in the hydrophobic core and the kinase explores high-energy conformations that have enhanced binding affinity for the substrate. One notable finding we found is that, aside from the fast timescale dynamics, the ATPγN-bound kinase also exhibited slow ms dynamics in the αB-helix, exchanging with an excited state conformation that has a chemical shift significantly different from the ground state. This slow dynamics was preserved in the balanol-bound kinase. The synchronous motions, together with the slow ms dynamics in αB-helix, allow the key

elements in the kinase (αB, αC, DFG, activation, as well as peptide positioning loops) to orient properly for substrate recognition. This contrast with the H89-bound complex, where the bromocinnamoyl moiety is unable to couple the two lobes structurally as manifested by the absence of polar interactions between the bromocinnamoyl moiety and the residues lining the phosphate binding site (**Figure 5.22C**), thus severing the allosteric communication between the ATP and substrate binding sites, and abrogating the allosteric cooperativity. Interestingly, motions along αB helix are absent with ATPγC, an ATP-mimic which lacks *K-type cooperativity[249]*, but remains dynamic along the hydrophobic spines [255]. In addition, the disruption of allosteric network and desynchronization of motions of the two lobes are also responsible for the Y204A mutant to exhibit negative cooperativity toward the pseudosubstrate[43, 44]. The totality of our observations indicates that the propagation of dynamically driven allostery through hydrophobic motifs is multifarious, with different timescales of motion within distinct regions of the kinase to modulate cooperativity and substrate binding.

Understanding the relationship between excited states and protein function has been a subject of study in recent years [254, 264]. Dynamic studies on CAP[113] and DHFR[265] suggest that conformationally excited states are required for protein function, inhibition, and substrate recognition [214, 266, 267]. Single-site allosteric mutants that disrupt the transition to competent excited states ablate binding and catalysis [43, 265]. Small molecules also have been shown to suppress excited states in several proteins, including DHFR [268], RAS [269], the R-subunit of PKA [270], and IGPS [271]. Ligand binding does not necessarily suppress excited states, but depending on their context, may increase or decrease the population of specific states, affecting the kinase's activity. This behavior is manifested in PKA-C where, binding of ATP enhances the population of the excited state that is competent for catalysis, priming the kinase for substrate binding. On the other hand, ATP-competitive inhibitors suppress the committed states for catalysis, reducing affinity for substrates, and abrogating both canonical and non-canonical function of the kinase.

In conclusion, we used PKA-C as a proof-of-concept to demonstrate that it is possible to control the binding affinity for substrates by using different ATP-competitive inhibitors. These results suggest a new way to modulate the substrate binding ability of kinases to activate or de-activate signaling irrespective of the catalytic (canonical)

activity, prospecting a new way to control kinase function *in vivo*. Future design of kinase inhibitors must take into account the dual activity of ATP-competitive inhibitors to fine-tune both catalytic and binding functions of kinases.

5.5 Materials and Methods

Materials. All reagents used were analytical grade or higher. N-[2-(p-bromocinnamylamino)ethyl]-5-isoquinolinesulfonamide (H89) was purchased from Sigma Aldrich (St. Louis, MO, USA). Balanol was a gift of Dr. M. Walters (Department of Medicinal Chemistry, Institute for Therapeutics Discovery and Development, University of Minnesota). Adenosine 5'-(β,γ-imido)triphosphate (ATPγN) was purchased from Roche Diagnostics (Indianapolis, IN, USA).

Sample Preparation. Uniformly-^{2}H ,^{15}N, $^{13}CH_3$ ILV-labeled murine PKA-C in a pRSETb vector was expressed recombinantly in *E. coli* BL21 (DE3) cells using M9 minimal media enriched with $^{15}NH_4Cl$ and [^{2}H]-D-glucose in 85% D_2O at 24°C as described previously [117]. Induction was carried out at OD_{600} ~ 1.2 with 0.4 mM IPTG. PKA-C was expressed for 12 hours overnight. The ^{13}C labeling of the methyl groups of ILV residues was achieved by adding 2-ketobutyric acid-4-^{13}C-3,3-d_2 and 2-keto-3-(methyl-d_3)-butyric acid-4-^{13}C-3-d sodium salts one hour prior to IPTG induction with final concentrations of 70 mg/L and 90 mg/L, respectively[155, 272]. PKA-C was purified by affinity chromatography using the His_6-RIIα(R213K) subunit as previously described [168]. PKA-C was subsequently dialyzed in a buffer containing 20 mM KH_2PO_4, 25 mM KCl, and 5 mM β-mercaptoethanol at pH 6.5. The different isoforms were separated by cation exchange using HiTrap SP column using a linear gradient of Buffer A (20 mM KH_2PO_4, pH 6.5) to Buffer B (20 mM KH_2PO_4, 1 M KCl, pH 6.5). PKA-C was quantified using UV absorbance at 280nm (ε = 52060 $M^{-1}cm^{-1}$). The NMR samples consisted of 0.20-0.42 mM PKA-C solubilized in buffer containing 20 mM KH_2PO_4, 90 mM KCl, 10 mM $MgCl_2$, 10 mM DTT, 1 mM NaN_3 at pH 6.5, except for CPMG relaxation dispersion and CEST experiments of PKA/ATPγN where 60 mM $MgCl_2$ was used to avoid ATPγN hydrolysis. The nucleotide-bound complex was prepared by saturating the PKA-C with 12 mM

ATPγN while the inhibitor-bound complexes were prepared by saturating the enzyme with 1.35 mM balanol and 2 mM H89, respectively.

NMR Spectroscopy. The assignment of the backbone[122] and side-chain methyl[183] groups has been determined previously. The combined chemical shifts were calculated according to the formula:

$$\Delta\delta = \sqrt{\Delta\delta_H^2 + a\Delta\delta_X^2} \tag{5.1}$$

where $\Delta\delta_H$ and $\Delta\delta_X$ are the proton and hetereonuclei chemical shift changes, respectively, a is a scaling factor for the chemical shift of the heteronuclei, which is equal to 0.154 for ^{15}N and 0.25 for ^{13}C, respectively. The 2D backbone amide spectrum was acquired using the CLEAN-TROSY[119] version of the original TROSY-HSQC pulse sequence, while the methyl side chain spectrum was acquired using the methyl TROSY-experiment[273] at 850.3 MHz. The data were acquired as 120 (t_1) x 2048 (t_2) complex points (for backbone amide) and 200 (t_1) x 2048 (t_2) complex points (for methyl side chain) using 16 scans and a recycle delay of 2.0 seconds.

The μs-ms timescale conformational dynamics of backbone amides and methyl groups from ILV of apo PKA-C, PKA-C/ATPγN, PKA-C/balanol, and PKA-C/H89 were measured using Carr-Purcell-Meiboom Gill (CPMG) relaxation dispersion experiments [58, 254]. The ^{15}N CPMG relaxation dispersion experiments were performed using the relaxation-compensated version of the CPMG experiment [68], with improved phase cycle according to Long *et al.* [274]. The ^{13}C SQ CPMG pulse sequence by Lundstrom *et al.* [275] was used for the methyl group relaxation dispersion experiments. Both ^{15}N and ^{13}C relaxation dispersion experiments were performed in an interleaved mode with υ_{CPMG} values of 0, 50, 100, 150, 200, 250, 300, 400, 500, 600, 800, and 1000 Hz. Effective transverse relaxation rate constant, $R_{2,eff}$, were determined at each υ_{CPMG} value using the peak intensities with and without relaxation period according to the equation[276]:

$$R_{2,eff} = \frac{\ln\left(\frac{I_0}{I}\right)}{T} \tag{5.2}$$

where I_0 and I are the peak intensities of the resonances in the 2D spectra acquired in the absence and presence of a relaxation period, respectively, and T is the total CPMG

time [277] which was 40 ms. Duplicate measurements were carried out at υ_{CPMG} values of 50, 500, and 1000 Hz for error estimation and errors were indicated as standard deviations. The backbone ^{15}N CPMG data were acquired on Bruker AVANCE III operating at 850.3 MHz; while the ^{13}C CPMG data were acquired at two different fields using Bruker AVANCE III spectrometers operating at 700.1 and 850.3 MHz, respectively. The ^{15}N CPMG spectra were acquired as 120 (t_1) x 2048 (t_2) complex points for apo and ATPγN-bound, 102 (t_1) x 2048 (t_2) complex points for balanol-bound, and 98 (t_1) x 2048 (t_2) complex points for H89-bound using 96 (for apo), 64 (for ATPγN-bound) and 128 (for inhibitor-bound) scans with a recycle delay ranging of 2.50 seconds. All ^{13}C CPMG spectra were acquired as 160 (t_1) x 2048 (t_2) complex points using 48 scans and a recycle delay of 2.50 seconds.

The TROSY Hahn-Echo experiments [57] were performed on the backbone residues using a Hahn-echo period corresponding to $2/J_{NH}$ (10.8 ms). The peak intensities of the α, β, zz spin states were used to calculate the R_{ex}^{TR-HE} according to the following equation [76, 278]:

$$R_{ex}^{TR-HE} \approx C_{zz} \ln\left(\rho_{zz}\right) + C_{\beta} \ln\left(\rho_{\beta}\right) \tag{5.3}$$

where $C_{zz} = (2\tau)^{-1}$, $C_{\beta} = (<\kappa> -1)(4\tau)^{-1}$, $\kappa = 1 - 2\ln\rho_{zz} / \ln\rho_{\beta}$, $\rho_{zz} = I_{zz}/I_{\alpha}$, and $\rho_{\beta} = I_{\beta}/I_{\alpha}$. <κ> is the trimmed mean of the κ value for the amide resonances not showing chemical exchange [57]. All spectra were acquired in an interleaved mode with 120 (t_1) x 2048 (t_2) complex points using 240 (for apo) or 256 (for inhibitor-bound) scans and a recycle delay of 2.0 seconds. The uncertainties on the R_{ex}^{TR-HE} values were calculated from propagating the errors using the root mean square noise from the spectra.

All ^{13}C methyl CEST experiments were recorded on a Bruker 900.21 MHz spectrometer equipped with a TCI cryoprobe using the pulse sequence by Bouvignies and Kay[257]. The CEST datasets were acquired using an exchange time of 400 ms and two different $\boldsymbol{B}_1$ field strengths ~15 Hz and ~30 Hz. A series of 79 2D HSQC spectra were acquired with 144 (t_1) x 2048 (t_2) complex points with the ^{13}C carrier offsets between 8.73 and 28.71 ppm at 58 Hz (0.256 ppm) intervals. Each 2D spectrum was acquired with 16 scans and 70 increments, using a recycle delay of 2.0 s. To construct

the CEST profiles, the ratio of peak intensities with (I) and without (I_0) the exchange delay, T_{ex}, as a function $\boldsymbol{B_1}$ offset was used [257].

The ^{1}HX-NOE values [76] were calculated from the ratio of signal intensities of the TROSY-select experiments with and without a ^{1}H saturation of 5 s [118]. The datasets were acquired as 120 (t_1) x 2048 (t_2) complex points using 184-196 scans and a recycle delay of 5.0 seconds. The uncertainties on the HX-NOE values were calculated using error propagation of the root mean square noise [279].

Data Processing and Analysis.

All data were processed using NMRPipe [120] and peak intensities were quantified using FuDA (http://pound.med.utoronto.ca/~flemming/fuda/) and Sparky [121]. Gaussian window function with a line broadening of -12 Hz was applied in the direct dimension while sine bell window function with an offset of 0.5 was applied in the indirect dimension. The data were zero-filled to the nearest power of 2. Twenty and nine side chains showed significant dispersion (R_{ex} > 2 s^{-1}) in the balanol-bound and H89-bound complex, respectively, and were subsequently fitted individually using a two-state exchange model using the GUARDD software [258] with k_{ex}, p_B, $\Delta\omega$, and R_2^0 as the fitting parameters. Among the side chains that showed chemical exchange, group fitting into a two-state exchange process were carried out for residues that satisfy: $\frac{\chi^2_{group}}{\chi^2_{individual}} < 1.20$. We were able to group fit twelve and seven side chains in the ATPγN-bound and balanol-bound complex, respectively, into a single two-state exchange process and extracted the group k_{ex} and p_B, as well as the individual $\Delta\omega$, and R_2^0. On the other hand, the CEST profiles were analyzed using a two-state exchange model included in the ChemEx software [56], with k_{ex}, p_B, and $\Delta\omega$ as the main fitting parameters. Among the side chains analyzed, three, two, three, and two side chains showed pronounced excited states in the CEST profiles for the apo, ATPγN-bound, balanol-bound, and H89-bound PKA-C, respectively.

Analysis of Chemical Shift Trajectories

The allosteric network of the backbone amide or methyl side chain residues in the nucleotide or inhibitor-bound PKA-C that report the open to close transition was

determined using the COordiNate ChemIcal Shift bEhavior(CONCISE)[125] to monitor the change in the equilibrium position associated with each PKA-C state. The reference states used were apo, ADP-bound, ATPγN/PLN_{1-19}-bound, and ATPγN/PKI_{5-24}-bound to measure the change of the equilibrium position along the open to closed conformational states. CONCISE uses Principal Component Analysis (PCA) to identify a set of residues whose chemical shifts respond linearly to the conformational transition. Each residue provides a measure of the equilibrium position for every state of PKA-C in form of scores along the first principal component. The equilibrium position for a given construct is given by the average of the PC-scores over all linear residues. To identify the residues whose chemical shifts follow a linear pattern, a threshold of 1.0 to 3.0 for the ratio of the standard deviations of PC1 over PC2 was used, and residues that were affected by chemical shifts perturbations below 0.05 ppm were also discarded.

To identify which residues respond in a correlated fashion to ligand binding, an adapted version of the chemical shift covariance analysis [104](CHESCA) method was applied to the cluster of linear residues identified using CONCISE. The correlation matrices between the linear residues identified from CONCISE were constructed from correlation coefficients (r_{ij}) that exceed 0.9. The correlations were mapped into the structure using the xPyder plugin [253] with a cutoff value of 0.98 for backbone amide groups for clarity and 0.90 for side-chain methyl groups.

Data Availability

All generated and processed data during this study are available from the authors upon request.

Code Availability

The script for CONCISE with CHESCA is available from the corresponding author upon request; while xPyder is a free PyMol plugin that can be accessed here: http://xpyder.sourceforge.net/. The programs used to extract peak intensities can be downloaded online: FuDA (http://pound.med.utoronto.ca/~flemming/fuda/) and Sparky (http://www.cgl.ucsf.edu/home/sparky/). The GUARDD software used to fit the CPMG relaxation dispersion data can be downloaded here: https://code.google.com/archive/p/guardd/downloads, while the ChemEx 0.6.0 software

used to fit the CEST profiles can be obtained here: https://github.com/gbouvignies/chemex/releases.

5.6 Acknowledgements

All NMR experiments were carried out at the Minnesota NMR Center. We thank Dr. Youlin Xia for assistance with the NMR experiments. We thank Sarah Nelson for critical reading of the manuscript. This work is supported by the NIH (GM 100310 to GV and T32AR007612 to JK).

Table 5.1. R_{ex} values of the backbone amide residues of the different states of PKA-C (apo, ATPγN-bound, balanol-bound, and H89 bound) measured using ^{15}N CPMG relaxation dispersion at 850 MHz and 27°C.

Residue	*R_{ex} (s^{-1})*			
	apo	***ATPγN-bound***	***Balanol-bound***	***H89-bound***
3	no exchange	no exchange	2.2 ± 0.5	0.4 ± 0.4
4	no exchange	no exchange	no exchange	no exchange
5	no exchange	no exchange	no exchange	no exchange
6	ND	no exchange	no exchange	0.7 ± 0.1
7	0.4 ± 0.2	no exchange	0.2 ± 0.1	0.1 ± 0.1
8	0.6 ± 0.1	no exchange	no exchange	no exchange
9	no exchange	no exchange	no exchange	no exchange
10	no exchange	0.3 ± 0.2	0.2 ± 0.2	no exchange
11	no exchange	1.6 ± 0.5	0.2 ± 0.2	no exchange
12	0.2 ± 0.1	1.2 ± 0.2	1.6 ± 0.2	0.3 ± 0.1
13	ND	1.3 ± 0.3	1.8 ± 0.3	no exchange
14	0.9 ± 0.3	1.3 ± 0.6	1.5 ± 0.3	ND
15	ND	ND	ND	no exchange
16	ND	3.5 ± 0.9	ND	0.5 ± 0.2
17	ND	1.7 ± 0.5	0.3 ± 0.5	no exchange
18	0.8 ± 0.4	no exchange	0.9 ± 0.5	0.2 ± 0.2
19	ND	5.5 ± 2.4	0.9 ± 0.3	2.1 ± 0.3
20	0.3 ± 1.2	ND	no exchange	ND
21	ND	8.2 ± 2.8	2.1 ± 0.4	no exchange
24	ND	no exchange	0.6 ± 0.6	no exchange
25	ND	no exchange	0.5 ± 0.4	1.2 ± 0.3
26	ND	ND	0.6 ± 0.5	0.6 ± 0.6
27	2.3 ± 0.7	10.4 ± 2.2	1.1 ± 0.3	no exchange
28	1.0 ± 0.6	ND	no exchange	2.0 ± 0.5
29	ND	5.9 ± 2.8	ND	ND
30	no exchange	7.0 ± 3.2	0.9 ± 0.3	4.0 ± 0.4
31	1.1 ± 1.3	ND	2.4 ± 1.3	0.1 ± 1.1
32	1.7 ± 0.6	2.8 ± 1.3	ND	1.4 ± 0.8
34	ND	4.1 ± 1.4	no exchange	ND
35	0.7 ± 0.2	3.5 ± 0.9	no exchange	no exchange
36	ND	ND	no exchange	0.5 ± 0.5
37	21.1 ± 5.2	59.3 ± 22.3	1.7 ± 0.6	3.5 ± 0.6
38	ND	14.6 ± 3.3	12.5 ± 0.8	1.6 ± 0.4
39	0.1 ± 0.3	no exchange	ND	0.4 ± 0.3
40	no exchange	ND	ND	ND
41	0.2 ± 0.4	no exchange	0.3 ± 0.4	ND
42	no exchange	ND	no exchange	no exchange
43	ND	ND	1.3 ± 0.6	ND
44	ND	ND	no exchange	0.1 ± 0.5
45	0.2 ± 0.3	no exchange	no exchange	0.7 ± 0.2

46	0.7 ± 0.4	4.2 ± 1.2	5.9 ± 1.1	ND
48	ND	ND	no exchange	no exchange
49	no exchange	43.9 ± 8.6	ND	1.6 ± 1.4
50	2.7 ± 1.9	ND	ND	ND
52	4.3 ± 0.6	ND	0.7 ± 0.6	2.7 ± 0.6
55	1.9 ± 0.5	ND	4.6 ± 0.7	2.5 ± 0.7
56	11.9 ± 0.6	ND	ND	ND
58	no exchange	17.7 ± 11.6	no exchange	1.0 ± 0.7
59	6.5 ± 0.9	11.2 ± 2.1	no exchange	2.3 ± 0.8
60	0.9 ± 0.8	3.9 ± 3.3	no exchange	0.3 ± 0.7
61	no exchange	ND	0.8 ± 0.2	0.2 ± 0.6
62	no exchange	no exchange	no exchange	0.3 ± 0.5
63	no exchange	no exchange	no exchange	no exchange
64	no exchange	1.8 ± 0.6	0.4 ± 0.4	no exchange
65	ND	1.9 ± 2.5	1.0 ± 0.9	2.7 ± 0.4
66	no exchange	no exchange	ND	no exchange
67	6.1 ± 0.2	3.6 ± 1.3	ND	ND
68	0.4 ± 0.4	ND	no exchange	no exchange
69	2.3 ± 0.6	ND	0.2 ± 0.4	1.5 ± 1.0
70	2.0 ± 0.7	ND	0.1 ± 0.4	2.8 ± 0.6
71	no exchange	ND	no exchange	0.7 ± 0.5
72	5.7 ± 0.9	ND	2.5 ± 0.8	3.8 ± 0.9
73	9.5 ± 1.0	ND	ND	no exchange
74	0.5 ± 0.5	8.1 ± 3.7	no exchange	1.8 ± 0.6
76	1.3 ± 0.5	ND	0.7 ± 0.3	1.1 ± 0.7
77	2.6 ± 0.6	4.1 ± 1.1	3.9 ± 0.7	ND
78	ND	ND	ND	no exchange
79	ND	ND	ND	no exchange
80	0.9 ± 0.7	8.5 ± 3.1	2.7 ± 0.9	0.8 ± 0.5
81	2.6 ± 0.8	no exchange	ND	ND
82	ND	9.1 ± 1.5	0.1 ± 0.3	no exchange
83	no exchange	8.4 ± 3.4	ND	2.2 ± 0.7
84	2.0 ± 1.0	ND	ND	ND
85	0.2 ± 0.7	ND	ND	ND
90	1.0 ± 0.5	10.1 ± 6.2	ND	ND
94	18.6 ± 3.4	ND	ND	ND
95	0.7 ± 0.9	ND	ND	ND
96	5.6 ± 0.5	ND	0.5 ± 0.7	0.4 ± 0.4
97	no exchange	ND	no exchange	no exchange
98	1.5 ± 0.9	no exchange	no exchange	no exchange
99	1.5 ± 0.7	ND	1.0 ± 0.5	ND
100	0.9 ± 0.4	2.5 ± 0.9	0.3 ± 0.4	ND
103	6.3 ± 0.6	no exchange	2.2 ± 0.7	0.2 ± 0.7
106	6.7 ± 0.5	4.1 ± 2.0	0.6 ± 0.3	ND
107	2.9 ± 1.1	ND	no exchange	1.8 ± 1.2

108	2.1 ± 0.7	3.3 ± 1.0	5.5 ± 1.7	ND
109	no exchange	ND	no exchange	ND
110	2.8 ± 0.6	6 ± 5.1	0.9 ± 0.5	0.8 ± 0.5
111	no exchange	no exchange	1.6 ± 1.0	0.5 ± 0.4
112	1.5 ± 0.5	2.3 ± 2.3	no exchange	no exchange
113	no exchange	ND	0.3 ± 0.6	ND
114	no exchange	no exchange	0.9 ± 0.4	ND
115	no exchange	10.1 ± 9.0	2.5 ± 1.2	no exchange
116	no exchange	ND	1.8 ± 0.7	no exchange
117	no exchange	2.5 ± 2.4	3.6 ± 1.0	1.3 ± 0.6
118	2.5 ± 0.6	11.6 ± 1.8	ND	0.5 ± 0.6
119	0.8 ± 0.8	no exchange	no exchange	1.5 ± 0.7
120	5.4 ± 1.1	ND	no exchange	2.2 ± 0.9
124	25.7 ± 2.9	15.9 ± 19.7	ND	1.0 ± 0.5
125	19.3 ± 2.2	ND	no exchange	2.1 ± 0.9
126	ND	ND	no exchange	3.9 ± 0.9
128	ND	ND	no exchange	2 ± 1.2
133	8.5 ± 0.9	ND	ND	ND
134	7.3 ± 1.0	ND	no exchange	1.2 ± 0.8
136	ND	ND	0.8 ± 1.0	ND
137	ND	7.2 ± 4.3	1.6 ± 0.4	1.8 ± 0.4
138	22.2 ± 1.1	ND	ND	ND
139	6.6 ± 0.5	3.7 ± 1.7	0.6 ± 0.5	0.4 ± 0.5
140	1.3 ± 0.4	2.0 ± 1.2	1.0 ± 0.5	ND
142	2.4 ± 0.7	5.6 ± 2.8	no exchange	1.0 ± 0.6
143	4.6 ± 0.9	no exchange	no exchange	0.6 ± 0.8
144	0.2 ± 1.6	no exchange	ND	no exchange
145	1.1 ± 0.7	ND	0.6 ± 1.0	ND
147	ND	ND	ND	ND
148	no exchange	no exchange	2.7 ± 2.7	no exchange
149	0.2 ± 1.6	no exchange	no exchange	no exchange
150	ND	17.7 ± 8.7	3.9 ± 3.2	ND
151	ND	ND	no exchange	1.4 ± 0.3
155	0.4 ± 1.0	ND	no exchange	no exchange
160	2.7 ± 1.1	ND	ND	ND
161	1.3 ± 0.4	7.4 ± 5.8	no exchange	0.5 ± 0.4
162	2.1 ± 0.5	8.8 ± 5.5	ND	no exchange
163	ND	15.4 ± 3.5	ND	ND
164	6.9 ± 1.7	ND	ND	0.5 ± 2.1
165	14.8 ± 4.3	ND	no exchange	ND
166	4.2 ± 0.7	38.0 ± 21.8	1.1 ± 0.6	1.3 ± 0.7
174	ND	no exchange	1.6 ± 0.4	ND
175	9.5 ± 0.7	ND	no exchange	1.1 ± 0.6
176	no exchange	no exchange	no exchange	2.2 ± 0.7
177	ND	10.6 ± 4	ND	0.1 ± 0.5

178	no exchange	ND	no exchange	1.1 ± 1.7
179	no exchange	4.2 ± 3.5	no exchange	no exchange
180	15.9 ± 1.6	13.7 ± 14.8	ND	1.0 ± 0.9
181	ND	17.5 ± 5.5	ND	ND
182	17.2 ± 1.2	8.0 ± 5.4	no exchange	ND
186	3.9 ± 1.4	ND	5.6 ± 1.7	2.8 ± 0.8
187	2.2 ± 1.0	ND	ND	ND
188	3.3 ± 0.9	ND	6.4 ± 0.9	1.2 ± 0.6
189	2.5 ± 0.6	ND	ND	ND
190	4.2 ± 0.8	10.2 ± 3.4	2.9 ± 0.5	1.0 ± 0.4
191	1.6 ± 0.5	7.1 ± 1.4	6.0 ± 0.5	1.9 ± 0.4
192	no exchange	ND	no exchange	ND
193	0.9 ± 0.5	no exchange	no exchange	ND
194	ND	ND	1.5 ± 0.2	ND
195	2.2 ± 0.5	ND	1.5 ± 0.5	ND
196	2.7 ± 0.7	15.6 ± 4.4	0.9 ± 0.5	ND
197	0.8 ± 2.5	ND	5.1 ± 2.2	no exchange
198	1.4 ± 0.5	8.6 ± 8.9	2.3 ± 0.7	2.0 ± 0.6
199	3.3 ± 0.7	ND	0.2 ± 0.4	3.6 ± 0.9
200	4.3 ± 0.7	ND	2.1 ± 1.0	2.7 ± 0.4
203	ND	ND	3.2 ± 2.4	ND
204	ND	ND	ND	0.7 ± 0.5
205	5.7 ± 0.6	ND	no exchange	ND
206	1.3 ± 0.7	ND	no exchange	0.3 ± 0.5
208	1.9 ± 0.9	no exchange	no exchange	0.6 ± 0.8
209	ND	ND	ND	ND
210	2.6 ± 1.2	24.6 ± 9.9	1.6 ± 1.1	1.1 ± 1.3
211	ND	8.5 ± 2.7	no exchange	ND
212	2.7 ± 0.5	2.8 ± 1.6	0.3 ± 0.5	0.5 ± 0.5
213	1.1 ± 0.6	3.8 ± 3.2	0.9 ± 0.4	0.9 ± 0.5
214	2.2 ± 0.6	7.2 ± 4.9	4.0 ± 0.7	1.3 ± 0.5
215	ND	no exchange	ND	ND
216	1.8 ± 0.7	17.7 ± 4.8	no exchange	0.8 ± 0.6
217	ND	ND	0.1 ± 0.4	ND
218	ND	7.0 ± 3.7	ND	ND
219	1.2 ± 1.0	20.6 ± 12.6	no exchange	ND
220	ND	ND	0.5 ± 0.7	ND
221	0.8 ± 0.5	12.0 ± 6.8	0.4 ± 0.4	0.5 ± 0.4
222	1.1 ± 0.5	no exchange	ND	ND
225	ND	ND	1.7 ± 2.4	ND
227	ND	ND	1.7 ± 0.5	ND
228	no exchange	ND	2.0 ± 2.6	ND
230	ND	ND	1.4 ± 3.0	0.3 ± 2.1
231	ND	no exchange	ND	ND
232	ND	11.5 ± 5.6	0.5 ± 0.3	ND

233	1.9 ± 1.3	no exchange	ND	4.4 ± 3.4
234	18.9 ± 3.1	no exchange	4.3 ± 1.0	ND
238	ND	ND	1.3 ± 0.8	ND
240	1.2 ± 0.6	26.2 ± 16.2	0.9 ± 1.5	3.5 ± 1.5
241	no exchange	3.2 ± 2.1	0.5 ± 0.5	no exchange
242	0.2 ± 0.3	9.6 ± 1.4	0.6 ± 0.2	2.1 ± 0.3
244	1.5 ± 0.4	1.9 ± 1.9	0.7 ± 0.4	ND
245	no exchange	no exchange	no exchange	no exchange
246	no exchange	8.2 ± 4.0	0.3 ± 0.8	no exchange
247	ND	ND	1.8 ± 0.4	ND
248	ND	no exchange	0.1 ± 0.5	0.1 ± 0.4
249	no exchange	ND	0.5 ± 0.3	2.0 ± 0.4
250	ND	no exchange	ND	ND
251	0.8 ± 0.8	4.3 ± 3.2	no exchange	1.1 ± 0.7
252	no exchange	7.4 ± 2.3	0.2 ± 0.5	no exchange
253	no exchange	3.3 ± 1.6	no exchange	no exchange
254	no exchange	3.2 ± 1.4	0.2 ± 0.3	0.5 ± 0.2
255	no exchange	ND	ND	ND
256	no exchange	2.4 ± 1.2	no exchange	no exchange
257	ND	3.2 ± 1.0	no exchange	ND
261	0.3 ± 0.3	5.6 ± 4.6	no exchange	no exchange
262	no exchange	4.8 ± 2.2	0.3 ± 0.6	no exchange
263	no exchange	1.5 ± 1.1	no exchange	no exchange
264	ND	3.8 ± 0.9	no exchange	1.0 ± 0.2
265	no exchange	no exchange	ND	no exchange
266	ND	ND	2.6 ± 1.0	ND
267	ND	ND	0.1 ± 0.3	ND
268	ND	ND	ND	no exchange
269	0.6 ± 2.3	no exchange	ND	1.1 ± 2.1
272	ND	ND	no exchange	ND
274	0.8 ± 1.1	no exchange	ND	ND
275	no exchange	1.5 ± 2.6	no exchange	0.1 ± 0.3
276	ND	ND	no exchange	0.6 ± 0.6
277	no exchange	ND	no exchange	no exchange
278	no exchange	9.3 ± 3.6	no exchange	no exchange
279	no exchange	4.6 ± 2.1	1.8 ± 0.7	no exchange
280	no exchange	ND	no exchange	ND
281	no exchange	3.3 ± 1.6	0.3 ± 0.5	no exchange
282	no exchange	no exchange	no exchange	ND
283	ND	2.0 ± 0.9	1.1 ± 0.6	no exchange
284	no exchange	ND	ND	ND
286	ND	no exchange	no exchange	no exchange
287	no exchange	no exchange	no exchange	no exchange
289	no exchange	3.7 ± 1.7	0.5 ± 0.4	1.1 ± 0.3
290	no exchange	no exchange	no exchange	no exchange

291	no exchange	1.5 ± 1.7	0.1 ± 0.6	no exchange
292	no exchange	ND	no exchange	ND
293	no exchange	1.4 ± 1.6	no exchange	no exchange
294	no exchange	ND	no exchange	no exchange
295	0.4 ± 0.4	no exchange	no exchange	no exchange
296	0.3 ± 0.7	no exchange	no exchange	no exchange
297	no exchange	ND	1.0 ± 0.9	no exchange
298	no exchange	no exchange	no exchange	no exchange
299	no exchange	no exchange	no exchange	no exchange
300	ND	ND	no exchange	1.1 ± 0.2
301	no exchange	no exchange	ND	no exchange
302	no exchange	no exchange	no exchange	no exchange
303	ND	ND	no exchange	ND
304	no exchange	ND	1.0 ± 0.5	no exchange
305	ND	ND	no exchange	no exchange
306	ND	no exchange	no exchange	no exchange
307	ND	ND	0.9 ± 0.7	ND
308	ND	ND	0.4 ± 0.5	0.9 ± 0.2
309	no exchange	2.4 ± 1.7	no exchange	no exchange
310	no exchange	9.4 ± 0.9	no exchange	no exchange
311	no exchange	no exchange	0.8 ± 0.3	0.2 ± 0.3
312	0.8 ± 0.3	no exchange	0.9 ± 0.4	0.3 ± 0.3
314	8.2 ± 1.5	4.1 ± 4.3	2.6 ± 0.7	0.1 ± 0.5
315	7.9 ± 0.4	3.9 ± 1.1	3.5 ± 0.4	1.3 ± 0.3
317	ND	7.0 ± 4.3	0.4 ± 2.0	ND
318	ND	3.1 ± 0.4	0.4 ± 0.2	0.9 ± 0.1
320	ND	ND	1.2 ± 0.5	1.5 ± 0.5
322	4.1 ± 0.7	no exchange	no exchange	2.8 ± 1.2
323	ND	ND	ND	no exchange
326	ND	ND	ND	no exchange
328	no exchange	ND	ND	ND
331	ND	9.0 ± 1.1	0.2 ± 0.3	1.7 ± 0.3
332	ND	15.2 ± 2.3	0.5 ± 0.3	2.9 ± 0.3
333	ND	11.9 ± 1.5	0.9 ± 0.5	no exchange
334	0.9 ± 0.3	8.9 ± 1.0	no exchange	0.4 ± 0.3
335	ND	4.5 ± 1.3	no exchange	0.4 ± 0.3
336	0.4 ± 0.2	2.9 ± 1.2	2.2 ± 0.3	no exchange
337	5.3 ± 0.3	ND	6.7 ± 0.3	ND
338	ND	ND	no exchange	no exchange
339	ND	ND	no exchange	no exchange
340	no exchange	no exchange	0.4 ± 0.5	no exchange
341	0.3 ± 0.2	3.4 ± 2.7	no exchange	no exchange
342	no exchange	2.3 ± 1.5	0.5 ± 0.4	no exchange
343	no exchange	6.2 ± 1.0	0.1 ± 0.4	no exchange
344	no exchange	ND	no exchange	no exchange

345	ND	7.9 ± 4.8	no exchange	0.3 ± 0.4
346	1.5 ± 1.1	ND	4.6 ± 1.5	ND
347	no exchange	no exchange	ND	no exchange
348	2.2 ± 0.6	10.1 ± 7.5	ND	no exchange
349	1.2 ± 0.4	ND	no exchange	0.2 ± 0.4
350	ND	ND	no exchange	no exchange

Data were not determined for those residues marked ND because the resonances are either broadened or severely overlapped.

Table 5.2. Results of the individual fits of methyl side chains in PKA-C/ATPγN complex that have chemical exchange (R_{ex}> 2 s^{-1}) measured using ^{13}C CPMG at 700 MHz and 850 MHz.

	k_{ex} (s^{-1})	Pa (%)	Δω (ppm)	R_{ex} (700 MHz, s^{-1})	R_{ex} (850 MHz, s^{-1})
LEU40Cδ1	810 ± 88	50.0 ± 16.4	0.2 ± 0.1	13.3 ± 0.6	19.8 ± 1.0
ILE46Cδ1	2087 ± 280	65.6 ± 18.2	0.4 ± 0.2	18.0 ± 0.6	26.7 ± 1.2
LEU49Cδ2	4032 ± 3867	61.5 ± 21.9	0.5 ± 1.5	21.5 ± 13.3	31.8 ± 19.6
LEU59Cδ1	2116 ± 554	64.7 ± 20.7	0.3 ± 0.4	8.7 ± 0.9	12.8 ± 1.3
ILE73Cδ1	269 ± 329	50.0 ± 20.2	0.1 ± 0.4	3.2 ± 10.2	4.8 ± 11.1
LEU74Cδ1	2635 ± 768	65.6 ± 20.0	0.4 ± 0.4	19.7 ± 1.6	29.2 ± 2.9
VAL79Cγ2	100 ± 542	97.6 ± 2.2	3.0 ± 0.4	2.4 ± 0.3	2.4 ± 0.3
VAL80Cγ1	24 ± 53	75.8 ± 6.2	4.9 ± 0.2	7.2 ± 1.2	7.2 ± 1.2
LEU82Cδ1	1683 ± 1652	85.2 ± 19.6	0.2 ± 0.7	2.5 ± 0.6	3.7 ± 1.0
ILE85Cδ1	96 ± 183	94.2 ± 4.5	1.2 ± 0.1	5.6 ± 0.3	5.7 ± 0.4
LEU89Cδ2	1918 ± 314	68.9 ± 20.5	0.2 ± 0.3	7.7 ± 0.5	11.3 ± 0.8
ILE94Cδ1	1894 ± 294	90.2 ± 19.0	0.4 ± 0.2	9.5 ± 0.4	13.8 ± 0.6
VAL98Cγ2	4087 ± 2811	50.0 ± 21.2	0.3 ± 1.4	6.9 ± 4.2	10.2 ± 5.6
LEU103Cδ1	2433 ± 1260	99.0 ± 20.1	1.3 ± 0.7	5.9 ± 0.9	7.8 ± 1.8
VAL104Cγ2	3896 ± 3371	50.0 ± 22.1	0.2 ± 1.8	2.0 ± 1.8	2.9 ± 2.2
LEU106Cδ1	2296 ± 313	73.3 ± 20.1	0.3 ± 0.3	11.2 ± 0.5	16.6 ± 0.8
LEU116Cδ1	530 ± 376	50.0 ± 20.7	0.1 ± 0.3	4.1 ± 3.1	6.1 ± 3.8
LEU116Cδ2	3043 ± 2181	81.3 ± 21.1	0.3 ± 1.2	5.3 ± 2.9	7.9 ± 3.9
VAL119Cγ1	997 ± 458	98.7 ± 11.7	0.8 ± 0.3	5.4 ± 0.4	6.7 ± 0.9
VAL119Cγ2	1151 ± 2349	99.8 ± 12.0	1.7 ± 1.1	2.0 ± 1.2	2.2 ± 1.5
VAL123Cγ2	3254 ± 1271	54.2 ± 19.6	0.3 ± 0.6	9.1 ± 2.3	13.5 ± 3.1
LEU132Cδ1	2549 ± 394	50.4 ± 19.1	0.5 ± 0.3	28.1 ± 1.2	41.6 ± 2.6
LEU132Cδ2	201 ± 162	94.9 ± 15.6	0.4 ± 0.2	8.2 ± 3.2	8.8 ± 5.8
ILE135Cδ1	2052 ± 1540	99.5 ± 14.9	1.2 ± 1.0	3.1 ± 1.2	4.1 ± 1.7
ILE150Cδ1	2181 ± 427	92.6 ± 15.2	1.0 ± 0.3	34.2 ± 1.5	46.6 ± 3.9
LEU157Cδ1	1325 ± 256	68.9 ± 20.4	0.2 ± 0.2	9.1 ± 0.6	13.5 ± 1.1
LEU160Cδ1	2266 ± 1135	71.4 ± 20.0	0.2 ± 0.4	4.5 ± 0.6	6.6 ± 1
LEU160Cδ2	2353 ± 654	98.8 ± 11.3	1.3 ± 0.4	7.4 ± 0.5	9.7 ± 0.8
LEU162Cδ1	1557 ± 586	56.4 ± 19.3	0.4 ± 0.3	36.0 ± 3.4	53.8 ± 6.9
LEU162Cδ2	2116 ± 519	64.7 ± 20.1	0.3 ± 0.4	8.7 ± 0.7	12.8 ± 1.1
ILE163Cδ1	422 ± 72	50.0 ± 16.9	0.1 ± 0.1	11.9 ± 1.9	17.8 ± 3.3

LEU167Cδ1	3254 ± 3974	74.2 ± 22.6	0.2 ± 2.1	2.5 ± 3.2	3.7 ± 3.6
LEU172Cδ2	2685 ± 272	66.5 ± 18.3	0.5 ± 0.2	24.2 ± 0.7	35.8 ± 1.2
LEU173Cδ1	2565 ± 466	58.8 ± 19.8	0.4 ± 0.3	19.0 ± 0.9	28.1 ± 2.2
LEU173Cδ2	25 ± 2720	88.3 ± 14.7	1.2 ± 0.9	3.3 ± 2.1	3.3 ± 2.8
ILE174Cδ1	863 ± 223	90.8 ± 9.9	0.7 ± 0.1	34.9 ± 1.5	43.4 ± 2.9
ILE180Cδ1	2805 ± 1032	83.8 ± 19.7	1.0 ± 0.5	59.8 ± 4.7	85.7 ± 12.9
VAL182Cγ2	2493 ± 282	61.2 ± 19.3	0.3 ± 0.2	12.5 ± 0.5	18.5 ± 0.8
VAL191Cγ1	2703 ± 225	65.7 ± 19.6	0.2 ± 0.2	5.4 ± 0.2	8.0 ± 0.2
LEU205Cδ1	8445 ± 2915	99.3 ± 12.2	3.9 ± 2.0	12.4 ± 4.4	16.7 ± 5.5
VAL226Cγ2	1428 ± 1653	99.8 ± 6.0	2.2 ± 0.9	2.6 ± 1.1	2.8 ± 1.5
LEU227Cδ2	4144 ± 2105	99.6 ± 1.4	6.6 ± 1.5	11.0 ± 6.7	11.9 ± 6.7
ILE246Cδ1	4889 ± 4676	50.0 ± 19.9	0.2 ± 0.8	3.4 ± 2.3	5.0 ± 3.4
VAL255Cγ2	2409 ± 1913	99.9 ± 0.9	5.0 ± 1.4	2.3 ± 1.9	2.4 ± 2.0
VAL288Cγ1	1182 ± 224	50.0 ± 20.6	0.1 ± 0.2	2.3 ± 0.1	3.4 ± 0.2
ILE303Cδ1	46 ± 743	93.6 ± 6.4	1.9 ± 0.4	3.0 ± 0.6	3.0 ± 0.7
VAL310Cγ1	794 ± 151	97.6 ± 0.5	0.7 ± 0.1	9.0 ± 0.3	10.9 ± 0.5
ILE315Cδ1	1275 ± 2589	77.6 ± 20.4	0.1 ± 0.5	2.6 ± 1.2	3.8 ± 2.0
ILE335Cδ1	2469 ± 969	94.1 ± 15.6	1.6 ± 0.4	50.1 ± 3.2	64.4 ± 7.3

Table 5.3. Results of the individual fits of methyl side chains in PKA-C/Balanol complex that have chemical exchange (R_{ex} > 2 s-1) measured using ^{13}C CPMG at 700 MHz and 850 MHz.

	k_{ex} (s^{-1})	Pa (%)	Δω (ppm)	R_{ex} (700 MHz, s^{-1})	R_{ex} (850 MHz, s^{-1})
ILE46Cδ1	390 ± 222	50.0 ± 19.1	0.1 ± 0.3	6.0 ± 9.2	9.0 ± 11
LEU49Cδ1	50 ± 113	91.7 ± 14.4	0.4 ± 0.2	4.2 ± 2.7	4.2 ± 4.1
VAL57Cγ2	14 ± 13	74.0 ± 6.3	0.8 ± 0.1	5.3 ± 0.3	5.3 ± 0.3
VAL80Cγ1	231 ± 540	94.8 ± 7.8	4.8 ± 0.5	12.1 ± 2.6	12.0 ± 2.7
VAL80Cγ2	97 ± 74	90.9 ± 6.7	0.6 ± 0.1	8.9 ± 0.5	8.9 ± 0.7
ILE85Cδ1	93 ± 45	91.8 ± 2.6	1.2 ± 0.04	7.8 ± 0.1	7.8 ± 0.1
LEU89Cδ2	527 ± 172	50.0 ± 20.4	0.1 ± 0.1	4.4 ± 2.7	6.5 ± 5.5
ILE94Cδ1	77 ± 77	81.6 ± 14.1	0.2 ± 0.2	13.4 ± 12.0	13.9 ± 15.3
LEU95Cδ1	13 ± 94	73.4 ± 14.4	0.4 ± 0.2	5.1 ± 4.5	5.1 ± 6.6
LEU103Cδ1	16 ± 142	86.5 ± 15.4	0.5 ± 0.2	2.6 ± 4.6	2.6 ± 6.1
VAL104Cγ1	871 ± 347	50.0 ± 22.2	0.1 ± 0.3	2.3 ± 0.6	3.4 ± 0.8
VAL104Cγ2	4 ± 3	71.7 ± 9.6	0.4 ± 0.1	3.1 ± 1.5	3.1 ± 1.5
VAL119Cγ1	1193 ± 304	64.6 ± 20.8	0.1 ± 0.2	2.2 ± 0.2	3.3 ± 0.4
VAL119Cγ2	1782 ± 389	82.0 ± 18.4	0.3 ± 0.3	6.8 ± 0.5	10.1 ± 0.7
LEU132Cδ1	456 ± 179	94.8 ± 21.1	0.2 ± 0.2	3.7 ± 2.1	5.1 ± 3.8
LEU152Cδ1	3695 ± 3996	75.7 ± 22.1	0.2 ± 1.1	2.3 ± 1.5	3.3 ± 2.2
LEU160Cδ2	2225 ± 1786	99.8 ± 0.8	2.8 ± 0.9	3.5 ± 1.9	3.9 ± 2.3
LEU173Cδ1	22 ± 67	77.4 ± 6.2	3.9 ± 0.3	6.3 ± 0.8	6.3 ± 0.8
LEU198Cδ2	67 ± 184	94.9 ± 16.8	0.3 ± 0.3	3.3 ± 2.1	3.3 ± 3.2
VAL288Cγ1	2040 ± 315	77.2 ± 20	0.2 ± 0.3	3.2 ± 0.2	4.7 ± 0.2
ILE303Cδ1	2449 ± 1121	99.2 ± 12.9	1.6 ± 0.5	6.6 ± 0.8	8.4 ± 1.6

Table 5.4. Results of the individual fits of methyl side chains in PKA-C/H89 complex that have chemical exchange (R_{ex} > 2 s^{-1}) measured using ^{13}C CPMG at 700 MHz and 850 MHz.

	k_{ex} (s^{-1})	Pa (%)	Δω (ppm)	R_{ex} (700 MHz, s^{-1})	R_{ex} (850 MHz, s^{-1})
LEU49Cδ1	667 ± 438	99.0 ± 8.8	0.9 ± 0.3	4.4 ± 0.4	4.9 ± 0.8
VAL57Cγ2	36 ± 382	90.6 ± 7.1	1.4 ± 0.3	3.6 ± 0.5	3.6 ± 0.6
LEU95Cδ2	780 ± 285	96.2 ± 21	0.3 ± 0.2	4.2 ± 0.5	5.8 ± 0.9
LEU103Cδ1	1238 ± 944	50.0 ± 20.9	0.1 ± 0.6	3.6 ± 0.9	5.3 ± 1.4
VAL104Cγ2	725 ± 32	50.0 ± 21.5	0.1 ± 0.2	3.6 ± 0.9	5.4 ± 1.6
LEU160Cδ2	1837 ± 669	85.5 ± 18.9	0.2 ± 0.4	3.7 ± 0.4	5.5 ± 0.7
LEU172Cδ1	57 ± 374	93.3 ± 5.0	2.4 ± 0.3	3.9 ± 0.6	3.9 ± 0.6
ILE335Cδ1	420 ± 248	50.0 ± 20.2	0.1 ± 0.3	3.2 ± 4.2	4.8 ± 5.9

Table 5.5. Group fit of ^{13}C CPMG parameters of methyl side chains in PKA-C bound to ATPγN.

	k_{ex} = 2400 ± 200 s^{-1}		P_A = 92.8 ± 0.4 %
	R_{ex} (700 MHz, s^{-1})	R_{ex} (850 MHz, s^{-1})	Δω (ppm)
Leu74Cδ1	20.3 ± 1.7	28.7 ± 2.3	0.82 ± 0.04
Ile94Cδ1	9.4 ± 1.2	13.6 ± 1.8	0.54 ± 0.04
Leu103Cδ1	5.8 ± 1.3	8.4 ± 1.9	0.42 ± 0.05
Leu106Cδ1	11.2 ± 1.1	16.1 ± 1.6	0.60 ± 0.04
Leu116Cδ2	5.6 ± 1.9	8.2 ± 2.7	0.42 ± 0.08
Ile150Cδ1	33.8 ± 1.8	46.3 ± 1.4	1.09 ± 0.04
Leu172Cδ2	24.8 ± 1.6	34.7 ± 2.1	0.92 ± 0.04
Leu173Cδ1	18.8 ± 2.0	26.6 ± 2.7	0.79 ± 0.05
Ile180Cδ1	57.9 ± 2.4	75.0 ± 3.4	1.54 ± 0.04
Val182Cγ2	12.5 ± 1.3	18.0 ± 1.9	0.63 ± 0.04
Val191Cγ1	5.4 ± 1.3	7.9 ± 1.9	0.41 ± 0.05
Ile335Cδ1	51.1 ± 2.4	67.3 ± 3.0	1.42 ± 0.04

Table 5.6. Group fit of ^{13}C CPMG parameters of methyl side chains in PKA-C bound to balanol.

	$k_{ex} = 90 \pm 50\ s^{-1}$		$P_A = 90.9 \pm 3.9\ \%$
	R_{ex} (700 MHz, s^{-1})	R_{ex} (850 MHz, s^{-1})	$\Delta\omega$ (ppm)
Val80Cγ2	7.8 $\pm$ 0.3	7.8 $\pm$ 0.3	0.69 ± 0.06
Ile85Cδ1	7.9 $\pm$ 0.4	7.9 $\pm$ 0.4	1.20 ± 0.08
Leu89Cδ2	7.0 $\pm$ 0.7	7.3 $\pm$ 0.5	0.25 ± 0.02
Ile94Cδ1	7.3 $\pm$ 0.5	7.5 $\pm$ 0.4	0.30 ± 0.02
Leu95Cδ1	6.9 $\pm$ 0.7	7.2 $\pm$ 0.6	0.23 ± 0.02
Leu103Cδ1	6.6 $\pm$ 0.9	7.0 $\pm$ 0.7	0.20 ± 0.02
Val104Cγ1	6.5 $\pm$ 1.0	6.9 $\pm$ 0.8	0.19 ± 0.02

Table 5.7. Results of the individual fits of ^{13}C CEST for the methyl side chains of PKA-C in the absence (Apo) and presence of nucleotide (ATPγN) or inhibitor (balanol and H89) measured at 900 MHz.

	k_{ex} (s^{-1})	Pa (%)	Δω (ppm)	χ^2_{red}
Apo PKA-C				
L95 Cδ2	457 ± 174	95.2 ± 0.6	2.48 ± 0.06	0.83
I150 Cδ1	804 ± 123	94.4 ± 0.5	1.24 ± 0.04	0.75
Val104 Cγ2	599 ± 243	96.6 ± 0.6	-1.55 ± 0.09	1.53
PKA-C/ATPγN				
V80 Cγ1	47 ± 60	91.7 ± 8.7	-3.58 ± 1.66	1.14
I85 Cδ1	337 ± 79	97.3 ± 0.2	-1.04 ± 0.03	1.86
PKA-C/Balanol				
V80 Cγ1	93 ± 17	93.2 ± 0.7	-4.45 ± 0.01	0.97
I85 Cδ1	209 ± 31	94.7 ± 0.3	-1.14 ± 0.01	1.69
L173 Cδ1	39 ± 25	92.5 ± 2.5	-3.58 ± 0.04	1.7
PKA-C/H89				
L49 Cδ1	51 ± 17	95.5 ± 0.9	1.09 ± 0.05	1.2
L172 Cδ1	42 ± 12	95.2 ± 1.4	1.61 ± 0.02	1.1

Table 5.8. R_{ex} values for the different states of PKA-C (apo, ATPγN-bound, balanol-bound, and H89 bound) measured using ^{15}N TROSY Hahn Echo measurements at 850 MHz and 27°C.

Residue	*R_{ex} (s^{-1})*			
	apo	*ATPγN-bound*	*Balanol-bound*	*H89-bound*
3	11.8 ± 4.6	21.4 ± 5.7	15.0 ± 2.4	20.9 ± 3.7
4	10.8 ± 1.2	11.1 ± 0.8	10.6 ± 0.7	13.7 ± 1.0
5	11.8 ± 1.3	11.9 ± 0.9	10.5 ± 0.7	13.7 ± 1.0
6	15.4 ± 2.0	12.2 ± 1.1	12.0 ± 1.0	15.2 ± 1.3
7	11.8 ± 1.2	11.5 ± 0.8	10.1 ± 0.6	13.0 ± 0.9
8	11.4 ± 1.1	12.1 ± 1.0	12.0 ± 0.9	16.6 ± 1.3
9	12.1 ± 1.6	11.4 ± 1.0	11.0 ± 0.9	15.1 ± 1.3
10	14.5 ± 1.9	14.2 ± 1.3	13.7 ± 1.2	18.7 ± 1.6
11	11.0 ± 1.2	11.8 ± 1.0	13.2 ± 1.1	16.0 ± 1.3
12	9.2 ± 0.9	9.7 ± 0.8	13.9 ± 1.2	13.1 ± 1.0
13	10.4 ± 1.2	6.5 ± 0.5	10.8 ± 1.1	11.4 ± 1.0
14	9.8 ± 1.5	5.9 ± 0.7	7.3 ± 0.8	7.9 ± 0.8
15	4.8 ± 0.8	0.10 ± 0.01	8.4 ± 1.4	3.2 ± 0.4
16	5.4 ± 0.8	7.5 ± 0.9	11.6 ± 1.5	9.1 ± 1.1
17	ND	1.5 ± 0.2	2.2 ± 0.3	5.6 ± 0.7
18	3.8 ± 0.6	-1.2 ± 0.1	-1.8 ± 0.3	ND
19	ND	2.9 ± 0.5	3.8 ± 0.4	8.2 ± 1.1
20	13.6 ± 4.4	2.6 ± 0.3	ND	ND
21	-0.5 ± 0.1	0.8 ± 0.1	5.4 ± 0.6	-0.20 ± 0.02
24	1.5 ± 0.3	-3.1 ± 0.5	-1.9 ± 0.3	-1.7 ± 0.2
25	ND	-2.6 ± 0.4	-1.2 ± 0.1	2.9 ± 0.3
26	ND	-1.2 ± 0.2	-2.6 ± 0.4	0.5 ± 0.1
27	3.7 ± 0.9	2.9 ± 0.6	-0.8 ± 0.1	ND
28	-0.6 ± 0.1	-1.1 ± 0.2	-2.2 ± 0.3	0.8 ± 0.1
29	ND	1.3 ± 0.3	-1.9 ± 0.3	1.4 ± 0.2
30	3.6 ± 1.4	2.6 ± 0.6	6.9 ± 0.8	15.5 ± 2.1
31	2.9 ± 0.9	3.3 ± 0.7	7.1 ± 1.7	10.3 ± 2.1
32	2.4 ± 0.5	1.1 ± 0.2	ND	1.2 ± 0.2
34	ND	4.9 ± 0.6	4.7 ± 0.4	7.8 ± 0.8
35	6.5 ± 0.8	12.3 ± 1.3	5.4 ± 0.5	9.1 ± 0.9
36	ND	ND	7.6 ± 1.3	14.3 ± 2.5
37	41.8 ± 23.4	48.5 ± 27.7	12.5 ± 2.0	16.2 ± 2.9
38	ND	11.2 ± 1.8	6.3 ± 0.9	5.0 ± 0.6
39	-2.1 ± 0.3	0.10 ± 0.01	ND	-1.6 ± 0.2
40	3.5 ± 0.7	ND	2.8 ± 0.4	ND

41	0.5 ± 0.1	3.6 ± 0.5	0.8 ± 0.1	ND
42	-0.10 ± 0.03	ND	-1.3 ± 0.2	-2.0 ± 0.3
43	ND	1.8 ± 0.3	3.2 ± 0.5	-1.1 ± 0.1
44	ND	5.6 ± 0.8	3.4 ± 0.5	7.9 ± 1.3
45	5.4 ± 0.8	3.1 ± 0.4	5.4 ± 0.6	7.8 ± 0.9
46	9.7 ± 1.6	4.9 ± 1.1	6.6 ± 1.4	ND
48	ND	ND	22.8 ± 5.5	29.5 ± 9.0
49	13.2 ± 3.7	16.5 ± 5.8	ND	10.3 ± 2.9
50	5.4 ± 1.8	ND	ND	3.6 ± 1.0
52	12.9 ± 2.7	ND	1.4 ± 0.2	6.6 ± 1.1
55	0.7 ± 0.1	17.3 ± 9.8	5.5 ± 0.9	2.5 ± 0.4
56	16.8 ± 3.3	ND	ND	ND
58	6.0 ± 1.1	17.4 ± 5.3	3.3 ± 0.5	8.8 ± 1.7
59	15.2 ± 3.8	23.7 ± 8.4	2.4 ± 0.4	9.2 ± 2.0
60	2.1 ± 0.4	2.7 ± 0.6	2.2 ± 0.4	4.7 ± 0.9
61	-1.8 ± 0.3	-2.4 ± 0.5	6.2 ± 0.6	3.3 ± 0.6
62	0.6 ± 0.1	3.5 ± 0.7	0.7 ± 0.1	3.7 ± 0.7
63	2.6 ± 0.5	-3.5 ± 0.6	-1.6 ± -0.2	-0.30 ± 0.05
64	3.2 ± 0.6	0.8 ± 0.1	3.9 ± 0.5	4.3 ± 0.5
65	ND	1.3 ± 0.3	0.20 ± 0.05	7.6 ± 1.0
66	0.3 ± 0.1	-0.30 ± 0.05	-0.9 ± 0.1	ND
67	7.0 ± 0.8	-1.1 ± 0.1	ND	ND
68	6.0 ± 1.1	8.3 ± 1.2	2.2 ± 0.3	8.3 ± 1.1
69	10.5 ± 2.1	7.7 ± 1.4	4.3 ± 0.5	7.5 ± 1.6
70	6.0 ± 1.2	5.2 ± 1.0	1.0 ± 0.1	3.3 ± 0.6
71	9.0 ± 1.5	7.4 ± 1.3	5.7 ± 0.8	17.7 ± 3.1
72	10.6 ± 2.7	ND	0.10 ± 0.02	7.7 ± 1.8
73	17.0 ± 4.8	ND	ND	3.9 ± 0.5
74	3.8 ± 0.7	9.8 ± 2.3	-0.3 ± 0.1	8.0 ± 1.5
76	4.6 ± 0.9	9.5 ± 2.2	2.2 ± 0.2	4.4 ± 0.8
77	5.2 ± 1.1	6.9 ± 1.6	10.4 ± 1.8	ND
78	ND	ND	ND	3.0 ± 0.5
79	ND	ND	ND	0.2 ± 0.04
80	-1.3 ± 0.3	5.7 ± 1.3	6.2 ± 1.3	ND
81	15.8 ± 5.5	7.7 ± 1.9	ND	ND
82	ND	ND	-0.40 ± 0.04	0.10 ± 0.03
83	-3.6 ± 0.8	0.20 ± 0.03	ND	3.5 ± 0.7
84	9.5 ± 2.3	20.2 ± 5.7	ND	6.9 ± 1.3
85	7.2 ± 1.8	ND	ND	ND

88	8.4 ± 2.1	ND	ND	ND
90	3.0 ± 0.6	5.0 ± 1.0	-5.0 ± 1.3	1.1 ± 0.4
91	3.7 ± 0.8	ND	ND	ND
92	1.6 ± 0.4	ND	ND	ND
94	24.5 ± 14	ND	ND	ND
95	1.9 ± 0.4	ND	ND	ND
96	6.7 ± 1.3	7.4 ± 3.0	1.7 ± 0.3	4.4 ± 0.6
97	-3.5 ± 0.6	11.4 ± 2.9	ND	0.007 ± 0.001
98	0.7 ± 0.2	ND	-1.4 ± 0.2	-2.3 ± 0.4
99	3.7 ± 0.8	0.7 ± 0.1	2.0 ± 0.3	ND
100	5.2 ± 0.9	3.1 ± 0.5	2.9 ± 0.3	ND
102	ND	0.9 ± 0.2	-1.6 ± 0.3	-2.9 ± 0.5
103	0.6 ± 0.1	-9.0 ± 2.2	0.20 ± 0.02	-4.9 ± 0.8
104	0.4 ± 0.1	ND	ND	ND
106	12.7 ± 2.4	3.4 ± 0.6	6.9 ± 0.8	ND
107	5.5 ± 1.5	ND	3.0 ± 0.5	9.4 ± 2.4
108	4.7 ± 1.0	6.5 ± 1.5	2.1 ± 0.6	ND
109	5.0 ± 1.3	4.7 ± 0.8	3.1 ± 0.4	ND
110	8.9 ± 1.9	8.9 ± 2.2	4.3 ± 0.6	8.3 ± 1.4
111	5.1 ± 0.9	4.2 ± 0.6	7.4 ± 1.5	7.3 ± 1.0
112	4.7 ± 0.9	3.7 ± 0.6	2.0 ± 0.3	5.8 ± 0.9
113	5.3 ± 1.0	7.6 ± 1.3	6.0 ± 0.8	ND
114	-0.8 ± 0.2	0.4 ± 0.1	3.4 ± 0.5	ND
115	4.0 ± 1.1	4.8 ± 1.3	6.2 ± 1.5	8.0 ± 1.8
116	2.5 ± 0.4	8.0 ± 1.9	3.9 ± 0.6	2.0 ± 0.4
117	7.9 ± 1.5	9.3 ± 2.1	6.0 ± 1.1	11 ± 1.9
118	2.8 ± 0.5	9.5 ± 1.5	7.3 ± 0.8	8.6 ± 1.6
119	6.5 ± 1.4	ND	3.7 ± 0.8	8.7 ± 1.7
120	13.9 ± 3.6	ND	6.2 ± 1.2	9.3 ± 2.1
122	ND	9.0 ± 3.5	ND	ND
123	20.0 ± 6.1	ND	ND	17.6 ± 5.3
124	28.3 ± 10.8	ND	6.0 ± 0.9	3.0 ± 0.5
125	28.5 ± 10.3	14.5 ± 10.4	-2.4 ± 0.4	1.3 ± 0.2
126	ND	ND	-7.9 ± 1.0	-6.4 ± 1.1
128	ND	ND	11.1 ± 1.7	17.2 ± 5.0
133	9.4 ± 2.3	ND	ND	ND
134	4.6 ± 1.2	ND	-2.6 ± 0.4	2.6 ± 0.4
136	ND	11.4 ± 2.7	3.6 ± 0.7	4.5 ± 0.8
137	ND	5.2 ± 0.7	2.0 ± 0.2	4.0 ± 0.5

138	26.8 ± 6.9	ND	ND	3.7 ± 0.4
139	13.0 ± 2.8	8.5 ± 1.3	6.5 ± 0.9	9.3 ± 1.5
140	9.2 ± 1.7	6.9 ± 1.1	6.3 ± 0.9	12.0 ± 1.7
142	0.4 ± 0.1	3.5 ± 0.6	-1.5 ± 0.2	0.20 ± 0.04
143	5.2 ± 1.5	6.9 ± 2.1	-4.6 ± 1.3	5.8 ± 1.5
144	2.5 ± 1.0	-0.2 ± 0.1	-1.1 ± 0.3	-1.8 ± 0.6
145	-2.5 ± 0.5	ND	-6.9 ± 1.6	ND
147	12.9 ± 6.4	10.6 ± 5.6	3.9 ± 1.2	4.2 ± 1.8
148	-5.9 ± 2.1	ND	4.4 ± 1.2	7.9 ± 2.5
149	1.9 ± 0.5	7.1 ± 2.0	-4.8 ± 1.2	7.5 ± 2.0
150	-9.9 ± 3.7	-10.7 ± 5.5	-4.3 ± 1.2	ND
151	6.1 ± 2.1	3.6 ± 1.7	-0.4 ± 0.1	10.5 ± 1.3
155	12.9 ± 3.4	4.7 ± 1.7	10.2 ± 3.3	14.2 ± 4.1
160	-1.2 ± 0.3	ND	ND	-2.9 ± 0.4
161	-0.3 ± 0.1	7.2 ± 1.4	-1.9 ± 0.2	1.8 ± 0.3
162	3.1 ± 0.6	12.2 ± 2.7	1.7 ± 0.2	2.1 ± 0.3
163	ND	31.0 ± 9.2	ND	ND
164	9.1 ± 4.4	ND	ND	19.8 ± 8.2
165	27.5 ± 20.3	ND	13.1 ± 4	20.6 ± 7.2
166	2.6 ± 0.6	15.7 ± 5.1	0.10 ± 0.02	1.1 ± 0.2
174	ND	12.2 ± 3.5	0.030 ± 0.004	ND
175	12.3 ± 3.1	5.8 ± 1.3	-0.10 ± 0.02	6.2 ± 1.1
176	5.6 ± 1.0	5.2 ± 1.4	3.4 ± 0.4	3.4 ± 0.6
177	ND	-0.10 ± 0.01	2.2 ± 0.3	4.5 ± 0.6
178	-4.0 ± 1.3	-7.4 ± 2.5	-3.2 ± 0.9	2.4 ± 0.7
179	0.10 ± 0.02	-0.4 ± 0.1	-0.3 ± 0.1	4.8 ± 0.9
180	20.4 ± 6.6	ND	6.1 ± 1.2	9.4 ± 2.0
181	ND	29.6 ± 15.2	ND	ND
182	21.1 ± 5.7	2.4 ± 1.0	2.0 ± 0.4	ND
185	2.1 ± 0.4	ND	ND	ND
186	17.4 ± 6.3	ND	3.7 ± 1.0	8.6 ± 1.7
187	8.8 ± 2.6	ND	ND	ND
188	6.4 ± 1.7	ND	4.9 ± 0.9	-0.3 ± 0.1
189	3.7 ± 0.7	ND	ND	ND
190	8.7 ± 2.0	11.9 ± 2.3	5.6 ± 0.7	5.4 ± 0.7
191	8.1 ± 1.4	10.2 ± 2.3	11.4 ± 1.5	9.1 ± 1.3
192	4.5 ± 0.9	11.4 ± 2.4	5.0 ± 0.7	ND
193	13.8 ± 2.8	10.5 ± 2.4	13.7 ± 2.1	10.8 ± 1.3
194	ND	4.6 ± 0.4	5.2 ± 0.4	ND

195	-1.2 ± 0.2	ND	0.7 ± 0.1	ND
196	2.4 ± 0.6	6.7 ± 1.4	-2.2 ± 0.3	-9.2 ± 1.4
197	20.7 ± 10.2	ND	13.6 ± 4.2	10.7 ± 2.7
198	3.8 ± 0.7	8.4 ± 1.7	6.7 ± 1.0	10.7 ± 2.0
199	4.1 ± 0.9	ND	2.4 ± 0.3	6.4 ± 1.2
200	5.5 ± 1.2	ND	4.9 ± 0.9	5.5 ± 0.8
203	10.3 ± 5.0	ND	16.0 ± 5.6	13.5 ± 5.2
204	ND	ND	ND	4.8 ± 0.8
205	5.8 ± 1.1	ND	-4.8 ± 0.7	ND
206	1.3 ± 0.3	2.5 ± 0.7	-1.0 ± 0.1	-0.6 ± 0.1
208	20.3 ± 5.3	13.4 ± 3.5	13.8 ± 2.5	20.5 ± 5.1
209	15.6 ± 4.9	19.0 ± 6.1	11.3 ± 3.4	17.5 ± 5.2
210	0.5 ± 0.1	5.4 ± 1.4	-1.1 ± 0.2	-1.3 ± 0.3
211	ND	0.4 ± 0.1	1.7 ± 0.2	ND
212	1.8 ± 0.3	ND	-0.20 ± 0.03	-1.3 ± 0.2
213	ND	1.6 ± 0.3	2.6 ± 0.3	2.4 ± 0.4
214	9.0 ± 1.9	17.8 ± 4.6	11.2 ± 1.9	9.4 ± 1.7
215	ND	3.8 ± 0.6	ND	ND
216	5.3 ± 1.1	1.5 ± 0.3	2.7 ± 0.4	2.6 ± 0.4
217	1.2 ± 0.2	6.3 ± 0.9	4.9 ± 0.5	ND
219	4.8 ± 1.2	6.8 ± 1.6	3.7 ± 0.6	1.4 ± 0.3
220	ND	ND	0.20 ± 0.04	0.10 ± 0.02
221	-0.8 ± 0.1	3.7 ± 0.6	-2.8 ± 0.3	-1.1 ± 0.1
222	-2.0 ± 0.5	-4.2 ± 1.7	-8.0 ± 2.6	ND
225	0.9 ± 0.4	1.8 ± 0.8	-6.2 ± 1.6	-0.9 ± 0.3
226	1.3 ± 0.6	2.4 ± 1.1	-1.7 ± 0.5	4.9 ± 1.8
227	ND	ND	4.3 ± 0.6	ND
228	5.2 ± 2.2	4.5 ± 2.6	0.10 ± 0.03	8.4 ± 3.4
230	22.5 ± 10.8	ND	3.4 ± 1.1	5.3 ± 2.1
231	ND	ND	ND	5.9 ± 2.4
232	ND	1.9 ± 0.4	0.10 ± 0.01	ND
233	19.9 ± 11.1	7.3 ± 3.4	7.2 ± 2.5	12.8 ± 5.6
234	33.3 ± 16.1	4.4 ± 1.2	6.2 ± 1.5	6.9 ± 1.5
238	ND	ND	1.5 ± 0.2	ND
240	0.20 ± 0.04	3.0 ± 0.5	3.8 ± 0.9	0.3 ± 0.1
241	0.7 ± 0.1	5.3 ± 0.9	5.0 ± 0.7	4.6 ± 0.6
242	0.7 ± 0.1	1.2 ± 0.1	2.3 ± 0.2	3.3 ± 0.3
244	2.4 ± 0.4	4.2 ± 0.6	5.5 ± 0.6	3.8 ± 0.5
245	-2.6 ± 0.5	-4.1 ± 0.7	-3.3 ± 0.4	-2.7 ± 0.4

246	-3.7 ± 0.7	-1.2 ± 0.2	-4.6 ± 0.7	-4.0 ± 0.7
247	ND	3.1 ± 0.6	ND	ND
248	ND	-2.1 ± 0.3	-2.3 ± 0.3	-3.0 ± 0.4
249	-2.3 ± 0.4	ND	-3.3 ± 0.3	-1.1 ± 0.1
250	2.3 ± 0.4	ND	0.6 ± 0.1	ND
251	1.1 ± 0.2	1.4 ± 0.3	0.10 ± 0.02	1.5 ± 0.2
252	ND	-1.6 ± 0.2	0.30 ± 0.03	-2.0 ± 0.3
253	-0.10 ± 0.02	1.2 ± 0.2	-2.2 ± 0.2	0.5 ± 0.1
254	0.6 ± 0.1	0.30 ± 0.03	5.1 ± 0.5	1.7 ± 0.2
255	2.4 ± 0.2	7.0 ± 0.6	1.9 ± 0.1	ND
256	0.20 ± 0.03	-1.2 ± 0.1	-0.20 ± 0.02	0.5 ± 0.1
257	ND	19.6 ± 8.2	11.2 ± 3.6	ND
261	-4.2 ± 0.7	-3.2 ± 0.4	-4.1 ± 0.5	-3.7 ± 0.4
262	11.7 ± 2.6	9.3 ± 1.8	12.0 ± 2.0	17.0 ± 3.3
263	6.0 ± 1.5	6.4 ± 1.6	3.0 ± 0.5	6.4 ± 1.2
264	ND	0.7 ± 0.1	0.6 ± 0.1	4.9 ± 0.6
265	7.3 ± 2.7	5.1 ± 1.9	ND	-0.7 ± 0.2
266	ND	ND	9.2 ± 1.9	ND
267	ND	4.1 ± 0.5	-2.9 ± 0.4	ND
268	ND	0.9 ± 0.4	1.4 ± 0.4	2.2 ± 0.7
269	4.6 ± 1.7	ND	1.7 ± 0.5	13.2 ± 5.0
272	ND	6.9 ± 2.9	ND	ND
273	15.1 ± 5.6	ND	ND	ND
274	-2.1 ± 0.5	-1.5 ± 0.5	-4.0 ± 0.9	-2.1 ± 0.5
275	0.5 ± 0.1	3.5 ± 0.6	1.1 ± 0.1	5.9 ± 0.7
276	3.9 ± 0.5	4.3 ± 0.6	1.9 ± 0.2	1.2 ± 0.2
277	4.4 ± 0.7	2.3 ± 0.3	-0.20 ± 0.02	4.2 ± 0.6
278	0.9 ± 0.3	4.5 ± 1.1	0.10 ± 0.02	7.8 ± 1.7
279	1.6 ± 0.3	-9.2 ± 2.0	-1.6 ± 0.3	-0.20 ± 0.04
280	-4.0 ± 0.7	-5.0 ± 0.8	-5.8 ± 0.7	-4.1 ± 0.6
281	1.1 ± 0.2	1.9 ± 0.3	1.0 ± 0.1	3.1 ± 0.5
282	-0.2 ± 0.1	2.2 ± 0.8	2.7 ± 0.7	ND
283	3.7 ± 0.6	-2.0 ± 0.4	1.2 ± 0.2	3.1 ± 0.5
284	2.2 ± 0.5	ND	ND	ND
286	ND	-1.2 ± 0.2	3.8 ± 0.5	5.1 ± 0.7
287	0.8 ± 0.1	0.8 ± 0.1	1.4 ± 0.2	2.1 ± 0.3
289	1.3 ± 0.2	-0.4 ± 0.1	-3.0 ± 0.4	3.0 ± 0.4
290	-3.8 ± 0.7	-5.1 ± 0.8	-4.6 ± 0.6	-3.9 ± 0.6
291	-3.4 ± 0.7	-2.3 ± 0.4	-3.5 ± 0.4	-4.0 ± 0.6

292	-5.1 ± 1.4	-1.8 ± 0.6	-3.9 ± 1.3	-3.2 ± 0.9
293	-0.30 ± 0.04	0.10 ± 0.01	-0.9 ± 0.1	0.30 ± 0.03
294	-5.1 ± 1.3	-4.0 ± 1.1	-3.9 ± 1.0	-1.9 ± 0.4
295	-3.1 ± 0.5	-0.7 ± 0.1	-0.8 ± 0.1	0.20 ± 0.03
296	31.9 ± 8.9	29.9 ± 7.0	31.2 ± 5.9	44.3 ± 11.5
297	-1.2 ± 0.5	ND	ND	5.0 ± 0.7
298	-1.8 ± 0.3	-0.9 ± 0.1	-1.6 ± 0.2	-0.5 ± 0.1
299	7.7 ± 2.6	2.5 ± 0.7	3.0 ± 0.6	6.0 ± 1.3
300	ND	2.9 ± 0.3	2.3 ± 0.4	6.2 ± 0.6
301	-0.6 ± 0.1	-1.1 ± 0.2	-1.8 ± 0.2	0.9 ± 0.1
302	-0.2 ± 0	-0.5 ± 0.1	0.10 ± 0.02	0.7 ± 0.1
303	ND	ND	-1.7 ± 0.2	ND
304	-2.6 ± 0.4	-3.5 ± 0.5	1.1 ± 0.1	0.6 ± 0.1
305	ND	32.8 ± 8.1	-3.1 ± 0.6	1.7 ± 0.4
306	-0.3 ± 0.1	-3.1 ± 0.8	1.1 ± 0.2	4.4 ± 0.8
307	1.2 ± 0.2	2.3 ± 0.4	-0.8 ± 0.1	ND
308	ND	-2.3 ± 0.4	-2.7 ± 0.4	0.7 ± 0.1
309	5.0 ± 1.0	0.4 ± 0.1	2.7 ± 0.4	4.6 ± 0.8
310	-2.2 ± 0.4	-3.1 ± 0.6	-3.6 ± 0.5	-3.2 ± 0.5
311	0.8 ± 0.1	-0.9 ± 0.1	0.40 ± 0.05	2.1 ± 0.3
312	0.9 ± 0.1	3.3 ± 0.4	2.2 ± 0.2	3.3 ± 0.4
314	6.2 ± 1.9	2.1 ± 0.4	1.0 ± 0.2	-5.1 ± 0.7
315	11.0 ± 1.8	3.8 ± 0.5	4.5 ± 0.5	1.7 ± 0.2
317	ND	6.0 ± 2.7	0.5 ± 0.2	5.5 ± 0.6
318	4.1 ± 0.8	ND	4.2 ± 0.4	4.9 ± 0.4
320	ND	ND	4.3 ± 0.6	6.2 ± 0.8
322	16.3 ± 3.9	14.7 ± 5.5	19.7 ± 4.4	21.9 ± 5.3
323	ND	0.4 ± 0.1	ND	-1.1 ± 0.2
325	ND	ND	ND	1.7 ± 0.4
326	ND	ND	ND	8.5 ± 1.6
329	ND	ND	ND	4.1 ± 0.4
331	ND	13.0 ± 7.5	3.7 ± 0.4	6.9 ± 0.7
332	ND	33.4 ± 16.4	5.8 ± 0.6	11.6 ± 1.3
333	ND	ND	4.5 ± 0.9	ND
334	7.8 ± 1.3	11.1 ± 1.6	3.6 ± 0.3	6.5 ± 0.7
335	ND	4.9 ± 0.6	ND	6.2 ± 0.7
336	2.5 ± 0.3	5.2 ± 0.6	5.6 ± 0.5	4.7 ± 0.5
337	9.3 ± 1.3	37.2 ± 8.2	10.3 ± 1.1	ND
338	ND	-0.6 ± 0.1	1.5 ± 0.2	1.0 ± 0.2

339	ND	4.6 ± 0.6	3.5 ± 0.5	5.8 ± 1.0
340	-0.6 ± 0.1	-2.4 ± 0.3	0.10 ± 0.02	-0.30 ± 0.03
341	3.3 ± 0.4	1.8 ± 0.2	2.3 ± 0.2	5.9 ± 0.6
342	5.2 ± 0.9	5.0 ± 0.8	3.4 ± 0.4	5.5 ± 0.8
343	6.3 ± 1.2	2.8 ± 0.4	3.7 ± 0.5	9.5 ± 1.3
344	3.5 ± 0.6	4.2 ± 0.6	1.7 ± 0.2	6.1 ± 0.9
345	ND	1.6 ± 0.2	2.7 ± 0.4	3.8 ± 0.5
346	5.3 ± 1.6	9.4 ± 2.7	14.5 ± 3.9	ND
347	-1.8 ± 0.4	-1.4 ± 0.2	12.3 ± 2.9	-1.9 ± 0.4
348	1.5 ± 0.3	3.1 ± 0.5	2.2 ± 0.4	3.1 ± 0.5
349	6.9 ± 1.2	5.9 ± 0.9	5.2 ± 0.7	7.0 ± 1.0
350	ND	-0.30 ± 0.04	-5.6 ± 0.6	-3.0 ± 0.4

ND=not determined due to broadening or overlap.

Table 5.9. HX-NOE values for the backbone residues the different states of PKA-C (apo, ATPγN-bound, balanol-bound, and H89-bound) measured on a 900 MHz spectrometer at 27°C.

Residue	*HX NOE*			
	apo	*ATPγN-bound*	*Balanol-bound*	*H89-bound*
3	-1.84 ± -0.05	-1.71 ± 0.11	-0.69 ± 0.03	-0.91 ± 0.03
4	-0.33 ± -0.01	-0.31 ± 0.01	-0.20 ± 0.01	-0.20 ± 0.01
5	-0.14 ± -0.01	-0.11 ± 0.01	ND	ND
6	-0.76 ± -0.01	-0.84 ± 0.02	-0.92 ± 0.02	-0.54 ± 0.01
7	0.32 ± 0.01	0.27 ± 0.01	0.490 ± 0.004	0.260 ± 0.005
8	0.240 ± 0.004	0.11 ± 0.01	0.21 ± 0.01	0.23 ± 0.01
9	0.29 ± 0.01	0.25 ± 0.01	0.33 ± 0.01	0.36 ± 0.01
10	0.52 ± 0.01	0.50 ± 0.01	0.52 ± 0.01	0.50 ± 0.01
11	0.45 ± 0.01	0.45 ± 0.01	0.48 ± 0.01	0.50 ± 0.01
12	0.52 ± 0.01	0.48 ± 0.01	0.49 ± 0.01	0.53 ± 0.01
13	0.48 ± 0.01	0.51 ± 0.01	0.62 ± 0.01	0.59 ± 0.01
14	0.60 ± 0.01	0.55 ± 0.02	0.62 ± 0.01	ND
15	ND	0.61 ± 0.03	1.00 ± 0.02	0.71 ± 0.01
16	0.66 ± 0.01	0.70 ± 0.02	0.70 ± 0.02	0.61 ± 0.01
17	ND	0.73 ± 0.02	0.74 ± 0.02	0.78 ± 0.01
18	0.79 ± 0.01	0.81 ± 0.02	0.83 ± 0.02	0.85 ± 0.01
19	ND	0.72 ± 0.05	0.88 ± 0.01	0.91 ± 0.01
20	ND	ND	0.81 ± 0.01	ND
21	0.82 ± 0.02	0.81 ± 0.03	0.80 ± 0.01	0.84 ± 0.01
24	0.92 ± 0.05	0.87 ± 0.03	0.87 ± 0.02	0.93 ± 0.02
25	0.91 ± 0.02	0.87 ± 0.03	0.91 ± 0.02	0.93 ± 0.01
26	ND	0.82 ± 0.03	0.82 ± 0.02	0.90 ± 0.02
27	0.83 ± 0.03	0.88 ± 0.03	0.91 ± 0.01	0.91 ± 0.02
28	0.86 ± 0.02	0.88 ± 0.03	0.80 ± 0.02	0.93 ± 0.02
29	ND	0.89 ± 0.03	0.77 ± 0.02	0.86 ± 0.02
30	0.89 ± 0.05	0.94 ± 0.04	0.73 ± 0.01	0.78 ± 0.02
31	0.77 ± 0.04	0.79 ± 0.03	0.96 ± 0.03	0.81 ± 0.02
32	0.76 ± 0.03	0.66 ± 0.03	ND	0.91 ± 0.02
34	ND	0.68 ± 0.02	0.68 ± 0.01	0.67 ± 0.01
35	0.67 ± 0.01	0.67 ± 0.02	0.66 ± 0.01	0.64 ± 0.01
36	ND	ND	0.81 ± 0.03	0.67 ± 0.02
37	0.78 ± 0.07	0.83 ± 0.06	0.79 ± 0.02	0.81 ± 0.02
38	ND	0.78 ± 0.02	0.91 ± 0.02	0.79 ± 0.01
39	0.86 ± 0.02	0.73 ± 0.02	ND	0.97 ± 0.01
40	0.87 ± 0.03	ND	0.88 ± 0.01	ND

41	0.86 ± 0.02	0.85 ± 0.02	0.87 ± 0.01	ND
42	0.89 ± 0.02	0.93 ± 0.02	0.93 ± 0.02	0.89 ± 0.02
43	ND	0.89 ± 0.03	0.82 ± 0.02	0.93 ± 0.01
44	ND	0.94 ± 0.02	0.91 ± 0.02	0.95 ± 0.02
45	0.79 ± 0.01	0.67 ± 0.07	0.84 ± 0.01	0.86 ± 0.01
46	0.88 ± 0.02	0.89 ± 0.03	0.94 ± 0.03	ND
48	ND	ND	0.89 ± 0.03	0.94 ± 0.03
49	0.85 ± 0.03	0.85 ± 0.06	ND	0.96 ± 0.03
50	0.74 ± 0.05	ND	ND	0.88 ± 0.03
52	0.69 ± 0.02	ND	0.98 ± 0.02	0.88 ± 0.02
55	0.78 ± 0.02	0.86 ± 0.09	0.81 ± 0.02	0.88 ± 0.02
56	0.78 ± 0.02	ND	ND	ND
58	0.90 ± 0.02	1.01 ± 0.05	0.88 ± 0.02	0.97 ± 0.02
59	0.84 ± 0.03	1.05 ± 0.05	0.92 ± 0.03	0.91 ± 0.02
60	0.93 ± 0.03	0.91 ± 0.03	0.97 ± 0.03	0.89 ± 0.02
61	0.83 ± 0.02	0.91 ± 0.03	0.89 ± 0.01	0.94 ± 0.02
62	0.84 ± 0.02	0.96 ± 0.03	0.89 ± 0.02	0.93 ± 0.02
63	0.84 ± 0.02	0.85 ± 0.03	0.82 ± 0.02	0.80 ± 0.02
64	0.34 ± 0.02	0.34 ± 0.02	0.29 ± 0.01	ND
65	ND	ND	0.68 ± 0.03	0.89 ± 0.01
66	0.91 ± 0.03	ND	0.98 ± 0.02	ND
67	0.82 ± 0.01	ND	0.97 ± 0.02	ND
68	0.87 ± 0.02	0.94 ± 0.04	0.92 ± 0.02	0.92 ± 0.01
69	0.79 ± 0.02	0.88 ± 0.03	0.89 ± 0.01	0.91 ± 0.03
70	0.85 ± 0.02	0.93 ± 0.03	0.95 ± 0.01	0.99 ± 0.02
71	0.88 ± 0.02	0.92 ± 0.02	0.89 ± 0.02	0.80 ± 0.02
72	0.94 ± 0.03	1.00 ± 0.16	0.96 ± 0.02	0.96 ± 0.02
73	0.89 ± 0.04	ND	ND	0.92 ± 0.02
74	0.90 ± 0.02	0.93 ± 0.03	0.95 ± 0.03	0.94 ± 0.02
76	0.94 ± 0.02	0.84 ± 0.03	0.49 ± 0.01	0.88 ± 0.02
77	0.84 ± 0.02	0.84 ± 0.04	0.89 ± 0.02	ND
78	0.92 ± 0.03	0.84 ± 0.05	ND	0.80 ± 0.02
79	ND	ND	ND	0.88 ± 0.03
80	0.91 ± 0.03	ND	0.85 ± 0.03	0.91 ± 0.01
81	0.94 ± 0.02	0.92 ± 0.04	ND	ND
82	0.91 ± 0.02	0.74 ± 0.04	0.88 ± 0.01	0.89 ± 0.02
83	0.85 ± 0.02	1.01 ± 0.04	ND	0.95 ± 0.02
84	0.83 ± 0.04	0.87 ± 0.05	ND	0.89 ± 0.02
85	0.77 ± 0.03	ND	ND	ND

88	0.87 ± 0.06	ND	ND	ND
90	0.86 ± 0.02	1.02 ± 0.03	0.94 ± 0.04	0.89 ± 0.06
91	0.92 ± 0.03	ND	ND	ND
94	0.76 ± 0.05	ND	ND	ND
95	0.88 ± 0.03	ND	ND	ND
96	0.86 ± 0.02	0.99 ± 0.05	0.96 ± 0.02	0.69 ± 0.01
97	0.87 ± 0.03	0.90 ± 0.04	ND	0.86 ± 0.02
98	0.90 ± 0.04	0.87 ± 0.03	0.91 ± 0.02	0.87 ± 0.02
99	0.86 ± 0.03	ND	0.88 ± 0.02	ND
100	0.78 ± 0.02	0.89 ± 0.03	0.86 ± 0.01	ND
102	ND	1.00 ± 0.04	0.89 ± 0.03	0.99 ± 0.03
103	0.86 ± 0.02	0.89 ± 0.03	0.88 ± 0.02	0.90 ± 0.02
104	0.97 ± 0.05	ND	ND	ND
106	0.86 ± 0.02	0.83 ± 0.03	0.91 ± 0.02	ND
107	0.80 ± 0.03	ND	0.85 ± 0.02	0.94 ± 0.03
108	0.84 ± 0.03	0.96 ± 0.04	0.91 ± 0.04	ND
109	1.01 ± 0.04	0.85 ± 0.03	0.86 ± 0.02	ND
110	0.94 ± 0.03	0.97 ± 0.04	0.88 ± 0.02	0.91 ± 0.02
111	0.9 ± 0.02	0.94 ± 0.02	0.98 ± 0.05	0.93 ± 0.01
112	0.88 ± 0.02	0.88 ± 0.03	1.01 ± 0.02	0.92 ± 0.01
113	0.87 ± 0.02	0.90 ± 0.02	0.88 ± 0.02	ND
114	0.87 ± 0.03	ND	0.87 ± 0.01	ND
115	0.90 ± 0.02	0.78 ± 0.03	1.06 ± 0.04	1.03 ± 0.03
116	0.94 ± 0.02	0.90 ± 0.04	0.95 ± 0.02	1.00 ± 0.02
117	0.93 ± 0.02	0.93 ± 0.03	0.90 ± 0.03	0.98 ± 0.02
118	0.89 ± 0.02	0.90 ± 0.02	0.91 ± 0.01	0.89 ± 0.02
119	0.94 ± 0.04	0.85 ± 0.02	1.03 ± 0.05	0.94 ± 0.02
120	1.00 ± 0.04	1.10 ± 0.23	0.89 ± 0.03	0.86 ± 0.01
122	ND	0.88 ± 0.09	ND	ND
123	0.70 ± 0.04	ND	ND	1.06 ± 0.04
124	0.75 ± 0.05	0.73 ± 0.09	ND	0.81 ± 0.02
125	0.66 ± 0.05	ND	0.80 ± 0.02	0.93 ± 0.02
126	ND	ND	0.98 ± 0.02	0.93 ± 0.02
128	ND	ND	1.01 ± 0.02	0.93 ± 0.03
133	0.82 ± 0.03	ND	ND	ND
134	0.90 ± 0.03	ND	0.98 ± 0.03	0.87 ± 0.02
136	ND	0.82 ± 0.04	0.89 ± 0.03	0.86 ± 0.02
137	ND	0.77 ± 0.03	0.74 ± 0.01	0.93 ± 0.02
138	0.90 ± 0.02	ND	ND	0.85 ± 0.01

139	0.91 ± 0.02	0.96 ± 0.03	0.88 ± 0.01	0.89 ± 0.02
140	0.96 ± 0.02	0.91 ± 0.02	0.88 ± 0.02	0.89 ± 0.01
142	0.89 ± 0.02	0.93 ± 0.03	0.92 ± 0.02	0.94 ± 0.02
143	0.69 ± 0.04	0.80 ± 0.06	0.92 ± 0.05	1.01 ± 0.04
144	1.11 ± 0.1	1.01 ± 0.12	0.86 ± 0.09	0.99 ± 0.07
145	0.79 ± 0.04	ND	0.95 ± 0.02	ND
147	ND	0.78 ± 0.14	1.07 ± 0.10	0.99 ± 0.10
148	0.87 ± 0.08	1.02 ± 0.13	0.92 ± 0.08	1.07 ± 0.07
149	0.55 ± 0.05	0.29 ± 0.05	1.09 ± 0.08	0.58 ± 0.04
150	0.54 ± 0.03	0.82 ± 0.12	1.19 ± 0.11	0.84 ± 0.06
151	0.87 ± 0.12	1.11 ± 0.12	0.85 ± 0.02	0.77 ± 0.01
155	0.87 ± 0.04	1.08 ± 0.11	0.89 ± 0.06	0.88 ± 0.04
160	0.82 ± 0.05	ND	ND	ND
161	0.84 ± 0.02	0.84 ± 0.02	0.99 ± 0.01	0.89 ± 0.01
162	0.89 ± 0.02	1.10 ± 0.04	0.90 ± 0.02	0.91 ± 0.01
163	ND	0.97 ± 0.07	ND	ND
164	ND	ND	ND	0.96 ± 0.05
165	1.11 ± 0.10	ND	0.88 ± 0.05	0.97 ± 0.04
166	0.82 ± 0.03	0.96 ± 0.08	0.74 ± 0.02	0.78 ± 0.02
174	ND	0.84 ± 0.04	0.84 ± 0.01	ND
175	0.87 ± 0.02	0.95 ± 0.04	0.94 ± 0.03	0.90 ± 0.02
176	0.81 ± 0.02	0.84 ± 0.07	0.75 ± 0.01	0.92 ± 0.02
177	ND	0.96 ± 0.03	0.88 ± 0.01	0.93 ± 0.01
178	1.07 ± 0.05	0.80 ± 0.05	0.84 ± 0.05	0.96 ± 0.04
179	0.90 ± 0.03	0.98 ± 0.05	0.98 ± 0.03	0.98 ± 0.02
180	0.93 ± 0.04	ND	0.82 ± 0.02	0.87 ± 0.02
181	ND	1.00 ± 0.09	ND	ND
182	0.87 ± 0.03	ND	0.96 ± 0.04	ND
186	0.78 ± 0.04	ND	0.90 ± 0.04	0.79 ± 0.02
187	0.72 ± 0.03	ND	ND	ND
188	0.92 ± 0.03	ND	0.81 ± 0.02	0.87 ± 0.02
189	0.91 ± 0.03	ND	ND	ND
190	0.83 ± 0.03	0.83 ± 0.04	0.90 ± 0.02	0.88 ± 0.02
191	0.90 ± 0.02	0.95 ± 0.05	0.84 ± 0.01	0.87 ± 0.01
192	0.69 ± 0.01	ND	0.73 ± 0.01	ND
193	ND	0.36 ± 0.03	0.49 ± 0.01	0.64 ± 0.01
194	ND	ND	0.69 ± 0.01	ND
195	0.86 ± 0.02	ND	0.84 ± 0.02	ND
196	0.91 ± 0.03	ND	0.87 ± 0.01	0.89 ± 0.01

197	1.02 ± 0.07	ND	0.88 ± 0.05	0.91 ± 0.03
198	0.89 ± 0.02	0.82 ± 0.03	0.84 ± 0.02	0.88 ± 0.02
199	ND	ND	0.85 ± 0.02	0.93 ± 0.02
200	0.73 ± 0.02	ND	0.78 ± 0.03	0.79 ± 0.02
203	0.91 ± 0.08	ND	0.65 ± 0.04	0.86 ± 0.06
205	0.92 ± 0.02	ND	0.90 ± 0.02	ND
206	0.90 ± 0.03	ND	0.84 ± 0.02	0.91 ± 0.02
208	0.89 ± 0.03	0.89 ± 0.04	0.95 ± 0.02	0.99 ± 0.03
209	0.96 ± 0.04	0.97 ± 0.05	0.88 ± 0.03	0.89 ± 0.03
210	1.03 ± 0.03	0.94 ± 0.05	0.82 ± 0.02	0.91 ± 0.03
211	ND	ND	0.94 ± 0.02	ND
212	0.84 ± 0.02	0.91 ± 0.02	0.88 ± 0.02	0.88 ± 0.01
213	0.88 ± 0.02	0.76 ± 0.03	0.83 ± 0.02	0.91 ± 0.02
214	0.83 ± 0.02	1.00 ± 0.04	0.85 ± 0.02	0.92 ± 0.02
215	ND	ND	0.85 ± 0.01	ND
216	0.99 ± 0.03	0.87 ± 0.04	0.91 ± 0.02	0.91 ± 0.02
217	0.72 ± 0.02	ND	0.85 ± 0.01	ND
218	ND	0.81 ± 0.04	ND	0.94 ± 0.01
219	1.00 ± 0.03	0.97 ± 0.04	0.99 ± 0.03	0.94 ± 0.02
220	ND	0.98 ± 0.08	0.97 ± 0.02	0.95 ± 0.02
221	0.94 ± 0.02	0.95 ± 0.03	0.94 ± 0.02	0.93 ± 0.02
222	0.80 ± 0.02	0.89 ± 0.06	ND	ND
225	1.02 ± 0.13	0.77 ± 0.09	0.88 ± 0.09	0.90 ± 0.07
226	ND	0.96 ± 0.14	0.92 ± 0.10	1.08 ± 0.09
227	ND	0.96 ± 0.19	0.83 ± 0.02	ND
228	1.02 ± 0.13	1.10 ± 0.16	0.90 ± 0.09	0.92 ± 0.09
230	ND	0.76 ± 0.10	0.97 ± 0.10	0.85 ± 0.06
231	ND	1.03 ± 0.19	ND	0.84 ± 0.05
232	ND	0.91 ± 0.03	0.75 ± 0.01	0.94 ± 0.02
233	ND	1.13 ± 0.24	0.89 ± 0.10	0.92 ± 0.09
234	0.99 ± 0.09	0.94 ± 0.04	0.97 ± 0.02	0.92 ± 0.02
238	ND	ND	0.96 ± 0.02	ND
240	0.71 ± 0.03	0.64 ± 0.05	0.77 ± 0.04	0.79 ± 0.04
241	0.59 ± 0.02	0.61 ± 0.03	0.62 ± 0.01	0.63 ± 0.02
242	0.50 ± 0.01	0.57 ± 0.02	0.60 ± 0.01	0.60 ± 0.01
244	0.64 ± 0.02	0.77 ± 0.02	0.67 ± 0.01	ND
245	0.68 ± 0.02	0.68 ± 0.02	0.69 ± 0.02	0.76 ± 0.02
246	0.81 ± 0.02	0.92 ± 0.04	0.82 ± 0.02	0.83 ± 0.02
247	ND	ND	0.88 ± 0.01	ND

248	0.83 ± 0.02	0.86 ± 0.02	0.83 ± 0.01	0.84 ± 0.01
249	0.89 ± 0.02	ND	0.80 ± 0.01	0.83 ± 0.02
250	0.86 ± 0.03	0.85 ± 0.04	0.97 ± 0.02	1.01 ± 0.03
251	0.92 ± 0.03	0.94 ± 0.03	0.87 ± 0.02	1.01 ± 0.02
252	0.88 ± 0.02	0.87 ± 0.02	0.81 ± 0.01	0.88 ± 0.01
253	0.74 ± 0.01	0.81 ± 0.02	0.74 ± 0.01	0.84 ± 0.01
254	0.69 ± 0.01	0.69 ± 0.02	0.66 ± 0.01	0.70 ± 0.01
255	ND	ND	0.57 ± 0.01	ND
256	0.75 ± 0.01	0.79 ± 0.02	0.80 ± 0.01	0.76 ± 0.01
257	ND	ND	0.84 ± 0.03	ND
261	0.91 ± 0.01	0.91 ± 0.02	0.86 ± 0.01	0.91 ± 0.01
262	0.91 ± 0.02	0.90 ± 0.03	0.99 ± 0.02	0.93 ± 0.02
263	0.95 ± 0.02	0.89 ± 0.03	0.96 ± 0.02	0.88 ± 0.02
264	ND	0.98 ± 0.02	0.87 ± 0.01	0.94 ± 0.01
265	0.70 ± 0.08	1.11 ± 0.11	1.07 ± 0.08	0.93 ± 0.05
266	ND	ND	0.85 ± 0.03	ND
267	ND	ND	0.98 ± 0.01	ND
268	0.87 ± 0.09	1.18 ± 0.13	0.92 ± 0.08	0.97 ± 0.06
269	1.02 ± 0.10	0.98 ± 0.11	0.83 ± 0.09	0.85 ± 0.07
273	0.97 ± 0.10	ND	ND	ND
274	0.66 ± 0.09	0.94 ± 0.08	0.99 ± 0.07	1.00 ± 0.05
275	0.86 ± 0.02	0.90 ± 0.03	0.91 ± 0.02	0.95 ± 0.01
276	0.80 ± 0.01	0.83 ± 0.02	0.89 ± 0.01	0.97 ± 0.02
277	0.85 ± 0.02	0.85 ± 0.02	ND	0.82 ± 0.01
278	0.93 ± 0.04	0.89 ± 0.04	0.77 ± 0.02	0.92 ± 0.03
279	0.86 ± 0.02	0.85 ± 0.03	0.84 ± 0.02	0.92 ± 0.02
280	0.79 ± 0.02	0.86 ± 0.02	0.87 ± 0.02	0.81 ± 0.02
281	0.97 ± 0.02	1.00 ± 0.02	0.88 ± 0.01	0.97 ± 0.02
282	0.84 ± 0.05	1.02 ± 0.07	0.93 ± 0.04	ND
283	0.87 ± 0.02	0.88 ± 0.03	0.96 ± 0.02	0.90 ± 0.02
284	0.88 ± 0.03	ND	ND	ND
286	ND	ND	0.75 ± 0.01	0.84 ± 0.02
287	0.88 ± 0.02	0.93 ± 0.02	0.88 ± 0.01	0.91 ± 0.01
289	0.85 ± 0.02	0.97 ± 0.02	0.88 ± 0.02	0.90 ± 0.01
290	0.90 ± 0.02	0.82 ± 0.02	0.93 ± 0.02	0.89 ± 0.02
291	0.91 ± 0.02	0.92 ± 0.03	0.88 ± 0.02	0.89 ± 0.02
292	ND	0.95 ± 0.06	0.91 ± 0.04	0.97 ± 0.04
293	0.93 ± 0.02	0.86 ± 0.02	0.96 ± 0.01	0.93 ± 0.01
294	1.12 ± 0.08	0.86 ± 0.05	0.94 ± 0.03	0.91 ± 0.03

295	0.92 ± 0.02	0.95 ± 0.02	0.90 ± 0.01	0.87 ± 0.01
296	ND	0.88 ± 0.02	0.96 ± 0.02	0.98 ± 0.02
297	0.93 ± 0.10	0.86 ± 0.10	0.98 ± 0.09	0.86 ± 0.02
298	0.87 ± 0.01	0.91 ± 0.02	0.93 ± 0.01	0.92 ± 0.01
299	0.81 ± 0.03	0.70 ± 0.03	0.81 ± 0.02	0.93 ± 0.03
300	ND	ND	0.86 ± 0.03	0.62 ± 0.01
301	0.82 ± 0.02	0.81 ± 0.02	ND	0.82 ± 0.01
302	0.86 ± 0.02	0.87 ± 0.02	0.85 ± 0.02	0.85 ± 0.01
303	0.81 ± 0.03	ND	0.87 ± 0.01	ND
304	0.90 ± 0.02	0.87 ± 0.02	0.89 ± 0.02	0.90 ± 0.01
305	ND	0.96 ± 0.08	0.97 ± 0.03	0.89 ± 0.03
306	ND	0.93 ± 0.07	0.91 ± 0.04	0.82 ± 0.02
307	0.81 ± 0.02	0.86 ± 0.03	0.86 ± 0.02	ND
308	ND	1.01 ± 0.03	0.98 ± 0.02	0.88 ± 0.01
309	0.82 ± 0.02	0.92 ± 0.03	0.95 ± 0.02	0.90 ± 0.02
310	0.81 ± 0.03	0.78 ± 0.04	0.77 ± 0.02	0.87 ± 0.02
311	0.82 ± 0.01	0.77 ± 0.02	0.84 ± 0.01	0.83 ± 0.01
312	0.63 ± 0.01	0.72 ± 0.02	0.72 ± 0.01	0.72 ± 0.01
314	1.01 ± 0.05	0.96 ± 0.04	0.94 ± 0.02	0.86 ± 0.02
315	0.82 ± 0.02	0.85 ± 0.02	0.89 ± 0.01	0.89 ± 0.01
317	ND	ND	1.02 ± 0.09	0.67 ± 0.01
318	ND	0.78 ± 0.03	0.68 ± 0.01	0.69 ± 0.01
320	ND	ND	0.24 ± 0.02	0.30 ± 0.02
322	0.55 ± 0.02	0.74 ± 0.08	0.64 ± 0.03	0.69 ± 0.03
323	ND	ND	ND	0.86 ± 0.02
325	ND	ND	ND	0.79 ± 0.03
326	ND	ND	ND	0.88 ± 0.02
329	ND	ND	ND	0.79 ± 0.01
331	0.57 ± 0.02	0.71 ± 0.05	0.74 ± 0.01	0.79 ± 0.01
332	ND	0.82 ± 0.06	0.72 ± 0.01	0.70 ± 0.01
333	ND	0.73 ± 0.03	0.93 ± 0.03	ND
334	0.58 ± 0.02	0.49 ± 0.02	0.48 ± 0.01	0.55 ± 0.01
335	ND	0.53 ± 0.02	ND	0.56 ± 0.01
336	0.62 ± 0.01	0.53 ± 0.02	0.61 ± 0.01	0.62 ± 0.01
337	0.66 ± 0.02	ND	0.51 ± 0.01	ND
338	ND	0.93 ± 0.02	0.85 ± 0.02	0.91 ± 0.02
339	ND	0.77 ± 0.02	0.77 ± 0.02	0.83 ± 0.02
340	0.89 ± 0.01	0.89 ± 0.02	0.90 ± 0.02	0.87 ± 0.01
341	0.76 ± 0.01	0.76 ± 0.02	0.87 ± 0.01	0.85 ± 0.01

342	0.88 ± 0.02	0.91 ± 0.02	0.90 ± 0.01	0.87 ± 0.01
343	0.89 ± 0.02	0.91 ± 0.02	0.82 ± 0.01	0.81 ± 0.01
344	0.83 ± 0.02	0.85 ± 0.02	0.78 ± 0.02	0.79 ± 0.01
345	0.77 ± 0.01	0.84 ± 0.02	0.83 ± 0.01	0.82 ± 0.02
346	0.80 ± 0.04	0.81 ± 0.04	0.93 ± 0.04	ND
347	1.08 ± 0.03	0.90 ± 0.03	ND	1.00 ± 0.03
348	0.90 ± 0.03	0.80 ± 0.03	0.93 ± 0.03	0.86 ± 0.02
349	0.87 ± 0.02	0.90 ± 0.02	0.83 ± 0.01	0.91 ± 0.01
350	ND	0.84 ± 0.02	0.81 ± 0.01	0.81 ± 0.01

ND=not determined due to broadening or overlap.

Bibliography

1. Krebs, E.G., *The phosphorylation of proteins: a major mechanism for biological regulation.* Biochemical Society Transactions, 1985. **13**(5): p. 813-820.
2. Manning, G., D.B. Whyte, R. Martinez, T. Hunter, and S. Sudarsanam, *The protein kinase complement of the human genome.* Science, 2002. **298**(5600): p. 1912-34.
3. Pearce, L.R., D. Komander, and D.R. Alessi, *The nuts and bolts of AGC protein kinases.* Nat Rev Mol Cell Biol, 2010. **11**(1): p. 9-22.
4. Collett, M.S. and R.L. Erikson, *Protein kinase activity associated with the avian sarcoma virus src gene product.* Proc Natl Acad Sci U S A, 1978. **75**(4): p. 2021-4.
5. Lahiry, P., A. Torkamani, N.J. Schork, and R.A. Hegele, *Kinase mutations in human disease: interpreting genotype-phenotype relationships.* Nat Rev Genet, 2010. **11**(1): p. 60-74.
6. Naranjan, S.D., *Role of protein kinase C and protein kinase A in heart function in health and disease.* Experimental and clinical cardiology., 1999. **4**(1): p. 7.
7. George, S., J.J. Rochford, C. Wolfrum, S.L. Gray, S. Schinner, J.C. Wilson, M.A. Soos, P.R. Murgatroyd, R.M. Williams, C.L. Acerini, D.B. Dunger, D. Barford, A.M. Umpleby, N.J. Wareham, H.A. Davies, A.J. Schafer, M. Stoffel, S. O'Rahilly, and I. Barroso, *A family with severe insulin resistance and diabetes due to a mutation in AKT2.* Science, 2004. **304**(5675): p. 1325-8.
8. Knighton, D.R., J.H. Zheng, L.F. Ten Eyck, V.A. Ashford, N.H. Xuong, S.S. Taylor, and J.M. Sowadski, *Crystal structure of the catalytic subunit of cyclic adenosine monophosphate-dependent protein kinase.* Science, 1991. **253**(5018): p. 407-14.
9. Knighton, D.R., J.H. Zheng, L.F. Ten Eyck, N.H. Xuong, S.S. Taylor, and J.M. Sowadski, *Structure of a peptide inhibitor bound to the catalytic subunit of cyclic adenosine monophosphate-dependent protein kinase.* Science, 1991. **253**(5018): p. 414-20.
10. Gill, G.N. and L.D. Garren, *A cyclic-3',5'-adenosine monophosphate dependent protein kinase from the adrenal cortex: comparison with a cyclic AMP binding protein.* Biochem Biophys Res Commun, 1970. **39**(3): p. 335-43.
11. Brostrom, M.A., E.M. Reimann, D.A. Walsh, and E.G. Krebs, *A cyclic 3',5'-amp-stimulated protein kinase from cardiac muscle.* Adv Enzyme Regul, 1970. **8**: p. 191-203.
12. Shabb, J.B., *Physiological substrates of cAMP-dependent protein kinase.* Chem Rev, 2001. **101**(8): p. 2381-411.
13. Kemp, B.E., *Phosphorylation of acyl and dansyl derivatives of the peptide Leu-Arg-Arg-Ala-Ser-Leu-Gly by the cAMP-dependent protein kinase.* Journal of Biological Chemistry, 1980. **255**(7): p. 2914-2918.

14. Johnson, D.A., P. Akamine, E. Radzio-Andzelm, M. Madhusudan, and S.S. Taylor, *Dynamics of cAMP-dependent protein kinase.* Chem Rev, 2001. **101**(8): p. 2243-70.
15. Hanks, S.K. and T. Hunter, *Protein kinases 6. The eukaryotic protein kinase superfamily: kinase (catalytic) domain structure and classification.* FASEB J, 1995. **9**(8): p. 576-96.
16. Meharena, H.S., P. Chang, M.M. Keshwani, K. Oruganty, A.K. Nene, N. Kannan, S.S. Taylor, and A.P. Kornev, *Deciphering the structural basis of eukaryotic protein kinase regulation.* PLoS Biol, 2013. **11**(10): p. e1001680.
17. Meharena, H.S., X. Fan, L.G. Ahuja, M.M. Keshwani, C.L. McClendon, A.M. Chen, J.A. Adams, and S.S. Taylor, *Decoding the Interactions Regulating the Active State Mechanics of Eukaryotic Protein Kinases.* PLOS Biology, 2016. **14**(11): p. e2000127.
18. De Bondt, H.L., J. Rosenblatt, J. Jancarik, H.D. Jones, D.O. Morgan, and S.H. Kim, *Crystal structure of cyclin-dependent kinase 2.* Nature, 1993. **363**(6430): p. 595-602.
19. Jeffrey, P.D., A.A. Russo, K. Polyak, E. Gibbs, J. Hurwitz, J. Massague, and N.P. Pavletich, *Mechanism of CDK activation revealed by the structure of a cyclinA-CDK2 complex.* Nature, 1995. **376**(6538): p. 313-20.
20. Taylor, S.S. and A.P. Kornev, *Protein kinases: evolution of dynamic regulatory proteins.* Trends Biochem Sci, 2011. **36**(2): p. 65-77.
21. Taylor, S.S., M.M. Keshwani, J.M. Steichen, and A.P. Kornev, *Evolution of the eukaryotic protein kinases as dynamic molecular switches.* Philos Trans R Soc Lond B Biol Sci, 2012. **367**(1602): p. 2517-28.
22. Yang, J., S.M. Garrod, M.S. Deal, G.S. Anand, V.L. Woods Jr, and S. Taylor, *Allosteric Network of cAMP-dependent Protein Kinase Revealed by Mutation of Tyr204 in the P+1 Loop.* Journal of Molecular Biology, 2005. **346**(1): p. 191-201.
23. Kornev, A.P., S.S. Taylor, and L.F. Ten Eyck, *A helix scaffold for the assembly of active protein kinases.* Proc Natl Acad Sci U S A, 2008. **105**(38): p. 14377-82.
24. Dar, A.C., T.E. Dever, and F. Sicheri, *Higher-order substrate recognition of eIF2alpha by the RNA-dependent protein kinase PKR.* Cell, 2005. **122**(6): p. 887-900.
25. Herberg, F.W., B. Zimmermann, M. McGlone, and S.S. Taylor, *Importance of the A-helix of the catalytic subunit of cAMP-dependent protein kinase for stability and for orienting subdomains at the cleft interface.* Protein Science, 1997. **6**(3): p. 569-579.
26. Kannan, N., N. Haste, S.S. Taylor, and A.F. Neuwald, *The hallmark of AGC kinase functional divergence is its C-terminal tail, a cis-acting regulatory module.* Proceedings of the National Academy of Sciences, 2007. **104**(4): p. 1272-1277.
27. Romano, R.A., N. Kannan, A.P. Kornev, C.J. Allison, and S.S. Taylor, *A chimeric mechanism for polyvalent trans-phosphorylation of PKA by PDK1.* Protein Sci, 2009. **18**(7): p. 1486-97.
28. Narayana, N., S. Cox, S. Shaltiel, S.S. Taylor, and N. Xuong, *Crystal structure of a polyhistidine-tagged recombinant catalytic subunit of cAMP-dependent protein*

kinase complexed with the peptide inhibitor PKI(5-24) and adenosine. Biochemistry, 1997. **36**(15): p. 4438-48.
29. Batkin, M., I. Schvartz, and S. Shaltiel, *Snapping of the Carboxyl Terminal Tail of the Catalytic Subunit of PKA onto Its Core: Characterization of the Sites by Mutagenesis†.* Biochemistry, 2000. **39**(18): p. 5366-5373.
30. Keshwani, M.M., C. Klammt, S. von Daake, Y. Ma, A.P. Kornev, S. Choe, P.A. Insel, and S.S. Taylor, *Cotranslational cis-phosphorylation of the COOH-terminal tail is a key priming step in the maturation of cAMP-dependent protein kinase.* Proceedings of the National Academy of Sciences, 2012. **109**(20): p. E1221–E1229.
31. Kornev, A.P., N.M. Haste, S.S. Taylor, and L.F. Eyck, *Surface comparison of active and inactive protein kinases identifies a conserved activation mechanism.* Proc Natl Acad Sci U S A, 2006. **103**(47): p. 17783-8.
32. Shaw, A.S., A.P. Kornev, J. Hu, L.G. Ahuja, and S.S. Taylor, *Kinases and pseudokinases: lessons from RAF.* Mol Cell Biol, 2014. **34**(9): p. 1538-46.
33. Boudeau, J., D. Miranda-Saavedra, G.J. Barton, and D.R. Alessi, *Emerging roles of pseudokinases.* Trends Cell Biol, 2006. **16**(9): p. 443-52.
34. Taylor, S.S., A. Shaw, J. Hu, H.S. Meharena, and A. Kornev, *Pseudokinases from a structural perspective.* Biochem Soc Trans, 2013. **41**(4): p. 981-6.
35. Poulikakos, P.I., C. Zhang, G. Bollag, K.M. Shokat, and N. Rosen, *RAF inhibitors transactivate RAF dimers and ERK signalling in cells with wild-type BRAF.* Nature, 2010. **464**(7287): p. 427-30.
36. Hu, J., H. Yu, A.P. Kornev, J. Zhao, E.L. Filbert, S.S. Taylor, and A.S. Shaw, *Mutation that blocks ATP binding creates a pseudokinase stabilizing the scaffolding function of kinase suppressor of Ras, CRAF and BRAF.* Proc Natl Acad Sci U S A, 2011. **108**(15): p. 6067-72.
37. Zheng, J., D.R. Knighton, N.H. Xuong, S.S. Taylor, J.M. Sowadski, and L.F. Ten Eyck, *Crystal structures of the myristylated catalytic subunit of cAMP-dependent protein kinase reveal open and closed conformations.* Protein Sci, 1993. **2**(10): p. 1559-73.
38. Akamine, P., Madhusudan, J. Wu, N.H. Xuong, L.F. Ten Eyck, and S.S. Taylor, *Dynamic features of cAMP-dependent protein kinase revealed by apoenzyme crystal structure.* J Mol Biol, 2003. **327**(1): p. 159-71.
39. Narayana, N., S. Cox, X. Nguyen-huu, L.F. Ten Eyck, and S.S. Taylor, *A binary complex of the catalytic subunit of cAMP-dependent protein kinase and adenosine further defines conformational flexibility.* Structure, 1997. **5**(7): p. 921-35.
40. Masterson, L.R., C. Cheng, T. Yu, M. Tonelli, A. Kornev, S.S. Taylor, and G. Veglia, *Dynamics connect substrate recognition to catalysis in protein kinase A.* Nat Chem Biol, 2010. **6**(11): p. 821-8.
41. Masterson, L.R., L. Shi, E. Metcalfe, J. Gao, S.S. Taylor, and G. Veglia, *Dynamically committed, uncommitted, and quenched states encoded in protein kinase A revealed by NMR spectroscopy.* Proc Natl Acad Sci U S A, 2011. **108**(17): p. 6969-74.

42. Gangal, M., S. Cox, J. Lew, T. Clifford, S.M. Garrod, M. Aschbaher, S.S. Taylor, and D.A. Johnson, *Backbone Flexibility of Five Sites on the Catalytic Subunit of cAMP-Dependent Protein Kinase in the Open and Closed Conformations.* Biochemistry, 1998. **37**(39): p. 13728-13735.
43. Srivastava, A.K., L.R. McDonald, A. Cembran, J. Kim, L.R. Masterson, C.L. McClendon, S.S. Taylor, and G. Veglia, *Synchronous opening and closing motions are essential for cAMP-dependent protein kinase A signaling.* Structure, 2014. **22**(12): p. 1735-43.
44. Masterson, L.R., A. Mascioni, N.J. Traaseth, S.S. Taylor, and G. Veglia, *Allosteric cooperativity in protein kinase A.* Proc Natl Acad Sci U S A, 2008. **105**(2): p. 506-11.
45. Colledge, M. and J.D. Scott, *AKAPs: from structure to function.* Trends Cell Biol, 1999. **9**(6): p. 216-21.
46. Herberg, F.W. and S.S. Taylor, *Physiological inhibitors of the catalytic subunit of cAMP-dependent protein kinase: effect of magnesium-ATP on protein-protein interactions.* Biochemistry, 1993. **32**(50): p. 14015-14022.
47. Scott, J.D., E.H. Fischer, J.G. Demaille, and E.G. Krebs, *Identification of an inhibitory region of the heat-stable protein inhibitor of the cAMP-dependent protein kinase.* Proc Natl Acad Sci U S A, 1985. **82**(13): p. 4379-83.
48. Hauer, J.A., P. Barthe, S.S. Taylor, J. Parello, and A. Padilla, *Two well-defined motifs in the cAMP-dependent protein kinase inhibitor (PKIα) correlate with inhibitory and nuclear export function.* Protein Science, 1999. **8**(3): p. 545-553.
49. Wen, W., S.S. Taylor, and J.L. Meinkoth, *The Expression and Intracellular Distribution of the Heat-stable Protein Kinase Inhibitor Is Cell Cycle Regulated.* Journal of Biological Chemistry, 1995. **270**(5): p. 2041-2046.
50. Boehr, D.D., H.J. Dyson, and P.E. Wright, *An NMR perspective on enzyme dynamics.* Chem Rev, 2006. **106**(8): p. 3055-79.
51. Kern, D. and E.R. Zuiderweg, *The role of dynamics in allosteric regulation.* Curr Opin Struct Biol, 2003. **13**(6): p. 748-57.
52. Boehr, D.D., D. McElheny, H.J. Dyson, and P.E. Wright, *The dynamic energy landscape of dihydrofolate reductase catalysis.* Science, 2006. **313**(5793): p. 1638-42.
53. Carr, H.Y. and E.M. Purcell, *Effects of Diffusion on Free Precession in Nuclear Magnetic Resonance Experiments.* Physical Review, 1954. **94**(3): p. 630-638.
54. Meiboom, S. and D. Gill, *Modified Spin-Echo Method for Measuring Nuclear Relaxation Times.* Review of Scientific Instruments, 1958. **29**(8): p. 688-691.
55. Forsén, S. and R. Hoffman, *Study of Moderately Rapid Chemical Exchange Reactions by Means of Nuclear Magnetic Double Resonance.* The Journal of Chemical Physics, 1963. **39**(11): p. 2892-2901.
56. Vallurupalli, P., G. Bouvignies, and L.E. Kay, *Studying "invisible" excited protein states in slow exchange with a major state conformation.* J Am Chem Soc, 2012. **134**(19): p. 8148-61.
57. Wang, C., M. Rance, and A.G. Palmer, 3rd, *Mapping chemical exchange in proteins with MW > 50 kD.* J Am Chem Soc, 2003. **125**(30): p. 8968-9.

58. Palmer, A.G., 3rd, C.D. Kroenke, and J.P. Loria, *Nuclear magnetic resonance methods for quantifying microsecond-to-millisecond motions in biological macromolecules.* Methods Enzymol, 2001. **339**: p. 204-38.
59. Bloch, F., *Nuclear Induction.* Physical Review, 1946. **70**(7-8): p. 460-474.
60. McConnell, H.M., *Reaction Rates by Nuclear Magnetic Resonance.* The Journal of Chemical Physics, 1958. **28**(3): p. 430-431.
61. Ishima, R. and D.A. Torchia, *Estimating the time scale of chemical exchange of proteins from measurements of transverse relaxation rates in solution.* Journal of Biomolecular Nmr, 1999. **14**(4): p. 369-372.
62. Millet, O., J.P. Loria, C.D. Kroenke, M. Pons, and A.G. Palmer, *The static magnetic field dependence of chemical exchange linebroadening defines the NMR chemical shift time scale.* Journal of the American Chemical Society, 2000. **122**(12): p. 2867-2877.
63. Korzhnev, D.M., T.L. Religa, P. Lundstrom, A.R. Fersht, and L.E. Kay, *The folding pathway of an FF domain: characterization of an on-pathway intermediate state under folding conditions by (15)N, (13)C(alpha) and (13)C-methyl relaxation dispersion and (1)H/(2)H-exchange NMR spectroscopy.* J Mol Biol, 2007. **372**(2): p. 497-512.
64. Deverell, C., R.E. Morgan, and J.H. Strange, *Studies of chemical exchange by nuclear magnetic relaxation in the rotating frame.* Molecular Physics, 1970. **18**(4): p. 553-559.
65. Jeener, J., B.H. Meier, P. Bachmann, and R.R. Ernst, *Investigation of exchange processes by two-dimensional NMR spectroscopy.* The Journal of Chemical Physics, 1979. **71**(11): p. 4546-4553.
66. Palmer, A.G., 3rd and F. Massi, *Characterization of the dynamics of biomacromolecules using rotating-frame spin relaxation NMR spectroscopy.* Chem Rev, 2006. **106**(5): p. 1700-19.
67. Farrow, N.A., O. Zhang, J.D. Forman-Kay, and L.E. Kay, *A heteronuclear correlation experiment for simultaneous determination of 15N longitudinal decay and chemical exchange rates of systems in slow equilibrium.* Journal of biomolecular NMR, 1994. **4**(5): p. 727-34.
68. Loria, J.P., M. Rance, and A.G. Palmer, *A Relaxation-Compensated Carr−Purcell−Meiboom−Gill Sequence for Characterizing Chemical Exchange by NMR Spectroscopy.* Journal of the American Chemical Society, 1999. **121**(10): p. 2331-2332.
69. Carver, J.P. and R.E. Richards, *A general two-site solution for the chemical exchange produced dependence of T2 upon the carr-Purcell pulse separation.* Journal of Magnetic Resonance (1969), 1972. **6**(1): p. 89-105.
70. Jen, J., *Chemical exchange and nmr T2 relaxation—The multisite case.* Journal of Magnetic Resonance (1969), 1978. **30**(1): p. 111-128.
71. Davis, D.G., M.E. Perlman, and R.E. London, *Direct Measurements of the Dissociation-Rate Constant for Inhibitor-Enzyme Complexes via the T1ρ and T2 (CPMG) Methods.* Journal of Magnetic Resonance, Series B, 1994. **104**(3): p. 266-275.

72. Luz, Z. and S. Meiboom, *Nuclear Magnetic Resonance Study of the Protolysis of Trimethylammonium Ion in Aqueous Solution—Order of the Reaction with Respect to Solvent.* The Journal of Chemical Physics, 1963. **39**(2): p. 366-370.
73. Kroenke, C.D., J.P. Loria, L.K. Lee, M. Rance, and A.G. Palmer, *Longitudinal and transverse H-1-N-15 dipolar N-15 chemical shift anisotropy relaxation interference: Unambiguous determination of rotational diffusion tensors and chemical exchange effects in biological macromolecules.* Journal of the American Chemical Society, 1998. **120**(31): p. 7905-7915.
74. Fushman, D., N. Tjandra, and D. Cowburn, *Direct measurement of N-15 chemical shift anisotropy in solution.* Journal of the American Chemical Society, 1998. **120**(42): p. 10947-10952.
75. Palmer, A.G., N.J. Skelton, W.J. Chazin, P.E. Wright, and M. Rance, *Suppression of the effects of cross-correlation between dipolar and anisotropic chemical shift relaxation mechanisms in the measurement of spin-spin relaxation rates.* Molecular Physics, 1992. **75**(3): p. 699-711.
76. Farrow, N.A., R. Muhandiram, A.U. Singer, S.M. Pascal, C.M. Kay, G. Gish, S.E. Shoelson, T. Pawson, J.D. Forman-Kay, and L.E. Kay, *Backbone dynamics of a free and phosphopeptide-complexed Src homology 2 domain studied by 15N NMR relaxation.* Biochemistry, 1994. **33**(19): p. 5984-6003.
77. Vold, R.L., J.S. Waugh, M.P. Klein, and D.E. Phelps, *Measurement of Spin Relaxation in Complex Systems.* The Journal of Chemical Physics, 1968. **48**(8): p. 3831-3832.
78. Lipari, G. and A. Szabo, *Model-Free Approach to the Interpretation of Nuclear Magnetic-Resonance Relaxation in Macromolecules .2. Analysis of Experimental Results.* Journal of the American Chemical Society, 1982. **104**(17): p. 4559-4570.
79. Lipari, G. and A. Szabo, *Model-Free Approach to the Interpretation of Nuclear Magnetic-Resonance Relaxation in Macromolecules .1. Theory and Range of Validity.* Journal of the American Chemical Society, 1982. **104**(17): p. 4546-4559.
80. Goodey, N.M. and S.J. Benkovic, *Allosteric regulation and catalysis emerge via a common route.* Nat Chem Biol, 2008. **4**(8): p. 474-82.
81. Changeux, J.P. and S.J. Edelstein, *Allosteric mechanisms of signal transduction.* Science, 2005. **308**(5727): p. 1424-8.
82. Monod, J., J. Wyman, and J.P. Changeux, *On the Nature of Allosteric Transitions: A Plausible Model.* J Mol Biol, 1965. **12**: p. 88-118.
83. Perutz, M.F., *Stereochemistry of Cooperative Effects in Haemoglobin: Haem-Haem Interaction and the Problem of Allostery.* Nature, 1970. **228**(5273): p. 726-734.
84. Perutz, M.F., *Mechanisms of cooperativity and allosteric regulation in proteins.* Q Rev Biophys, 1989. **22**(2): p. 139-237.
85. Koshland, D.E., Jr., G. Nemethy, and D. Filmer, *Comparison of experimental binding data and theoretical models in proteins containing subunits.* Biochemistry, 1966. **5**(1): p. 365-85.
86. Cui, Q. and M. Karplus, *Allostery and cooperativity revisited.* Protein Sci, 2008. **17**(8): p. 1295-307.

87. Popovych, N., S. Sun, R.H. Ebright, and C.G. Kalodimos, *Dynamically driven protein allostery.* Nat Struct Mol Biol, 2006. **13**(9): p. 831-8.
88. Cooper, A. and D.T. Dryden, *Allostery without conformational change. A plausible model.* Eur Biophys J, 1984. **11**(2): p. 103-9.
89. Tsai, C.J., A. del Sol, and R. Nussinov, *Allostery: absence of a change in shape does not imply that allostery is not at play.* J Mol Biol, 2008. **378**(1): p. 1-11.
90. Ascenzi, P. and M. Fasano, *Allostery in a monomeric protein: the case of human serum albumin.* Biophys Chem, 2010. **148**(1-3): p. 16-22.
91. Gunasekaran, K., B. Ma, and R. Nussinov, *Is allostery an intrinsic property of all dynamic proteins?* Proteins, 2004. **57**(3): p. 433-43.
92. Kumar, S., B. Ma, C.J. Tsai, N. Sinha, and R. Nussinov, *Folding and binding cascades: dynamic landscapes and population shifts.* Protein Sci, 2000. **9**(1): p. 10-9.
93. McClendon, C.L., A.P. Kornev, M.K. Gilson, and S.S. Taylor, *Dynamic architecture of a protein kinase.* Proc Natl Acad Sci U S A, 2014. **111**(43): p. E4623-31.
94. Azam, M., M.A. Seeliger, N.S. Gray, J. Kuriyan, and G.Q. Daley, *Activation of tyrosine kinases by mutation of the gatekeeper threonine.* Nat Struct Mol Biol, 2008. **15**(10): p. 1109-18.
95. Hu, J., E.C. Stites, H. Yu, E.A. Germino, H.S. Meharena, P.J. Stork, A.P. Kornev, S.S. Taylor, and A.S. Shaw, *Allosteric activation of functionally asymmetric RAF kinase dimers.* Cell, 2013. **154**(5): p. 1036-46.
96. Mirsky, A.E. and L. Pauling, *On the Structure of Native, Denatured, and Coagulated Proteins.* Proc Natl Acad Sci U S A, 1936. **22**(7): p. 439-47.
97. Loh, S.N. and J.L. Markley. *Measurement of amide hydrogen deuterium/hydrogen fractionation factors in proteins by NMR spectroscopy*. 1993. Academic.
98. Schowen, K.B. and R.L. Schowen, *Solvent isotope effects of enzyme systems.* Methods Enzymol, 1982. **87**: p. 551-606.
99. Kreevoy, M.M., T. Liang, and K.C. Chang, *Structures and Isotopic Fractionation Factors of Complexes Aha-*. Journal of the American Chemical Society, 1977. **99**(15): p. 5207-5209.
100. Cleland, W.W., P.A. Frey, and J.A. Gerlt, *The low barrier hydrogen bond in enzymatic catalysis.* J Biol Chem, 1998. **273**(40): p. 25529-32.
101. Loh, S.N. and J.L. Markley, *Hydrogen bonding in proteins as studied by amide hydrogen D/H fractionation factors: application to staphylococcal nuclease.* Biochemistry, 1994. **33**(4): p. 1029-36.
102. Harris, T.K., C. Abeygunawardana, and A.S. Mildvan, *NMR studies of the role of hydrogen bonding in the mechanism of triosephosphate isomerase.* Biochemistry, 1997. **36**(48): p. 14661-75.
103. Cao, Z. and J.U. Bowie, *An energetic scale for equilibrium H/D fractionation factors illuminates hydrogen bond free energies in proteins.* Protein Sci, 2014. **23**(5): p. 566-75.

104. Selvaratnam, R., S. Chowdhury, B. VanSchouwen, and G. Melacini, *Mapping allostery through the covariance analysis of NMR chemical shifts.* Proc Natl Acad Sci U S A, 2011. **108**(15): p. 6133-8.
105. Selvaratnam, R., M.T. Mazhab-Jafari, R. Das, and G. Melacini, *The Auto-Inhibitory Role of the EPAC Hinge Helix as Mapped by NMR.* PLoS ONE, 2012. **7**(11): p. e48707.
106. Selvaratnam, R., B. VanSchouwen, F. Fogolari, M.T. Mazhab-Jafari, R. Das, and G. Melacini, *The projection analysis of NMR chemical shifts reveals extended EPAC autoinhibition determinants.* Biophys J, 2012. **102**(3): p. 630-9.
107. Cembran, A., L.R. Masterson, C.L. McClendon, S.S. Taylor, J. Gao, and G. Veglia, *Conformational equilibrium of N-myristoylated cAMP-dependent protein kinase A by molecular dynamics simulations.* Biochemistry, 2012. **51**(51): p. 10186-96.
108. Englander, S.W. and M.M. Krishna, *Hydrogen exchange.* Nat Struct Biol, 2001. **8**(9): p. 741-2.
109. Skinner, J.J., W.K. Lim, S. Bedard, B.E. Black, and S.W. Englander, *Protein dynamics viewed by hydrogen exchange.* Protein Sci, 2012. **21**(7): p. 996-1005.
110. Korzhnev, D.M., T.L. Religa, W. Banachewicz, A.R. Fersht, and L.E. Kay, *A transient and low-populated protein-folding intermediate at atomic resolution.* Science, 2010. **329**(5997): p. 1312-6.
111. Neudecker, P., P. Robustelli, A. Cavalli, P. Walsh, P. Lundstrom, A. Zarrine-Afsar, S. Sharpe, M. Vendruscolo, and L.E. Kay, *Structure of an intermediate state in protein folding and aggregation.* Science, 2012. **336**(6079): p. 362-6.
112. Tzeng, S.R. and C.G. Kalodimos, *Protein activity regulation by conformational entropy.* Nature, 2012. **488**(7410): p. 236-40.
113. Tzeng, S.R. and C.G. Kalodimos, *Allosteric inhibition through suppression of transient conformational states.* Nat Chem Biol, 2013. **9**(7): p. 462-5.
114. Lipchock, J.M. and J.P. Loria, *Nanometer propagation of millisecond motions in V-type allostery.* Structure, 2010. **18**(12): p. 1596-607.
115. Whittier, S.K., A.C. Hengge, and J.P. Loria, *Conformational motions regulate phosphoryl transfer in related protein tyrosine phosphatases.* Science, 2013. **341**(6148): p. 899-903.
116. Li, Y., N.L. Altorelli, F. Bahna, B. Honig, L. Shapiro, and A.G. Palmer, 3rd, *Mechanism of E-cadherin dimerization probed by NMR relaxation dispersion.* Proc Natl Acad Sci U S A, 2013. **110**(41): p. 16462-7.
117. Slice, L.W. and S.S. Taylor, *Expression of the catalytic subunit of cAMP-dependent protein kinase in Escherichia coli.* J Biol Chem, 1989. **264**(35): p. 20940-6.
118. Pervushin, K., R. Riek, G. Wider, and K. Wüthrich, *Attenuated T2 relaxation by mutual cancellation of dipole–dipole coupling and chemical shift anisotropy indicates an avenue to NMR structures of very large biological macromolecules in solution.* Proceedings of the National Academy of Sciences, 1997. **94**(23): p. 12366-12371.

119. Nietlispach, D., *Suppression of anti-TROSY lines in a sensitivity enhanced gradient selection TROSY scheme.* Journal of Biomolecular NMR, 2005. **31**(2): p. 161-166.
120. Delaglio, F., S. Grzesiek, G.W. Vuister, G. Zhu, J. Pfeifer, and A. Bax, *NMRPipe: a multidimensional spectral processing system based on UNIX pipes.* J Biomol NMR, 1995. **6**(3): p. 277-93.
121. Goddard, T.D.K., D.G. *SPARKY 3*. 1999.
122. Kim, J., L.R. Masterson, A. Cembran, R. Verardi, L. Shi, J. Gao, S.S. Taylor, and G. Veglia, *Dysfunctional conformational dynamics of protein kinase A induced by a lethal mutant of phospholamban hinder phosphorylation.* Proc Natl Acad Sci U S A, 2015. **112**(12): p. 3716-21.
123. Mildvan, A.S., T.K. Harris, and C. Abeygunawardana, *Nuclear magnetic resonance methods for the detection and study of low-barrier hydrogen bonds on enzymes.* Methods Enzymol, 1999. **308**: p. 219-45.
124. Bastidas, A.C., M.S. Deal, J.M. Steichen, Y. Guo, J. Wu, and S.S. Taylor, *Phosphoryl transfer by protein kinase A is captured in a crystal lattice.* J Am Chem Soc, 2013. **135**(12): p. 4788-98.
125. Cembran, A., J. Kim, J. Gao, and G. Veglia, *NMR mapping of protein conformational landscapes using coordinated behavior of chemical shifts upon ligand binding.* Phys Chem Chem Phys, 2014. **16**(14): p. 6508-18.
126. LiWang, A.C. and A. Bax, *Equilibrium protium/deuterium fractionation of backbone amides in U-C-13/N-15 labeled human ubiquitin by triple resonance NMR.* Journal of the American Chemical Society, 1996. **118**(50): p. 12864-12865.
127. Khare, D., P. Alexander, and J. Orban, *Hydrogen Bonding and Equilibrium Protium−Deuterium Fractionation Factors in the Immunoglobulin G Binding Domain of Protein G.* Biochemistry, 1999. **38**(13): p. 3918-3925.
128. Bowers, P.M. and R.E. Klevit, *Hydrogen bonding and equilibrium isotope enrichment in histidine-containing proteins.* Nat Struct Biol, 1996. **3**(6): p. 522-31.
129. Bastidas, A.C., J. Wu, and S.S. Taylor, *Molecular features of product release for the PKA catalytic cycle.* Biochemistry, 2015. **54**(1): p. 2-10.
130. Chestukhin, A., L. Litovchick, D. Schourov, S. Cox, S.S. Taylor, and S. Shaltiel, *Functional malleability of the carboxyl-terminal tail in protein kinase A.* J Biol Chem, 1996. **271**(17): p. 10175-82.
131. Nick Pace, C., J.M. Scholtz, and G.R. Grimsley, *Forces stabilizing proteins.* FEBS Lett, 2014. **588**(14): p. 2177-84.
132. Gardino, A.K., J. Villali, A. Kivenson, M. Lei, C.F. Liu, P. Steindel, E.Z. Eisenmesser, W. Labeikovsky, M. Wolf-Watz, M.W. Clarkson, and D. Kern, *Transient non-native hydrogen bonds promote activation of a signaling protein.* Cell, 2009. **139**(6): p. 1109-18.
133. Levinson, N.M. and S.G. Boxer, *A conserved water-mediated hydrogen bond network defines bosutinib's kinase selectivity.* Nat Chem Biol, 2014. **10**(2): p. 127-132.

134. Andersen, M.D., J. Shaffer, P.A. Jennings, and J.A. Adams, *Structural characterization of protein kinase A as a function of nucleotide binding. Hydrogen-deuterium exchange studies using matrix-assisted laser desorption ionization-time of flight mass spectrometry detection.* J Biol Chem, 2001. **276**(17): p. 14204-11.
135. Das, R., M. Abu-Abed, and G. Melacini, *Mapping allostery through equilibrium perturbation NMR spectroscopy.* Journal of the American Chemical Society, 2006. **128**(26): p. 8406-8407.
136. Mazhab-Jafari, M.T., R. Das, S.A. Fotheringham, S. SilDas, S. Chowdhury, and G. Melacini, *Understanding cAMP-dependent allostery by NMR spectroscopy: comparative analysis of the EPAC1 cAMP-binding domain in its apo and cAMP-bound states.* J Am Chem Soc, 2007. **129**(46): p. 14482-92.
137. Das, R., S. Chowdhury, M.T. Mazhab-Jafari, S. Sildas, R. Selvaratnam, and G. Melacini, *Dynamically driven ligand selectivity in cyclic nucleotide binding domains.* J Biol Chem, 2009. **284**(35): p. 23682-96.
138. Abu-Abed, M., R. Das, L. Wang, and G. Melacini, *Definition of an electrostatic relay switch critical for the cAMP-dependent activation of protein kinase A as revealed by the D170A mutant of RIalpha.* Proteins, 2007. **69**(1): p. 112-24.
139. Das, R., V. Esposito, M. Abu-Abed, G.S. Anand, S.S. Taylor, and G. Melacini, *cAMP activation of PKA defines an ancient signaling mechanism.* Proc Natl Acad Sci U S A, 2007. **104**(1): p. 93-8.
140. McNicholl, E.T., R. Das, S. SilDas, S.S. Taylor, and G. Melacini, *Communication between tandem cAMP binding domains in the regulatory subunit of protein kinase A-Ialpha as revealed by domain-silencing mutations.* J Biol Chem, 2010. **285**(20): p. 15523-37.
141. Lin, J., W.M. Westler, W.W. Cleland, J.L. Markley, and P.A. Frey, *Fractionation factors and activation energies for exchange of the low barrier hydrogen bonding proton in peptidyl trifluoromethyl ketone complexes of chymotrypsin.* Proc Natl Acad Sci U S A, 1998. **95**(25): p. 14664-8.
142. Veglia, G. and A. Cembran, *Role of conformational entropy in the activity and regulation of the catalytic subunit of protein kinase A.* FEBS J, 2013. **280**(22): p. 5608-15.
143. Masterson, L.R., A. Cembran, L. Shi, and G. Veglia, *Allostery and binding cooperativity of the catalytic subunit of protein kinase A by NMR spectroscopy and molecular dynamics simulations.* Adv Protein Chem Struct Biol, 2012. **87**: p. 363-89.
144. Li, F., M. Gangal, C. Juliano, E. Gorfain, S.S. Taylor, and D.A. Johnson, *Evidence for an internal entropy contribution to phosphoryl transfer: a study of domain closure, backbone flexibility, and the catalytic cycle of cAMP-dependent protein kinase.* J Mol Biol, 2002. **315**(3): p. 459-69.
145. Herberg, F.W., M.L. Doyle, S. Cox, and S.S. Taylor, *Dissection of the Nucleotide and Metal−Phosphate Binding Sites in cAMP-Dependent Protein Kinase.* Biochemistry, 1999. **38**(19): p. 6352-6360.

146. Crespi, H.L. and J.J. Katz, *High resolution proton magnetic resonance studies of fully deuterated and isotope hybrid proteins.* Nature, 1969. **224**(5219): p. 560-2.
147. Crespi, H.L., Rosenberg, R.M. Katzz, J.J., *proton magnetic resonance of proteins fully deuterated except for 1H-leucine side chains.* Science, 1968. **161**: p. 795-796.
148. Markley, J.L., I. Putter, and O. Jardetzky, *High-resolution nuclear magnetic resonance spectra of selectively deuterated staphylococcal nuclease.* Science, 1968. **161**(3847): p. 1249-51.
149. Putter, I., A. Barreto, J.L. Markley, and O. Jardetzky, *Nuclear magnetic resonance studies of the structure and binding sites of enzymes. X. Preparation of selectively deuterated analogs of staphylococcal nuclease.* Proc Natl Acad Sci U S A, 1969. **64**(4): p. 1396-403.
150. Meissner, A. and O.W. Sorensen, *Optimization of three-dimensional TROSY-type HCCH NMR correlation of aromatic (1)H-(13)C groups in proteins.* J Magn Reson, 1999. **139**(2): p. 447-50.
151. Kainosho, M., T. Torizawa, Y. Iwashita, T. Terauchi, A. Mei Ono, and P. Guntert, *Optimal isotope labelling for NMR protein structure determinations.* Nature, 2006. **440**(7080): p. 52-7.
152. Kasinath, V., K.G. Valentine, and A.J. Wand, *A 13C labeling strategy reveals a range of aromatic side chain motion in calmodulin.* J Am Chem Soc, 2013. **135**(26): p. 9560-3.
153. Venters, R.A., C.C. Huang, B.T. Farmer, 2nd, R. Trolard, L.D. Spicer, and C.A. Fierke, *High-level 2H/13C/15N labeling of proteins for NMR studies.* J Biomol NMR, 1995. **5**(4): p. 339-44.
154. Nietlispach, D., R.T. Clowes, R.W. Broadhurst, Y. Ito, J. Keeler, M. Kelly, J. Ashurst, H. Oschkinat, P.J. Domaille, and E.D. Laue, *An Approach to the Structure Determination of Larger Proteins Using Triple Resonance NMR Experiments in Conjunction with Random Fractional Deuteration.* Journal of the American Chemical Society, 1996. **118**(2): p. 407-415.
155. Goto, N.K., K.H. Gardner, G.A. Mueller, R.C. Willis, and L.E. Kay, *A robust and cost-effective method for the production of Val, Leu, Ile (delta 1) methyl-protonated 15N-, 13C-, 2H-labeled proteins.* J Biomol NMR, 1999. **13**(4): p. 369-74.
156. Gardner, K.H. and L.E. Kay, *Production and Incorporation of15N,13C,2H (1H-δ1 Methyl) Isoleucine into Proteins for Multidimensional NMR Studies.* Journal of the American Chemical Society, 1997. **119**(32): p. 7599-7600.
157. Gelis, I., A.M. Bonvin, D. Keramisanou, M. Koukaki, G. Gouridis, S. Karamanou, A. Economou, and C.G. Kalodimos, *Structural basis for signal-sequence recognition by the translocase motor SecA as determined by NMR.* Cell, 2007. **131**(4): p. 756-69.
158. Velyvis, A., A.M. Ruschak, and L.E. Kay, *An economical method for production of (2)H, (13)CH3-threonine for solution NMR studies of large protein complexes: application to the 670 kDa proteasome.* PLoS One, 2012. **7**(9): p. e43725.

159. Ayala, I., R. Sounier, N. Use, P. Gans, and J. Boisbouvier, *An efficient protocol for the complete incorporation of methyl-protonated alanine in perdeuterated protein.* J Biomol NMR, 2009. **43**(2): p. 111-9.
160. Tugarinov, V., P.M. Hwang, J.E. Ollerenshaw, and L.E. Kay, *Cross-correlated relaxation enhanced 1H[bond]13C NMR spectroscopy of methyl groups in very high molecular weight proteins and protein complexes.* J Am Chem Soc, 2003. **125**(34): p. 10420-8.
161. Religa, T.L., R. Sprangers, and L.E. Kay, *Dynamic regulation of archaeal proteasome gate opening as studied by TROSY NMR.* Science, 2010. **328**(5974): p. 98-102.
162. Ruschak, A.M., T.L. Religa, S. Breuer, S. Witt, and L.E. Kay, *The proteasome antechamber maintains substrates in an unfolded state.* Nature, 2010. **467**(7317): p. 868-71.
163. Sprangers, R. and L.E. Kay, *Quantitative dynamics and binding studies of the 20S proteasome by NMR.* Nature, 2007. **445**(7128): p. 618-22.
164. Shi, L. and L.E. Kay, *Tracing an allosteric pathway regulating the activity of the HslV protease.* Proc Natl Acad Sci U S A, 2014. **111**(6): p. 2140-5.
165. Saio, T., X. Guan, P. Rossi, A. Economou, and C.G. Kalodimos, *Structural basis for protein antiaggregation activity of the trigger factor chaperone.* Science, 2014. **344**(6184): p. 1250494.
166. Ruschak, A.M., A. Velyvis, and L.E. Kay, *A simple strategy for (1)(3)C, (1)H labeling at the Ile-gamma2 methyl position in highly deuterated proteins.* J Biomol NMR, 2010. **48**(3): p. 129-35.
167. Religa, T.L., A.M. Ruschak, R. Rosenzweig, and L.E. Kay, *Site-directed methyl group labeling as an NMR probe of structure and dynamics in supramolecular protein systems: applications to the proteasome and to the ClpP protease.* J Am Chem Soc, 2011. **133**(23): p. 9063-8.
168. Hemmer, W., M. McGlone, and S.S. Taylor, *Recombinant strategies for rapid purification of catalytic subunits of cAMP-dependent protein kinase.* Anal Biochem, 1997. **245**(2): p. 115-22.
169. Yonemoto, W.M., M.L. McGlone, L.W. Slice, and S.S. Taylor, *Prokaryotic expression of catalytic subunit of adenosine cyclic monophosphate-dependent protein kinase.* Methods Enzymol, 1991. **200**: p. 581-96.
170. Gardner, K.H., X. Zhang, K. Gehring, and L.E. Kay, *Solution NMR Studies of a 42 KDaEscherichiaColiMaltose Binding Protein/β-Cyclodextrin Complex: Chemical Shift Assignments and Analysis.* Journal of the American Chemical Society, 1998. **120**(45): p. 11738-11748.
171. Studier, F.W., *Protein production by auto-induction in high density shaking cultures.* Protein Expr Purif, 2005. **41**(1): p. 207-34.
172. Kay, L.E., M. Ikura, R. Tschudin, and A. Bax, *Three-dimensional triple-resonance NMR spectroscopy of isotopically enriched proteins.* Journal of Magnetic Resonance (1969), 1990. **89**(3): p. 496-514.

173. Yang, D.W. and L.E. Kay, *TROSY triple-resonance four-dimensional NMR spectroscopy of a 46 ns tumbling protein.* Journal of the American Chemical Society, 1999. **121**(11): p. 2571-2575.
174. Salzmann, M., K. Pervushin, G. Wider, H. Senn, and K. Wuthrich, *TROSY in triple-resonance experiments: new perspectives for sequential NMR assignment of large proteins.* Proc Natl Acad Sci U S A, 1998. **95**(23): p. 13585-90.
175. Salzmann, M., G. Wider, K. Pervushin, H. Senn, and K. Wuthrich, *TROSY-type triple-resonance experiments for sequential NMR assignments of large proteins.* Journal of the American Chemical Society, 1999. **121**(4): p. 844-848.
176. Sattler, M., J. Schleucher, and C. Griesinger, *Heteronuclear multidimensional NMR experiments for the structure determination of proteins in solutions employing pulsed field gradients.* Prog. Nucl. Magn. Reson. Spectrosc., 1999. **34**: p. 93-158.
177. Tugarinov, V. and L.E. Kay, *Side chain assignments of Ile delta 1 methyl groups in high molecular weight proteins: an application to a 46 ns tumbling molecule.* J Am Chem Soc, 2003. **125**(19): p. 5701-6.
178. Tugarinov, V. and L.E. Kay, *Ile, Leu, and Val methyl assignments of the 723-residue malate synthase G using a new labeling strategy and novel NMR methods.* J Am Chem Soc, 2003. **125**(45): p. 13868-78.
179. Sheppard, D., C. Guo, and V. Tugarinov, *Methyl-detected 'out-and-back' NMR experiments for simultaneous assignments of Alabeta and Ilegamma2 methyl groups in large proteins.* J Biomol NMR, 2009. **43**(4): p. 229-38.
180. Tugarinov, V., V. Venditti, and G. Marius Clore, *A NMR experiment for simultaneous correlations of valine and leucine/isoleucine methyls with carbonyl chemical shifts in proteins.* J Biomol NMR, 2014. **58**(1): p. 1-8.
181. Velyvis, A., H.K. Schachman, and L.E. Kay, *Assignment of Ile, Leu, and Val methyl correlations in supra-molecular systems: an application to aspartate transcarbamoylase.* J Am Chem Soc, 2009. **131**(45): p. 16534-43.
182. Xu, Y., M. Liu, P.J. Simpson, R. Isaacson, E. Cota, J. Marchant, D. Yang, X. Zhang, P. Freemont, and S. Matthews, *Automated assignment in selectively methyl-labeled proteins.* J Am Chem Soc, 2009. **131**(27): p. 9480-1.
183. Chao, F.A., J. Kim, Y. Xia, M. Milligan, N. Rowe, and G. Veglia, *FLAMEnGO 2.0: an enhanced fuzzy logic algorithm for structure-based assignment of methyl group resonances.* J Magn Reson, 2014. **245**: p. 17-23.
184. Xu, Y. and S. Matthews, *MAP-XSII: an improved program for the automatic assignment of methyl resonances in large proteins.* J Biomol NMR, 2013. **55**(2): p. 179-87.
185. Venditti, V., N.L. Fawzi, and G.M. Clore, *Automated sequence- and stereo-specific assignment of methyl-labeled proteins by paramagnetic relaxation and methyl-methyl nuclear Overhauser enhancement spectroscopy.* J Biomol NMR, 2011. **51**(3): p. 319-28.
186. Chao, F.A., L. Shi, L.R. Masterson, and G. Veglia, *FLAMEnGO: a fuzzy logic approach for methyl group assignment using NOESY and paramagnetic relaxation enhancement data.* J Magn Reson, 2012. **214**(1): p. 103-10.

187. Battiste, J.L. and G. Wagner, *Utilization of site-directed spin labeling and high-resolution heteronuclear nuclear magnetic resonance for global fold determination of large proteins with limited nuclear overhauser effect data.* Biochemistry, 2000. **39**(18): p. 5355-65.
188. Sahakyan, A.B., W.F. Vranken, A. Cavalli, and M. Vendruscolo, *Structure-based prediction of methyl chemical shifts in proteins.* J Biomol NMR, 2011. **50**(4): p. 331-46.
189. Han, B., Y. Liu, S.W. Ginzinger, and D.S. Wishart, *SHIFTX2: significantly improved protein chemical shift prediction.* J Biomol NMR, 2011. **50**(1): p. 43-57.
190. Li, D.W. and R. Bruschweiler, *PPM: a side-chain and backbone chemical shift predictor for the assessment of protein conformational ensembles.* J Biomol NMR, 2012. **54**(3): p. 257-65.
191. Fischer, E.H. and E.G. Krebs, *Conversion of phosphorylase b to phosphorylase a in muscle extracts.* J Biol Chem, 1955. **216**(1): p. 121-32.
192. Manning, G., G.D. Plowman, T. Hunter, and S. Sudarsanam, *Evolution of protein kinase signaling from yeast to man.* Trends Biochem Sci, 2002. **27**(10): p. 514-20.
193. Johnson, L.N. and R.J. Lewis, *Structural basis for control by phosphorylation.* Chem Rev, 2001. **101**(8): p. 2209-42.
194. Manning, G., D.B. Whyte, R. Martinez, T. Hunter, and S. Sudarsanam, *The Protein Kinase Complement of the Human Genome.* Science, 2002. **298**(5600): p. 1912-1934.
195. Endicott, J.A., M.E. Noble, and L.N. Johnson, *The structural basis for control of eukaryotic protein kinases.* Annu Rev Biochem, 2012. **81**: p. 587-613.
196. Reiterer, V., P.A. Eyers, and H. Farhan, *Day of the dead: pseudokinases and pseudophosphatases in physiology and disease.* Trends Cell Biol, 2014. **24**(9): p. 489-505.
197. Iyer, G.H., M.J. Moore, and S.S. Taylor, *Consequences of lysine 72 mutation on the phosphorylation and activation state of cAMP-dependent kinase.* J Biol Chem, 2005. **280**(10): p. 8800-7.
198. Dar, A.C. and K.M. Shokat, *The evolution of protein kinase inhibitors from antagonists to agonists of cellular signaling.* Annu Rev Biochem, 2011. **80**: p. 769-95.
199. Hatzivassiliou, G., K. Song, I. Yen, B.J. Brandhuber, D.J. Anderson, R. Alvarado, M.J. Ludlam, D. Stokoe, S.L. Gloor, G. Vigers, T. Morales, I. Aliagas, B. Liu, S. Sideris, K.P. Hoeflich, B.S. Jaiswal, S. Seshagiri, H. Koeppen, M. Belvin, L.S. Friedman, and S. Malek, *RAF inhibitors prime wild-type RAF to activate the MAPK pathway and enhance growth.* Nature, 2010. **464**(7287): p. 431-5.
200. Cowan-Jacob, S.W., W. Jahnke, and S. Knapp, *Novel approaches for targeting kinases: allosteric inhibition, allosteric activation and pseudokinases.* Future Med Chem, 2014. **6**(5): p. 541-61.
201. Fang, Z., C. Grutter, and D. Rauh, *Strategies for the selective regulation of kinases with allosteric modulators: exploiting exclusive structural features.* ACS Chem Biol, 2013. **8**(1): p. 58-70.

202. Arencibia, J.M., D. Pastor-Flores, A.F. Bauer, J.O. Schulze, and R.M. Biondi, *AGC protein kinases: from structural mechanism of regulation to allosteric drug development for the treatment of human diseases.* Biochim Biophys Acta, 2013. **1834**(7): p. 1302-21.
203. Wu, P., T.E. Nielsen, and M.H. Clausen, *FDA-approved small-molecule kinase inhibitors.* Trends Pharmacol Sci, 2015.
204. Whitehouse, S., J.R. Feramisco, J.E. Casnellie, E.G. Krebs, and D.A. Walsh, *Studies on the kinetic mechanism of the catalytic subunit of the cAMP-dependent protein kinase.* J Biol Chem, 1983. **258**(6): p. 3693-701.
205. Taylor, S.S., J. Yang, J. Wu, N.M. Haste, E. Radzio-Andzelm, and G. Anand, *PKA: a portrait of protein kinase dynamics.* Biochim Biophys Acta, 2004. **1697**(1-2): p. 259-69.
206. Taylor, S.S., C. Kim, D. Vigil, N.M. Haste, J. Yang, J. Wu, and G.S. Anand, *Dynamics of signaling by PKA.* Biochim Biophys Acta, 2005. **1754**(1-2): p. 25-37.
207. Sims, P.C., I.S. Moody, Y. Choi, C. Dong, M. Iftikhar, B.L. Corso, O.T. Gul, P.G. Collins, and G.A. Weiss, *Electronic measurements of single-molecule catalysis by cAMP-dependent protein kinase A.* J Am Chem Soc, 2013. **135**(21): p. 7861-8.
208. Adams, J.A., *Kinetic and catalytic mechanisms of protein kinases.* Chem Rev, 2001. **101**(8): p. 2271-90.
209. Cheng, H.C., B.E. Kemp, R.B. Pearson, A.J. Smith, L. Misconi, S.M. Van Patten, and D.A. Walsh, *A potent synthetic peptide inhibitor of the cAMP-dependent protein kinase.* J Biol Chem, 1986. **261**(3): p. 989-92.
210. Bhatnagar, D., R. Roskoski, Jr., M.S. Rosendahl, and N.J. Leonard, *Adenosine cyclic 3',5'-monophosphate dependent protein kinase: a new fluorescence displacement titration technique for characterizing the nucleotide binding site on the catalytic subunit.* Biochemistry, 1983. **22**(26): p. 6310-7.
211. Ni, D.Q., J. Shaffer, and J.A. Adams, *Insights into nucleotide binding in protein kinase A using fluorescent adenosine derivatives.* Protein Science, 2000. **9**(9): p. 1818-1827.
212. Zimmermann, B., S. Schweinsberg, S. Drewianka, and F.W. Herberg, *Effect of metal ions on high-affinity binding of pseudosubstrate inhibitors to PKA.* Biochem J, 2008. **413**(1): p. 93-101.
213. Freire, E., A. Schön, and A. Velazquez-Campoy, *Chapter 5 Isothermal Titration Calorimetry.* 2009. **455**: p. 127-155.
214. Masterson, L.R., T. Yu, L. Shi, Y. Wang, M. Gustavsson, M.M. Mueller, and G. Veglia, *cAMP-dependent protein kinase A selects the excited state of the membrane substrate phospholamban.* J Mol Biol, 2011. **412**(2): p. 155-64.
215. Metcalfe, E.E., N.J. Traaseth, and G. Veglia, *Serine 16 phosphorylation induces an order-to-disorder transition in monomeric phospholamban.* Biochemistry, 2005. **44**(11): p. 4386-96.
216. Axe, J.M., E.M. Yezdimer, K.F. O'Rourke, N.E. Kerstetter, W. You, C.-e.A. Chang, and D.D. Boehr, *Amino Acid Networks in a (β/α)8 Barrel Enzyme Change*

during Catalytic Turnover. Journal of the American Chemical Society, 2014. **136**(19): p. 6818-6821.
217. Boulton, S., M. Akimoto, R. Selvaratnam, A. Bashiri, and G. Melacini, *A tool set to map allosteric networks through the NMR chemical shift covariance analysis.* Sci Rep, 2014. **4**: p. 7306.
218. Ruschak, A.M. and L.E. Kay, *Proteasome allostery as a population shift between interchanging conformers.* Proc Natl Acad Sci U S A, 2012. **109**(50): p. E3454-62.
219. Velyvis, A. and L.E. Kay, *Measurement of active site ionization equilibria in the 670 kDa proteasome core particle using methyl-TROSY NMR.* J Am Chem Soc, 2013. **135**(25): p. 9259-62.
220. Chijiwa, T., A. Mishima, M. Hagiwara, M. Sano, K. Hayashi, T. Inoue, K. Naito, T. Toshioka, and H. Hidaka, *Inhibition of forskolin-induced neurite outgrowth and protein phosphorylation by a newly synthesized selective inhibitor of cyclic AMP-dependent protein kinase, N-[2-(p-bromocinnamylamino)ethyl]-5-isoquinolinesulfonamide (H-89), of PC12D pheochromocytoma cells.* J Biol Chem, 1990. **265**(9): p. 5267-72.
221. Kulanthaivel, P., Y.F. Hallock, C. Boros, S.M. Hamilton, W.P. Janzen, L.M. Ballas, C.R. Loomis, J.B. Jiang, and B. Katz, *Balanol: a novel and potent inhibitor of protein kinase C from the fungus Verticillium balanoides.* Journal of the American Chemical Society, 1993. **115**(14): p. 6452-6453.
222. Koide, K., M.E. Bunnage, L. Gomez Paloma, J.R. Kanter, S.S. Taylor, L.L. Brunton, and K.C. Nicolaou, *Molecular design and biological activity of potent and selective protein kinase inhibitors related to balanol.* Chem Biol, 1995. **2**(9): p. 601-8.
223. Kivi, R., P. Jemth, and J. Jarv, *Thermodynamic aspects of cAMP dependent protein kinase catalytic subunit allostery.* Protein J, 2014. **33**(4): p. 386-93.
224. Fersht, A.R., *Catalysis, binding and enzyme-substrate complementarity.* Proc R Soc Lond B Biol Sci, 1974. **187**(1089): p. 397-407.
225. Schramm, V.L., *Enzymatic transition states, transition-state analogs, dynamics, thermodynamics, and lifetimes.* Annu Rev Biochem, 2011. **80**(1): p. 703-32.
226. Gerlits, O., M.J. Waltman, S. Taylor, P. Langan, and A. Kovalevsky, *Insights into the phosphoryl transfer catalyzed by cAMP-dependent protein kinase: an X-ray crystallographic study of complexes with various metals and peptide substrate SP20.* Biochemistry, 2013. **52**(21): p. 3721-7.
227. Whitehouse, S. and D.A. Walsh, *Mg X ATP2-dependent interaction of the inhibitor protein of the cAMP-dependent protein kinase with the catalytic subunit.* Journal of Biological Chemistry, 1983. **258**(6): p. 3682-3692.
228. Toyoshima, C. and T. Mizutani, *Crystal structure of the calcium pump with a bound ATP analogue.* Nature, 2004. **430**(6999): p. 529-35.
229. Polier, S., R.S. Samant, P.A. Clarke, P. Workman, C. Prodromou, and L.H. Pearl, *ATP-competitive inhibitors block protein kinase recruitment to the Hsp90-Cdc37 system.* Nat Chem Biol, 2013. **9**(5): p. 307-12.

230. Gibbs, C.S. and M.J. Zoller, *Rational scanning mutagenesis of a protein kinase identifies functional regions involved in catalysis and substrate interactions.* J Biol Chem, 1991. **266**(14): p. 8923-31.
231. Narayana, N., T.C. Diller, K. Koide, M.E. Bunnage, K.C. Nicolaou, L.L. Brunton, N.H. Xuong, L.F. Ten Eyck, and S.S. Taylor, *Crystal structure of the potent natural product inhibitor balanol in complex with the catalytic subunit of cAMP-dependent protein kinase.* Biochemistry, 1999. **38**(8): p. 2367-76.
232. Foda, Z.H., Y. Shan, E.T. Kim, D.E. Shaw, and M.A. Seeliger, *A dynamically coupled allosteric network underlies binding cooperativity in Src kinase.* Nat Commun, 2015. **6**: p. 5939.
233. Wiseman, T., S. Williston, J.F. Brandts, and L.N. Lin, *Rapid Measurement of Binding Constants and Heats of Binding Using a New Titration Calorimeter.* Analytical Biochemistry, 1989. **179**(1): p. 131-137.
234. Kim, J., L.R. Masterson, A. Cembran, R. Verardi, L. Shi, J. Gao, S.S. Taylor, and G. Veglia, *Dysfunctional conformational dynamics of protein kinase A induced by a lethal mutant of phospholamban hinder phosphorylation.* Proc Natl Acad Sci U S A, 2015: p. 201502299.
235. Roberts, P.J. and C.J. Der, *Targeting the Raf-MEK-ERK mitogen-activated protein kinase cascade for the treatment of cancer.* Oncogene, 2007. **26**(22): p. 3291-3310.
236. Patterson, H., R. Nibbs, I. McInnes, and S. Siebert, *Protein kinase inhibitors in the treatment of inflammatory and autoimmune diseases.* Clin Exp Immunol, 2014. **176**(1): p. 1-10.
237. Zhang, J., P.L. Yang, and N.S. Gray, *Targeting cancer with small molecule kinase inhibitors.* Nat Rev Cancer, 2009. **9**(1): p. 28-39.
238. Dar, A.C. and K.M. Shokat, *The evolution of protein kinase inhibitors from antagonists to agonists of cellular signaling.* Annu Rev Biochem, 2011. **80**(1): p. 769-95.
239. Wang, Q., J.A. Zorn, and J. Kuriyan, *Chapter Two - A Structural Atlas of Kinases Inhibited by Clinically Approved Drugs*, in *Methods in Enzymology*, M.S. Kevan, Editor. 2014, Academic Press. p. 23-67.
240. Tong, M. and M.A. Seeliger, *Targeting conformational plasticity of protein kinases.* ACS Chem Biol, 2015. **10**(1): p. 190-200.
241. Dar, A.C. and K.M. Shokat, *The Evolution of Protein Kinase Inhibitors from Antagonists to Agonists of Cellular Signaling.* Annual Review of Biochemistry, Vol 80, 2011. **80**: p. 769-795.
242. Huse, M. and J. Kuriyan, *The conformational plasticity of protein kinases.* Cell, 2002. **109**(3): p. 275-82.
243. Taylor, S.S., R. Ilouz, P. Zhang, and A.P. Kornev, *Assembly of allosteric macromolecular switches: lessons from PKA.* Nat Rev Mol Cell Biol, 2012. **13**(10): p. 646-58.
244. Kim J., A.L.G., Chao F.A., Xia, Y., McClendon, C., Kornev A., Taylor S.S. and Veglia G, *A Dynamic Hydrophobic Core Orchestrates Allostery in Protein Kinases.* (under review), 2016.

245. Hanks, S.K., A.M. Quinn, and T. Hunter, *The protein kinase family: conserved features and deduced phylogeny of the catalytic domains.* Science, 1988. **241**(4861): p. 42-52.
246. Murray, A.J., *Pharmacological PKA inhibition: all may not be what it seems.* Sci Signal, 2008. **1**(22): p. re4.
247. Kulanthaivel, P., Y.F. Hallock, C. Boros, S.M. Hamilton, W.P. Janzen, L.M. Ballas, C.R. Loomis, J.B. Jiang, B. Katz, J.R. Steiner, and J. Clardy, *Balanol - a Novel and Potent Inhibitor of Protein-Kinase-C from the Fungus Verticillium-Balanoides (Vol 115, Pg 6452, 1993).* Journal of the American Chemical Society, 1993. **115**(22): p. 10468-10468.
248. Lochner, A. and J.A. Moolman, *The many faces of H89: a review.* Cardiovasc Drug Rev, 2006. **24**(3-4): p. 261-74.
249. Kim, J., G. Li, M.A. Walters, S.S. Taylor, and G. Veglia, *Uncoupling Catalytic and Binding Functions in the Cyclic AMP-Dependent Protein Kinase A.* Structure, 2016. **24**(3): p. 353-63.
250. Li, G.C., A.K. Srivastava, J. Kim, S.S. Taylor, and G. Veglia, *Mapping the Hydrogen Bond Networks in the Catalytic Subunit of Protein Kinase A Using H/D Fractionation Factors.* Biochemistry, 2015. **54**(26): p. 4042-9.
251. Engh, R.A., A. Girod, V. Kinzel, R. Huber, and D. Bossemeyer, *Crystal structures of catalytic subunit of cAMP-dependent protein kinase in complex with isoquinolinesulfonyl protein kinase inhibitors H7, H8, and H89. Structural implications for selectivity.* J Biol Chem, 1996. **271**(42): p. 26157-64.
252. Pucheta-Martinez, E., G. Saladino, M.A. Morando, J. Martinez-Torrecuadrada, M. Lelli, L. Sutto, N. D'Amelio, and F.L. Gervasio, *An Allosteric Cross-Talk Between the Activation Loop and the ATP Binding Site Regulates the Activation of Src Kinase.* Sci Rep, 2016. **6**: p. 24235.
253. Pasi, M., M. Tiberti, A. Arrigoni, and E. Papaleo, *xPyder: a PyMOL plugin to analyze coupled residues and their networks in protein structures.* J Chem Inf Model, 2012. **52**(7): p. 1865-74.
254. Baldwin, A.J. and L.E. Kay, *NMR spectroscopy brings invisible protein states into focus.* Nat Chem Biol, 2009. **5**(11): p. 808-14.
255. Kim J., A.L.G., Chao F.A., Xia, Y., McClendon, C., Kornev A., Taylor S.S. and Veglia G, *A Dynamic Hydrophobic Core Orchestrates Allostery in Protein Kinases.* (submitted), 2016.
256. Mittermaier, A. and L.E. Kay, *New tools provide new insights in NMR studies of protein dynamics.* Science, 2006. **312**(5771): p. 224-8.
257. Bouvignies, G. and L.E. Kay, *A 2D (1)(3)C-CEST experiment for studying slowly exchanging protein systems using methyl probes: an application to protein folding.* J Biomol NMR, 2012. **53**(4): p. 303-10.
258. Kleckner, I.R. and M.P. Foster, *GUARDD: user-friendly MATLAB software for rigorous analysis of CPMG RD NMR data.* J Biomol NMR, 2012. **52**(1): p. 11-22.

259. Massi, F., M.J. Grey, and A.G. Palmer, *Microsecond timescale backbone conformational dynamics in ubiquitin studied with NMR R-1p relaxation experiments.* Protein Science, 2005. **14**(3): p. 735-742.
260. Kung, J.E. and N. Jura, *Structural Basis for the Non-catalytic Functions of Protein Kinases.* Structure, 2016. **24**(1): p. 7-24.
261. Lavoie, H., N. Thevakumaran, G. Gavory, J.J. Li, A. Padeganeh, S. Guiral, J. Duchaine, D.Y.L. Mao, M. Bouvier, F. Sicheri, and M. Therrien, *Inhibitors that stabilize a closed RAF kinase domain conformation induce dimerization.* Nature Chemical Biology, 2013. **9**(7): p. 428-+.
262. Hari, S.B., E.A. Merritt, and D.J. Maly, *Conformation-selective ATP-competitive inhibitors control regulatory interactions and noncatalytic functions of mitogen-activated protein kinases.* Chem Biol, 2014. **21**(5): p. 628-35.
263. Hantschel, O., *Unexpected off-targets and paradoxical pathway activation by kinase inhibitors.* ACS Chem Biol, 2015. **10**(1): p. 234-45.
264. Lisi, G.P. and J.P. Loria, *Solution NMR Spectroscopy for the Study of Enzyme Allostery.* Chem Rev, 2016.
265. Bhabha, G., J. Lee, D.C. Ekiert, J. Gam, I.A. Wilson, H.J. Dyson, S.J. Benkovic, and P.E. Wright, *A dynamic knockout reveals that conformational fluctuations influence the chemical step of enzyme catalysis.* Science, 2011. **332**(6026): p. 234-8.
266. Gustavsson, M., N.J. Traaseth, and G. Veglia, *Probing ground and excited states of phospholamban in model and native lipid membranes by magic angle spinning NMR spectroscopy.* Biochim Biophys Acta, 2012. **1818**(2): p. 146-53.
267. Gustavsson, M., R. Verardi, D.G. Mullen, K.R. Mote, N.J. Traaseth, T. Gopinath, and G. Veglia, *Allosteric regulation of SERCA by phosphorylation-mediated conformational shift of phospholamban.* Proc Natl Acad Sci U S A, 2013. **110**(43): p. 17338-43.
268. Carroll, M.J., R.V. Mauldin, A.V. Gromova, S.F. Singleton, E.J. Collins, and A.L. Lee, *Evidence for dynamics in proteins as a mechanism for ligand dissociation.* Nature Chemical Biology, 2012. **8**(3): p. 246-252.
269. Long, D., C.B. Marshall, G. Bouvignies, M.T. Mazhab-Jafari, M.J. Smith, M. Ikura, and L.E. Kay, *A comparative CEST NMR study of slow conformational dynamics of small GTPases complexed with GTP and GTP analogues.* Angew Chem Int Ed Engl, 2013. **52**(41): p. 10771-4.
270. Akimoto, M., R. Selvaratnam, E.T. McNicholl, G. Verma, S.S. Taylor, and G. Melacini, *Signaling through dynamic linkers as revealed by PKA.* Proc Natl Acad Sci U S A, 2013. **110**(35): p. 14231-6.
271. Lisi, G.P., G.A. Manley, H. Hendrickson, I. Rivalta, V.S. Batista, and J.P. Loria, *Dissecting Dynamic Allosteric Pathways Using Chemically Related Small-Molecule Activators.* Structure, 2016.
272. Gardner, K.H. and L.E. Kay, *Production and Incorporation of 15N, 13C, 2H (1H-δ1 Methyl) Isoleucine into Proteins for Multidimensional NMR Studies.* Journal of the American Chemical Society, 1997. **119**(32): p. 7599-7600.

273. Tugarinov, V. and L.E. Kay, *Methyl Groups as Probes of Structure and Dynamics in NMR Studies of High-Molecular-Weight Proteins.* ChemBioChem, 2005. **6**(9): p. 1567-1577.
274. Long, D., M. Liu, and D. Yang, *Accurately Probing Slow Motions on Millisecond Timescales with a Robust NMR Relaxation Experiment.* Journal of the American Chemical Society, 2008. **130**(8): p. 2432-2433.
275. Lundstrom, P., P. Vallurupalli, T.L. Religa, F.W. Dahlquist, and L.E. Kay, *A single-quantum methyl 13C-relaxation dispersion experiment with improved sensitivity.* J Biomol NMR, 2007. **38**(1): p. 79-88.
276. Mulder, F.A.A., N.R. Skrynnikov, B. Hon, F.W. Dahlquist, and L.E. Kay, *Measurement of Slow (μs−ms) Time Scale Dynamics in Protein Side Chains by15N Relaxation Dispersion NMR Spectroscopy: Application to Asn and Gln Residues in a Cavity Mutant of T4 Lysozyme.* Journal of the American Chemical Society, 2001. **123**(5): p. 967-975.
277. Mulder, F.A., N.R. Skrynnikov, B. Hon, F.W. Dahlquist, and L.E. Kay, *Measurement of slow (micros-ms) time scale dynamics in protein side chains by (15)N relaxation dispersion NMR spectroscopy: application to Asn and Gln residues in a cavity mutant of T4 lysozyme.* J Am Chem Soc, 2001. **123**(5): p. 967-75.
278. Fenwick, M.K. and R.E. Oswald, *NMR spectroscopy of the ligand-binding core of ionotropic glutamate receptor 2 bound to 5-substituted willardiine partial agonists.* J Mol Biol, 2008. **378**(3): p. 673-85.
279. Palmer, A.G., 3rd, *Nmr probes of molecular dynamics: overview and comparison with other techniques.* Annu Rev Biophys Biomol Struct, 2001. **30**: p. 129-55.